Ph.D. Thesis

Ultrafast Molecular Dynamics and Third-order Nonlinear Optical Studies of Novel Organic, Inorganic and Energetic Materials

K. N. Krishnakanth

प्रतिष्ठित संस्थान
INSTITUTION OF EMINENCE
राष्ट्रीय अपेक्षाएँ, वैश्विक मानक
National Needs, Global Standards
हैदराबाद विश्वविद्यालय
UNIVERSITY OF HYDERABAD

Advanced Centre of Research in High Energy materials
School of Physics
University of Hyderabad
Hyderabad 500046, Telangana, India

July 2020

A Thesis Entitled

Ultrafast Molecular Dynamics and Third-order Nonlinear Optical Studies of Novel Organic, Inorganic and Energetic Materials.

Submitted to the

University of Hyderabad
Towards partial fulfilment for the degree of
Doctor of Philosophy in Physics

By

Katturi Naga Krishnakanth

Under the Supervision of

Prof. Soma Venugopal Rao

Advanced Centre of Research in High Energy Materials **(ACRHEM),**
School of Physics, University of Hyderabad,
Hyderabad 500046, Telangana, India.

July 2020

Dedicated to my supervisor Prof. Soma Venugopal Rao

And

My Family

Declaration

I, **Katturi Naga Krishnakanth**, hereby declare that the work reported in this thesis entitled **"Ultrafast molecular dynamics and third-order nonlinear optical properties of novel organic, inorganic and energetic ~~[illegible]~~ materials"** is original and has been carried out by me under the supervision of **Prof. Soma Venugopal Rao**, Professor in ACRHEM (School of Physics), University of Hyderabad, Hyderabad, Telangana, India, as per the Ph.D. ordinances of the University, which is also free from plagiarism. I further declare that this work has not submitted for the award of a research degree of any other University. I hereby agree that my thesis can be deposited in Shodhganga/INFLIBNET. A report on plagiarism statistics from the University Librarian is enclosed.

S. Venugopal Rao
24/7/2020

Krishnakanth
24/07/20

Katturi Naga Krishnakanth
Reg. No: 15ACPA06

S. Venugopal Rao
24/7/2020

Prof. Soma Venugopal Rao
Thesis Supervisor,
ACRHEM,
University of Hyderabad.

Dr. S. VENUGOPAL RAO
Professor
Advance Centre of Research in
High Energy Materials (ACRHEM)
UNIVERSITY OF HYDERABAD
Hyderabad-500 046. T.S. INDIA.

Prof. Soma Venugopal Rao

Tel.: +91-40 2313 8811
Fax: +91-40 2301 2800
E-mail: svrsp@uohyd.ernet.in
soma_venu@uohyd.ac.in

ACRHEM
University of Hyderabad,
Prof. C. R. Rao Road,
Gachibowli, Hyderabad
500046, Telangana, India

Certificate

This is to certify that the thesis entitled **“Ultrafast molecular dynamics and third-order nonlinear optical properties of novel organic, inorganic and energetic ~~[illegible]~~ materials”** being submitted to the University of Hyderabad by **Katturi Naga Krishnakanth** (Reg. No. 15ACPA06), for the award of the degree of Doctor of Philosophy in Physics, is a record of *bonafide* work carried out by him under my supervision and is free of plagiarism. The matter embodied in this report has not been submitted to any other University or Institution for the award of any degree or diploma.

S.Venugopal Rao
24/7/2020

S.Venugopal Rao
24/7/2020

Prof. Soma Venugopal Rao
(Supervisor)

Dr. S. VENUGOPAL RAO
Professor
Advance Centre of Research in
High Energy Materials (ACRHEM)
UNIVERSITY OF HYDERABAD
Hyderabad-500 046. T.S. INDIA.

V. Kameswara

Director
ACRHEM

Dr. V. KAMESWARA RAO
Director
(ACRHEM)

Dean
School of Physics

DEAN
School of Physics
University of Hyderabad
Hyderabad-500 046, INDIA

CERTIFICATE

This is to certify that the thesis entitled **"Ultrafast molecular dynamics and third-order nonlinear optical properties of novel organic, inorganic and energetic** [redacted] materials" submitted by **Katturi Naga Krishnakanth** bearing registration number **15ACPA06** in partial fulfillment of the requirements for award of **Doctor of Philosophy in physics at ACRHEM, School of physics, University of Hyderabad** is a bonafide work carried out by him under my supervision and guidance. This thesis is free from plagiarism and has not been submitted previously in part or in full to this or any other University or Institution for award of any degree or diploma. Further, the student has the following publications before submission of the thesis for adjudication.

S.Venugopal Rao.
24/7/2020

1. **Katturi, Naga Krishnakanth**, Shivaprasad Achari Balahoju, A. R. Ramya, Chinmoy Biswas, Sai Santhosh Kumar Raavi, Lingamallu Giribabu, and Venugopal Rao Soma. "Ultrafast photophysical and nonlinear optical properties of novel free base and axially substituted phosphorus (V) corroles." *Journal of Molecular Liquids* 311 (2020): 113308.
2. **Katturi, Naga Krishnakanth**, Govind Reddy, Chinmoy Biswas, Sai Santosh Kumar Raavi, Lingamallu Giribabu, and Venugopal Rao Soma. "Ultrafast nonlinear optical properties and excited-state dynamics of Soret-band excited D-π-D porphyrins." *Optical Materials* 107 (2020): 110041.
3. **K. N., Krishnakanth,** Byram Chandu, M. S. S. Bharathi, Sai Santhosh Kumar Raavi, and S. Venugopal Rao. "Ultrafast excited state dynamics and femtosecond nonlinear optical properties of laser fabricated Au and Ag50Au50 nanoparticles." *Optical Materials* 95 (2019): 109239.
4. **K. N., Krishnakanth,** Sudipta Seth, Anunay Samanta, and S. Venugopal Rao. "Broadband ultrafast nonlinear optical studies revealing exciting multi-photon absorption coefficients in phase pure zero-dimensional Cs_4PbBr_6 perovskite films." *Nanoscale* 11, no. 3 (2019): 945-954.
5. **Katturi Naga**, **Krishnakanth,** Sudipta Seth, Anunay Samanta, and Soma Venugopal Rao. "Broadband femtosecond nonlinear optical properties of $CsPbBr_3$ perovskite nanocrystals." *Optics Letters* 43, no. 3 (2018): 603-606.
6. Ultrafast Coherent Anti-Stokes Raman Spectroscopic Studies of Nitro/Nitrogen Rich Aryl-Tetrazole Derivatives., **Naga Krishnakanth Katturi**, Sarang Dev G, Nagarjuna Kommu, Gopala Krishna Podagatlapalli, Venugopal Rao Soma, Chemical Physics Letters (*Under Review*).

The following courses have taken as the part of the course work:

Course No.	Course offered at	Title of the course	Credits	Pass/Fail
1	SoP	Advanced electromagnetic theory	4	Pass
2	SoP	Advanced Experimental techniques	4	Pass
3	SEST	Characterization of Materials-Microscopy	4	Pass
4	ACRHEM	Research methodology	4	Pass

S.Venugopal Rao
24/7/2020

Supervisor

Prof. Soma Venugopal Rao
ACRHEM, University of Hyderabad,
Hyderabad, India.

Dr. S. VENUGOPAL RAO
Professor
Advance Centre of Research in
High Energy Materials (ACRHEM)
UNIVERSITY OF HYDERABAD
Hyderabad-500 046. T.S. INDIA.

Director

ACRHEM
University of Hyderabad,
Hyderabad, India.

Dr. V. KAMESWARA RAO
Director
(ACRHEM)

Dean

School of Physics
University of Hyderabad,
Hyderabad, India.

DEAN
School of Physics
University of Hyderabad
Hyderabad-500 046, INDIA

Acknowledgements

First and foremost, I would like to express my sincere gratitude to my supervisor, **Prof. Soma Venugopal Rao,** for his exceptional guidance, motivation, and unconditional support in carrying out this research work. I consider myself blessed for getting a chance to pursue my doctoral studies with him. I truly enjoyed working with him in the last five years and his skilful guidance and patience are greatly admired. It is my pleasure to thank the present director, Dr V. Kameswara Rao, and former directors of ACRHEM for their support in all aspects towards completion of this work. I also thank the Dean, School of Physics (SoP), UoH, for the academic support. I sincerely thank my doctoral committee members Prof. A.K. Chaudhary and Prof. Sunil Singh for their invaluable suggestions in and out of the doctoral committee meetings. I would like to thank Defence Research and Development Organization (DRDO), India for providing me the financial support (through ACRHEM) to carry out my PhD. I thank all the teaching staff of ACRHEM and SoP for conducting the classes and explaining the nitty-gritty things in the core subjects. I would also like to thank all the non-teaching staff of ACRHEM and SoP for their co-operation as when required. I would also like to thank Dr Sai Santhosh Kumar Raavi and Chinmoy Biswas IIT-Hyderabad (collaborative work) for their valuable suggestions and support. Also, I would like to thank Prof. Giribabu Lingamallu IICT-Hyderabad for his support in providing us samples to carry out my research work. I would like to thank Prof. Samanta and Dr. Sudipta Seth, School of Chemistry, UoH for their fruitful collaboration work. I would like to thank my senior specially Dr. M. Venkatesh for his help in solving the LabVIEW programme and also Dr. P. Gopala Krishna, Dr Syed Hamad, Dr E. Nageswara Rao, Dr Y Balaji, Dr P T Anusha, Dr E Narasimha Rao for helping me to understand the experiments and for fruitful discussions. I would like to thank my friends Mr. G. Sarang dev, Ms. M.S.S. Bharathi and Mr. D. Ganesh for their help and support during the experiment and also Mr. Samuel Anurag, Mr. J Rajendhar, Dr. Abdul Kalam S, Mr. G Nagaraju, Mr. J yellaigh, Mr. N. Lingamurthy for their fruitful discussions in these years. Without their company and help these years would have been much tougher. Most importantly I am grateful to have a loving family my father Mr Katturi Rama Kutumba Rao, Mother Mrs Prameela, my Brother Mr Satya Prakash, and my sister G. Janaki for their unconditional love, endless support, encouragement giving me strength to achieve my ambitions. Finally, I would like to thank again my Prof. S. Venugopal Rao without his support these words have no meaning.

K N Krishnakanth.

Contents

List of Figures

List of Tables

List of Tables

Chapter 1 Introduction

Abstract

This Chapter presents an introduction to the thesis work, mainly revealing the motivation of the present study and background of the investigated materials. We discuss the significance and principles of different ultrafast spectroscopic techniques employed in this study. Various spectroscopic processes occurring in a molecule after the photoexcitation, along with their third-order nonlinear optical properties, are elaborated. We also deliberate the importance of ultrafast photophysical processes of these materials, as well as the significance of ultrafast spectroscopy in understanding energetic materials is explained. Finally, we provide a summary and outline of the thesis towards the end of the Chapter.

1.1 Introduction and Motivation

Light triggers the most fundamental processes on earth, mainly photosynthesis, which is the primary reaction which nurtures life on earth, and photoreception or light reception of plants for possible vision. To drive these reactions efficiently the primary processes either have to be faster than dissipation of energy or to take place in a specific geometry that drives the reaction along the required pathway. Molecules which participate in such reactions (reception and transduction) are usually light absorbers with strong spectral properties. The optical spectroscopic techniques are powerful tools to investigate the molecular structure and dynamics. The absorption of light upon illumination initiates most of the chemical reactions, the fact that motivates several of us to study the photophysical and photochemical reactions of different associated molecules using a variety of time-resolved spectroscopic techniques. Many researchers have studied these reactions earlier (in the 1950-60s) using flash photolysis and photon and electron pulse techniques. A few of these findings were awarded the Nobel prize for chemists M. Eigen, G.W. Ronald, and G. Porter in 1967 for studying the fast chemical reactions.[1] The generation of optical pulses of the order of few femtoseconds (10^{-15} s) brought to light new era of opportunities for studying the molecular reactions in the femtosecond and sub-femtosecond time domain.[2-4] Recent technologies have facilitated the development of ultrashort laser pulses of the order of few attoseconds (10^{-18} s), achieved using higher harmonic generation[5-7], which falls under the soft X-ray regime of the electromagnetic (EM) spectrum. Time-resolved spectroscopies, typically utilizing 10-100 femtosecond (fs) pulses, provide a powerful tool, and play an active role in investigating the ultrafast dynamics.[4] These developments were awarded the Nobel prize in chemistry for Prof. A.H. Zewail in 1999 for his seminal contributions to the understandings of chemical reactions using fs spectroscopy.[8-9] These original experiments stimulated the research in complex reaction dynamics such as photosynthesis,[10-12] and light-induced reaction dynamics of artificial systems.[13-15] Various spectroscopic techniques such as transient absorption (TA) and time-resolved fluorescence are generally used to study the excited state dynamics and motion of vibrational wave packets in real-time.

The effect of an intense or short laser pulse on the optical properties of the materials opens up new opportunities for investigations and applications in optical switching, optical communications, and bio-imaging technologies. The invention of the second harmonic generation (SHG) by Franken et al.[16] from a quartz crystal in 1961 led to the birth of the field of nonlinear optics (NLO). The third-order NLO properties, i.e. nonlinear refraction, absorption, and response, play a crucial role in the development and advancement of photonic device applications. The electric polarization (induced dipole moment per unit volume) has an essential role in the nonlinear optical properties upon illumination of the active optical fields (~10^8 V/m). An efficient NLO process requires that the material should have control over the amplitude, phase, polarization, and frequency of the input field with high sensitivity.[17-18] In this contest, a variety of complex materials are synthesized such as organometallic compounds and nanocrystals, etc., and studied by different techniques such as (i) Z-scan (ii) Degenerate four-wave-mixing (DFWM) (iii) Electric field induced second harmonic generation (EFISHG) (iv) Third harmonic generation (THG) etc..[19-20] The NLO properties of organic materials, in particular, can be tailored by introducing metals (in the core) and π- conjugation backbone, donor, and/or acceptor groups. Apart from these materials, metal nanoparticles, mainly those of gold (Au), have been demonstrated to possess strong third-order NLO properties depending on their size and shape due to their localized surface plasmon resonance. [21-23] Recently, lead halide based Perovskite nanocrystals (NCs) have emerged as an excellent NLO material possessing strong two-photon absorption (TPA) and multi-photon absorption coefficients, stronger than many of the state-of-the-art materials investigated thus far.[24-26] The requirement of efficient NLO materials with fast response and large third-order NLO susceptibility $\chi^{(3)}$ brings the new technological advances in the materials processing or synthesis in both organic and inorganic materials. The miniaturization of the material size up to a nanoscale level opens new possibilities of achieving efficient NLO materials. In this work we present our studies of NLO properties and excited state dynamics of both organic (porphyrins, corroles) and inorganic (perovskite NCs, metal nanoparticles) materials.

Recently, metal halide Perovskites (MHPs) have also gained notable interest due to their versatility and applicability in diverse areas such as photonics and optoelectronics for preparing LEDs,[27-28] lasers,[29-34] and photodetectors. Because of their (a) tunable broad absorption capability (b) narrow emission (c) high charge carrier mobility (d) great photoluminescence quantum yield (PL QY).[35-38] Higher-order NLO properties such as MPA[24-25, 39-40] and saturable absorption (SA)[38, 41-42] from Perovskite NCs triggered an extensive research resulting in a range of applications in ultrafast lasers and optical data storage.[43] The organometallic halide ($CH_3NH_3PbX_3$, X = Br, Cl, I) Perovskite NC films have demonstrated NLO properties strong i.e. two-photon absorption and nonlinear refraction ($\beta = 10^{-9}$ mW^{-1}, $n_2 = 10^{-13}$ cm^2 W^{-1}).[44] On the other hand, all inorganic $CsPbBr_3$ Perovskite NCs demonstrated a large two-photon absorption (2PA) cross-section values (~10^5 GM)[45] combined with stability,[46] tunablity,[47-48] and lasing capabilities. The combination of organic-inorganic halide perovskite with structural modification demonstrated superior NLO properties such as multi-photon absorption in NIR region [24] and second harmonic generation (SHG).[49] Recent studies of the MPA cross-section of organic-inorganic perovskite NCs ($CsPbBr_3$/$MAPbI_3$) have shown large 2PA cross-section values of ~10^6 GM, which are one or two orders of magnitude stronger than conventional semiconductor (CdSe and CdTe) QDs.

Furthermore, π-conjugated organic molecules (e.g., Corroles, porphyrins, and phthalocyanines,) have also demonstrated superior third-order NLO properties compared to other organic molecules.[50-51] Particularly, organic molecules having large π-conjugation including corroles and porphyrins with donor-acceptor (D-π-A, D-π-D, and A-π-A) systems are found to be suitable for many applications such as photovoltaics[52-57] and up-conversion[58] and they possess characteristics similar to the natural photosynthetic pigments.[59-61] Likewise, their NLO properties are found to be superior to other organic compounds, which mainly arises from their extended large π-electron conjugation having large transition dipole moments in their ground and excited states.[62-68] It is known that the organic materials having large π-bond conjugation are known to illustrate significant dipole moments and create a delocalized distribution of electric charges due to intramolecular charge transfer (ICT) resulting in high electrical polarization, which is advantageous for significant NLO response.[69-74]

Among several organic materials porphyrins possessing incredible chemical and optical properties.[75-77] It has been successfully proven that alteration of the macrocyclic structure (core and other peripheral substituents) of these molecules significantly affects their chemical, optical, and optoelectronic properties.[56-57, 77-78] The schematic of unsubstituted porphyrin ring is shown in figure 1.1(a) which contains four pyloric rings connected through four methane bridges to form a cyclic molecule (macrocycle) with 20 corban and 4 nitrogen atoms, which can accommodate a metal ion in the centre. The porphyrins are substituted on the periphery 12 positions (eight β positions, four meso positions).[60-70] Porphyrins are highly coloured compounds due to its complicated electronic structure, which possess intense absorption band in the visible region (Q-band) and more intense absorption band (Soret-band) in the UV region. Their optical properties are easily tuned by incorporating the metals or non-metals into the core and peripheral substituents.[83-84] As a consequence, several research groups are demonstrated porphyrins in artificial photo-devices such as photonic devices,[79] molecular switches,[80] and dye-sensitized solar cells (DSSCs) for solar energy conversion.[57, 81-82] There exists great flexibility in modulating physicochemical attributes by synthetic substitutions on planar π-conjugated porphyrin ring and central metal ion, which can be incorporated into donor-acceptor assemblies. In general, D-π-A porphyrin systems possess good light-harvesting properties and favourable electrical properties.[68, 83] By amending the D-π-A design as sensitizers for DSSC applications to the D-π-A approach, porphyrins can be potential candidates as hole-transporting materials for optoelectronic applications.[84]

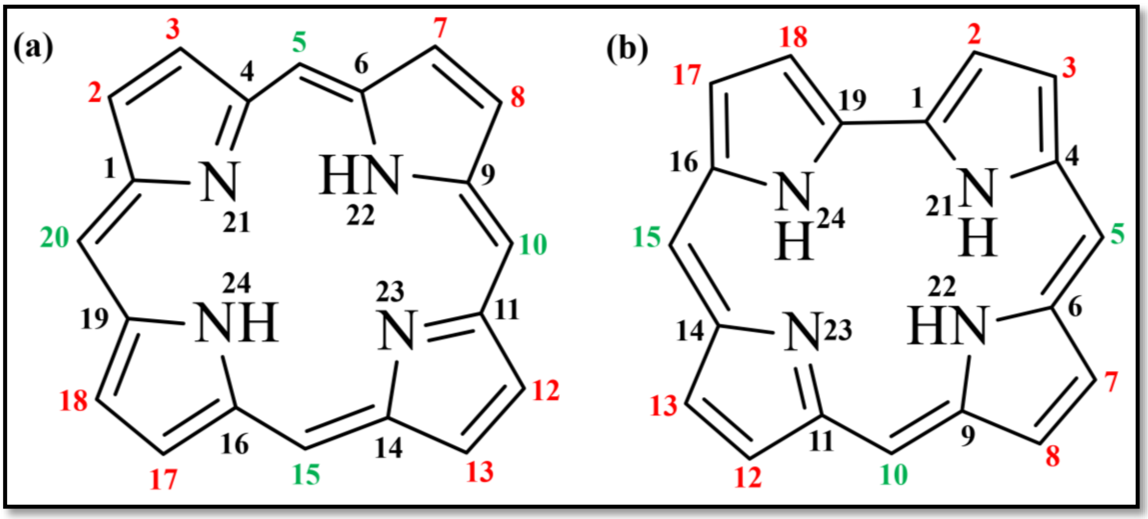

Figure 1.1 (a) Parent structure of a porphyrin molecule (b) Corrole molecule

Understanding the excited state or charge transfer dynamics are crucial for many applications such as solar energy conversion, information storage, catalysis, and photonics. Thus, understanding their excited state properties are important for fundamental science and applications of such molecules. Also, the NLO properties of porphyrins was explored extensively arising mainly from the delocalized π-electrons, which find applications in many fields such as optical limiting, optical switching, storage, bio-imaging, etc.. The metal incorporated porphyrins offers large transition dipole moments in the ground and excited states for a given electric field, which is possibly responsible for the observed strong optical nonlinearities in these molecules.[56, 85-86] The applications of porphyrins are mostly associated with electronic transitions taking place in Q-band transitions. Accordingly, it is important to study their excited state dynamics involving singlet and triplet absorption properties due to their importance in photonics applications.[87-88] Also, the nonlinear transmission properties of these porphyrin molecules depend on the characteristics of excited states and corresponding energy transfer processes.

Apart from porphyrins, corroles too belong to the tetrapyrrolic family, despite having one less *meso*-carbon. The corroles preserve the aromaticity (18 π–electron) of porphyrins, as shown in figure 1.1(b). The corrole ring consists of four nitrogen atoms in the centre and 19 carbons atoms in the molecule. The corroles possess attractive properties compared to porphyrins, such as (i) higher fluorescence (ii) stability (iii) lower oxidation potentials (iv) broad absorption and (v) more significant stoke shifts. Similar to porphyrins, by adding various metals or transition metals to the corrole macrocycle, the optical properties can be tuned due to changes in the energy gap of the molecular orbitals. They find applications in fields such as biomedical imaging, photonic devices.[89-93] The addition of the metal/transition metal to the corrole macrocycle improves the (a) PL QY (b) photoinduced electron transfer process (c) triplet yields.[58, 94-98] On the other hand, the NLO response of corroles has gained tremendous interest compared to porphyrins due to its highly conjugated π-electron distribution. Although the NLO response is higher in corroles only a few researchers have investigated the NLO response of corroles, and they achieved good NLO coefficients compared to porphyrins. [65, 99] The corroles macrocycle cavity is smaller than the porphyrin, which can accommodate the trivalent group 13 metals (Zn, Mg, Al and Ga) and forms metallocorroles. As a result, their photophysical and spectroscopic properties are efficiently tuned, such as robust PL QYs, i.e. fluorescence from S_1-S_0, dual fluorescence (S_2-S_0, S_1-S_0) and higher triplet yields, superior to that of porphyrins. These properties are attractive in the case of DSSCs, photodynamic therapy, and photonic devices. Liu et al.[100] have demonstrated corroles possess a planar rigid molecular structure with large Frank-Condon vibration states and large S_2 displacements compared to metalloporphyrins. Understanding these processes is essential to develop new molecules with dynamic optical properties.

We further extended our studies to the electronic and vibrational dynamics of energetic materials (EMs) to comprehensively understand their excited and ground-state dynamics. EMs contains vast energy in the chemical form which can be converted to kinetic energy upon molecular decomposition and used for industrial and military applications.[101] Excited-states of the EMs provide an insight into the molecular decomposition mechanisms.[102-104] The detailed investigation of the electronic, chemical and structural changes of the excited states of EMs enables us to comprehend the behaviour of EMs at the molecular level. Consequently, vast amount of research has been carried out to understand the reaction mechanisms and to enhance the inherent properties of EMs.[105-111] The nonradiative transitions in EMs produce local heating that creates hotspots which initiate the chain reactions in EMs.[112] Under the influence of shock waves, the EMs goes through a series of energy transfer (ET) processes before the disruption of their bonds. For example, Wu et al. have shown the energy relaxation/dissociation process in liquid nitromethane which occurs at a time scale of 2.56 ps by using transient grating spectroscopy as shown in figure 1.2.[113] When an EM is influenced by a shock wave, initially, several phonons gets generated, and later, the low-frequency modes will be excited via phonon-vibron coupling known as multi-phonon up-pumping.[114-115] Further, the vibrational energy transfer takes place from one vibrational mode to another mode via intramolecular vibrational redistribution (IVR). As a consequence, the distributed energies localized in one or a few chemical bonds, resulting in the dissociation, which initiates the ignition in EMs.[106] Hence, IVR is believed to be directly participating in the vibrational energy transfer and breaking of chemical bonds in energetic materials (EMs). However, the visualization of ultrafast coherent phenomena such as IVR is tedious since it involves the coupling of several vibrational modes.[116] In this context, excitation, and relaxations of vibrational modes (to their lower vibrational states) of EMs were performed in the UV or IR spectral range and typically happens in 100’s of fs duration. The EMs can be excited to higher states under UV laser illumination, and it leads to decomposition.[117-118] Previous research studies reveal that the ground electronic, vibrational states of EMs have been recognized to be prominent in the energy transfer processes. Nitro substituted arene compounds are essential in the field of defense and civilian applications due to their extended energetic properties.[119] However, the well-known polynitro arenes such as TNT, TATB, Picric acid, etc. exhibit moderate performance.[120] Recently, it was reported that the derivatives of azole substituted polynitro-arenes enhance densities and performance.[121] Especially, the substitution of azoles such as triazole or tetrazole improves the positive heat of formation due to the presence of higher amounts of nitrogen.[122-125]

One of our main motives at ACRHEM is to understand the laser pulse interaction with high energy materials for designing superior energetics. To realize this, we have developed ultrafast time-resolved spectroscopic techniques that allow us to probe the molecular excited and ground-state dynamics, which are responsible for molecular decomposition and detonation mechanism processes. This thesis mainly focuses on the investigation of NLO properties of novel organic and inorganic compounds, which are corroles, porphyrins, perovskite NCs and metal NPs. Also, their dynamics in the excited or ground state were studied using degenerate four-wave mixing and transient absorption spectroscopic techniques. Since the last few years, our efforts have focused on setting up the femtosecond time-resolved Coherent Anti-stokes Raman spectroscopy (TR-CARS) to reveal the ground and excited-state vibrational dynamics of Ems. It is interesting to note that most of the EMs tend to decompose in their ground-state by vibrational energy redistribution from low energy modes to high energy modes. In this regard, CARS is an efficient technique to probe the ground state vibrational dynamics of the molecules with higher temporal and spectral resolutions in both gas and liquid phases.[126-133]

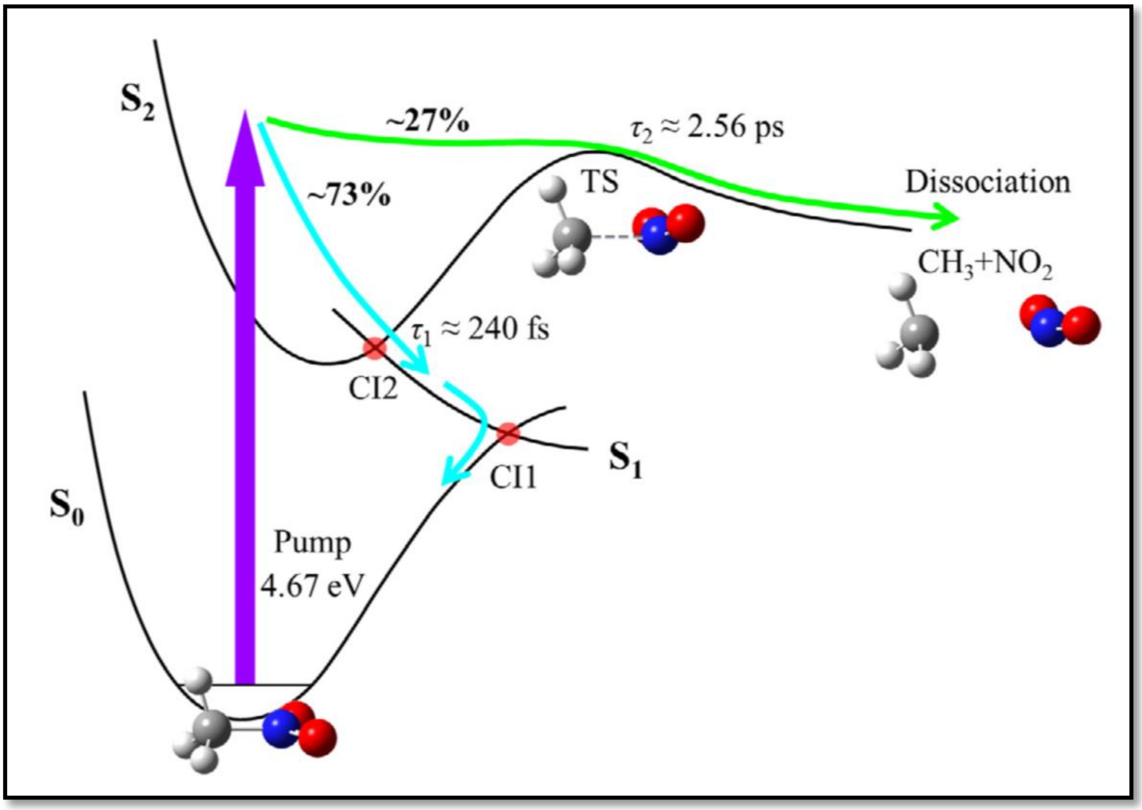

Figure 1.2 Energy relaxation path diagram of liquid nitromethane.[113]

CARS is a nonlinear spectroscopic technique that eliminates the low spontaneous Raman scattering cross-section. Spontaneous Raman is an incoherent process wherein the photons scatter in all the directions. In contrast, CARS is a coherent technique in which all the Raman scattered photons emerge out in one direction, similar to a laser. CARS is a versatile as well as a resourceful method for imaging and characterizing the materials even with strong fluorescence background. The employment of ultrafast lasers enables the novel possibilities of time and frequency-resolved spectroscopies to probe the vibrational dynamics that occur in the time scales shorter than the molecular vibration period ~100 fs. In a femtosecond time-resolved CARS (TR-CARS) experiment, several vibrational modes of the molecules can be excited simultaneously, and the relaxation processes can be probed in real-time. TR-CARS also enables us to estimate the dephasing times and collisional relaxation times of the preferred vibrational modes in solutions. Additionally, TR-CARS can probe the excited state vibrational dynamics. However, the excitation of molecular vibrational modes with fs broadband pulses in CARS experiment limits the spectral resolution, and this could be eliminated by employing pulse shaping techniques[134-136] to trigger selective absorptions. The analysis of TR-CARS spectra provokes the insight on intermolecular interactions as well as the molecular structure. Also, the advantage of CARS is its standoff detection capabilities due to its mechanism of coherent excitation and detection. The transient absorption spectroscopy provides information about the reaction or relaxation pathways of electronic excited-states. The CARS data provide the information of different vibrational modes which are involved in the energy transfer process and its dephasing time in the electronic ground state. We have successfully demonstrated these experiments in our lab and well-studied some of the organic and energetic molecules.

Transient absorption (TA) spectroscopy is a pump-probe technique in which a pump pulse ($t = 0$) initiates the photoinduced reaction, and the next evolution could be probed by the probe pulse ($t > 0$). To understand the various ultrafast processes in molecules, ultrashort pulses are necessary. The advancement of lasers pulse technology is accredited for accessibility to the ultrafast pulses of <100 fs. Since the femtosecond pulses are shorter than most of the intramolecular processes timescale, they enable the measurement of the ultrafast processes occurring in molecular excited states, which plays a crucial role in the performance of the photo-biological or chemical systems. Several chemical compounds are investigated in which upon photoexcitation, several processes take place, or more than one transient species exists. TA spectroscopy records the change in optical density (ΔOD) by pump-probe method, which comprises the overlapping of several processes, i.e., excited-state absorption (ESA), stimulated emission (SE), and ground state bleach (GSB) arising from the different–species in the molecular excited-states. The complete description of TA and data analysis are discussed in chapter 2. The following sections will provide a brief introduction about the ultrafast process and NLO properties of organic and inorganic materials. In case of organic molecules, we have studied porphyrins, corroles, and whereas in inorganic materials, we have studied perovskite NCs and metal (Au, $Au_{50}Ag_{50}$) NPs.

1.2 Ultrafast Photo-processes in Organic Molecules

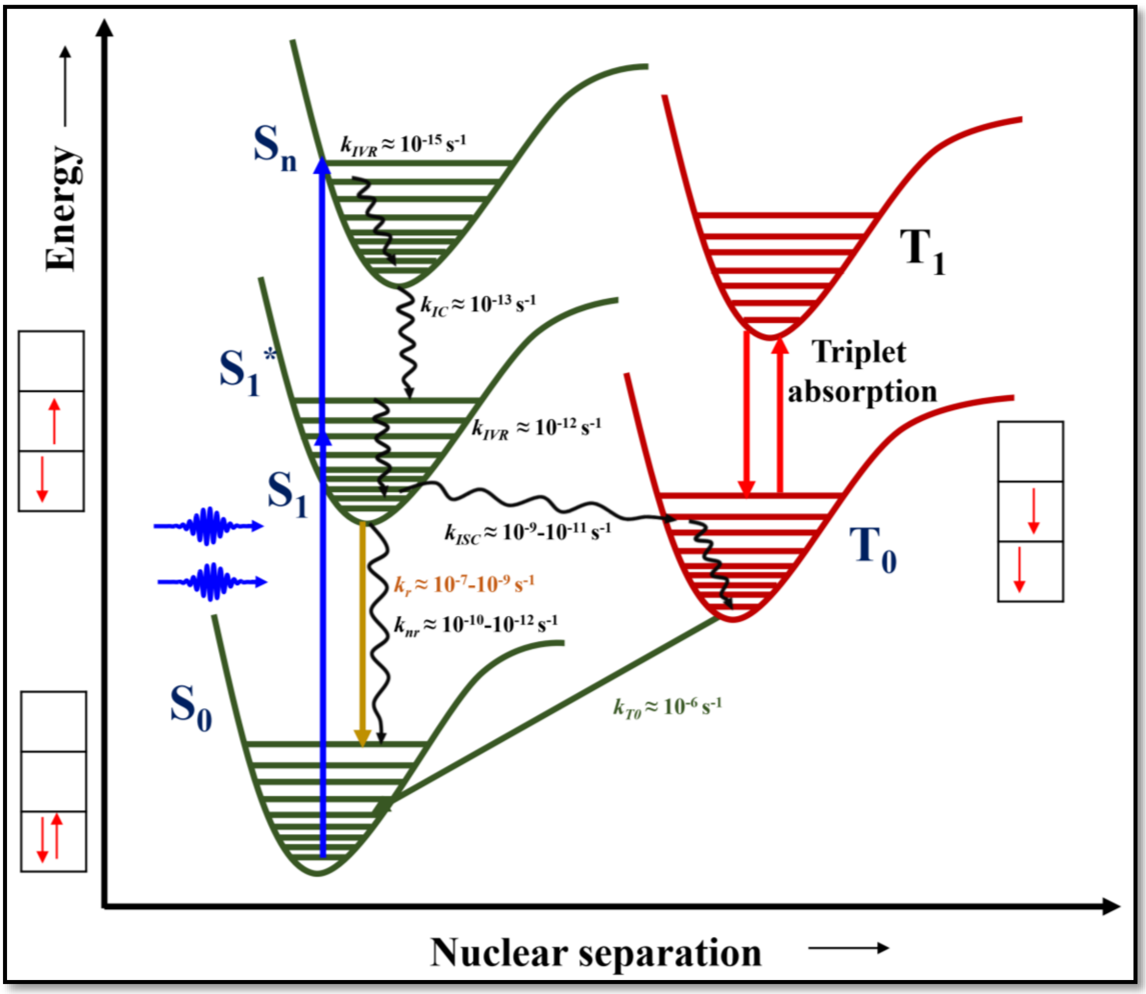

Figure 1.3 Jablonski diagram representing various ultrafast photo-processes where the wriggly and dashed lines represent the nonradiative process, and straight lines shows radiative processes.

In organic molecules, upon photoexcitation, several processes take place while excited-state population while returning to the ground state. These processes can be well understood by the Jablonski diagram, as shown in figure 1.3. The absorption of a photon creates a population in the electronically excited state (S_n, where n = 1, 2…) from the electronic ground state (S_0). The absorption is an instantaneous process that takes in the order of 10^{-15} s.[137-139] Beers-Lambert's law directs the absorption process. Under linear absorption, the relaxation of the excited state population to the ground state takes through several processes.[137] The transition follows the Frank-Condon (FC) principle, where the position of the nucleus is unaffected in both the excited state and ground state. Vibrational relaxation occurs through intermolecular collision (solute-solvent interaction, reorientation relaxation in anisotropic molecules) on a picosecond time scale. Further, a shift in the potential curve towards the right is witnessed. In the case of anisotropic molecules, the reorientation of individual molecules have different absorption due to the random distribution.[139] The reorientation of molecules takes place short time, losing energy to the surrounding (solvent).

If higher electronic excited states (S_2) are populated the relaxation of S_2 to lowest electronic excited state S_1 occurs through internal conversion (IC). Subsequently, the population transfer from higher vibrational state to low energy vibrational state of S_1 through vibrational relaxation (VR) nonradiatively. The population from the low energy vibrational states of S_1 relaxes through radiatively (fluorescence) and nonradiatively followed by Kasha's rule.[140] A possible transition from singlet to triplet (T) state takes place non-radiatively by changing the spin of electrons that are different from the S_1. This process is entitled as intersystem crossing (ISC) and it occurs in the picosecond to nanosecond time scales. Further, the population from T_0 states relax radiatively (Phosphorescence) to $S_{0,}$ which occurs in a time scale of few microseconds to milliseconds. This is because of the forbidden transition from T_0 - $S_{0;}$ thus, it takes a longer time. Apart from these relaxation processes, another process takes place in concise time scales, i.e., the dephasing process where the loss of coherence in the excited electronic states. To investigate these ultrafast processes, many spectroscopic techniques emerged due to the slow response of conventional detectors.

1.3 Ultrafast Processes in Metal Nanoparticles

Nobel metals (Au, Ag, Cu) constitute of monovalent atoms with a similar electronic configuration. The atomic d-orbitals are filled (d-band) and the hybridized s-p orbitals are partially filled which forms p-band (table 1).[141-142] The electrons in this partially filled orbitals are delocalized (forms conduction band), which are subject to the thermal and electrical properties where the filled d-orbitals (valence band) contributes less to these. Figure 1.4 shows the band structure of metals; E_f is the fermi level, i.e., the highest occupied electronic state at zero temperature. A remarkable effect called surface plasmon resonance (SPR) associated with a collective electron motion is evident upon the size reduction of the metals. This property of metals creates spatial localization and enhancement of the EM fields in the metal NPs.[143] The metal NPs are excited through Interband or intraband transitions depending on the pump wavelength. The electron scattering ($\tau = \gamma^{-1}$) takes place in few femtoseconds upon photoexcitation.[144]

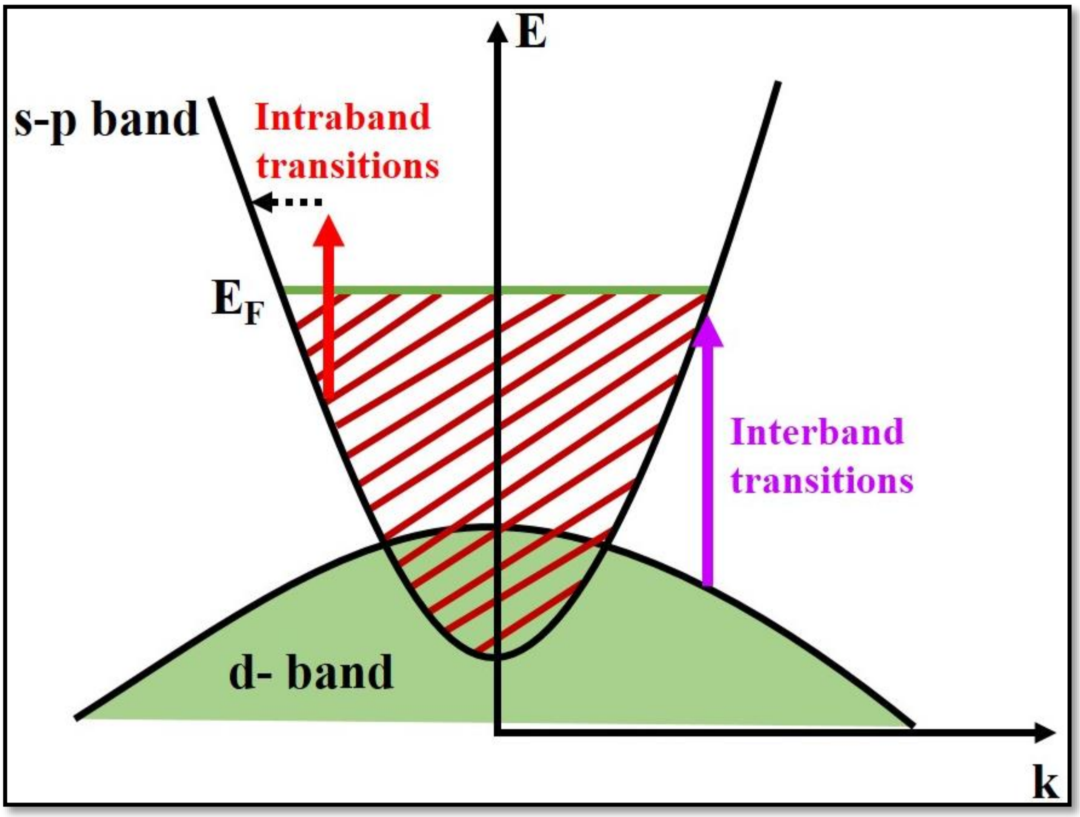

Figure 1.4 Illustration of the band structure of metals with filled d-band (low dispersed valence band) and a partially filled s-p band (conduction band). Absorption of a photon (solid arrow) by a d-band electron may cause a transition towards the s-p band. The excited electron in the conduction band relaxes through intraband transitions either by electron or phonon (dashed arrow) scattering.

The heat capacity of the electron is smaller than the heat capacity of the lattice and, therefore, we can selectively excite and monitor the electron dynamics in real-time. Upon laser pulse excitation, the electrons relax through internal thermalization by electron-electron collision followed by electron-phonon coupling from external thermalization. In the case of interband excitation the generated electron-hole pairs recombine within a few femtoseconds. NPs are sound light absorbers can create highly excited electron-hole pairs and these hot charge carriers used in photocatalysis, biology and solar energy conversion applications.[145-146] The Au NPs exhibit the surface plasmon modes in the visible region due to the oscillations of conduction electrons. The plasmon peak depends mainly on the shape and size of the NPs, as the size increases, the peak shifts to the red and broadens.[147-148] Ultrafast electron relaxation processes entangled with localized surface plasmonic phenomena has been demonstrated to be the basis for high performance of optical switching devices based on the metal nanostructures.[149-150] The electron dynamics and the third-order NLO properties of metal and metal-alloy NPS by different spectroscopic techniques are well studied.[151-152]

Table 1.1 Nobel metals electronic configuration, lattice parameters, and electron density.

Metal	Configuration	a (A^0)	n_e($\times 10^{22}$ cm^{-3})
Cu	[Ar] $3d^{10}4s^1$	3.61	8.47
Au	[Xe] $4f^{14}5d^{10}6s^1$	4.07	5.90
Ag	[Kr] $4d^{10}5s^1$	4.08	5.86

Metal and metal alloy nanoparticles (NPs) or colloids have unusual physical and electrical properties depending on their shape and size, which has a tremendous interest in catalytic reactions and plasmonic lasers.[153] The nonlinear optical (NLO) properties of gold (Au) and gold-silver (Au-Ag) alloy NPs have attracted significant interest in numerous fields for various applications.[154-155] The advantage of doping metal nanoparticles with semiconductors, metals can significantly tune the intrinsic plasmon band over the visible-NIR region. Many researchers have investigated the electron dynamics of Au and Au-Ag alloy of differently synthesized NPs in both solution form (colloids) as well as in a thin film by using fs-TAS.[151-152, 156]

The geometry of the NPs affects the NLO properties and the corresponding ultrafast electron dynamics in the excited states.[22, 157] Following the laser pulse excitation, the electrons relax through internal thermalization by electron-electron collision followed by electron-phonon coupling from external thermalization.[158-159] The non-thermal (non-Fermi) electron distribution following intense laser excitation above the Fermi level has been probed by various laser-based techniques.[160-161] The electron thermalization dynamics at intraband and interband excitation in mixed metal NPs are mostly not explored. Recently, Zhang and co-workers[149] have explored the interband and intraband contribution to localized surface plasmon oscillations in pure Au NPs, wherein they have observed a red-shifted induced LSPR feature with 400 nm pumping. When pumped above the threshold energy of 2.38 eV, it induces the electronic transition from 5d band to the 6sp band resulting in a transient increase of population in the conduction band. The exciting 5d electrons relax to plasmonic oscillation with a time delay of 1 ps has been demonstrated.

1.4 NLO Properties of Organic Compounds

The search for unique materials with strong nonlinear optical (NLO) properties apt for photonic device applications has opened up new possibilities in materials preparation. In the past 30 years, specific attention was accorded to organic compounds, special glasses, and semiconductors, which possess strong NLO coefficients with fast response time in sub-ps time scale. Among these, organic compounds exhibit strong NLO properties in quick response times, which are foremost to photonic implementations. The NLO properties in organic molecules are related to the electron density distribution and charge transfer processes.[162-163] Materials with Large conjugated systems, strong intramolecular charge transfer (ICT), and better co-planarity are a prerequisite for strong NLO properties in organic materials.[164-165] In conjugated systems, the orbital overlap is the main requirement; therefore, the conjugated systems should be nearly planar.

Consequently, the lone pairs that engage in conjugation will mostly occupy orbitals of pure p character instead of sp^n hybrid orbitals. Also, it is possible to optimize the molecular structures to maximize the NLO response. This is because, in organic molecules, the delocalized π electrons exhibit strong hyper polarizabilities.[166] Notably, organic molecules possessing large π-conjugation, specially corroles and porphyrins with donor-acceptor (D-A) systems, are suitable for several applications, mainly photovoltaics[52-55, 167] and up-conversion.[58,59-61] They also exhibit strong NLO properties arising from its larger π-electron conjugation.[62-67] Organic moieties with strong π-bond conjugation are known to illustrate stronger dipole moments and create a delocalized distribution of electric charges due to ICT resulting in high electrical polarization, which is advantageous for large NLO response.[69-74] Organic moieties designed in Donor-π-Acceptor-π-Donor structure by attaching different electron acceptor groups to patent ring to increase the molecular π-conjugation are found to improve NLO activity. Choosing an excellent parent ring is the key to impressive molecular design of organic NLO materials.[168] Several compounds with the heterocyclic structure are typically used as parent rings of organic NLO materials, such as coumarin, quinacridone, benzothiazole, and benzofuran.[165, 169-172] A few reports on natural photosynthetic phenomena of D-A systems based corroles and porphyrins are available in literature.[173-177] Such D-A systems were designed by altering the local position of metal ion of the macrocycle, for example, either at the axial or at the meso-phenyl position. Among several organic compounds, porphyrins, corroles have been found to be efficient NLO materials due to their versatility in tuning the NLO properties by incorporating different metals or peripheral substituents to the macrocycle, this can reduce the energy gap and promote the ICT process. In this thesis we have studied differently synthesized corroles and porphyrins and having studied them we have observed strong NLO coefficients with fast response time. Also, their excited state dynamics were studied using TAS and time-resolved fluorescence spectroscopy.

1.5 NLO Properties of Perovskite NCs

Recently, all-inorganic perovskite nanocrystals (NCs) gained large attention due to excellent optical properties (strong absorption and high luminescence yield), which can be synthesized by low-temperature solution processes. It has been demonstrated that these materials are used in light-emitting diodes, thin-film solar cells, optical switches, and lasers. Besides their excellent optical properties, lead halide perovskites also own unique nonlinear optical (NLO) properties.[178] The strong quantum confinement of perovskite NCs in the desired direction can significantly improve optical properties. Lead halide perovskites also own unique nonlinear optical (NLO) properties. These exceptional optoelectronic properties of the perovskite NCs stem from (a) a long carrier lifetime (b) strong band-to-band absorption (c) low densities of defects/traps (d) long diffusion lengths. The NLO properties of semiconductor NCs are heavily dependent on their geometries. Scott et al. have shown the magnitude of two-photon absorption (2PA) cross-sections [$\sigma^{(2)}$] of CdSe 2D NPs and nanorods (NRs) are proportional to the square of the volume.[179] The cross-section dependence on volume is ascribed to the different degrees of quantum confinement, which is less for spherical NCs and high for 2D NPs and NRs. He et al. have observed a linear dependence of the three-photon absorption (3PA) cross-section [$\sigma^{(3)}$] of CdSe NCs on their volume.[180] The semiconductor two-dimensional nanoplatelets (2D NPs) possess strong optical properties such as room temperature narrow PL emission and considerable oscillator strengths. These can be further altered by their thickness, both their linear and nonlinear optical properties, which are essential for high performance in photonic device applications. Metal Halide Perovskites (MHPs) have been demonstrated as high-quality optoelectronic devices. The chemical formula of perovskites is ABX_3, where A is cation typically fixed as organic [methylammonium (MA), $CH_3NH_3^+$], or inorganic (Cesium, Cs^+), B is a metal (typically Pb), and X is a halide (Br^-, Cl^-, and I^-). Generally, MHPs are direct bandgap semiconductors that can be synthesized by low-cost solution process techniques in different forms, i.e., polycrystalline thin films or nanoparticles (NPs). MHPs have demonstrated unique properties, large carrier diffusion lengths, and low nonradiative recombination rates. Apart from this, these materials have also been demonstrated to be an excellent active medium in the construction of lasers due to their tunable and robust emission at room temperature. Therefore, MHPs are shown to be applicable in lasers or optical amplifiers and light-emitting diodes. Currently, the current technologies have adapted MHP materials in amplification/photodetection functionalities. On the other side, their NLO properties (nonlinear absorption and refractive index n_2) have potential applications optical limiting, data storage, and devices, switching, Supercontinuum generation.[181]

1.6 Outline of Thesis

The primary objective of this thesis work is to investigate the molecular excited state dynamics and third-order NLO properties of novel (a) organic/inorganic molecules for photonic devices and biological applications and (b) energetic molecules for a better understanding of the EMs, thereby enhancing the possibility to achieve superior designs in future for real-time purposes. To realize this, we have studied (a) porphyrins (b) corroles

(c) metal nanoparticles and (d) perovskite nanocrystals extensively. We have particularly elucidated the following:

- Multi-photon absorption properties of $CsPbBr_3$ nanocrystals and Cs_4PbBr_6 zero-dimensional perovskite nanocrystals using the femtosecond Z-scan technique in the near-IR spectral region
- 2PA and excited-state dynamics of metal and metal-alloy nanoparticles using femtosecond Z-scan and TA techniques
- Third-order NLO properties and electron relaxation dynamics in porphyrins and corroles utilizing femtosecond Z-scan, DFWM, and TA techniques
- The electronic and vibrational dynamics of meso and amino-substituted tetrazole molecules, performed to understand the vibrational energy redistribution dynamics by making use of transient absorption spectroscopy and coherent anti-stokes Raman spectroscopy techniques with fs pulses.

This thesis has been organized into eight (8) chapters. The content of each of these chapters are summarized and delivered as follows:

Chapter 1

This Chapter provides a broad introduction and motivation to the investigated molecules. Mainly the following aspects are explained in detail: (a) the significance of these molecules over the state of the art materials existing so far with a brief literature survey (b) the advantage of nano-sized materials such as perovskite nanocrystals (NCs) and metal nanoparticles for photonic applications (c) organic molecules and their nonlinear characteristics (d) ultrafast electronic and vibrational relaxation processes of energetic molecules for a better understanding of the performance of different EMs (e) the importance of different ultrafast spectroscopic techniques employed in this thesis is discussed.

Chapter 2

This Chapter provides a complete description of the femtosecond lasers and experimental techniques used. Further, (a) methods of ultrafast pulse generation (nanosecond to femtosecond) and different components used to generate these pulses in the cavity (b) chirped pulse amplification process (c) regenerative amplification (d) ultrashort pulse propagation and dispersion effects in different media (e) pulse characterization using intensity and single-shot autocorrelation techniques (f) preparation of samples and steady-state measurements such as absorption and emission experimental details are summarized. Experimental techniques used such as (i) Z-scan (ii) Transient absorption with global and target analysis (iii) Degenerate Four-Wave Mixing, and (iv) Time-resolved Coherent Anti-Stokes Raman spectroscopies have been described in detail.

Chapter 3

This Chapter contains the details of all NLO studies of different molecules investigated, mainly results obtained from the single beam Z-scan and Degenerate Four-Wave mixing experiments. The complete details of the NLO studies and their properties (nonlinear refractive index and multi-photon absorption) along with the responses of perovskite nanocrystals ($CsPbBr_3$ NCs and Cs_4PbBr_6 zero-dimensional NCs) are described. We have obtained substantial two-photon absorption coefficients order of 10^4 GM from $CsPbBr_3$ NCs and multi-photon absorption studies on Cs_4PbBr_6 zero-dimensional NCs showed strong cross-section values (two-photon absorption cross-section, ~10^6 GM in the spectral range of 500–800 nm, three-photon absorption cross-section, $\sigma^{(3)}$ ~10^{-73} cm^6 s^2 in the 900–1200 nm range and four-photon absorption cross-section, $\sigma^{(4)}$ ~10^{-100} cm^8 s^3 in the spectral region of 1300–1500 nm. The DFWM measurements confirmed an ultrafast response.

Chapter 4

This Chapter presents the intra and interband relaxation dynamics of pure Au and $Au_{50}Ag_{50}$ laser-ablated bimetallic nanoparticles at 400 nm and 800 nm photoexcitation. The electron-electron relaxation was discussed for Au and $Ag_{50}Au_{50}$ alloy NPs which happens in <0.5 ps. Electron-phonon relaxation times (<4 ps) found to be similar in these NPs, which shows the homogeneity of the composite material. The obtained electron dynamics from these NPs are exhibiting fast response compared to other studies on Au and $Ag_{50}Au_{50}$ nanocomposite materials. The NLO properties and time-resolved data pure Au and $Ag_{50}Au_{50}$ nanoparticles, prepared by using ultrafast laser ablation in liquid technique, are also presented.

Chapter 5

This Chapter discusses the ultrafast photophysical processes and third-order nonlinear optical properties of porphyrins. From the transient absorption spectroscopy, we have obtained different decay rate and time constants, corresponding to internal conversion from (S_n-S_1), of <1 picosecond, vibrational relaxation within S_1 states in <10 ps, radiative relaxation of S_1-S_0 in nanosecond time scale, intersystem crossing from S_1-T_0 in ps and ns time scales and triplet relaxation from T_0-S_0 in microsecond time scale (1-100 µs). The third-order nonlinear (NLO) coefficients recorded with ~50 fs, 1 kHz repetition rate pulses at a wavelength of 800 nm. The magnitude of the TPA coefficients and cross-sections ($\sim 10^3$ GM) of these molecules was compared with some of the recently reported porphyrin moieties and were found to be superior. The time-resolved degenerate four-wave mixing (DFWM) measurements and the data obtained confirmed a large magnitude and an ultrafast response of the $\chi^{(3)}$ in these molecules.

Chapter 6

This Chapter presents results from studies on ultrafast photophysical processes and third-order nonlinear optical properties of newly synthesized donor-acceptor based free-base [$(C_6F_5)_3$] and phosphorus [$P\text{-}(OH)_2(C_6F_5)_3$] corroles. The femtosecond transient absorption data revealed several photophysical processes such as (a) internal conversion (τ_{IC}) in the 260-280 fs range (b) vibrational relaxation (τ_{VR}) in the 2.5-5ps range and (c) nonradiative relaxation times (τ_{nr}) in the 4.15-7.6 ns range and finally (d) the triplet lifetimes in the range of 25-50 µs. The NLO measurements were performed using the fs, kHz pulses using the standard Z-scan technique at 600 nm and 800 nm. The TPA cross-section values were in the range of $\sim 10^2$ GM. Degenerate four-wave mixing measurements illustrated a significant third-order nonlinear optical susceptibility [$\chi^{(3)}$] with a magnitude of 6.9×10^{-14} esu and instantaneous (sub-picosecond) response, suggesting a predominant pure electronic contribution to the nonlinearity of these corroles.

Chapter 7

This Chapter explains and elaborates the molecular dynamics of the complex and nitrogen-rich amino, and nitro substituted tetrazole derivatives [2,6-dinitro-4-(1H-tetrazole-1-yl) aniline ($C_7H_5N_7O_4$) and 1-(3,4,5-trinitrophenol)-1H-tetrazole($C_7H_3N_7O_6$) are labelled as 6 and 8] with the results obtained from femtosecond Time-Resolved Coherent Anti-

Stokes Raman Spectroscopy and transient absorption. The present study is advantageous in enhancing the applications of energetic materials since the tetrazole derivative 8 demonstrated energetic properties those comparable with the secondary explosives such as RDX and TNT. Fourier transforms of the recorded CARS transients revealed the possible IVR mechanisms in tetrazole-N-(hetero)aryl derivatives. Further, dephasing times estimated from the CARS transients were ~137-200 fs. We have found that the low energy modes that are corresponding to the C-H vibrations exhibiting faster dephasing times compared to higher energy vibrational modes. Consequently, the C-H vibrational modes could be excited first upon photoexcitation and causing an initial chemical reaction. The transient absorption spectroscopy at 400 nm photoexcitation with the help of target analysis different decay rate and time constants have been discussed. The vibrational relaxation within S_1 occurs within 0.3-0.8 ps time scale, and a possible intermediate state (S_1-S^*-T_0) is addressed in the intersystem crossing with a lifetime of 9.7 and 120 ps. The S_1 state decays to S^* with a lifetime of 2.2 to 4.7 ps and the triplet lifetime if found to in a µs time scale.

Chapter 8

This Chapter summarises the contents of the thesis. It discloses the various future work possibilities including (i) extension of transient absorption experiments to the UV and near-infrared (NIR) regime to study the structural dynamics of organic and energetic molecules (ii) development of femtosecond standoff CARS setup and (iii) multi-photon absorption studies such as five-photon and above at NIR wavelengths for biological applications.

References

1. Roberts, R., Fast Reactions and Primary Processes in Chemical Kinetics. Proceedings of the 5th Nobel Symposium, Stockholm, Aug.-Sept. 1967. Stig Claesson, Ed. Interscience (Wiley), New York; Almqvist and Wiksells, Stockholm, 1967. 487 Pp., Illus. $27.50. *Science* **1968**, *161*, 1335-1335.
2. Anfinrud, P.; de Vivie-Riedle, R.; Engel, V., Ultrafast Detection and Control of Molecular Dynamics. *Proceedings of the National Academy of Sciences* **1999**, *96*, 8328-8329.
3. Chergui, M., Femtochemistry. In *Femtochemistry*, WORLD SCIENTIFIC: 1996.
4. Sundstrom, V., Femtosecond Photobiology. In *Technical Digest. 1998 EQEC. European Quantum Electronics Conference (Cat. No.98TH8326)*, IEEE.
5. Wang, X.; Wang, L.; Xiao, F.; Zhang, D.; Lü, Z.; Yuan, J.; Zhao, Z., Generation of 88 as Isolated Attosecond Pulses with Double Optical Gating*. *Chinese Physics Letters* **2020**, *37*, 023201.
6. Zhang, Y. X.; Rykovanov, S.; Shi, M.; Zhong, C. L.; He, X. T.; Qiao, B.; Zepf, M., Giant Isolated Attosecond Pulses from Two-Color Laser-Plasma Interactions. *Physical Review Letters* **2020**, *124*.
7. Duris, J., et al., Tunable Isolated Attosecond X-Ray Pulses with Gigawatt Peak Power from a Free-Electron Laser. *Nature Photonics* **2019**, *14*, 30-36.
8. Zewail, A. H., Laser Femtochemistry. *Science* **1988**, *242*, 1645-1653.
9. Zewail, A. H., Femtochemistry: Atomic-Scale Dynamics of the Chemical Bond Using Ultrafast Lasers (Nobel Lecture). *Angewandte Chemie International Edition* **2000**, *39*, 2586-2631.
10. Di Donato, M.; Groot, M. L., Ultrafast Infrared Spectroscopy in Photosynthesis. *Biochimica et Biophysica Acta (BBA)-Bioenergetics* **2015**, *1847*, 2-11.
11. Richards, G. H.; Wilk, K. E.; Curmi, P. M.; Davis, J. A., Disentangling Electronic and Vibrational Coherence in the Phycocyanin-645 Light-Harvesting Complex. *The journal of physical chemistry letters* **2014**, *5*, 43-49.
12. Jimenez, R.; Fleming, G. R., Ultrafast Spectroscopy of Photosynthetic Systems. In *Biophysical Techniques in Photosynthesis*, Springer: 1996; pp 63-73.

13. Nikolaou, V.; Charisiadis, A.; Stangel, C.; Charalambidis, G.; Coutsolelos, A. G., Porphyrinoid–Fullerene Hybrids as Candidates in Artificial Photosynthetic Schemes. *C—Journal of Carbon Research* **2019**, *5*, 57.
14. Maiuri, M.; Snellenburg, J.; Van Stokkum, I.; Pillai, S.; Gust, D.; Moore, T. A.; Moore, A. L.; Van Grondelle, R.; Cerullo, G.; Polli, D. In *Ultrafast Energy Transfer in an Artificial Photosynthetic Antenna*, EPJ Web of Conferences, EDP Sciences: 2013; p 08010.
15. Han, D.; Xue, B.; Du, J.; Kobayashi, T.; Miyatake, T.; Tamiaki, H.; Xing, X.; Yuan, W.; Li, Y.; Leng, Y., Excitonic and Vibrational Coherence in Artificial Photosynthetic Systems Studied by Negative-Time Ultrafast Laser Spectroscopy. *Physical Chemistry Chemical Physics* **2016**, *18*, 24252-24260.
16. Franken, P. A.; Hill, A. E.; Peters, C. W.; Weinreich, G., Generation of Optical Harmonics. *Physical Review Letters* **1961**, *7*, 118-119.
17. Boyd, R., Preface to the Third Edition. In *Nonlinear Optics*, Elsevier: 2008; pp xiii-xiv.
18. Hora, H., Y. R. Shen, the Principles of Nonlinear Optics, John Wiley & Sons, New York, 1984, 576 Pages. *Laser and Particle Beams* **1986**, *4*, 318-319.
19. Zyss, J.; Chemla, D. S., Quadratic Nonlinear Optics and Optimization of the Second-Order Nonlinear Optical Response of Molecular Crystals. In *Nonlinear Optical Properties of Organic Molecules and Crystals*, Elsevier: 1987; pp 23-191.
20. Kajzar, F.; Rau*, I., Materials for Nonlinear Optics | Organic Nonlinear Materials. In *Encyclopedia of Modern Optics*, Elsevier: 2005; pp 42-60.
21. Zhang, Y.-x.; Wang, Y.-h., Nonlinear Optical Properties of Metal Nanoparticles: A Review. *RSC Advances* **2017**, *7*, 45129-45144.
22. Hua, Y.; Chandra, K.; Dam, D. H. M.; Wiederrecht, G. P.; Odom, T. W., Shape-Dependent Nonlinear Optical Properties of Anisotropic Gold Nanoparticles. *The Journal of Physical Chemistry Letters* **2015**, *6*, 4904-4908.
23. Fu, Y.; Ganeev, R. A.; Krishnendu, P. S.; Zhou, C.; Rao, K. S.; Guo, C., Size-Dependent Off-Resonant Nonlinear Optical Properties of Gold Nanoparticles and Demonstration of Efficient Optical Limiting. *Optical Materials Express* **2019**, *9*, 976.
24. Chen, W.; Bhaumik, S.; Veldhuis, S. A.; Xing, G.; Xu, Q.; Grätzel, M.; Mhaisalkar, S.; Mathews, N.; Sum, T. C., Giant Five-Photon Absorption from Multidimensional

Core-Shell Halide Perovskite Colloidal Nanocrystals. *Nature Communications* **2017**, *8*.

25. Manzi, A.; Tong, Y.; Feucht, J.; Yao, E.-P.; Polavarapu, L.; Urban, A. S.; Feldmann, J., Resonantly Enhanced Multiple Exciton Generation through Below-Band-Gap Multi-Photon Absorption in Perovskite Nanocrystals. *Nature Communications* **2018**, *9*.
26. Li, J.; Zhang, S.; Dong, H.; Yuan, X.; Jiang, X.; Wang, J.; Zhang, L., Two-Photon Absorption and Emission in $CsPb(Br/I)_3$ cesium Lead Halide Perovskite Quantum Dots. *CrystEngComm* **2016**, *18*, 7945-7949.
27. Dohner, E. R.; Jaffe, A.; Bradshaw, L. R.; Karunadasa, H. I., Intrinsic White-Light Emission from Layered Hybrid Perovskites. *Journal of the American Chemical Society* **2014**, *136*, 13154-13157.
28. Li, X.; Wu, Y.; Zhang, S.; Cai, B.; Gu, Y.; Song, J.; Zeng, H., Quantum Dots: $CsPbX_3$ quantum Dots for Lighting and Displays: Room-Temperature Synthesis, Photoluminescence Superiorities, Underlying Origins and White Light-Emitting Diodes (Adv. Funct. Mater. 15/2016). *Advanced Functional Materials* **2016**, *26*, 2584-2584.
29. Zhang, J.; Jiang, T.; Zheng, X.; Shen, C.; Cheng, X. a., Thickness-Dependent Nonlinear Optical Properties of $CsPbBr_3$ Perovskite Nanosheets. *Optics Letters* **2017**, *42*, 3371.
30. Li, P., et al., Two-Dimensional $CH_3NH_3PbI_3$ Perovskite Nanosheets for Ultrafast Pulsed Fiber Lasers. *ACS Applied Materials & Interfaces* **2017**, *9*, 12759-12765.
31. Fu, Y.; Zhu, H.; Stoumpos, C. C.; Ding, Q.; Wang, J.; Kanatzidis, M. G.; Zhu, X.; Jin, S., Broad Wavelength Tunable Robust Lasing from Single-Crystal Nanowires of Cesium Lead Halide Perovskites ($CsPbX_3$, X = Cl, Br, I). *ACS Nano* **2016**, *10*, 7963-7972.
32. Xu, Y., et al., Two-Photon-Pumped Perovskite Semiconductor Nanocrystal Lasers. *Journal of the American Chemical Society* **2016**, *138*, 3761-3768.
33. Gao, Y.; Wang, S.; Huang, C.; Yi, N.; Wang, K.; Xiao, S.; Song, Q., Room Temperature Three-Photon Pumped $CH_3NH_3PbBr_3$ Perovskite Microlasers. *Scientific Reports* **2017**, *7*.
34. Yakunin, S.; Protesescu, L.; Krieg, F.; Bodnarchuk, M. I.; Nedelcu, G.; Humer, M.; De Luca, G.; Fiebig, M.; Heiss, W.; Kovalenko, M. V., Low-Threshold Amplified

Spontaneous Emission and Lasing from Colloidal Nanocrystals of Caesium Lead Halide Perovskites. *Nature Communications* **2015**, *6*.

35. Ramasamy, P.; Lim, D.-H.; Kim, B.; Lee, S.-H.; Lee, M.-S.; Lee, J.-S., All-Inorganic Cesium Lead Halide Perovskite Nanocrystals for Photodetector Applications. *Chemical Communications* **2016**, *52*, 2067-2070.
36. Protesescu, L.; Yakunin, S.; Bodnarchuk, M. I.; Krieg, F.; Caputo, R.; Hendon, C. H.; Yang, R. X.; Walsh, A.; Kovalenko, M. V., Nanocrystals of Cesium Lead Halide Perovskites ($CsPbX_3$, X = Cl, Br, and I): Novel Optoelectronic Materials Showing Bright Emission with Wide Color Gamut. *Nano Letters* **2015**, *15*, 3692-3696.
37. Wehrenfennig, C.; Eperon, G. E.; Johnston, M. B.; Snaith, H. J.; Herz, L. M., High Charge Carrier Mobilities and Lifetimes in Organolead Trihalide Perovskites. *Advanced Materials* **2013**, *26*, 1584-1589.
38. Kang, J.; Wang, L.-W., High Defect Tolerance in Lead Halide Perovskite $CsPbBr_3$. *The Journal of Physical Chemistry Letters* **2017**, *8*, 489-493.
39. Liu, W.; Xing, J.; Zhao, J.; Wen, X.; Wang, K.; Lu, P.; Xiong, Q., Giant Two-Photon Absorption and Its Saturation in 2d Organic-Inorganic Perovskite. *Advanced Optical Materials* **2017**, *5*, 1601045.
40. Kalanoor, B. S.; Gouda, L.; Gottesman, R.; Tirosh, S.; Haltzi, E.; Zaban, A.; Tischler, Y. R., Third-Order Optical Nonlinearities in Organometallic Methylammonium Lead Iodide Perovskite Thin Films. *ACS Photonics* **2016**, *3*, 361-370.
41. Krishnakanth, K. N.; Seth, S.; Samanta, A.; Rao, S. V., Broadband Femtosecond Nonlinear Optical Properties of $CsPbBr_3$ Perovskite Nanocrystals. *Optics Letters* **2018**, *43*, 603.
42. Li, J.; Dong, H.; Xu, B.; Zhang, S.; Cai, Z.; Wang, J.; Zhang, L., $CsPbBr_3$ Perovskite Quantum Dots: Saturable Absorption Properties and Passively Q-Switched Visible Lasers. *Photonics Research* **2017**, *5*, 457.
43. Náfrádi, B.; Szirmai, P.; Spina, M.; Lee, H.; Yazyev, O. V.; Arakcheeva, A.; Chernyshov, D.; Gibert, M.; Forró, L.; Horváth, E., Optically Switched Magnetism in Photovoltaic Perovskite $CH_3NH_3(Mn{:}Pb)I_3$. *Nature Communications* **2016**, *7*.
44. Yi, J.; Miao, L.; Li, J.; Hu, W.; Zhao, C.; Wen, S., Third-Order Nonlinear Optical Response of $CH_3NH_3PbI_3$ Perovskite in the Mid-Infrared Regime. *Optical Materials Express* **2017**, *7*, 3894.

45. Wang, Y.; Li, X.; Zhao, X.; Xiao, L.; Zeng, H.; Sun, H., Nonlinear Absorption and Low-Threshold Multiphoton Pumped Stimulated Emission from All-Inorganic Perovskite Nanocrystals. *Nano Letters* **2015**, *16*, 448-453.

46. Pan, J., et al., Air-Stable Surface-Passivated Perovskite Quantum Dots for Ultra-Robust, Single- and Two-Photon-Induced Amplified Spontaneous Emission. *The Journal of Physical Chemistry Letters* **2015**, *6*, 5027-5033.

47. Liu, Z.; Yang, J.; Du, J.; Hu, Z.; Shi, T.; Zhang, Z.; Liu, Y.; Tang, X.; Leng, Y.; Li, R., Sub-Wavelength Single-Mode All-Inorganic Perovskite $CsPbBr_3$ Nanolaser. In *Conference on Lasers and Electro-Optics*, OSA: 2019.

48. Liu, S.; Chen, G.; Huang, Y.; Lin, S.; Zhang, Y.; He, M.; Xiang, W.; Liang, X., Tunable Fluorescence and Optical Nonlinearities of All Inorganic Colloidal Cesium Lead Halide Perovskite Nanocrystals. *Journal of Alloys and Compounds* **2017**, *724*, 889-896.

49. Stoumpos, C. C.; Frazer, L.; Clark, D. J.; Kim, Y. S.; Rhim, S. H.; Freeman, A. J.; Ketterson, J. B.; Jang, J. I.; Kanatzidis, M. G., Hybrid Germanium Iodide Perovskite Semiconductors: Active Lone Pairs, Structural Distortions, Direct and Indirect Energy Gaps, and Strong Nonlinear Optical Properties. *Journal of the American Chemical Society* **2015**, *137*, 6804-6819.

50. Clavian, L.; Kumar, P. R.; Kumar, K. A.; Rao, D. N.; Shihab, N.; Ganesh, S., Enhanhanced Third Order Optical Nonlinearity in Ultrathin Amorphous Film of Tetraphenyl-Porphyrin in Picosecond Regime. *Optics & Laser Technology* **2019**, *119*, 105642.

51. Bharati, M.; Bhattacharya, S.; Krishna, J. S.; Giribabu, L.; Rao, S. V., Femtosecond, Broadband Nonlinear Optical Studies of a Zinc Porphyrin and Zinc Phthalocyanine. *Optics & Laser Technology* **2018**, *108*, 418-425.

52. D'Souza, F.; Ito, O., Photosensitized Electron Transfer Processes of Nanocarbons Applicable to Solar Cells. *Chem. Soc. Rev.* **2012**, *41*, 86-96.

53. Mishra, R.; Basumatary, B.; Singhal, R.; Sharma, G. D.; Sankar, J., Corrole-Bodipy Dyad as Small-Molecule Donor for Bulk Heterojunction Solar Cells. *ACS Appl Mater Interfaces* **2018**, *10*, 31462-31471.

54. Lu, J.; Liu, S.; Wang, M., Push-Pull Zinc Porphyrins as Light-Harvesters for Efficient Dye-Sensitized Solar Cells. *Frontiers in Chemistry* **2018**, *6*.

55. Reddy, G.; Katakam, R.; Devulapally, K.; Jones, L. A.; Della Gaspera, E.; Upadhyaya, H. M.; Islavath, N.; Giribabu, L., Ambient Stable, Hydrophobic, Electrically Conductive Porphyrin Hole-Extracting Materials for Printable Perovskite Solar Cells. *Journal of Materials Chemistry C* **2019**, *7*, 4702-4708.
56. Senge, M. O.; Fazekas, M.; Notaras, E. G. A.; Blau, W. J.; Zawadzka, M.; Locos, O. B.; Ni Mhuircheartaigh, E. M., Nonlinear Optical Properties of Porphyrins. *Advanced Materials* **2007**, *19*, 2737-2774.
57. Mahmood, A.; Hu, J.-Y.; Xiao, B.; Tang, A.; Wang, X.; Zhou, E., Recent Progress in Porphyrin-Based Materials for Organic Solar Cells. *Journal of Materials Chemistry A* **2018**, *6*, 16769-16797.
58. Mahammed, A.; Chen, K.; Vestfrid, J.; Zhao, J.; Gross, Z., Phosphorus Corrole Complexes: From Property Tuning to Applications in Photocatalysis and Triplet–Triplet Annihilation Upconversion. *Chemical Science* **2019**, *10*, 7091-7103.
59. Kc, C. B.; Lim, G. N.; Nesterov, V. N.; Karr, P. A.; D'Souza, F., Phenothiazine-Bodipy-Fullerene Triads as Photosynthetic Reaction Center Models: Substitution and Solvent Polarity Effects on Photoinduced Charge Separation and Recombination. *Chemistry* **2014**, *20*, 17100-12.
60. González-Rodríguez, D.; Bottari, G., Phthalocyanines, Subphthalocyanines and Porphyrins for Energy and Electron Transfer Applications. *Journal of Porphyrins and Phthalocyanines* **2009**, *13*, 624-636.
61. Gust, D.; Moore, T. A.; Moore, A. L., Mimicking Photosynthetic Solar Energy Transduction. *Accounts of Chemical Research* **2001**, *34*, 40-48.
62. Rao, S. V.; Srinivas, N. K. M. N.; Rao, D. N.; Giribabu, L.; Maiya, B. G.; Philip, R.; Kumar, G. R., Studies of Third-Order Optical Nonlinearity and Nonlinear Absorption in Tetra Tolyl Porphyrins Using Degenerate Four Wave Mixing and Z-Scan. *Optics Communications* **2000**, *182*, 255-264.
63. Jadhav, T.; Maragani, R.; Misra, R.; Sreeramulu, V.; Rao, D. N.; Mobin, S. M., Design and Synthesis of Donor–Acceptor Pyrazabole Derivatives for Multiphoton Absorption. *Dalton Transactions* **2013**, *42*, 4340.
64. Wojciechowski, A.; Raposo, M. M. M.; Castro, M. C. R.; Kuznik, W.; Fuks-Janczarek, I.; Pokladko-Kowar, M.; Bureš, F., Nonlinear Optoelectronic Materials Formed by Push–Pull (Bi)Thiophene Derivatives Functionalized with

Di(Tri)Cyanovinyl Acceptor Groups. *Journal of Materials Science: Materials in Electronics* **2014**, *25*, 1745-1750.

65. Rebane, A.; Drobizhev, M.; Makarov, N. S.; Koszarna, B.; Tasior, M.; Gryko, D. T., Two-Photon Absorption Properties of Meso-Substituted A3-Corroles. *Chemical Physics Letters* **2008**, *462*, 246-250.
66. Garai, A.; Kumar, S.; Sinha, W.; Purohit, C. S.; Das, R.; Kar, S., A Comparative Study of Optical Nonlinearities of Trans-A2b-Corroles in Solution and in Aggregated State. *RSC Advances* **2015**, *5*, 28643-28651.
67. Hamad, S.; Tewari, S. P.; Giribabu, L.; Rao, S. V., Picosecond and Femtosecond Optical Nonlinearities of Novel Corroles. *Journal of Porphyrins and Phthalocyanines* **2012**, *16*, 140-148.
68. Krishna, N. V.; Krishna, J. V. S.; Singh, S. P.; Giribabu, L.; Han, L.; Bedja, I.; Gupta, R. K.; Islam, A., Donor-Π–Acceptor Based Stable Porphyrin Sensitizers for Dye-Sensitized Solar Cells: Effect of Π-Conjugated Spacers. *The Journal of Physical Chemistry C* **2017**, *121*, 6464-6477.
69. Wen, L.; Fang, Y.; Yang, J.; Han, Y.; Song, Y., Third-Order Nonlinear Optical Properties and Ultrafast Excited-State Dynamics of Benzothiazolium Salts: Transition in Absorption and Refraction under Different Time Regimes. *Dyes and Pigments* **2018**, *156*, 26-32.
70. Wen, L.; Fang, Y.; Yang, J.; Han, Y.; Song, Y., Comparison of Third-Order Nonlinear Optical Properties of Benzothiazolium Salt and Neutral Benzothiazole Derivative: Broadband Absorption Response and Transient Dynamic Analysis. *Dyes and Pigments* **2019**, *168*, 28-35.
71. Xie, Q.; Shao, Z.; Zhao, Y.; Yang, L.; Wu, Q.; Xu, W.; Li, K.; Song, Y.; Hou, H., Novel Photo-Controllable Third-Order Nonlinear Optical (Nlo) Switches Based on Azobenzene Derivatives. *Dyes and Pigments* **2019**, 107599.
72. Xu, W.; Wang, W.; Li, J.; Wu, Q.; Zhao, Y.; Hou, H.; Song, Y., Two-Photon Absorption Property and Excellent Optical Limiting Response of Three Schiff Base Derivatives with Large Conjugated System. *Dyes and Pigments* **2019**, *160*, 1-8.
73. Zhai, G.; Wu, X.; Jin, P.; Song, T.; Xiao, J.; Song, Y., Synthesis, Optoelectronic Properties and Third-Order Nonlinear Optical Behaviors of the Functionalized Acene Derivatives. *Dyes and Pigments* **2018**, *155*, 93-99.

74. Yang, Y.; Wu, X.; Jia, J.; Shen, L.; Zhou, W.; Yang, J.; Song, Y., Investigation of Ultrafast Optical Nonlinearities in Novel Bis-Chalcone Derivatives. *Optics & Laser Technology* **2020**, *123*, 105903.
75. Higuchi, T.; Uzu, S.; Hirobe, M., Synthesis of a Highly Stable Iron Porphyrin Coordinated by Alkylthiolate Anion as a Model for Cytochrome P-450 and Its Catalytic Activity in Oxygen-Oxygen Bond Cleavage. *Journal of the American Chemical Society* **1990**, *112*, 7051-7053.
76. Vicente, M. G. H.; Jaquinod, L.; Smith, K. M., Oligomeric Porphyrin Arrays. *Chemical Communications* **1999**, 1771-1782.
77. Arnold, L.; Müllen, K., Modifying the Porphyrin Core — a Chemist's Jigsaw. *Journal of Porphyrins and Phthalocyanines* **2011**, *15*, 757-779.
78. Di Carlo, G.; Caramori, S.; Casarin, L.; Orbelli Biroli, A.; Tessore, F.; Argazzi, R.; Oriana, A.; Cerullo, G.; Bignozzi, C. A.; Pizzotti, M., Charge Transfer Dynamics in B- and Meso-Substituted Dithienylethylene Porphyrins. *The Journal of Physical Chemistry C* **2017**, *121*, 18385-18400.
79. Imahori, H.; Fukuzumi, S., Porphyrin- and Fullerene-Based Molecular Photovoltaic Devices. *Advanced Functional Materials* **2004**, *14*, 525-536.
80. O'Neil, M. P.; Niemczyk, M. P.; Svec, W. A.; Gosztola, D.; Gaines, G. L.; Wasielewski, M. R., Picosecond Optical Switching Based on Biphotonic Excitation of an Electron Donor-Acceptor-Donor Molecule. *Science* **1992**, *257*, 63-65.
81. Reddy, G.; Devulapally, K.; Islavath, N.; Giribabu, L., Metallated Macrocyclic Derivatives as a Hole - Transporting Materials for Perovskite Solar Cells. *Chem Rec* **2019**.
82. Higashino, T.; Imahori, H., Porphyrins as Excellent Dyes for Dye-Sensitized Solar Cells: Recent Developments and Insights. *Dalton Transactions* **2015**, *44*, 448-463.
83. Arpaçay, P.; Maity, P.; El-Zohry, A. M.; Meindl, A.; Akca, S.; Plunkett, S.; Senge, M. O.; Blau, W. J.; Mohammed, O. F., Controllable Charge-Transfer Mechanism at Push–Pull Porphyrin/Nanocarbon Interfaces. *The Journal of Physical Chemistry C* **2019**, *123*, 14283-14291.
84. Kang, S. H.; Lu, C.; Zhou, H.; Choi, S.; Kim, J.; Kim, H. K., Novel Π-Extended Porphyrin-Based Hole-Transporting Materials with Triarylamine Donor Units for High Performance Perovskite Solar Cells. *Dyes and Pigments* **2019**, *163*, 734-739.

85. Terazima, M.; Shimizu, H.; Osuka, A., The Third-Order Nonlinear Optical Properties of Porphyrin Oligomers. *Journal of Applied Physics* **1997**, *81*, 2946-2951.
86. Chen, L.; Hu, R.; Xu, J.; Wang, S.; Li, X.; Li, S.; Yang, G., Third-Order Nonlinear Optical Properties of a Series of Porphyrin-Appended Europium(Iii) Bis(Phthalocyaninato) Complexes. *Spectrochimica Acta Part A: Molecular and Biomolecular Spectroscopy* **2013**, *105*, 577-581.
87. Enescu, M.; Steenkeste, K.; Tfibel, F.; Fontaine-Aupart, M.-P., Femtosecond Relaxation Processes from Upper Excited States of Tetrakis(N-Methyl-4-Pyridyl)Porphyrins Studied by Transient Absorption Spectroscopy. *Physical Chemistry Chemical Physics* **2002**, *4*, 6092-6099.
88. Shelby, M. L., et al., Ultrafast Excited State Relaxation of a Metalloporphyrin Revealed by Femtosecond X-Ray Absorption Spectroscopy. *Journal of the American Chemical Society* **2016**, *138*, 8752-8764.
89. Teo, R. D.; Hwang, J. Y.; Termini, J.; Gross, Z.; Gray, H. B., Fighting Cancer with Corroles. *Chemical Reviews* **2016**, *117*, 2711-2729.
90. Aviv-Harel, I.; Gross, Z., Aura of Corroles. *Chemistry - A European Journal* **2009**, *15*, 8382-8394.
91. Buckley, H. L.; Chomitz, W. A.; Koszarna, B.; Tasior, M.; Gryko, D. T.; Brothers, P. J.; Arnold, J., Synthesis of Lithium Corrole and Its Use as a Reagent for the Preparation of Cyclopentadienyl Zirconium and Titanium Corrole Complexes. *Chemical Communications* **2012**, *48*, 10766.
92. Agadjanian, H.; Ma, J.; Rentsendorj, A.; Valluripalli, V.; Hwang, J. Y.; Mahammed, A.; Farkas, D. L.; Gray, H. B.; Gross, Z.; Medina-Kauwe, L. K., Tumor Detection and Elimination by a Targeted Gallium Corrole. *Proceedings of the National Academy of Sciences* **2009**, *106*, 6105-6110.
93. Capuano, R.; Pomarico, G.; Paolesse, R.; Di Natale, C., Corroles-Porphyrins: A Teamwork for Gas Sensor Arrays. *Sensors (Basel)* **2015**, *15*, 8121-30.
94. Nardis, S.; Mandoj, F.; Stefanelli, M.; Paolesse, R., Metal Complexes of Corrole. *Coordination Chemistry Reviews* **2019**, *388*, 360-405.
95. Mahammed, A.; Gross, Z., Corroles as Triplet Photosensitizers. *Coordination Chemistry Reviews* **2019**, *379*, 121-132.

96. Stensitzki, T.; Yang, Y.; Berg, A.; Mahammed, A.; Gross, Z.; Heyne, K., Ultrafast Electronic and Vibrational Dynamics in Brominated Aluminum Corroles: Energy Relaxation and Triplet Formation. *Structural Dynamics* **2016**, *3*, 043210.
97. Pomarico, E.; Pospisil, P.; Bouduban, M. E.; Vestfrid, J.; Gross, Z.; Záliš, S.; Chergui, M.; Vlček, A. n., Photophysical Heavy-Atom Effect in Iodinated Metallocorroles: Spin–Orbit Coupling and Density of States. *The Journal of Physical Chemistry A* **2018**, *122*, 7256-7266.
98. Yang, Y.; Jones, D.; von Haimberger, T.; Linke, M.; Wagnert, L.; Berg, A.; Levanon, H.; Zacarias, A.; Mahammed, A.; Gross, Z., Assignment of Aluminum Corroles Absorption Bands to Electronic Transitions by Femtosecond Polarization Resolved Vis-Pump Ir-Probe Spectroscopy. *The Journal of Physical Chemistry A* **2012**, *116*, 1023-1029.
99. Yadav, P.; Anand, T.; Moram, S. S. B.; Bhattacharya, S.; Sankar, M.; Rao, S. V., Synthesis and Femtosecond Third Order Nonlinear Optical Properties of Push-Pull Trans- a 2 B-Corroles. *Dyes and Pigments* **2017**, *143*, 324-330.
100. Liu, X.; Mahammed, A.; Tripathy, U.; Gross, Z.; Steer, R. P., Photophysics of Soret-Excited Tetrapyrroles in Solution. Iii. Porphyrin Analogues: Aluminum and Gallium Corroles. *Chemical Physics Letters* **2008**, *459*, 113-118.
101. Rodriguez, L. G.; Lockett, S. J.; Holtom, G. R., Coherent Anti-Stokes Raman Scattering Microscopy: A Biological Review. *Cytometry Part A* **2006**, *69A*, 779-791.
102. Sharma, J.; Beard, B. C.; Chaykovsky, M., Correlation of Impact Sensitivity with Electronic Levels and Structure of Molecules. *The Journal of Physical Chemistry* **1991**, *95*, 1209-1213.
103. Williams, F., Electronic States of Solid Explosives and Their Probable Role in Detonations. In *Advances in Chemical Physics*, John Wiley & Sons, Inc.: 2007; pp 289-302.
104. Kuklja, M. M.; Aduev, B. P.; Aluker, E. D.; Krasheninin, V. I.; Krechetov, A. G.; Mitrofanov, A. Y., Role of Electronic Excitations in Explosive Decomposition of Solids. *Journal of Applied Physics* **2001**, *89*, 4156-4166.
105. Chu, G.; Lu, F.; Xin, J.; Xi, T.; Shui, M.; He, W.; Gu, Y.; Xiong, Y.; Cheng, K.; Xu, T., Excited-State Dynamics and Electron Transfer Process of 1,3,5-Triamino-2,4,6-Trinitrobenzene. *RSC Advances* **2016**, *6*, 55560-55567.

106. Adamo, C.; Jacquemin, D., The Calculations of Excited-State Properties with Time-Dependent Density Functional Theory. *Chem. Soc. Rev.* **2013**, *42*, 845-856.
107. Dreger, Z. A.; Gruzdkov, Y. A.; Gupta, Y. M.; Dick, J. J., Shock Wave Induced Decomposition Chemistry of Pentaerythritol Tetranitrate Single Crystals: Time-Resolved Emission Spectroscopy. *The Journal of Physical Chemistry B* **2002**, *106*, 247-256.
108. Zhurova, E. A.; Tsirelson, V. G.; Stash, A. I.; Yakovlev, M. V.; Pinkerton, A. A., Electronic Energy Distributions in Energetic Materials: Nto and the Biguanidinium Dinitramides. *The Journal of Physical Chemistry B* **2004**, *108*, 20173-20179.
109. Zhu, W.; Huang, H.; Huang, H.; Xiao, H., Initial Chemical Events in Shocked Octahydro-1,3,5,7-Tetranitro-1,3,5,7- Tetrazocine: A New Initiation Decomposition Mechanism. *The Journal of Chemical Physics* **2012**, *136*, 044516.
110. Ge, N.-N.; Wei, Y.-K.; Ji, G.-F.; Chen, X.-R.; Zhao, F.; Wei, D.-Q., Initial Decomposition of the Condensed-Phase Β-Hmx under Shock Waves: Molecular Dynamics Simulations. *The Journal of Physical Chemistry B* **2012**, *116*, 13696-13704.
111. Thurston, R.; Brister, M. M.; Tan, L. Z.; Champenois, E. G.; Bakhti, S.; Muddukrishna, P.; Weber, T.; Belkacem, A.; Slaughter, D. S.; Shivaram, N., Ultrafast Dynamics of Excited Electronic States in Nitrobenzene Measured by Ultrafast Transient Polarization Spectroscopy. *The Journal of Physical Chemistry A* **2020**.
112. Chen, M.-W.; You, S.; Suslick, K. S.; Dlott, D. D., Hot Spot Generation in Energetic Materials Created by Long-Wavelength Infrared Radiation. *Applied Physics Letters* **2014**, *104*, 061907.
113. Wu, H.; Song, Y.; Yu, G.; Wang, Y.; Wang, C.; Yang, Y., Tracking the Photodissociation Dynamics of Liquid Nitromethane at 266 Nm by Femtosecond Time-Resolved Broadband Transient Grating Spectroscopy. *Chemical Physics Letters* **2016**, *652*, 152-156.
114. Dlott, D. D.; Fayer, M. D., Shocked Molecular Solids: Vibrational up Pumping, Defect Hot Spot Formation, and the Onset of Chemistry. *The Journal of Chemical Physics* **1990**, *92*, 3798-3812.
115. Chen, S.; Tolbert, W. A.; Dlott, D. D., Direct Measurement of Ultrafast Multiphonon up-Pumping in High Explosives. *The Journal of Physical Chemistry* **1994**, *98*, 7759-7766.

116. Nesbitt, D. J.; Field, R. W., Vibrational Energy Flow in Highly Excited Molecules: Role of Intramolecular Vibrational Redistribution. *The Journal of Physical Chemistry* **1996**, *100*, 12735-12756.
117. Rajchenbach, C.; Jonusauskas, G.; Rulliere, C., Sub-Picosecond Time-Resolved Spectroscopy of Energetic Materials : The Nitromethane and Nitro-Stilbenes. *Le Journal de Physique IV* **1995**, *05*, C4-365-C4-378.
118. Kenkre, V. M.; Tokmakoff, A.; Fayer, M. D., Theory of Vibrational Relaxation of Polyatomic Molecules in Liquids. *The Journal of Chemical Physics* **1994**, *101*, 10618-10629.
119. Menke, K., Organic Chemistry of Explosives, J. P. Agrawal, R. D. Hodgson. *Propellants, Explosives, Pyrotechnics* **2007**, *32*, 182-182.
120. Zeng, Z.; Guo, Y.; Twamley, B.; Shreeve, J. n. M., Energetic Polyazole Polynitrobenzenes and Their Coordination Complexes. *Chemical Communications* **2009**, 6014.
121. Gao, H.; Shreeve, J. n. M., Azole-Based Energetic Salts. *Chemical Reviews* **2011**, *111*, 7377-7436.
122. Kommu, N.; Ghule, V. D.; Kumar, A. S.; Sahoo, A. K., Triazole-Substituted Nitroarene Derivatives: Synthesis, Characterization, and Energetic Studies. *Chemistry - An Asian Journal* **2013**, *9*, 166-178.
123. Kumar, A. S.; Kommu, N.; Ghule, V. D.; Sahoo, A. K., Synthesis of Trifluoromethyl-Substituted N-Aryl-Poly-1,2,3-Triazole Derivatives. *Journal of Materials Chemistry A* **2014**, *2*, 7917.
124. Kommu, N.; Kumar, A. S.; Raveendra, J.; Ghule, V. D.; Sahoo, A. K., Synthesis, Characterization, and Energetic Studies of Polynitro Aryl-1,2,3-2 H-Triazoles. *Asian Journal of Organic Chemistry* **2015**, *5*, 138-146.
125. Kumar, A. S.; Ghule, V. D.; Subrahmanyam, S.; Sahoo, A. K., Synthesis of Thermally Stable Energetic 1,2,3-Triazole Derivatives. *Chemistry - A European Journal* **2012**, *19*, 509-518.
126. Liu, X.; Zhang, W.; Song, Y.; Zheng, Z.; Lv, Z.; Yang, Y., Selective Excitation of Vibrational Modes and Probe for Asymmetric Intramolecular Energy Redistribution. *Physica Scripta* **2019**, *94*, 065402.
127. Wang, S.; Yang, Y.; Sun, Z.; Dlott, D. D., Fast Spectroscopy of Energy Release in Nanometric Explosives. *Chemical Physics Letters* **2003**, *368*, 189-194.

128. Namboodiri, M.; Kazemi, M. M.; Zeb Khan, T.; Materny, A.; Kiefer, J., Ultrafast Vibrational Dynamics and Energy Transfer in Imidazolium Ionic Liquids. *Journal of the American Chemical Society* **2014**, *136*, 6136-6141.
129. Zhao, Y.; Zhang, S.; Zhou, B.; Dong, Z.; Chen, D.; Zhang, Z.; Xia, Y., Spectrally Dispersed Femtosecond Cars Investigation of Vibrational Characteristics in Ethanol. *Journal of Raman Spectroscopy* **2014**, *45*, 826-829.
130. Niu, K.; Lee, S.-Y., Analysis of Time Resolved Femtosecond and Femtosecond/Picosecond Coherent Anti-Stokes Raman Spectroscopy: Application to Toluene and Rhodamine 6g. *The Journal of Chemical Physics* **2012**, *136*, 064504.
131. Wrzesinski, P. J.; Stauffer, H. U.; Kulatilaka, W. D.; Gord, J. R.; Roy, S., Time-Resolved Femtosecond Cars from 10 to 50 Bar: Collisional Sensitivity. *Journal of Raman Spectroscopy* **2013**, *44*, 1344-1348.
132. Kiefer, J.; Namboodiri, M.; Kazemi, M. M.; Materny, A., Time-Resolved Femtosecond Cars of the Ionic Liquid 1-Ethyl-3-Methylimidazolium Ethylsulfate. *Journal of Raman Spectroscopy* **2015**, *46*, 722-726.
133. Engel, S. R.; Miller, J. D.; Dedic, C. E.; Seeger, T.; Leipertz, A.; Meyer, T. R., Hybrid Femtosecond/Picosecond Coherent Anti-Stokes Raman Scattering for High-Speed Ch4/N2measurements in Binary Gas Mixtures. *Journal of Raman Spectroscopy* **2013**, *44*, 1336-1343.
134. Levitt, J. M.; Katz, O.; Silberberg, Y., Frequency-Encoded Multiplexed Cars Microscopy by Rapid Pulse Shaping. *Journal of Modern Optics* **2014**, *61*, 872-876.
135. Müller, N.; Brückner, L.; Motzkus, M., Invited Article: Coherent Raman and Mid-Ir Microscopy Using Shaped Pulses in a Single-Beam Setup. *APL Photonics* **2018**, *3*, 092406.
136. Kolesnichenko, P. V.; Tollerud, J. O.; Davis, J. A., Background-Free Time-Resolved Coherent Raman Spectroscopy (CSRS and CARS): Heterodyne Detection of Low-Energy Vibrations and Identification of Excited-State Contributions. *APL Photonics* **2019**, *4*, 056102.
137. Lanzani, G., *The Photophysics Behind Photovoltaics and Photonics*; John Wiley & Sons, **2012**.
138. Montalti, M.; Credi, A.; Prodi, L.; Gandolfi, M., Photophysical Properties of Organic Compounds. *Handbook of Photochemistry* **2006**, *3*, 255.

139. Kumpulainen, T.; Lang, B.; Rosspeintner, A.; Vauthey, E., Ultrafast Elementary Photochemical Processes of Organic Molecules in Liquid Solution. *Chemical reviews* **2017**, *117*, 10826-10939.

140. del Valle, J. C.; Catalán, J., Kasha's Rule: A Reappraisal. *Physical Chemistry Chemical Physics* **2019**, *21*, 10061-10069.

141. Johnson, P. B.; Christy, R.-W., Optical Constants of the Noble Metals. *Physical review B* **1972**, *6*, 4370.

142. Ashcroft, N. W.; Mermin, N. D., Solid State Physics [by] Neil W. Ashcroft [and] N. David Mermin. New York: Holt, Rinehart and Winston: **1976**.

143. Petryayeva, E.; Krull, U. J., Localized Surface Plasmon Resonance: Nanostructures, Bioassays and Biosensing—a Review. *Analytica chimica acta* **2011**, *706*, 8-24.

144. Voisin, C.; Christofilos, D.; Loukakos, P.; Del Fatti, N.; Vallée, F.; Lermé, J.; Gaudry, M.; Cottancin, E.; Pellarin, M.; Broyer, M., Ultrafast Electron-Electron Scattering and Energy Exchanges in Noble-Metal Nanoparticles. *Physical Review B* **2004**, *69*, 195416.

145. Rana, A.; Gupta, N.; Lochan, A.; Sharma, G. D.; Chand, S.; Kumar, M.; Singh, R. K., Charge Carrier Dynamics and Surface Plasmon Interaction in Gold Nanorod-Blended Organic Solar Cell. *Journal of Applied Physics* **2016**, *120*, 063102.

146. Hartland, G. V.; Besteiro, L. V.; Johns, P.; Govorov, A. O., What’s So Hot About Electrons in Metal Nanoparticles? *ACS Energy Letters* **2017**, *2*, 1641-1653.

147. Kerker, M., *The Scattering of Light and Other Electromagnetic Radiation: Physical Chemistry: A Series of Monographs*; Academic press, **2013**; Vol. 16.

148. Bohren, C.; Huffman, D., Absorption and Scattering of Light by Small Particles Wiley New York Google Scholar. **1983**.

149. Zhang, X.; Huang, C.; Wang, M.; Huang, P.; He, X.; Wei, Z., Transient Localized Surface Plasmon Induced by Femtosecond Interband Excitation in Gold Nanoparticles. *Scientific Reports* **2018**, *8*.

150. Ren, M.; Jia, B.; Ou, J.-Y.; Plum, E.; Zhang, J.; MacDonald, K. F.; Nikolaenko, A. E.; Xu, J.; Gu, M.; Zheludev, N. I., Nanostructured Plasmonic Medium for Terahertz Bandwidth All-Optical Switching. *Advanced Materials* **2011**, *23*, 5540-5544.

151. Link, S.; Burda, C.; Wang, Z. L.; El-Sayed, M. A., Electron Dynamics in Gold and Gold–Silver Alloy Nanoparticles: The Influence of a Nonequilibrium Electron

Distribution and the Size Dependence of the Electron–Phonon Relaxation. *The Journal of Chemical Physics* **1999**, *111*, 1255-1264.

152. Zarick, H. F.; Boulesbaa, A.; Talbert, E. M.; Puretzky, A.; Geohegan, D.; Bardhan, R., Ultrafast Excited-State Dynamics in Shape- and Composition-Controlled Gold–Silver Bimetallic Nanostructures. *The Journal of Physical Chemistry C* **2017**, *121*, 4540-4547.
153. Li, Y.; Lan, J. Y.; Liu, J.; Yu, J.; Luo, Z.; Wang, W.; Sun, L., Synthesis of Gold Nanoparticles on Rice Husk Silica for Catalysis Applications. *Industrial & engineering chemistry research* **2015**, *54*, 5656-5663.
154. Heilweil, E.; Hochstrasser, R., Nonlinear Spectroscopy and Picosecond Transient Grating Study of Colloidal Gold. *The Journal of chemical physics* **1985**, *82*, 4762-4770.
155. Bloemer, M. J.; Haus, J. W.; Ashley, P. R., Degenerate Four-Wave Mixing in Colloidal Gold as a Function of Particle Size. *JOSA B* **1990**, *7*, 790-795.
156. Lin, Y.; Zhang, X., Ultrafast Multipolar Plasmon for Unidirectional Optical Switching in a Hemisphere-Nanoshell Array. *Advanced Optical Materials* **2017**, *5*, 1601088.
157. Karam, T. E.; Smith, H. T.; Haber, L. H., Enhanced Photothermal Effects and Excited-State Dynamics of Plasmonic Size-Controlled Gold–Silver–Gold Core–Shell–Shell Nanoparticles. *The Journal of Physical Chemistry C* **2015**, *119*, 18573-18580.
158. Elsayed-Ali, H. E.; Juhasz, T.; Smith, G. O.; Bron, W. E., Femtosecond Thermoreflectivity and Thermotransmissivity of Polycrystalline and Single-Crystalline Gold Films. *Physical Review B* **1991**, *43*, 4488-4491.
159. Wright, O. B., Ultrafast Nonequilibrium Stress Generation in Gold and Silver. *Physical Review B* **1994**, *49*, 9985-9988.
160. Sun, C. K.; Vallée, F.; Acioli, L. H.; Ippen, E. P.; Fujimoto, J. G., Femtosecond-Tunable Measurement of Electron Thermalization in Gold. *Physical Review B* **1994**, *50*, 15337-15348.
161. Schoenlein, R. W.; Lin, W. Z.; Fujimoto, J. G.; Eesley, G. L., Femtosecond Studies of Nonequilibrium Electronic Processes in Metals. *Physical Review Letters* **1987**, *58*, 1680-1683.

162. Li, M.; Zhang, H.; Zhang, Y.; Hou, B.; Li, C.; Wang, X.; Zhang, J.; Xiao, L.; Cui, Z.; Ao, Y., Facile Synthesis of Benzothiadiazole-Based Chromophores for Enhanced Performance of Second-Order Nonlinear Optical Materials. *Journal of Materials Chemistry C* **2016**, *4*, 9094-9102.

163. Zhai, G.; Li, X.; Jin, P.; Semin, S.; Xiao, J.; Rasing, T.; Xu, J., Functionalized Twistacenes for Solid State Nonlinear Optical Materials. *Dyes and Pigments* **2018**, *149*, 876-881.

164. de Torres, M.; Semin, S.; Razdolski, I.; Xu, J.; Elemans, J. A. A. W.; Rasing, T.; Rowan, A. E.; Nolte, R. J. M., Extended Π-Conjugated Ruthenium Zinc–Porphyrin Complexes with Enhanced Nonlinear-Optical Properties. *Chemical Communications* **2015**, *51*, 2855-2858.

165. Faurie, A.; Gohier, F.; Frère, P., Facile Synthesis and Optical Properties of Extended Tpa-Benzodifuran Derivatives Connected by Cyano-Vinylene Junctions. *Dyes and Pigments* **2018**, *154*, 38-43.

166. Chemla, D. S., *Nonlinear Optical Properties of Organic Molecules and Crystals*; Elsevier, 2012; Vol. 1.

167. Raavi, S. S. K.; Biswas, C., Femtosecond Pump-Probe Spectroscopy for Organic Photovoltaic Devices. In *Digital Encyclopedia of Applied Physics*, Wiley-VCH Verlag GmbH & Co. KGaA: **2019**; pp 1-49.

168. Erande, Y.; Kothavale, S.; Sreenath, M. C.; Chitrambalam, S.; Joe, I. H.; Sekar, N., Nlophoric Multichromophoric Auxiliary Methoxy Aided Triphenylamine D-Π-a Chromophores–Spectroscopic and Computational Studies. *Optical Materials* **2017**, *73*, 602-616.

169. Jia, J.; Hu, C.; Cui, Y.; Li, Y.; Wang, W.; Han, L.; Li, Y.; Gao, J., Design and Synthesis of a Series of N-Donor Quinacridone Derivatives with Novel Nonlinear Optical Properties. *Dyes and Pigments* **2018**, *149*, 843-850.

170. Zhou, S.; Jia, J.; Gao, J.; Han, L.; Li, Y.; Sheng, W., The One-Pot Synthesis and Fluorimetric Study of 3-(2′-Benzothiazolyl) Coumarins. *Dyes and Pigments* **2010**, *86*, 123-128.

171. Yang, J.; Aili, D.; Li, Q.; Xu, Y.; Liu, P.; Che, Q.; Jensen, J. O.; Bjerrum, N. J.; He, R., Benzimidazole Grafted Polybenzimidazoles for Proton Exchange Membrane Fuel Cells. *Polymer Chemistry* **2013**, *4*, 4768-4775.

172. Ge, Y. Q.; Jia, J.; Yang, H.; Tao, X. T.; Wang, J. W., The Synthesis, Characterization and Optical Properties of Novel Pyrido [1, 2-a] Benzimidazole Derivatives. *Dyes and pigments* **2011**, *88*, 344-349.
173. Giribabu, L.; Kandhadi, J.; Kanaparthi, R. K., Phosphorus(V)Corrole- Porphyrin Based Hetero Trimers: Synthesis, Spectroscopy and Photochemistry. *Journal of Fluorescence* **2013**, *24*, 569-577.
174. Kandhadi, J.; Yeduru, V.; Bangal, P. R.; Giribabu, L., Corrole-Ferrocene and Corrole-Anthraquinone Dyads: Synthesis, Spectroscopy and Photochemistry. *Phys Chem Chem Phys* **2015**, *17*, 26607-20.
175. Ngo, T. H., et al., Engaging Copper(Iii) Corrole as an Electron Acceptor: Photoinduced Charge Separation in Zinc Porphyrin-Copper Corrole Donor-Acceptor Conjugates. *Chemistry* **2016**, *22*, 1301-12.
176. Tasior, M.; Gryko, D. T.; Shen, J.; Kadish, K. M.; Becherer, T.; Langhals, H.; Ventura, B.; Flamigni, L., Energy- and Electron-Transfer Processes in Corrole−Perylenebisimide−Triphenylamine Array. *The Journal of Physical Chemistry C* **2008**, *112*, 19699-19709.
177. Ding, T.; Alemán, E. A.; Modarelli, D. A.; Ziegler, C. J., Photophysical Properties of a Series of Free-Base Corroles. *The Journal of Physical Chemistry A* **2005**, *109*, 7411-7417.
178. White, T. P.; Deleporte, E.; Sum, T.-C., Feature Issue Introduction: Halide Perovskites for Optoelectronics. *Optical Materials Express* **2018**, *8*, 231-234.
179. Scott, R.; Achtstein, A. W.; Prudnikau, A.; Antanovich, A.; Christodoulou, S.; Moreels, I.; Artemyev, M.; Woggon, U., Two Photon Absorption in Ii–Vi Semiconductors: The Influence of Dimensionality and Size. *Nano letters* **2015**, *15*, 4985-4992.
180. Leuthold, J.; Koos, C.; Freude, W., Nonlinear Silicon Photonics. *Nature photonics* **2010**, *4*, 535.
181. Boyd, R. W., *Nonlinear Optics*; Academic press, 2019.

Intentional blank page

Chapter 2 Theoretical Concepts and Experimental Details

Abstract

This chapter presents the details of the characterization of ultrashort optical pulses used in various experiments and an overview of the experimental techniques used in detail, such as Z-scan, degenerate four-wave mixing, transient absorption spectroscopy, and coherent anti-Stokes Raman spectroscopy. The details of the input laser source (LIBRA, M/s Coherent, USA), spectrometer (MAYA), lock-in amplifier, and the detectors employed in carrying out all the measurements are briefly described. The generation mechanisms of ultrashort laser pulses by mode-locking and following amplification of pulses using chirped pulse amplification (CPA) method are discussed. The details involved in optical parametric generation and amplification (OPA) are also briefed. The pulse characteristics (duration, phase) measurements of the amplifier (LIBRA) output were achieved using a spectrometer, intensity autocorrelation and single-shot autocorrelation (SSA) techniques.

2.1 Introduction

The aim of this section is to provide a concise introduction to the different techniques for the generation of optical pulses. The most commonly used techniques, such as (a) Q-switching (b) cavity dumping and (c) mode-locking techniques, are discussed. The main constituents used for all the experiments, such as laser (ultrafast lasers) sources and their functioning, detector, and spectrometer, are elaborated. The generation and maintenance of femtosecond (fs) pulses, followed by amplification based on chirped pulse amplification (CPA), is discussed in detail. The components of the amplifier laser are elaborated, such as oscillator, pump lasers, and stretch/compressor. The working and operation of an optical parametric amplifier (OPA) is reviewed. The pulse characteristics of the amplified femtosecond pulses were measured using single shot and intensity autocorrelation methods and those details are discussed. The data acquisition and some of the initial measurements from carbon tetrachloride (CCl_4) and β- barium borate (BBO) are presented along with.

2.2 Cavity dumping

Cavity dumping is a process used to generate intense short optical pulses, which can be combined with both Q-switching as well as Mode-locking techniques. The basic principle behind the cavity dumping is to maintain the cavity losses inside the laser resonator as low as possible until the laser energy build-up inside the resonator with multiple round trips.[1-2] An optical switch inside the cavity is placed to extract the photon bursts in the form of pulses at about one cavity round trip time; this is the main advantage of cavity dumping. The kind of optical switches used in cavity dumping is acousto-optic modulator (AOM) or Pockels cell.[1, 3] Whenever the AOM device is on, we see a pulse output for every cavity roundtrip, as shown in figure 2.1. The intracavity power (P_c) when AOM is turned on (t = 0) can be expressed as,

$$P_c = P_0 exp\left(\frac{-2\eta t}{2L/C}\right) \tag{1}$$

P_0 = initial cavity power

L = cavity length

η = AOM deflection (cavity loss)

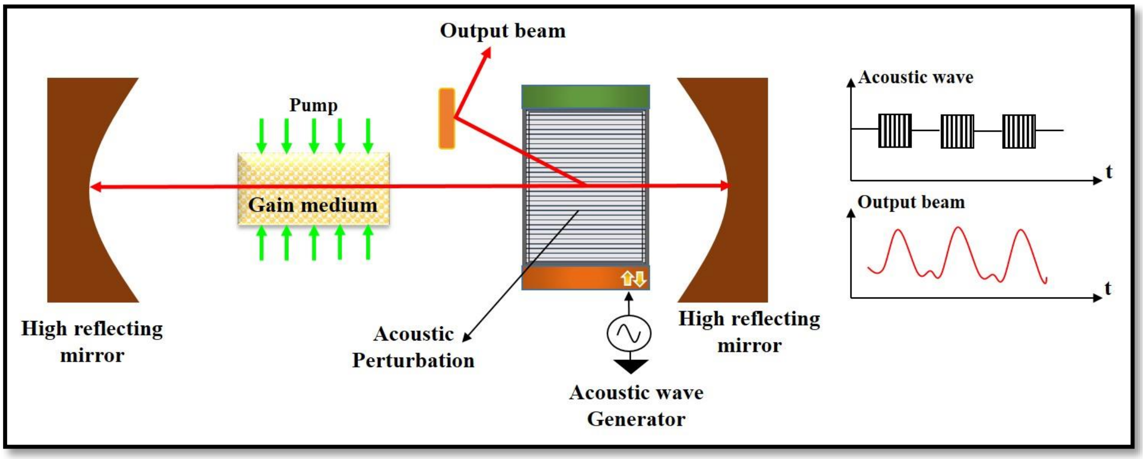

Figure 2.1 Working principle of cavity dumping.

The efficiency of cavity-dumping can be expressed in terms of a ratio of output power to the optimum output power at steady state (CW) operation. Since the total energy is stored in the cavity by modulating the AOM, a very short ns pulse with high repetition rate can be generated in contrast to Q-switching, whereby increasing the repetition rate the pulse duration increases due to the stored energy is in the gain medium.

2.2.1 Acousto-optic Modulator

The acousto-optic modulator uses sound waves to diffract light inside a medium (TeO_2, SiO_2, quartz crystal); therefore, a shift in the frequency of light is obtained.[4] As shown in figure 2.2 at one end of the glass material, a piezoelectric transducer is attached by using an external oscillating electric field that drives the transducer to vibrate. The sound waves which are produced from the transducer are transmitted within the material (quartz crystal) to the other end. The acoustic waves create a deformation in the material due to compression and rarefaction of the sound wave, due to which the material’s refractive index is modulated periodically. Within the material where the compression occurs, the incoming light encounters a high refractive index, and at places where rarefaction occurs, the less refractive index is exhibited. Therefore, the light which travelled through this material exhibits diffraction due to the dynamic periodic variation in the refractive index. In the case of Q-switching, when the pump source is ON the AOM is also kept on, so due to the diffraction losses, the loss in the resonator is high with low Q value, so lasing is suppressed inside resonator (due to the diffracted beams directed out of the resonator). Once the AOM is off, an intense laser pulse is generated. In cavity dumping, whenever the AOM is off, we are allowing lasing to take place to build up the laser energy inside the resonator, so by turning on the AOM, an intense photon burst in the form of an optical pulse is generated. The width of pulse is determined by the cavity length (1m of cavity length can produce a *ns* pulse).[3]

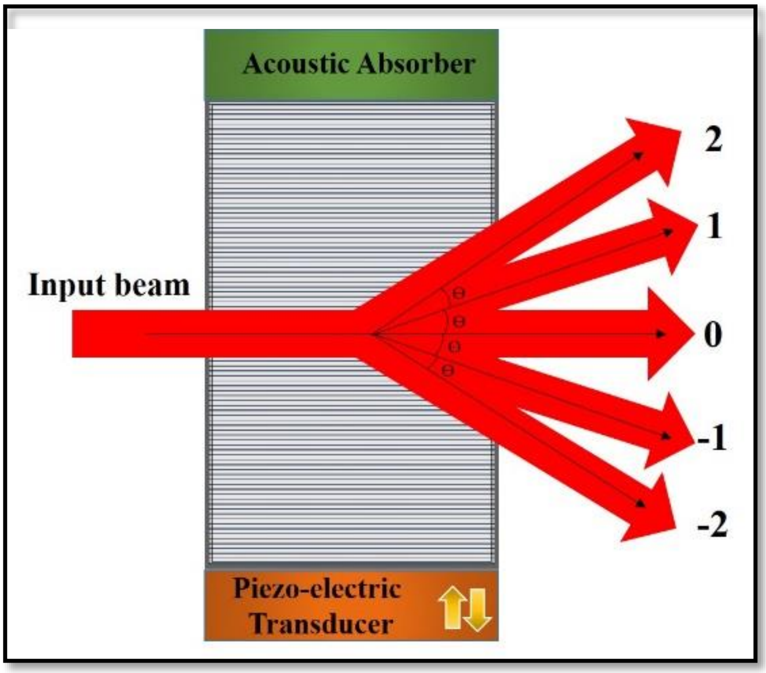

Figure 2.2 A typical acousto-optic modulator

2.2.2 Electro-optic Modulator

An electro-optic modulator basically a crystal that becomes birefringent on applying an electric field (E) across the crystal. This can alter the polarization of the incoming laser beam by a certain voltage applied to it.[5] As shown in figure 2.3, the pulse generation from the electro-optic modulation mainly required polarizing component (LP), quarter-wave plate (QWP) and a Pockels cell. When the voltage V = 0 condition, laser beam through the polarizer is horizontally polarized after passing the QWP at 45^0 the transmitted beam becomes a left circular polarized light after the reflection from the mirror the right circular polarized light again when it passes through QWP it becomes a plane-polarized light, which is orthogonal to the input polarization, so the net electric field is nullified. By switching on the Pockels cell ($V \neq 0$), the polarization after the Pockels cell becomes horizontal, so the lasing takes place. There are two types of electro-optic modulators Pockels cell and Kerr cell. Pockels cell is mainly preferred because it works at a lower voltage. In the case of Q-switching, the low and high Q value is maintained by triggering the voltage of a Pockels or Kerr cell depending on the cavity build-up time. For Nd: YAG laser, the voltage applied is 4 kV for five µs duration, and the lifetime of the population inversion (PI) is up to 200 µs.

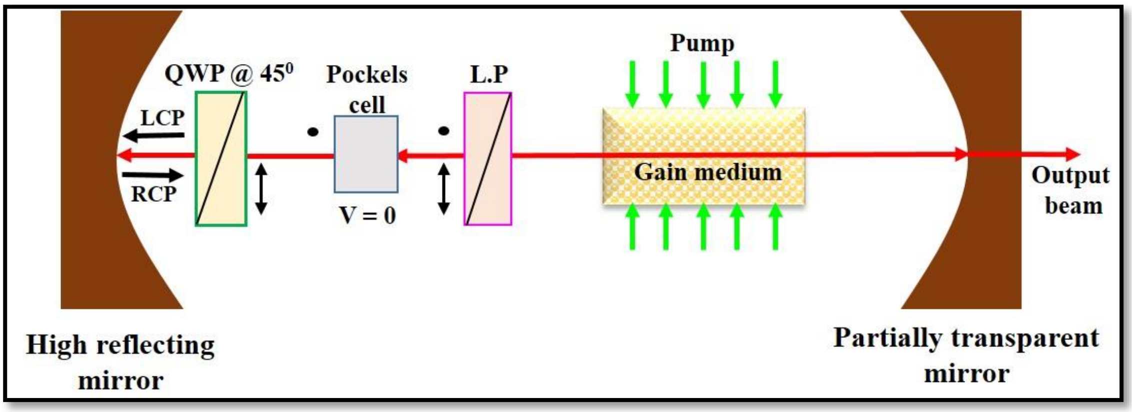

Figure 2.3 Generation of optical pulses using an electro-optic modulator.

2.2.3 Saturable Absorber

It is a passive switching device, which means no external electric field is required for the modulation of the laser cavity. At low input intensities, it acts like absorber and at high input intensities it saturates, therefore allowing the high intense beam.[6-7] As we pump the gain medium, the upper laser level population is continuously increasing, down there is a spontaneous emission increasing while increasing population inversion, which gets absorbed. After a PI decays suddenly, a burst of photons will Travers to the SA, so the losses will be very less and high energy laser beam builds-up inside the cavity, which depends on the excited-state lifetime of the SA. Generally, the SA is placed very close to the one end of the mirror. Typically, SA is preferably organic dyes.

2.3 Q-switching

Q-switching is another process contrary to cavity dumping, wherein cavity dumping the energy is stored in the laser resonator.[3, 6] In Q-switching, the energy is stored in gain medium itself, in the form of population inversion. In this process, the laser resonator quality factor ‘Q’ is defined as,

$$Q = 2\pi \frac{Energy\ stored}{energy\ loss\ per\ optical\ cycle} \tag{2}$$

Furthermore, switching means switching between low and high Q values. By blocking the laser oscillations inside the resonator cavity, using a shutter for a certain period of time depends on the period in which the spontaneous emission is very negligible, thereby no loss in population inversion in the excited state. This condition is called low Q value due to the cavity losses; therefore, no lasing takes place. Once enough population inversion is achieved which depends upon the excited state lifetime of the gain medium and pump source, the shutter opens at a time so that the beam can propagate between two end mirrors followed by a burst of photons in the form of a pulse to be generated; this is the condition for high Q value. The shutters which are used in the cavity mainly are electro-optical shutters such as Pockels cell or Kerr cell and acousto-optic shutters. Q-switched laser pulses are produced by storing energy in the excited state of the gain medium by a steady pump pulse having a duration on the order of the excited state lifetime, as seen from the figure 2.4. There are two ways to achieve Q-switching; these are active and passive Q-switching. Active Q-switching, a mechanical shutter, is placed inside the laser cavity, which is externally controlled by electrical or mechanical processes, wherein passive Q-switch does not involve electrical or mechanical control; instead, we place a saturable absorber (SA), i.e., whose absorption decreases with intensity as described above. Passive shutters are mainly used for single pulse operation.

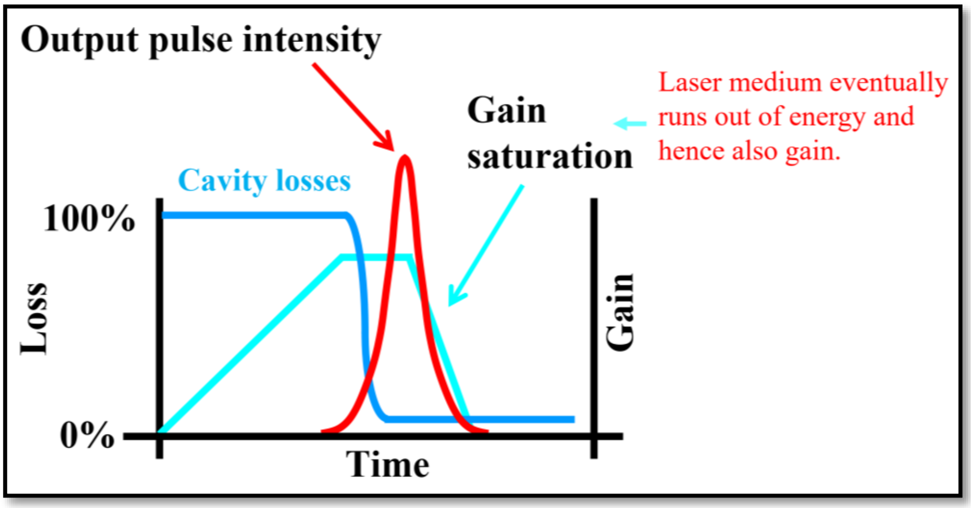

Figure 2.4 Process of Q-switched laser pulse generation.

The requirements to achieve necessary high inversion in Q-switching are (a) the upper laser level lifetime τ_u needs to be longer than the cavity build-up time τ_c so that the excess energy can be pumped to the upper level (b) the pumping duration τ_p must be longer than the upper-level lifetime (c) initial cavity losses must be high enough than the cavity gain to prevent the oscillations during τ_u (d) cavity loses must be reduced instantaneously by introducing high Q-value, so the laser oscillations start to build-up and extract all the energy which is stored in upper laser level. However, Q-switching can generate pulses of up to a few nanoseconds, and therefore to produce very short pulses at five fs, there are other techniques called mode-locking described below.

2.4 Mode-locking

A laser typically consists of a gain medium and optical resonator. The frequency band of laser oscillation is defined by the frequency band over which the gain surpasses the resonator losses. Generally, several modes of the resonator cavity will fall under this oscillation-band, so the output laser radiation comprises a number of closely spaced frequencies. Thus, the output of such laser frequencies as a function of time [ω(t)] will depend upon the (i) frequencies (ii) amplitudes and (iii) relative phases of all these oscillating modes. By fixing these parameters, we can avoid the random fluctuations and nonlinear effects within the laser medium. If all the oscillating frequencies are having a fixed phase relative to each other and equal frequency spacing, the output as a function of time will vary in a controlled manner. Such a laser is called mode-locked (ML), it is possible to get continues and a periodic pulse train of light on the laser exit mirror.[8] Consider n modes with amplitude E_0 and frequency ω_n and phase Φ_n, the total field $E(t)$ can be expressed as

$$E(t) = \sum_n E_n e^{i[\omega_n t + \varphi_n]} + c.c \tag{3}$$

The resultant intensity is given by $I(t) = NE_0^2$, means the N times the intensity of the individual modes. If $\Phi_n = \Phi_0$ and $\omega_n = \omega_{N-1} - n\Delta\omega$ (equal mode spacing) ω_0 optical frequency of laser output, $\Delta\omega = 2\pi(c/2L)$, then

$$E(t) = E_0 e^{i\varphi_0}\left\{\sum_n e^{i[\omega_{n-1} - n\Delta\omega]t}\right\} + c.c \tag{4}$$

The total intensity is defined as

$$I(t) = E_0^2 \frac{sin^2(N\Delta\omega t/2)}{sin^2(\Delta\omega t/2)}, \text{ Where } \frac{\Delta\omega t}{2} = 0, \pi, 2\pi \dots n\pi \tag{5}$$

We have pulses at interval $\Delta t_p = \frac{1}{\Delta\vartheta_{sep}} = \frac{2L}{C}$ this is the time it takes for a pulse to make one round trip in the cavity, as shown in figure 2.5. Therefore, the total intensity is given as $I(t) = N^2 E_0^2$ increased by a factor of N when $\varphi_n = \varphi_0$

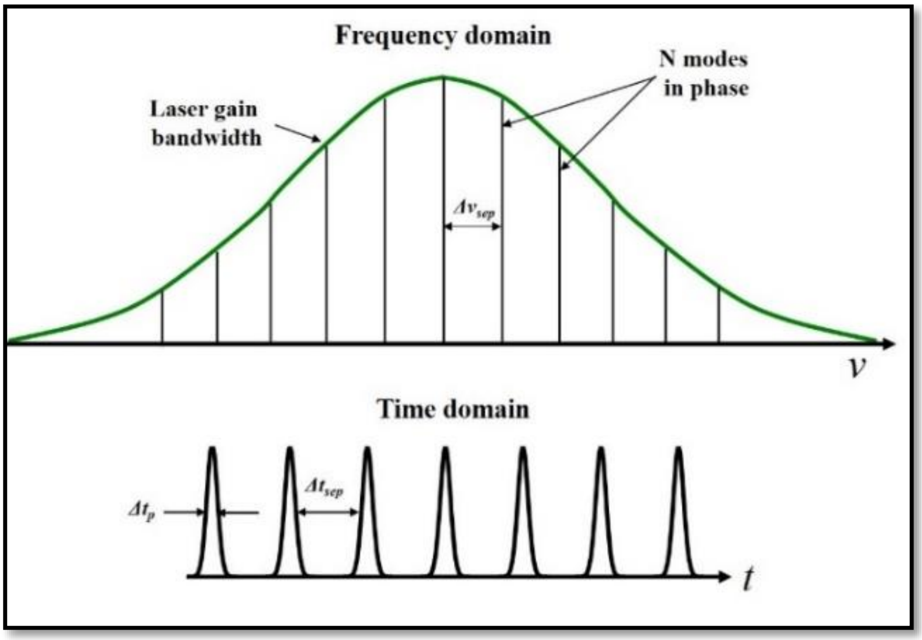

Figure 2.5 Frequency and time domain parameters of mode-locked pulses.

The mode-locking process is categorized into two ways passive and active mode-locking. In the case of active mode-locking, an external driven device is placed inside the laser cavity to modulate intra-cavity frequency or amplitude at cavity repetition rate frequency. The passive ML can be achieved by introducing the saturable absorber (SA) in the cavity. Which allows the high-intensity light due to the saturation of absorption and continuous wave will undergo absorption losses; therefore, the leading edge of the pulse saturates the absorption, and the main pulse will encounter no loss. The SA acts as a shutter that the pulse itself triggers with much faster modulation than electronic shutters.

2.4.1 Kerr-lens Mode Locking

Kerr-lens mode locking (KLM) works on the foundation of variation in nonlinear refractive index, entitled as self-focusing. The principle behind this process is an intensity-dependent change of refractive index of material.[3, 9] For Gaussian-shaped pulses traveling through a medium with more intensity at the centre than the edges, have a large change of refractive index at the central portion then edges due to the following equation $n=n_0+n_2I$ (n_0 is the refractive index, n_2 is the ‘nonlinear’ refractive index), therefore creating a lens that focuses the beam inside the material. The intensity and path length defines how much focusing occurs. In the KLM technique, an aperture is placed at one end of the mirror; in CW condition, the beam encounters high loss as intensity increases due to self-focusing the beam starts to focus, therefore beam size reduces and less loss can be achieved than CW mode. The aperture can be replaced by pumping with a smaller beam diameter pump. The advantage of focusing effect inside the material improves the self-phase modulation (SPM), it broadens the frequency spectrum of the pulse, which compresses the pulse to a shorter duration.

2.4.2 Self-Phase Modulation

Self-phase modulation occurs due to the interaction of time-dependent optical pulse with the intensity-dependent refractive index of a material (self-focusing effect).[10-11] The additional frequency components are added to the pulse as it propagates within the medium (nonlinear). When a sufficient intensity of a laser pulse is propagating inside the material, it starts to focus on the material due to the intensity-dependent refractive index. The pulse which is propagating in such material encounters an SPM, which broadens the frequency spectrum of the input pulse. The physical process is as follows when the pulse is propagating within the material; the leading edge of the laser pulse encounters a large refractive index change, thereby decreasing the velocity of the beam. This decrease in velocity reflects the arrival time the electromagnetic waves of the rising edge at the exit side of the material, therefore a reduction in the frequency spectrum. On the trailing edge of the pulse, the index of refraction decreases, thereby increasing the velocity of the beam, so increase in the frequency of the trailing edge. This process is also known as frequency chirping or pulse chirping.

2.4.3 Group Velocity Dispersion

Group velocity dispersion (GVD) is a pulse shortening or lengthening technique.[11] Consider a wave of frequency ω_0 with finite width $\Delta\omega$. The propagation constant k_0 at frequency ω_0 is varying a with frequency ω around ω_0 can be expressed as

$$k = k_0 + \left(\frac{dk}{d\omega}\right)_{\omega=\omega_0} (\omega - \omega_0) + \cdots \tag{6}$$

Fourier expansion for the electric field

$$E(z,t) = \int E(\omega) e^{-i(kz-\omega t)} d\omega \tag{7}$$

Insert the above equation

$$E(z,t) = e^{-i(kz-\omega t)} \int_{-\Delta\omega/2}^{+\Delta\omega/2} E(\omega) exp\left\{-i\left[\left(\frac{dk}{d\omega}\right)_{\omega_0} z - t\right]\Delta\omega\right\} d\Delta\omega \quad (8)$$

Where $\Delta\omega = \omega - \omega_0$. The velocity of the modulated wave can be obtained by taking $[(dk/d\omega)z-t] = constant$; therefore, $dz/dt = V_G = d\omega/dk$. V_G is called group velocity (velocity at which the information is transferred, because which involves the modulation). A finite value of V_G signifies a shift in velocity with different wavelengths. A medium with such property is known as a dispersive medium. For a nondispersive medium $d\omega/dk = 0$. The group velocity dispersion can be expressed as,

$$GVD = \frac{d^2k}{d\omega^2} = \frac{d}{d\omega}\left(\frac{1}{V_G}\right) = \frac{-1}{V_G^2}\frac{dV_G}{d\omega} \quad (9)$$

A short optical pulse passing through a medium with significant GVD, the pulse can be either shortened or lengthened due to the frequency-dependent dispersion within the medium. For a positive GVD (V_G red > V_G blue) means, the group velocity decreases with increasing frequency components of the pulse; as a result, the pulse stretches and for negative GVD (V_G blue > V_G red) the pulse tend to shorten.[8]

2.4.4 Chirped Pulse Amplification (CPA):

Chirped pulse amplification (CPA) of ultrafast light pulses from solid-state lasers has allowed the generation of light pulses up to terawatt peak powers or more.[3] CPA technology is commonly used in all-solid-state lasers for high peak powers. The CPA process is shown in figure 2.6, the low energy input pulses from the seed laser (100 fs) send it to a dispersive pulse stretcher leading to a highly chirped stretched pulse, i.e., temporally broadened up to larger than 200 ps to avoid the optical damage and self-focusing effects without affecting the bandwidth. The pulse from the stretcher is amplified either by single-stage or multi-stage amplifiers. The stretched amplified pulse is further sent to an opposite (i.e., stretcher) dispersive medium; as a result, the amplified pulse is compressed to bandwidth limit. The chirp of the amplified pulse is controlled by introducing the group-delay dispersion of different signs before and compression. The conventional CPA lasers use the diffraction gratings or prism pairs for pulse stretching/compression and their angular dispersion introduces the wavelength-dependent delay.[3, 8] In our laser (LIBRA) the seed laser (100 fs, 80 MHz) pulses with nJ energy is stretched up to 200 ps thereby reducing the peak power up to 10^4 which is further amplified in the regenerative amplifier followed by compression. The Pockels cell (PC) switches the seed pulses to the amplifier, which is synchronized to the seed laser. Therefore, seed pulses with nJ energy are amplified to ≈ mJ.

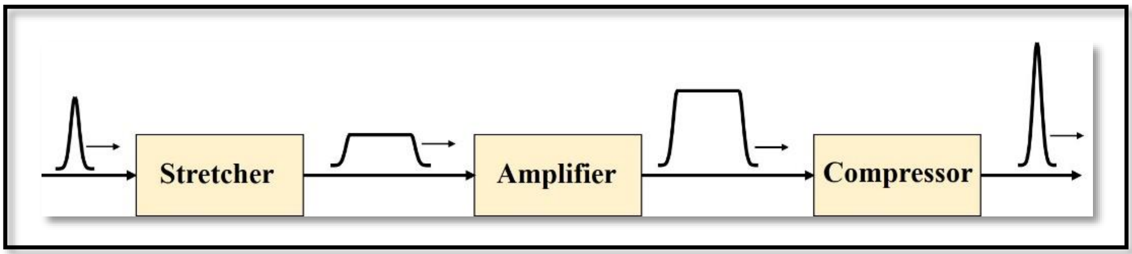

Figure 2.6 Schematic of CPA process

2.4.5 Regenerative Amplification

In the regenerative amplification process (RGA), the pulse to be amplified is trapped within the cavity by using a polarization gating method.[12] As shown in figure 2.7, during pumping of the gain medium any light emitted into the resonator by spontaneous emission (SE) is suppressed by polarizing the SE passing through a thin film polarizer rotated by 90^0 in double passing through the wave plate and Pockels cell (when V=0, Hence no polarization change), thereby amplified SE will be reflected out of the cavity.[13] At the beginning of the amplification, the pulse to be amplified is injected into the cavity through a polarizer at certain polarization, so that it reflects into the cavity. After double pass through the wave plate, the polarization is rotated and the beam is now transmitted through the polarizer towards the gain medium. Before the pulse returns back the polarizer, a voltage is applied to the PC such that it acts like a wave plate so that no net change in polarization takes place upon reflection from the cavity end mirrors. Sot that the pulse is trapped within the cavity, which allows repeated passes through the gain medium. Finally, during the pulse ejection from the cavity, the PC voltage is deactivated; therefore, polarization is rotated by 90^0 at polarizer after double passing through the wave plate so that the pulse can reflected out of the cavity. Further PC timing is adjusted depending on the number of passes through the gain medium (i.e., total amplification factor). RGA is more advantageous than a multi-pass amplifier; it allows many passes to the gain medium and good overlap of pump and signal beams. However, there is a disadvantage of the RGA scheme for femtosecond applications, i.e., larger material path lengths, which leads to large dispersion effects. This makes it more difficult to achieve complete compression of the amplified pulse in RGA systems.

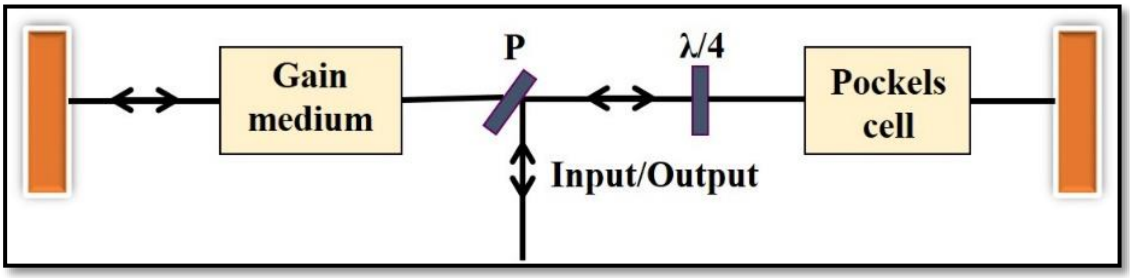

Figure 2.7 Schematic of the regenerative amplifier

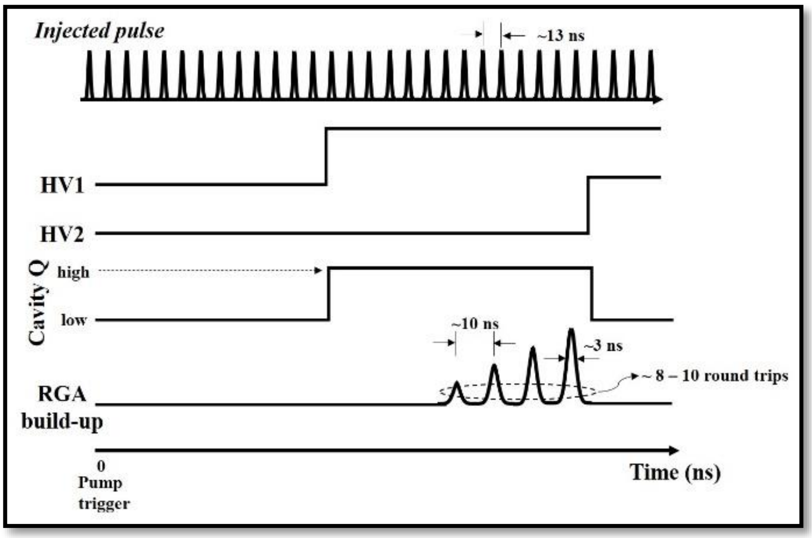

Figure 2.8 Timing of Pockels cell (PC) voltage and their effect in the amplification. HV1 changes the cavity Q to high, where one pulse is trapped and amplified. HV2 changes the cavity Q to low, and the amplified pulse is cavity dumped.

The LIBRA amplifier system works on the same principle, the repetition rate of the (Vittese) laser is 80 MHz. This is synchronously reduced to 1 kHz and the timing for amplification is depicted in figure 2.8. The seed pulses initially have vertical polarization, which is fed into the RGA cavity. The crystal (at Brewster angle) and polarizer can transmit horizontal polarization but blocks the vertical polarization; however, after a double pass from the wave-plate, the polarization is rotated by 90^0, i.e., from S to P. After the pulse leaves the wave plate voltage is applied to PC1 (HV1) double passing through PC1, and the wave plate results in no change in polarization. The pulse remains p-polarized, which passes through an active medium (Ti: Sapphire) for multiple times (~15) during this time it gets amplified, which cavity Q high. All other seed pulses with S-polarization is reflected out of the cavity. After a certain round, trips voltage is applied to the PC2 (HV2), which makes the amplified pulse shift back to S-polarization, which further reflected from the active medium and which dropped the cavity Q low. Typically, the gap between the seed pulses is ~ 13 ns.

2.4.6 Libra, M/s Coherent Ultrafast laser system:

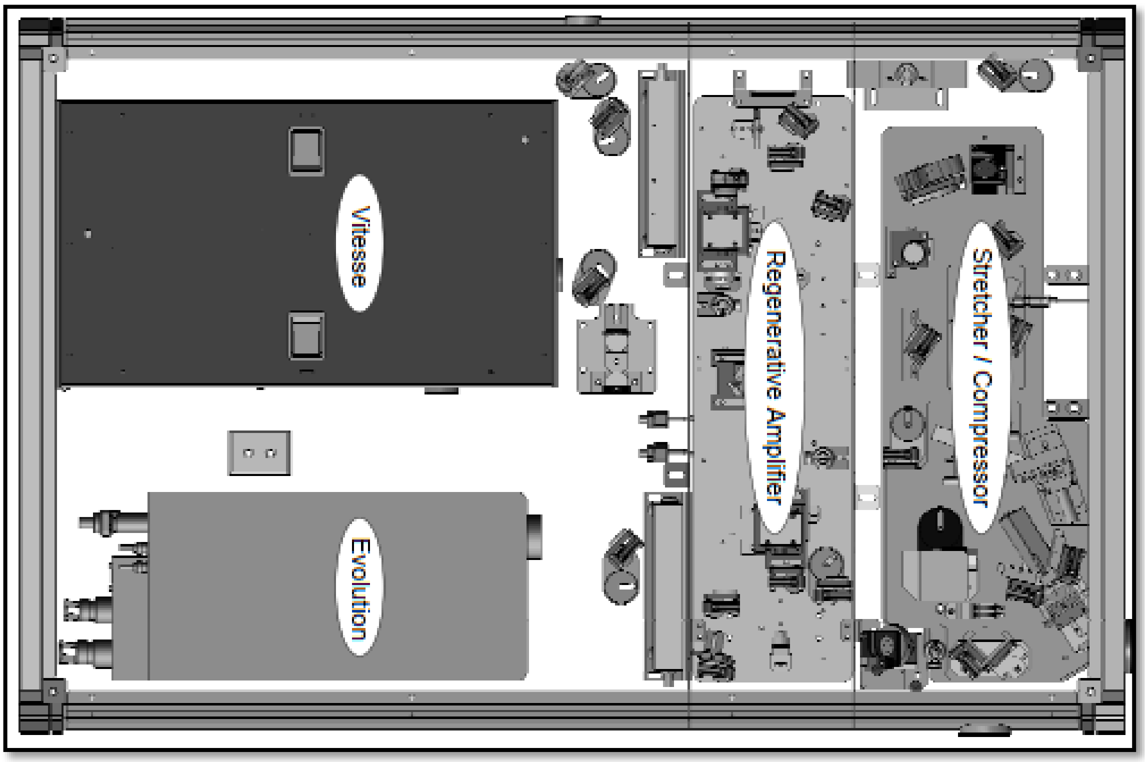

Figure 2.9 Top view of the Femtosecond amplifier system (LIBRA) shows the essential modules (i) Vitesse (seed) (ii) Evolution (Pump) (iii) RGA cavity (iv) Stretcher/compressor region. *(Image adopted from Coherent LIBRA manual).*

The Libra laser system (M/s Coherent, 50 fs pulse duration, 4 mJ of maximum pulse energy, operating at 1 kHz) is scientific and industrial grade amplified Ti: Sapphire laser system operating at a central wavelength of 797 nm. The output beam diameter is ~9 mm ($1/e^2$). The optical layout of the Libra assembly is shown in figure 2.9. It mainly consists of four modules (i) A seed laser called Vitesse (Oscillator) (ii) evolution as pump laser (iii) RGA and (iv) compressor followed by Stretcher part integrated and situated into a single box. The un-chirped output pulse spectrum of Libra amplifier shown in Figure 2.10 with central wavelength ~ 797 nm, pulse duration of ~36.8 fs, and bandwidth of 18.4 nm was measured using spectra suite provided by Ocean optics. The spectra were measured just after the compressor of the Libra system.

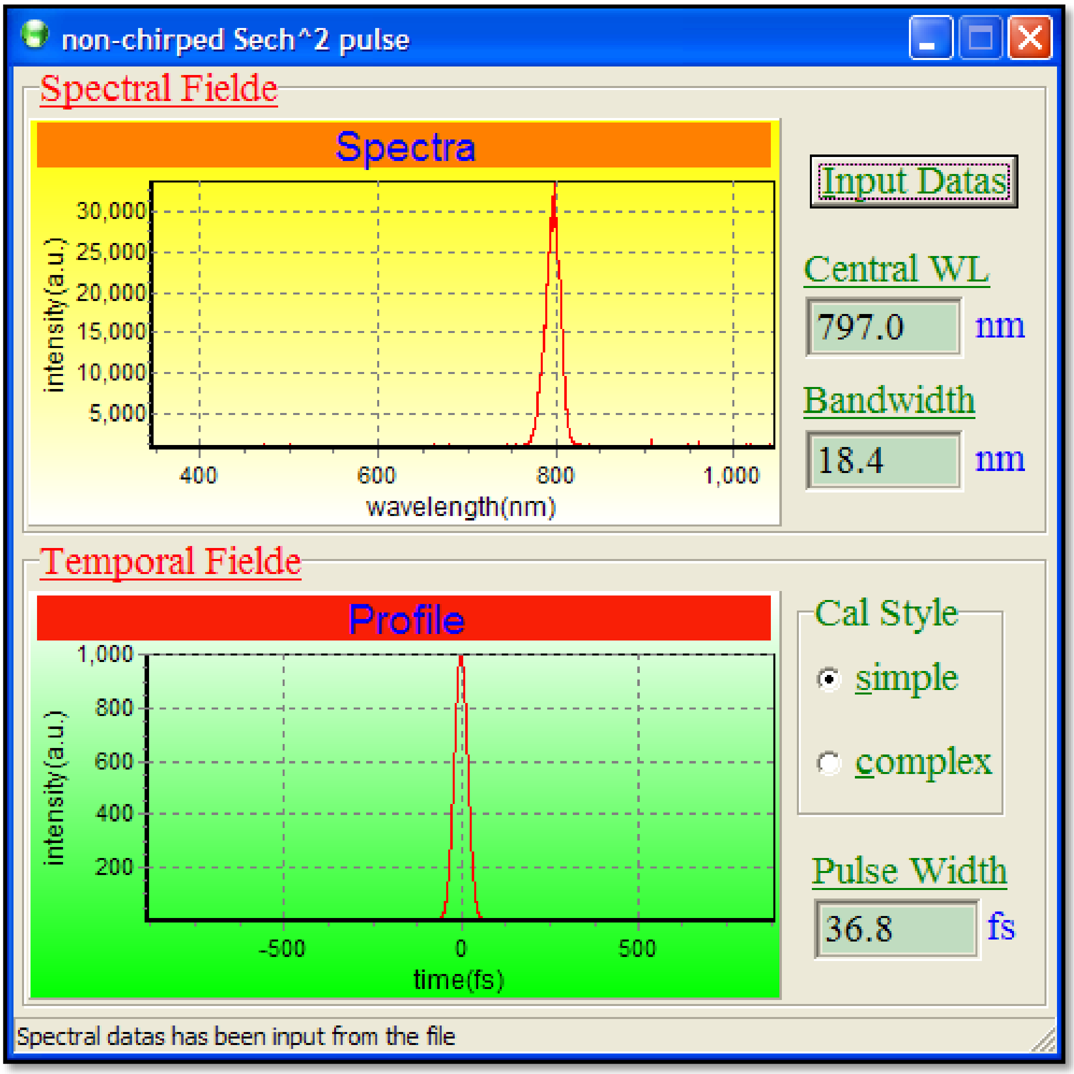

Central WL 797.0 nm

Bandwidth 18.4 nm

Cal Style

● simple

○ complex

Pulse Width 36.8 fs

Spectral datas has been input from the file

Figure 2.10 Spectral and temporal filed of LIBRA output. It was measured by the Ocean Optics Spectra suite software.

2.4.7 Vitesse (Oscillator)

The Vitesse laser is classified as class IV laser based on European community standards EN-60825-1. It is a Verdi-pumped mode-locked laser that produces sub-100 fs pulses at an 80 MHz repetition rate with an average power of >250 mW at 800 nm, which acts as seed laser (called Oscillator) in the Libra system. It gives a bandwidth of ~ 30 – 100 nm at 800 nm central wavelength. Vitesse laser consists of (1) Verdi laser (2) Verdi Pumped Ultra-Fast (VPUF) laser (3) power track mirror and, as shown in figure 2.11. All the individual components are sealed separately to reduce environmental contamination.

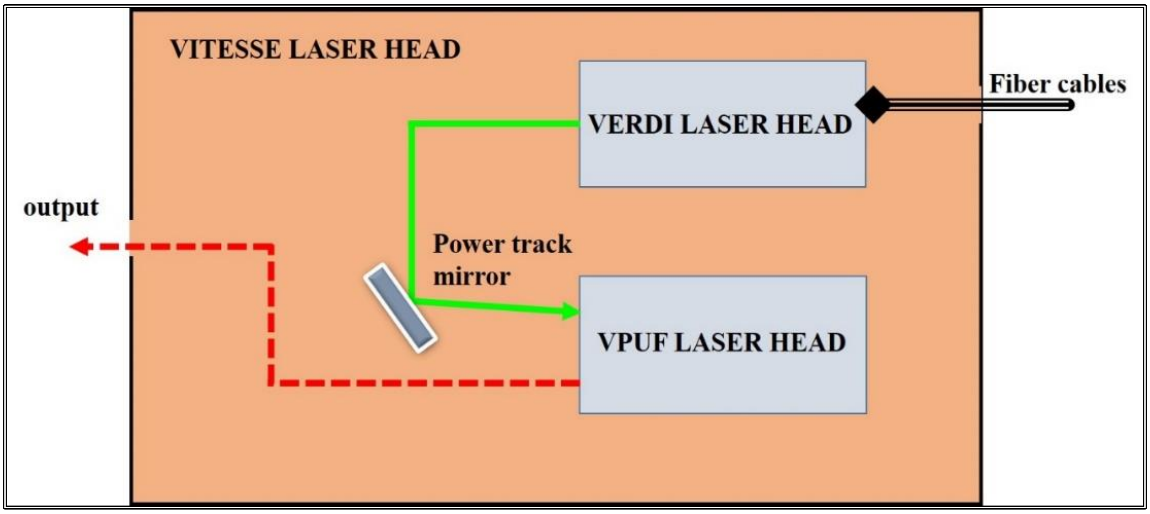

Figure 2.11 Layout of the Vitesse laser.

Verdi laser acts as a pump laser for Vitesse laser. It consists of Nd: YVO_4 (Vanadate) gain medium, which is pumped by two diodes (5 Watt) lasers providing a continuous laser at 1064 nm with 2 W average power, as shown in figure 2.12 (a). The diode lasers are placed in the Vitesse laser head, by utilising optical fiber cables, the diode laser (808 nm wavelength) output is connected to the Verdi. The Verdi laser major optical components are Lithium Triborate, LiB_3O_5 (called LBO) for frequency doubling crystal (from 1064 to 532 nm), an etalon for frequency filter, stigmatic compensator, optical diode, two end mirrors, and two pump mirrors. A piezo-driven mirror is used to align the pump laser into the VPUF laser head's cavity.

VPUF laser head consists of a gain medium (Ti: Sapphire crystal) with a negative dispersion mirrors (NDM). The gain medium (Ti: Sapphire crystal) inside the VPUF laser head is pumped by the Verdi laser output at 532 nm. Negative dispersion mirrors (NDMs) providing the negative dispersion and multiple reflections from NDMs compensate the ND, this is needed to produce <100 fs pulses, as shown in figure 2.12 (b). A passive mode-locking technique, i.e., Kerr-lens Mode locking (KLM), was utilized to get ML in Vitesse. Thus, the low noise ultrashort pulses < 100 fs with a bandwidth of 35 nm, an average power of ~ 300 mW at 80 MHz repetition rate are produced. Figure 2.13 shows the output characteristics of the Vitesse laser-measured using Ocean optics spectra suite software.

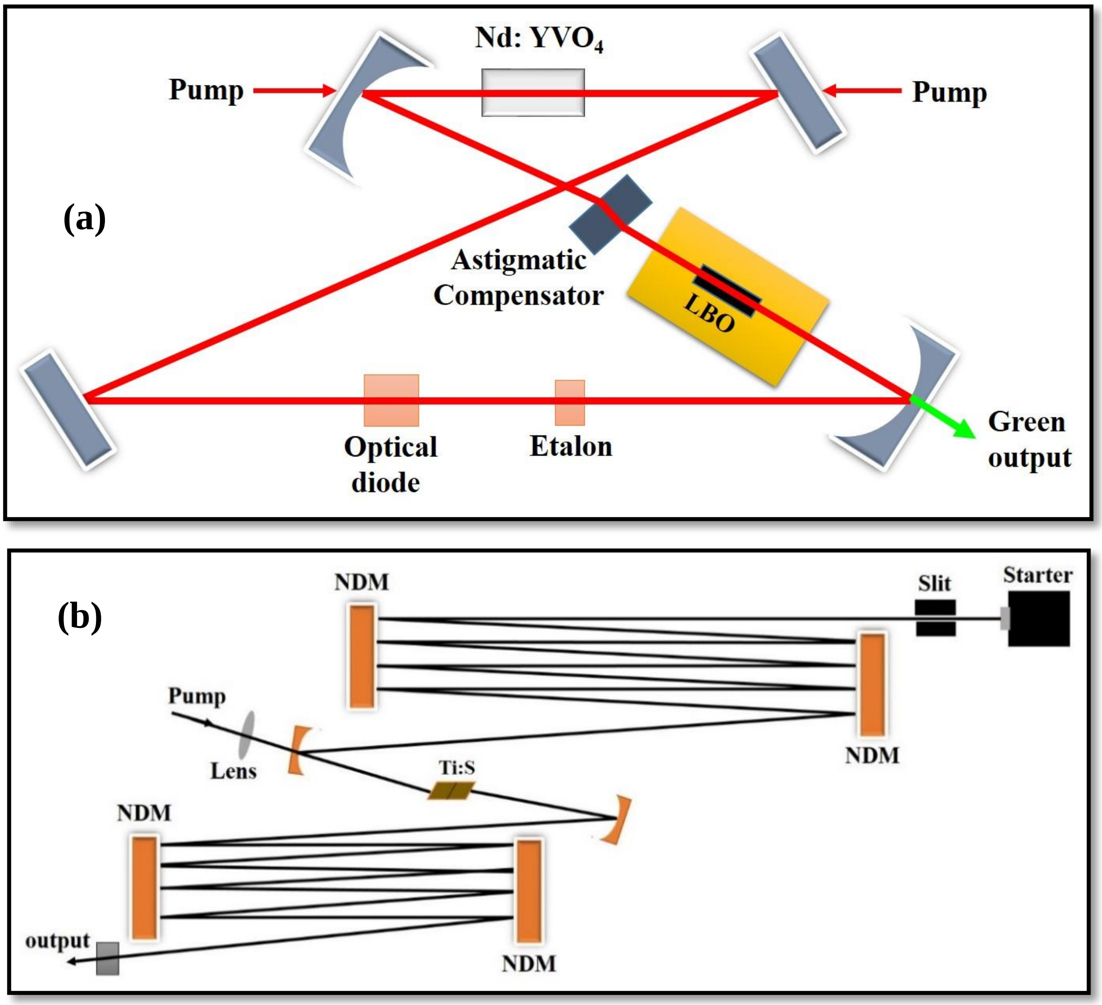

Figure 2.12 Internal schematic layouts of (a) Vitesse seed laser and (b) Verdi laser layouts.

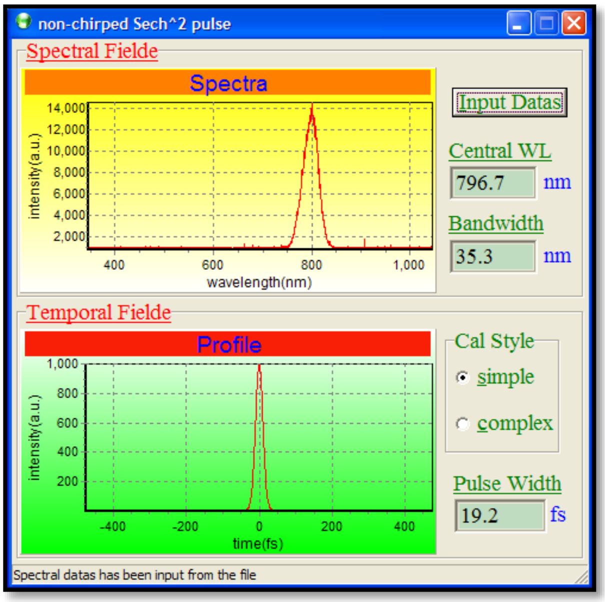

Central WL 796.7 nm

Bandwidth 35.3 nm

Cal Style

● simple

○ complex

Pulse Width 19.2 fs

Spectral datas has been input from the file

Figure 2.13 Spectral and temporal profile of Vitesse output. This was measured by the Ocean optics Spectra suite software.

2.4.8 Evolution-HE (Pump laser)

The Evolution-HE is a diode (Aluminium Gallium Arsenide) pumped, Q-switched Nd: YLiF4, yttrium lithium fluoride (Nd: YLF) laser produces 45 W of average power and >45 mJ pulse energy at 1 kHz. It operates at 527 nm wavelength second harmonic from 1053 nm, which is ideal for pumping ultrafast high-power Ti: Sapphire amplifiers. The Evolution-HE offers high efficiency and excellent beam quality. Which comprises mainly four elements (1) Optical laser bench assembly contains electrical, optomechanical, and cooling assemblies (2) power supply to drive the laser diodes and to maintain the LBO crystal temperature, (3) computer control and (4) closed-loop chiller for a heat sink. The specifications of the LIBRA and Vitesse oscillator is given in table (2.1).

Table 2.1 Specifications of Vitesse and LIBRA systems

S. No.	Parameters	Vitesse oscillator	Libra fs amplifier
1	Average power	300 mW @ 2 W Verdi	4 W
2	Pulse duration	< 100 fs	~35 fs
3	Band width	~ 35 nm	~ 20 nm
4	Max output energy	~ 3-5 nJ	~4 mJ
5	Repetition rate	~80 MHz	1 kHz
6	Beam diameter	~ 1.25 mm	~9 mm (1/e^2)
7	Polarization	Horizontal	Horizontal

2.4.9 Optical Parametric amplification (OPA)

OPA is a well-known nonlinear optical (NLO) process takes place in second-order nonlinear materials consisting of energy transfer from high-frequency pump beam to low-frequency beam known as a signal, during the energy transfer another beam is generated known as idler.[14-15] For higher pump frequencies, the energy conversion rule is $\omega_P = \omega_S + \omega_I$. Optical parametric generation (OPG) often proceeds OPA. In OPG, the input is one light beam at frequency ω_P and output is two beams with frequency ω_S and ω_I. The wavelength of the output beams is determined by phase-matching. The output beams after OPG are generally relatively weak and spread-out in direction. This issue is solved by using OPA as a second step; in OPA, the input beams are two with frequency ω_P and ω_S, as shown in figure 2.14. Therefore, the OPA amplifies the signal beam ω_S by making pump beam ω_P weak and also generates a new beam called idler at frequency ω_I.

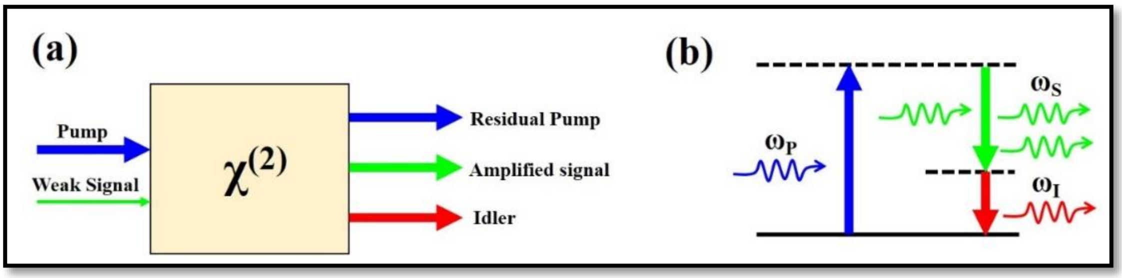

Figure 2.14 The flow of pump energy to the signal beam in OPA (b) stimulated emission of signal photons from the virtual level created by the pump beam.

2.4.9.1 TOPAS-C

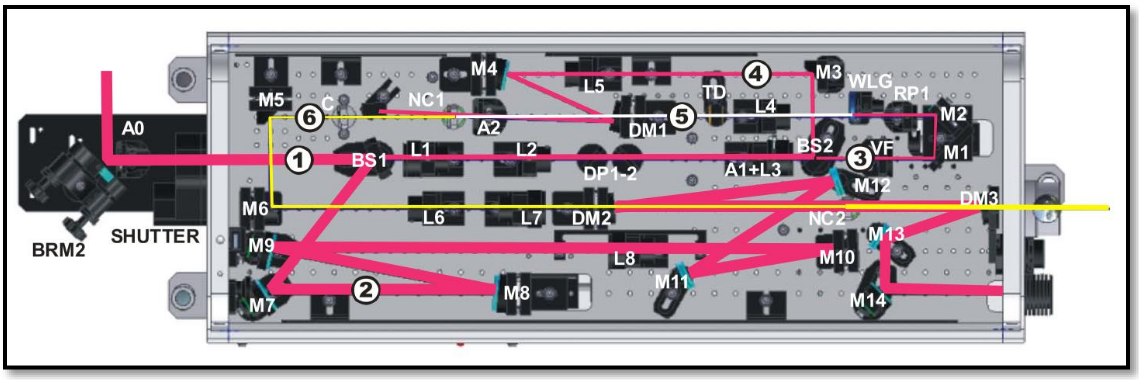

Figure 2.15 Optical layout of the TOPAS-C. *(Image adopted from Light Conversion Manual)*

TOPAS (Traveling wave optical parametric amplifier) is a two-stage amplifier that is pumped by the output of LIBRA at 800 nm. This provides a wavelength range of 1100 nm-1600 nm with additional frequency mixers; this range can be extended to 260 nm-2600 nm. Its basic arrangement consists of several subunits: pump beam guiding and white light continuum generation (WLC), pre-amplifier (PA1) stage, signal beam collimator, and expander (SE), and a power amplifier (PA2). These components are arranged in a single compact unit. All the components in this device, such as mirrors, translation stages, rotation of the crystals, and tuning of output wavelength, are precisely controlled by a software called WinTopas provided by Ms/ Ultrafast Systems, USA. The complete layout of the TOPAS-C is presented in figure 2.15.

A small amount of the input pump beam (1.3 µJ, from BS1) at 800 nm wavelength is used to generate WLC using a sapphire plate. The other part of the pump beam 800 nm (30-50 µJ) and WLC are collimated non-collinearly onto the pre-amplifier crystal (NC1), where the parametric amplification takes place. The advantage of non-collinear geometry is it's easy to separate amplified signals from the remaining idler and pump beams. After the pre-amplification of the signal (PA1), the beam is collimated by a telescopic lens and transformed to the power amplification (PA2) stage. At this stage, the remaining high energy pump beam is further collimated to the power amplifier stage. Both the amplified signal and a high-power pump beam are overlapped collinearly into a second nonlinear crystal (NC2). Thus, the output from the TOPAS-C is well-collimated collinear idler and signal beams is achieved. The optional frequency mixer can be used at TOPAS output to extend the tuning range from UV to NIR. The wavelength tuning in the PA1 stage is attained by varying the delay between the WLC and the first pump beam and adjusting the angle of crystal for optimum phase-matching. Also, the wavelength tuning at PA2 stage is archived by primary optimizing the wavelength at the PA1 stage and then adjusting the second crystal angle and delay between amplified signal and second pump beam. The wavelength can be changed by computer dedicated software called WinTOPAS.

2.5 Characterization of Ultrashort Pulses

Measuring ultrafast pulses of duration <20 ps is difficult due to the limitation on the response time of electronic devices. Several approaches were discovered, mainly Intensity autocorrelation, frequency-resolved optical gating (FROG), etc. Among these, intensity autocorrelation technique is widely to measure the pulse width of short pulses. However, the phase information cannot be measured from this method. It is the pulse used to measure itself in the time domain.

2.5.1 Intensity Autocorrelation

The correlation of the pulse in the $\chi^{(2)}$ medium is obtained in Michelson interferometer geometry.[3, 8] The input pulse at 800 nm is split into two equal parts, as shown in figure 2.16. Therefore, the two pulses with an intensity $I(t)$ and $I(t+\tau)$ are non-collinearly overlapped into a second-order nonlinear crystal (β-barium borate, BBO) with proper delay line by using linear translation stage. Under the non-collinear phase-matching condition, a signal at the second harmonic frequency of the input pulse is generated. The autocorrelation signal, i.e., SHG, depends on the extent of overlapping of two input pulses in time. The temporal evolution of the SHG signal with respect to the delay is shown in figure 2.17. The intensity of the SH signal is related to the overlap of the two incoming pulses.

The electric field of the second harmonic signal is defined as,

$$E_{Sig}^{SHG}(t,\tau) = E(t)E(t-\tau) \qquad (10)$$

where 'τ' is the delay between the two incoming pulses. The resultant intensity of the SHG signal is proportional to the product of the two pulse intensities.

$$I_{Sig}^{SHG}(t,\tau) = I(t)I(t-\tau) \qquad (11)$$

The expression for the intensity autocorrelation is given by

$$A^{(2)}(\tau) = \int_{-\infty}^{\infty} I(t)I(t-\tau)\, dt \qquad (12)$$

The trace of autocorrelation provides a measure of pulse width and a rough estimation of the spectral width, but it says nothing about the actual pulse spectrum. Therefore, a pulse shape and phase must be assumed prior to the autocorrelation. The resulting pulse width will depend on the shape chosen. We have performed an intensity autocorrelation experiment of the LIBRA amplifier output and the data is shown in figure 2.17. The output from the amplifier is divided into two equal parts with a beam splitter (BS). A part of the beam is kept on a linear translational stage, and both beams are guided and focused non-collinearly into a BBO (type 1 critical phase matching, 29.1^0 cut for SHG) crystal. The SHG signal is collected with a photodiode (PD, SM1PD2A-Thorlabs) and fed to a lock-in amplifier (Stanford instruments-7602). The linear stage is controlled by the motion controller (Newport ESP300). The SHG signal intensity was measured at each probe delay, and data acquisition is achieved by using a LabVIEW program. The autocorrelation signal, as seen in figure 2.17, was fitted by using a Gaussian equation, which yielded the full-width half maxima to be 174 fs.

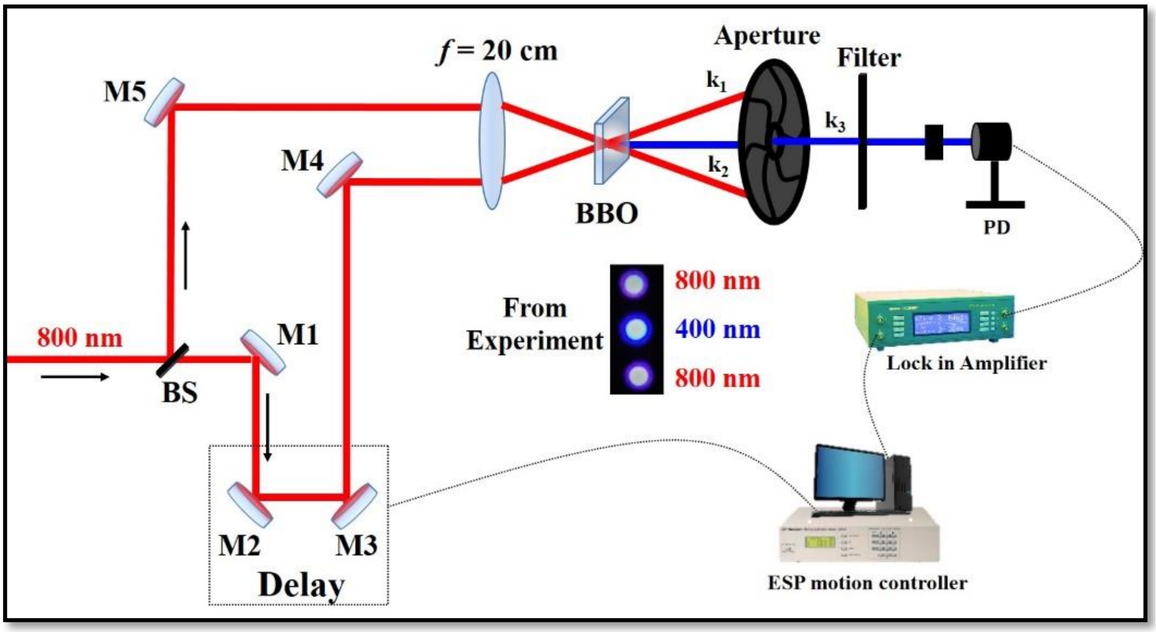

Figure 2.16 Experimental setup of the intensity autocorrelation and inset shows the SHG signal. (M- mirror, BS-beam splitter, PD-photodiode, BBO-β barium borate crystal)

Since the ultrafast pulse holds large bandwidth, dispersion effects need to be countered due to the phase change while propagation in a dispersive medium. Experiments were performed at 800 nm wavelength with a 2 mm thick BBO crystal. As a pulse propagating through a medium with refractive index n(ω) and length L the corresponding modified phase with the central frequency ω_0 and propagation vector k is defined as,

$$\varphi(\omega) = -k(\omega)L \tag{13}$$

The k-vector is expanded in Tylor series around ω_0

$$k(\omega) = k(\omega_0) + k_1(\omega_0)[\omega - \omega_0] + \frac{1}{2}k_2(\omega_0)[\omega - \omega_0]^2 + \frac{1}{6}k_3(\omega_0)[\omega - \omega_0]^3 + \cdots \tag{14}$$

Here $k_n = \partial^n/\partial\omega^n$ and all the derivatives are estimated at $\omega = \omega_0$. The initial term corresponding to the phase velocity. The second term is corresponding to the (quadratic spectral phase variation) group velocity V_g, i.e. speed at which the envelope travels inside medium and third term corresponds to the group velocity dispersion (GVD), i.e., the first derivative of group velocity.[8] The cubic spectral phase variation leads to the time variation to different frequency components, called frequency chirping. Thus, either the blue component or red component of the pulse travels faster or slower depending on the sign of GVD, which makes the pulse broadening. The Gaussian pulse remains Gaussian as it propagates within a medium, just the pulse duration increases with length L. The extent of broadening can be obtained from,

$$\tau_{out} = \tau_{in}\sqrt{1 + \left(4ln2\frac{GVD}{\tau_{in}^2}\right)^2} \qquad (15)$$

Where τ_{in} is incoming un-chirped pulse duration and GVD can be obtained from Sellmeier's equation.[16-17]

$$\Delta\tau = \frac{\Delta t_{ac}FWHM}{1.414} \qquad (16)$$

$$\Delta\tau = 123\ fs$$

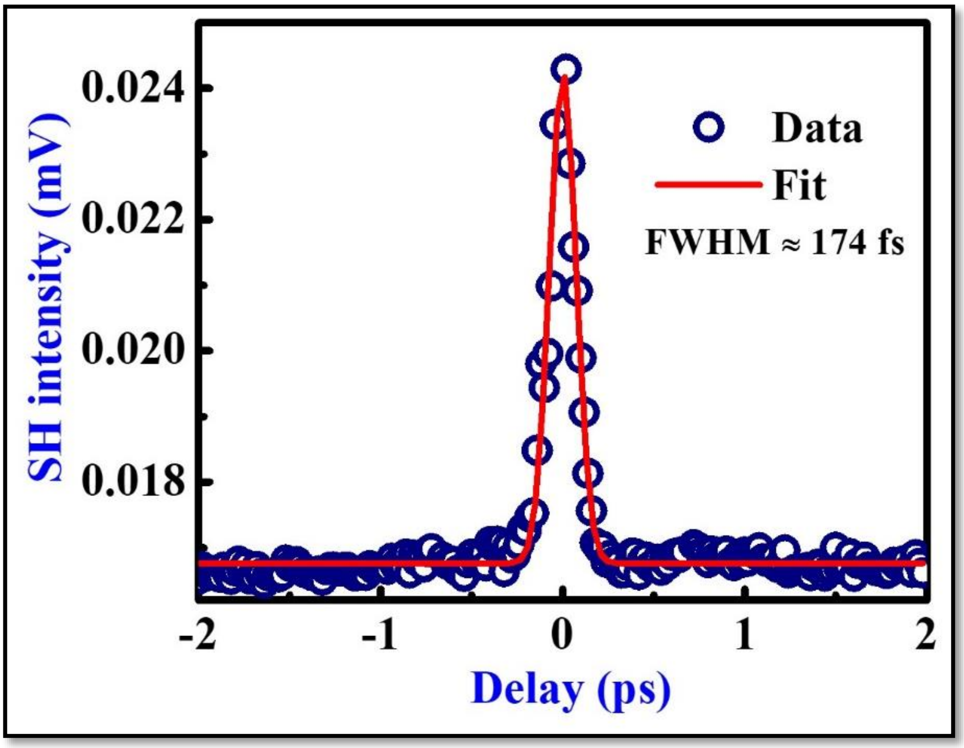

Figure 2.17 Autocorrelation signal of the LIBRA amplifier system.

2.5.2 Single shot autocorrelator (SSA)

Single-shot autocorrelator (SSA, Coherent M/S) data provides a complete description of ultrashort pulses. Inside SSA, the input 800 nm wavelength (LIBRA amplifier output) is divide into two equal parts, and overlapped non-collinearly onto a nonlinear crystal KD*P (Potassium dihydrogen phosphate). The relative wave front tilt yields a spatial time delay in the second harmonic signal, providing autocorrelation of the temporal intensity profile of the ultrafast pulse. Figure 2.18 shows the optical layout of SSA wherein the autocorrelation signal is usually measured with a CCD array, which is connected to the oscilloscope (Tektronix 1320B). A variable delay line is provided to ensure the spatial overlap of the input pulses.

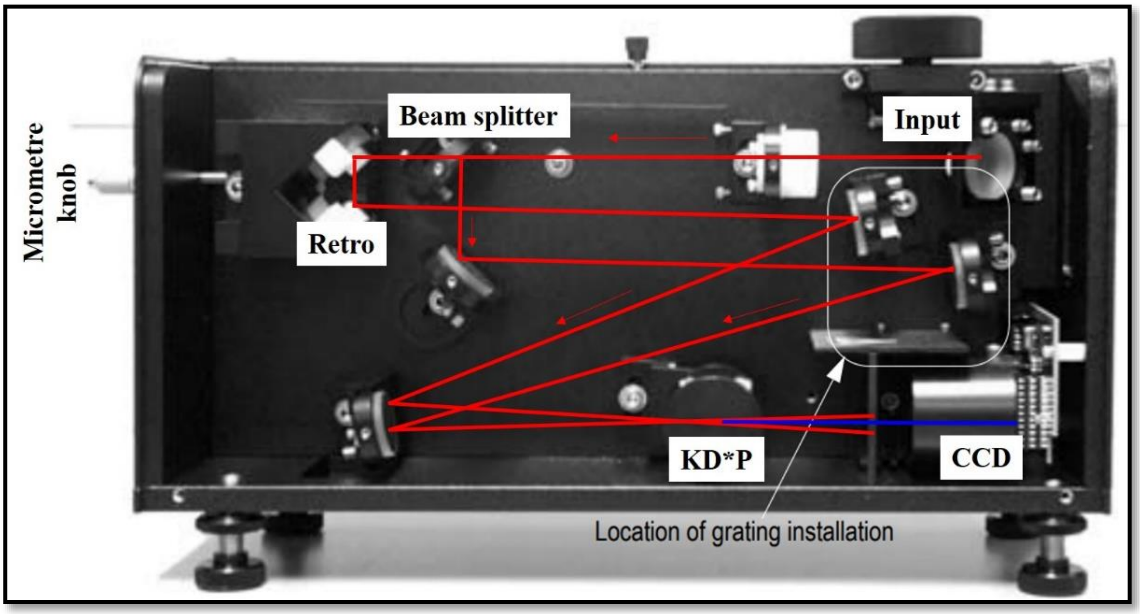

Figure 2.18 Optical layout of the single-shot autocorrelator. *(Image adopted from Coherent SSA manual).*

As shown in figure 2.19 the cross-beam size D_z of the second harmonic beam depends on input pulse width t as,

$$D_z = \frac{tu}{\sin\frac{\varphi}{2}} \tag{17}$$

Where φ is the angle of combined beams, and u is the velocity of the light in crystal. If a time delay Δt is exists between the two pulses, then the centre of second harmonic cross-distribution is shifted by an amount Z_0.

$$Z_0 = \frac{u\Delta t}{2\sin\frac{\varphi}{2}} \tag{18}$$

The pulse duration can be obtained from the above two equations.

$$t = \frac{D_z \Delta t}{2Z_0} \tag{19}$$

Hence, by measuring the D_z, Z_0, and Δt, it is possible to obtain input beam pulse duration. The Δt can be achieved by introducing an optical delay, and Z_0 is obtained from two-micrometer knob positions (L_1 and L_2), i.e., at two centres of SH energy distribution (Z_{01} and Z_{02}). For a Gaussian shape pulse, the pulse duration is obtained from bellow equation.[18-19]

$$t = \frac{2D_z(L_1 - L_2)}{1.414(Z_{01} - Z_{02})c} \tag{20}$$

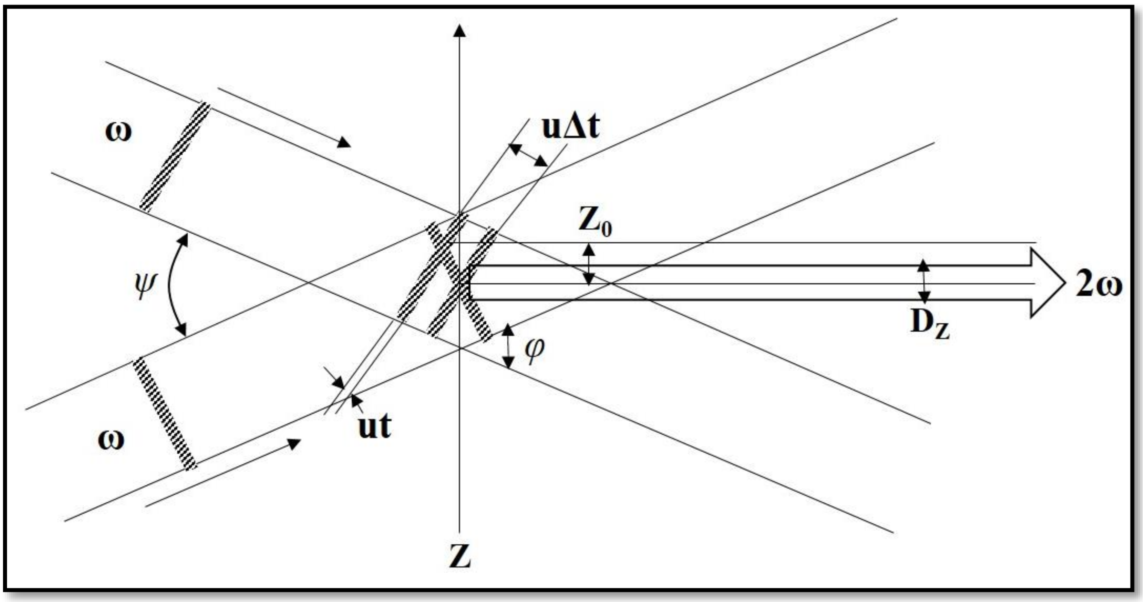

Figure 2.19 Schematic of SSA process, the 2nd order autocorrelation of fs optical pulses from spatial intensity profile of SH beam generated in KDP.

Figure 2.20 shows the SSA signal obtained at maximum of overlap between two pulses in KDP recoded in oscilloscope. The detailed calculation of pulse duration is discussed below:

The FWHM of the of SSA signal is ≈ 2.47×10^{-4} ≈ 0.247 *ms*

Delay stage movement = 0.04 *mm*

Optical path length = 0.08 *mm*

Change in optical delay = 0.08 *mm* / 3×10^{8} *m/s* = 266 *fs*

Amount of peak shift in oscilloscope ≈ 550 *µs*

Calibration = 266 *fs* × 550 *µs* = 0.483 *fs/µs*

= 0.483 *fs/µs* × 0.247 *ms* = 119 fs

Assuming the pulse shape to be Gaussian, the pulse duration is estimated to be 119 *fs*/√2 = 84 *fs*. The difference in the measured pulse width (84 fs) and the input pulses width (50 fs) mainly arises from the temporal broadening of the two input pulses because of the propagation of input laser pulse in dispersive media such as KDP crystal and ND filters.

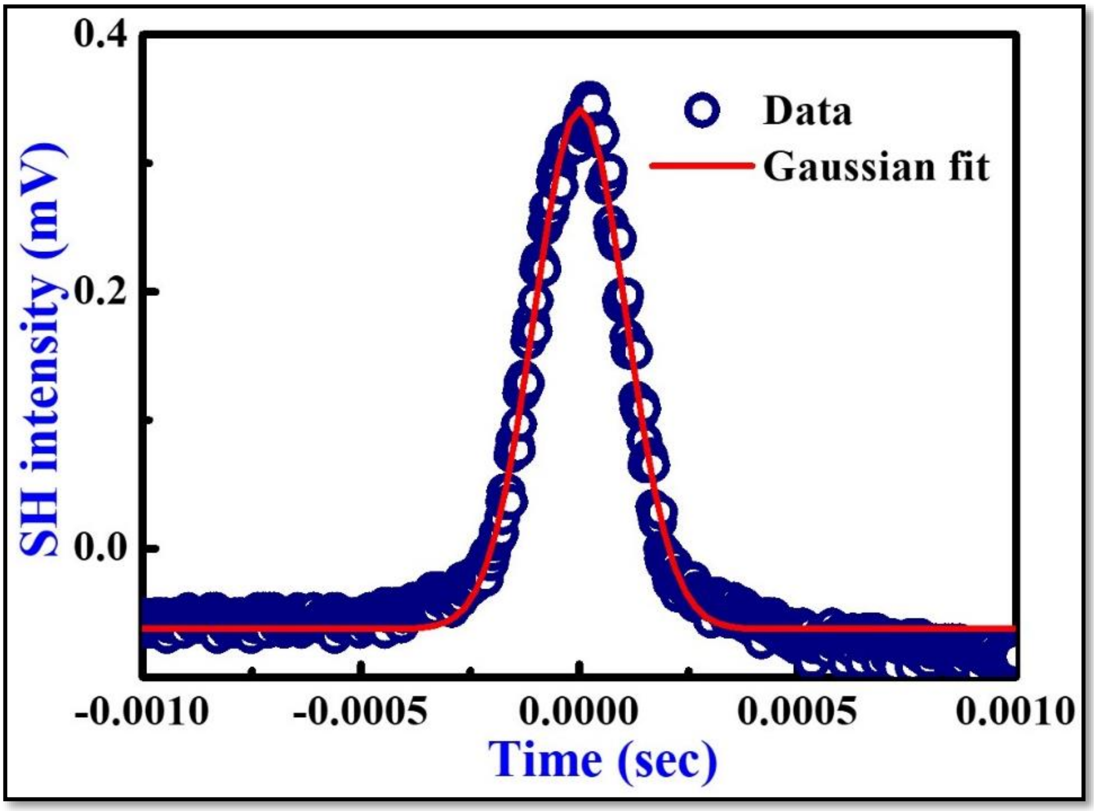

Figure 2.20 SSA signal from the oscilloscope.

2.6 Experimental details

2.6.1 Introduction to Z-scan technique

The Z-scan technique reveals the nonlinear change in absorption and refractive index, in solids and liquids. In the nonlinear optics community, Z-scan has increased most acceptance as a standard technique for measuring nonlinear absorption (NLA) and refractive index (NLR) separately, due to the simplicity of the technique and data interpretation.[20-21] However, the underlying physical process which causes the nonlinear change in absorption and refractive index by the Z-scan technique is not possible in general. Z-scan Measurements with various pulse durations, repetition rate, and focusing geometries, etc. together with other experiments (transient absorption, Four-wave mixing) are needed to determine the origin of nonlinearity or nonlinear optical mechanism. Z-scan experiment can be done in two ways of convention i.e. termed as open and closed aperture modes, which yields information about the sign and magnitude of nonlinear refractive index and absorption [i.e. total $\chi^{(3)}$].

2.6.1.1 Z-scan - Open Aperture

Open aperture (OA) Z-scan measurements provide info about the nonlinear absorption (NLA) coefficient β of the nonlinear medium by collecting transmittance as a function of medium position. Figure 2.21 illustrates the process of the Z-scan experiment and the corresponding nonlinear transmission signals. In the OA regime, the optical aperture in front of the photodiode is removed, so that the transmittance of the sample around the focus (Z=0) is expected to be accumulated symmetrically as well as completely. In the experiment, the sample is traversed around the focus (Z=0) from one end (far-field) to the other end. In the case of far-field linear absorption is expected due to the lower intensity of the input field. When the sample approaches focus (Z=0), the transmittance either decreases or increases, forming a valley or peak. The increase in the transmittance forming a peak around the focus is known as saturable absorption (SA) with negative type nonlinearity. Similarly, the decrease in transmittance denotes reverse saturable absorption (RSA) with positive type nonlinearity. Using the OA z-scan measurements the NLA coefficient β can be obtained which is related to the imaginary part of third-order nonlinear susceptibility [$\chi^{(3)}$] by the relation,[21]

$$\chi^{(3)} = \chi_R^{(3)} + i\chi_I^{(3)} \tag{21}$$

With the imaginary part of $\chi^{(3)}$ being

$$\chi_I^{(3)} = \frac{n_0^2 \varepsilon_0 c \lambda \beta}{2\pi} \tag{22}$$

here c is the speed of light, ε_0 is vacuum permittivity, n_0 is the linear refractive index, and λ is wavelength of the input laser. Also, the NLR n_2 in esu is related to the γ in m^2/W as,

$$n_2(esu) = \frac{cn_0}{40\pi}\gamma(m^2/W) \tag{23}$$

The real part of $\chi^{(3)}$ is related to the NLR γ,

$$\chi_R^{(3)} = 2n_0^2\varepsilon_0 c\gamma \tag{24}$$

From Beer’s law, the intensity-dependent NLA coefficient can be expressed as,

$$I(z) = I_0 e^{-\alpha(\omega)z} \tag{25}$$

$$\frac{dI}{dZ} = -\alpha(\omega)I \tag{26}$$

Where α is the linear absorption (LA) coefficient, and Z is the sample length. If NLA effects are included, then in the above differential equation must include the higher-order intensity terms

$$\frac{dI}{dZ} = -\alpha(\omega)I - \beta(\omega)I^2 - \gamma(\omega)I^3 - \cdots \tag{27}$$

Where $\beta(\omega)$is the two-photon absorption coefficient, $\gamma(\omega)$ is the three-photon absorption coefficient. If a material exhibits negligible linear absorption and with strong two-photon absorption, then only the second-order term is crucial, and other terms are neglected.

$$\frac{dI}{dZ} = -\beta(\omega)I^2 \tag{28}$$

This can be solved by using separation of variables[20] which gives the beam irradiance I(z) and phase shift $\Delta\varphi$ at the exit surface of the sample, [20]

$$I(z) = \frac{I_0}{1+\beta I_0 Z} \tag{29}$$

$$\Delta\varphi = \frac{k\gamma}{\beta}\ln[1 + \beta I_0 Z] \tag{30}$$

Where I_0 is the input intensity, z is the sample length, and β is the two-photon absorption coefficient. Consequently, two-photon absorption (2PA) processes result in stronger absorption and, therefore, more beam attenuation.

By combining the above equations, the complex filed at the exit surface of the sample is obtained by,

$$E_e = E(z,r,t)e^{-\frac{\alpha L}{2}}(1+q)^{(ik\gamma/\beta - 1/2)}, \tag{31}$$

$$E_e(r,z,t) = E(z,r,t)e^{-\frac{\alpha L}{2}}e^{i\Delta\varphi(z,r,t)}, \tag{32}$$

A zeroth-order Hankel transformation of the above equation provides the distribution of field at the aperture, which yields the transmittance by

$$T(z) = \frac{\int_{-\infty}^{\infty} P_T(\Delta\varphi_0(t))dt}{S\int_{-\infty}^{\infty} P_i(t)dt} \tag{33}$$

Where Transmitted power $P_T\big(\Delta\varphi_0(t)\big) = c\varepsilon_0 n_0 \pi \int_0^{r_0} |E_a(r,t)|^2 r dr$, $P_i(t) = \pi\omega_0^2 I_0(t)/2$

Instantaneous input power, $S = 1 - e^{(-2r_a^2/\omega_a^2)}$ is the aperture linear transmittance where ω_a is radius of the beam at the aperture. So that the variation in Z-scan transmittance can be calculated (for S=1).

$$T_{OA}(Z) = \frac{1}{\sqrt{\pi}q_0(z,0)}\int_{-\infty}^{\infty} \ln(1 + q_0(z,0)e^{-t^2})\, dt \tag{34}$$

$$T_{OA}(Z) = \frac{1}{\sqrt{\pi}p_0(z,0)}\int_{-\infty}^{\infty} \ln\left[\sqrt{\ln(1 + p_0^2(z,0)e^{-2t^2})} + p_0(z,0)e^{-t^2}\right] dt \tag{35}$$

Where $T_{OA}(Z)$ is the OA transmittance (normalized), $q_0 = \beta L_{eff} I_0$, $p_0 = (2\gamma L'_{eff} I_{00}^2)^{1/2}$, and β, γ corresponds to the 2PA and three-photon absorption (3PA) coefficients, I_{00} is peak intensity at focus, $L_{eff} = 1 - e^{-\alpha_0 L}/\alpha_0$, $L'_{eff} = 1 - e^{-2\alpha_0 L}/2\alpha_0$ are corresponds to the effective path lengths of the sample for two-photon and three-photon absorption, respectively. For SA, the intensity-dependent absorption is $\alpha(I) = \alpha_0/(1 + I/I_s)^{1/2}$, here I_s is the saturation intensity defined as $I_s = h\nu/\sigma_g\tau$, where τ is an excited-state lifetime. If $I < I_s$ which is corresponds to the third-order nonlinear process with the absorption coefficient $-\alpha_0/I_s$.[20]

For $q_0<1$ from equation (34), the transmittance can be expressed in terms as peak irradiance,[20]

$$T(z, S = 1) = \sum_{m=0}^{\infty} \frac{[-q_0(z,0)]^m}{(m+1)^{3/2}} \tag{36}$$

Hence, from the OA measurements (S=1), the NLR coefficient β can be determined.

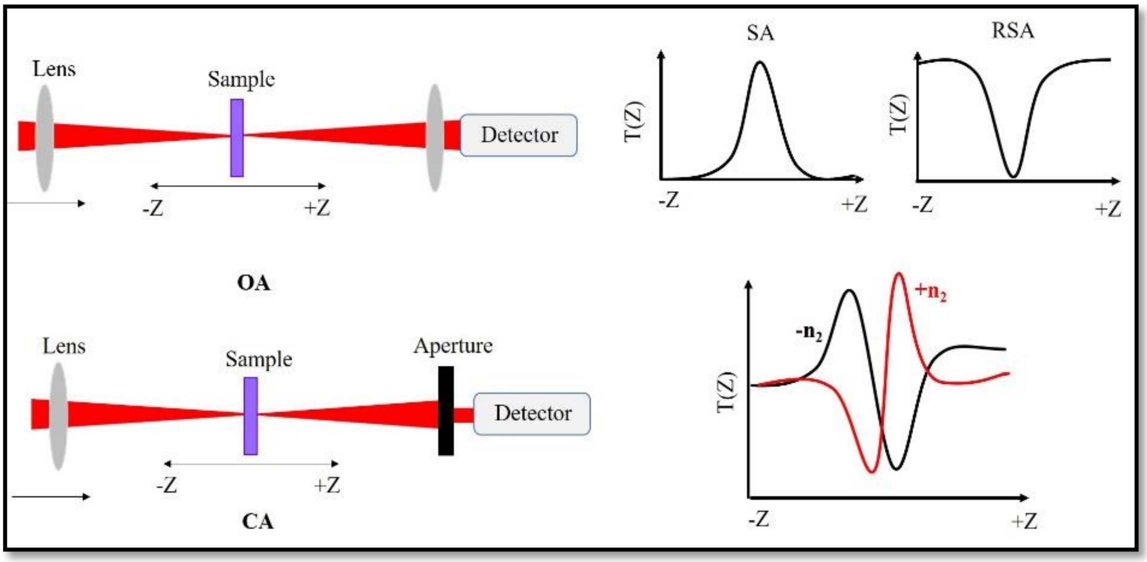

Figure 2.21 Processes of OA and CA Z-scan measurements and their corresponding transmission curves.

2.6.1.2 Z-Scan - Closed Aperture

The closed aperture (CA) Z-scan provides the NLR of the sample, and is related to the real part of $\chi^{(3)}$.[21] By measuring the input electric field phase $\Delta\varphi$ distortion as it goes through the nonlinear medium of length L. Under thin sample approximation ($L << Z_0$) and slowly varying envelope approximation (SVPA) $L << Z_0/\Delta\varphi_0$, within-sample, the beam profile should not change, here Z_0 is Rayleigh range $\Delta\varphi_0$ is the phase distortion. The phase change $\Delta\varphi$ with respect to the propagation distance Z is written as,

$$\frac{d\Delta\varphi}{dz} = k\Delta n(I) \tag{37}$$

Where $\Delta n(I) = n_2 I$, $n_2(cm^2/W)$ is the NLR and $k=2\pi/\lambda$ where λ is wavelength of the input beam. By solving the equation (37) gives the $\Delta\varphi$ as:

$$\Delta\varphi_0(z,t) = \frac{\Delta\varphi_0(t)}{1+(z/z_0)^2} \tag{38}$$

Where $\Delta\varphi_0(t) = kn_2 I_{00} L_{eff}$ here I_{00} is on-axis peak intensity. The electric filed of the input light entering into the sample is,

$$E(r,z,t) = E_0(t)\left(\frac{\omega_0}{\omega(z)}\right) exp\left(\frac{-r^2}{\omega^2(z)} - \frac{ikr^2}{2R(z)}\right) \exp(-i\varphi(z,t)) \tag{39}$$

Where ω_0, $\omega(z)$ is beam waist and radius, $R(z)$ the radius of curvature of a wave front. The exiting light electric field with phase change $\Delta\varphi$ is defined as,

$$E_e(r,z,t) = E(r,z,t)\exp(-\alpha_0 \mathrm{L}/2)\exp(-i\Delta\varphi(z,r,t)) \tag{40}$$

The far-field pattern E_e can be obtained at the aperture plane using the zeroth-order Henkel transformation. The E_e is integrated spatially from zero to r_a (radius of aperture) to get the transmitted power over the aperture. From equation (9) in the normalized transmittance at position *Z*, the S value is in the range of 0.1 - 0.5 to obtain the NLR (n_2).

2.6.2 Experimental details

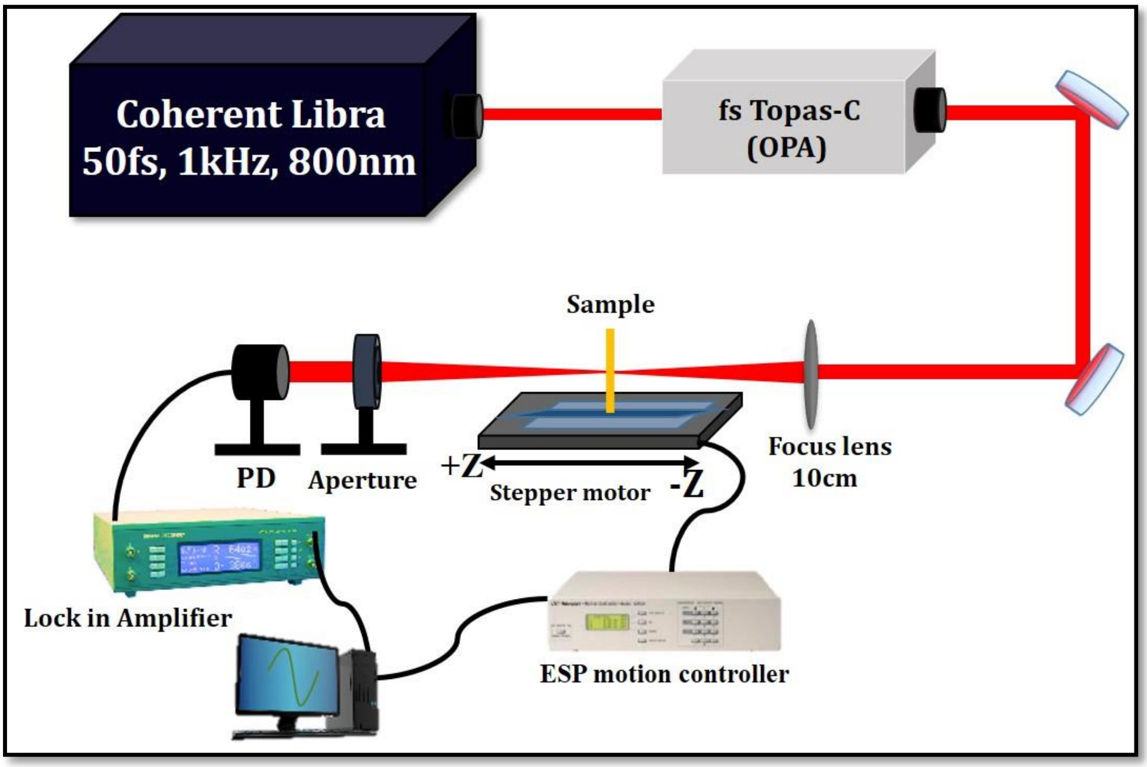

Figure 2.22 A typical fs - Z-scan experimental setup.

A Ti:sapphire amplifier laser providing ~50 fs pulses at 800 nm and a 1 kHz repetition rate was used to perform all the measurements. A broadband seed laser (~30 fs at 800 nm with a bandwidth of ~35 nm and a repetition rate of 80 MHz) was used for the amplifier and a nanosecond Nd: YAG laser at 532 nm was used to pump the amplifier. The output from the laser amplifier system has a maximum of ~4 mJ energy, centered at 800 nm wavelength, and a bandwidth of ~28 nm. In order to tune the output wavelength of the amplifier laser an optical parametric amplifier (OPA) was used, which gives a laser pulses of ~70 fs. The output pulses from the OPA were focused usually with a 15 cm plano-convex lens. The beam waists ($2\omega_o$) were estimated to be in the range of 50-140 µm (wavelength range of 500-1500 nm). The samples were placed on a linear translation stage and the transmission was collected using a photodiode [Thorlabs - SM1PD2A (VIS), DET10C/M (NIR)], the output of which was fed to a digital lock-in amplifier (signal recovery 7265). All the instruments were controlled using a home-built LabVIEW program. A typical Z-scan experimental schematic is provided in figure 2.22.

2.7 Degenerate Four-wave Mixing (DFWM)

The general case of third-order nonlinear interaction is four-wave mixing. Interaction of three input fields and generation fourth scattered beam is a formidable task. Degenerate four wave-mixing (DFWM) is one of its kind, where the process involves, the interaction of three laser beams in a medium and generation of the fourth beam with the identical frequency as input.[22-23] The interaction mediates via third-order nonlinear polarization $P^{(3)}$. The frequency mixing can be performed in two geometries such as forward (i.e., BOXCARS) and backward (i.e., phase conjugate geometry); the selection can be made depending on the conditions.[24-25] Experimentally there are two different cases resonant and non-resonant DFWM. In the non-resonant DFWM, wavelength far from the absorption band leads to optical phase conjugation, i.e., the formation of phase grating due to spatial modulation of refractive index. This is attained by overlapping the first two input beams, which writes the gating was third beam probes or reads the grating by scattering from it, thus generating the fourth beam in a direction determined by the phase-matching condition. The non-resonant DFWM provides the absolute magnitude and spectral width of the Kerr-effect nonlinearity (n_2). The DFWM signal have contribution from both nonlinear absorption and refractive index from equation (41)

$$\left|\chi^{(3)}\right|^2 = \left|Re\{\chi^{(3)}\} + Im\{\chi^{(3)}\}\right|^2 \tag{41}$$

$\chi^{(3)}$ is a third-ranked tensor by using different polarization of input fields; all of the tensor components can be measured independently. In the case of resonant DFWM, there is a contribution from optical absorption due to the input frequency of light. Thereby generating the population grating due to spatial modulation of the excited state population. In general, both absorption and phase grating are present in resonant DFWM. The fourth beam contains more information about the sample under study. The time-resolved DFWM measurements can give information about the dynamics of the induced nonlinear polarization. The resonant DFWM provides information about the coherent response of the optically coupled eigenstates of the system. The width of the diffracted pulse states the rate at which the physical process broadens the transition. The nonlinear polarization dies off due to the mechanisms such as scattering, diffusion, and population relaxation associated with coupled states.

2.7.1 BOXCAR geometry

The phase-matching concept was introduced by Girod-Maine[26] in 1962. Phase-matching is a geometrical arrangement of input beams by maintaining the conservation of momentum ($\sum k_i = 0$) and energy ($\sum \omega_i = 0$) there by generating a well-defined spatially separated output signal at maximum intensity. Eckbreth[27] has introduced boxcars geometry, where the input beams were incident from three different directions (corners) in a boxlike shape. The BOXCARS geometry is more advantageous than collinear geometry was the input and output signal travel in the same direction mainly, the spatial separation of signal from background.

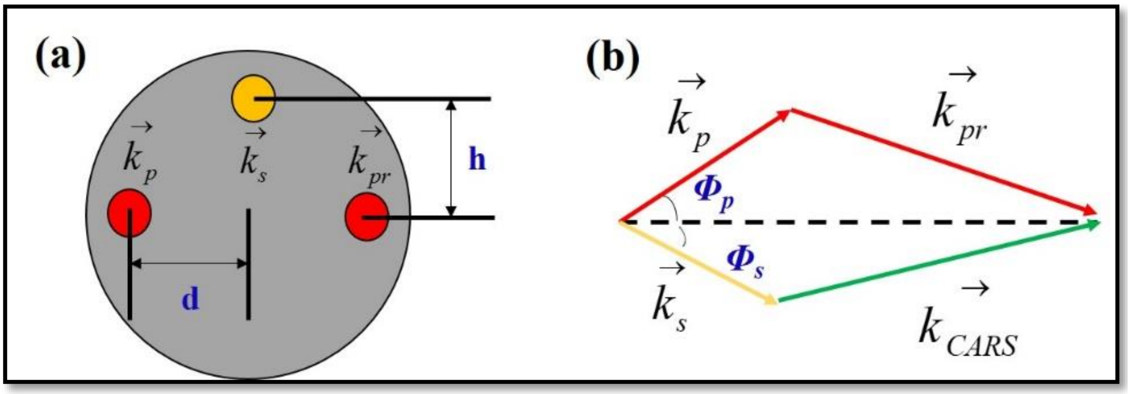

Figure 2.23 (a) BOXCARS beam arrangement at the focus lens, (b) phase-matching diagram.

In case of non-degenerate four-wave mixing (nDFWM) process such as Coherent Anti-stokes Raman spectroscopy (CARS) involving pump/probe beams at a frequency ω_p, and a stokes beam at ω_s. Where all the three input beams interact in a medium and produces a fourth beam at anti-stokes frequency ω_{CARS} following conservation of energy $\omega_{CARS} = \omega_p - \omega_s - \omega_{pr}$. The CARS signal strength depends on the overlapping of three beams and the deference of the population between the excited state and ground state. As shown in figure 2.23, the two beams pump/probe at the focusing lens are arranged in a horizontal plane with distance d, and the Stokes beam is impinging at a distance h above the plane of pump beams.

For *h* much less than focal length *f* of the lens the optimized values for h, d is obtained by using the following equations[24-25]

$$sin\phi_s = sin\phi_p\sqrt{2\frac{\omega_{pump}}{\omega_s} - 1} \qquad (42)$$

$$h(\omega_s) = d \times \sqrt{2\frac{\omega_{pump}}{\omega_s} - 1} \qquad (43)$$

2.7.2 Experimental details

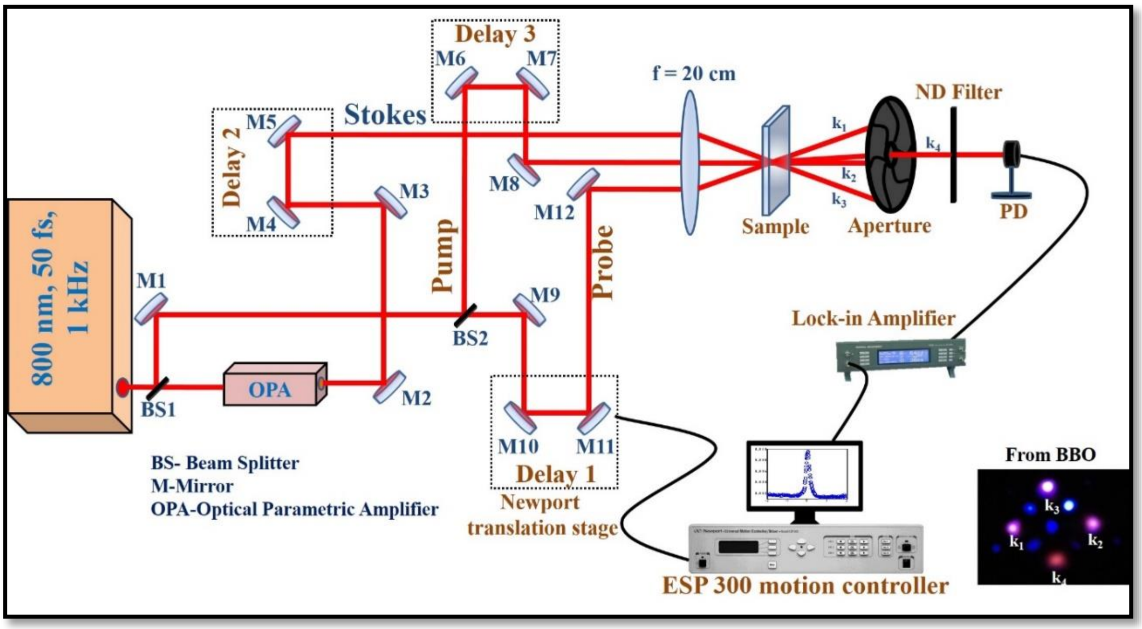

Figure 2.24 fs-DFWM experimental setup (inset shows the output signal from β-Barium Borate crystal).

The input laser pulses at 800 nm were divided into three equal parts with electric fields $\boldsymbol{E_1}(\boldsymbol{t}), \boldsymbol{E_2}(\boldsymbol{t}-\boldsymbol{\tau})$ and $\boldsymbol{E_3}[\boldsymbol{t}-(\boldsymbol{\tau}+\boldsymbol{T})]$ [with wave vectors of $\vec{\boldsymbol{k}}_1$, $\vec{\boldsymbol{k}}_2$, $\vec{\boldsymbol{k}}_3$] using appropriate beam splitters. The three beams were aligned in forwarding phase-matching geometry (BOXCAR). A 20 cm plano-convex lens was used to focus the input beams. The signal (fourth beam) in the direction $\vec{\boldsymbol{k}}_4$ was collected using a photodiode (Thorlabs SM1PD2A), which was connected to a lock-in amplifier. A quartz cuvette with 5-mm thickness was used to hold the sample solution. The phase matching ($\vec{\boldsymbol{k}}_4$=$\vec{\boldsymbol{k}}_1$+$\vec{\boldsymbol{k}}_2$-$\vec{\boldsymbol{k}}_3$)

condition was ensured by performing the DFWM measurements with (β-Barium borate) BBO crystal, as shown in figure 2.24. The time-resolved DFWM measurements were performed by delaying one of the beams, and the signal was recorded at each delay. The stage, PD, and the lock-in were interfaced with a computer and a LabVIEW program.

2.8 Transient Absorption Spectroscopy

The invention of ultrafast tunable lasers has unfolded a new attractive area of research towards studying ultrafast events at a molecular level. Spectroscopies base on ultrashort pulses have deployed to elucidate the ultrafast photophysical processes, charge transfer, and structural dynamics, which could not be accessed with other methods. Transient absorption spectroscopy (TAS) is a powerful tool to investigate the dynamics of photo-excited states which are probed by monitoring their absorption. In TAS, a strong pump beam at frequency ω_p excite the molecules to higher excited states, and a low energy probe beam ω_{pr} see the pump induced changes in delay time t. In general, the probe beam in TAS is a broadband light that ranges from UV to NIR spectral range. By taking the difference absorption spectrum (ΔA) of the ground state and excited state at each probe delay time t and wavelengths λ, i.e. (ΔA (t, λ)) are obtained. The $\Delta A(t, \lambda)$ contains all the info about the excited state process after photoexcitation, such as excited-state energy relaxation, charge transfer, and vibrational relaxation. The advantage of absorption spectroscopy over the emission spectroscopic techniques is the evolution of the non-radiative process can be investigated. The ΔA (t, λ) spectrum has contributions from various photo-processes as shown in figure 2.25,

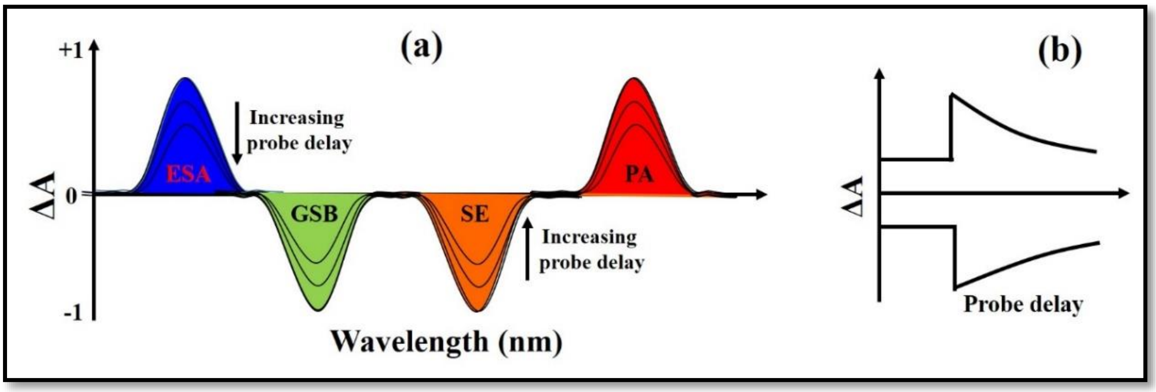

Figure 2.25 (a) typical transient absorption spectra *(ESA; excited-state absorption, PA; product absorption, GSB; ground state bleach, SE; stimulated emission)* (b) absorption decay curves at positive and negative ΔA spectra.

- ✓ Ground state bleach (GSB): Upon pump pulse excitation, a part of the molecules is excited to excited states. Consequently, the number of molecules in the ground state gets significantly reduced. This results in the ground state absorption of an excited state sample to be less than that of a non-excited sample. Therefore, a negative signal appears in the ΔA spectrum at ground state absorption of the sample.
- ✓ Excited-state absorption (ESA): Upon pump pulse illumination, the excited states can further absorb the transmitted probe photons, thereby promote the population to achieve higher excited states. As a result, a positive signal in the ΔA spectrum appears.
- ✓ Stimulated emission (SE): In case of a two-level system, Einstein absorption (A_{12}) and emission (A_{21}) coefficients are identical. Therefore, upon pump pulse illumination, a stimulated emission occurs from an excited state to the ground state when the probe pulse passes through the pump pulse excited volume. So, a negative signal appears in the ΔA spectrum. SE will only occur for optically allowed states with spectral features that of the fluorescence spectrum of the sample of interest, i.e., SE band is stoke shifted with respect to the GSB band. In this process, a probe pulse creates the SE photon from the excited state population. The SE photon travels in the same direction as the probe pulse; as a result, an amplified probe beam reaches the detector.
- ✓ Product absorption (PA): Upon photoexcitation of the sample, mainly photochemical or photobiological systems, different reactions may take place. As a result, long-lived or transient molecular states will form, such as charge-separated states, triplet states and isomerized states. The product absorption will appear as a positive signal in the ΔA spectrum. Also, a GSB signal appears at the wavelengths where the sample (chromophore) on which the product state lives, has a ground-state absorption.

Since the transient signal results from a light-matter interaction by the third-order nonlinear susceptibility $\chi^{(3)}$, the ΔA spectrum can have non-resonant contributions such as cross-phase modulation and coherent artefacts. Such contributions can be avoided in the data interpretation by avoiding the initial dynamics within the pulse duration. In the experiment, these contributions can be subtracted from the data by recoding the TA spectra for solvent alone. In the case of anisotropic materials, excited species follow pump beam polarization in such case the probe beam (with parallel or orthogonal to the pump beam) will have a contribution from both population and reorientation of the excited state species. This contribution is generally avoided be maintaining the angel between pump and probe polarization at 54.7^0 known as magic angle.[28]

2.8.1 Principle

The intuition of time-resolved spectroscopy is to understand the dynamics of molecules through their optical properties such as absorption and emission. According to Beer-Lamberts law, the absorbance A(λ) of a species is given by

$$A(\lambda) = \varepsilon(\lambda).c.d \qquad (44)$$

Where d is the sample length, c is the molar concentration (in M) and $\varepsilon(\lambda)$ molar extinction coefficient (in M^{-1} cm^{-1}). If we have many species in the sample, then the above equation

$$A(\lambda, t) = \sum_i \varepsilon_i(\lambda).c_i.d \qquad (45)$$

Therefore, monitoring the absorption changes in time not only gives information about the species and also their dynamic. The difference absorption of the sample at given delay time Δt, i.e., before (with concentration c_{i0}) and after the absorption is given by,

$$\Delta A(\lambda, \Delta t) = \sum_i \varepsilon_i(\lambda).\Delta c_i(\Delta t).d \qquad (46)$$

The $\Delta A(\lambda, \Delta t)$ gives information about the concentration changes Δc_i. The dynamics we are interested in are in ultrafast time scales; therefore, conventional electronic devices do not work due to response limitations (ns). The pump-probe technique breaks this condition by using ultrafast pulses to pump and probe the sample.[29-30] The probe absorbance is collected at different delay times using a spectrometer. The change in absorption before and after the pump, i.e., by recording the probe intensity before (I_{np}) and after (I_p) pump pulse gives the differential absorption spectrum as,

$$\Delta A(\lambda, \Delta t) = \sum_i \varepsilon_i(\lambda).(c_i(\Delta t) - c_{i0})d \qquad (47)$$

Which contains all the dynamics information about the species present in the sample.

2.8.2 HELIOS

HELIOS is a broadband transient absorption spectrometer (Ultrafast systems M/S) based on the femtosecond amplifier (LIBRA, Coherent M/S), providing ~50 fs pulses at a repetition rate of 1 kHz and 800 nm wavelength, is shown in figure 2.26. It comes with an optical unit and PC unit containing necessary software and hardware. The output of the LIBRA amplifier system was split into two parts, a part of the amplifier beam is used to pump the OPA, and the output from OPA was used for pump beam while the other part of the laser was used to generate a WLC by focusing on to a 2 mm thick Sapphire crystal. The probe beam was aligned through a 5 ns delay stage. A set of parabolic mirrors was used to compress the probe beam before it reaches the sample. The pump beam was collimated onto the sample with a diameter of ~ 100 µm, and transmission of pump beam from the sample was blocked. The pump beam was chopped at 500 Hz for achieving better signal to noise ratio, and the chopper input signal was drawn from a laser system at 1 kHz from PC2 in Libra amplifier (figure 2.15 black curve). Thus, chopper has to block one pulse for every other pulse, so the output from the chopper has a frequency of 500 Hz.

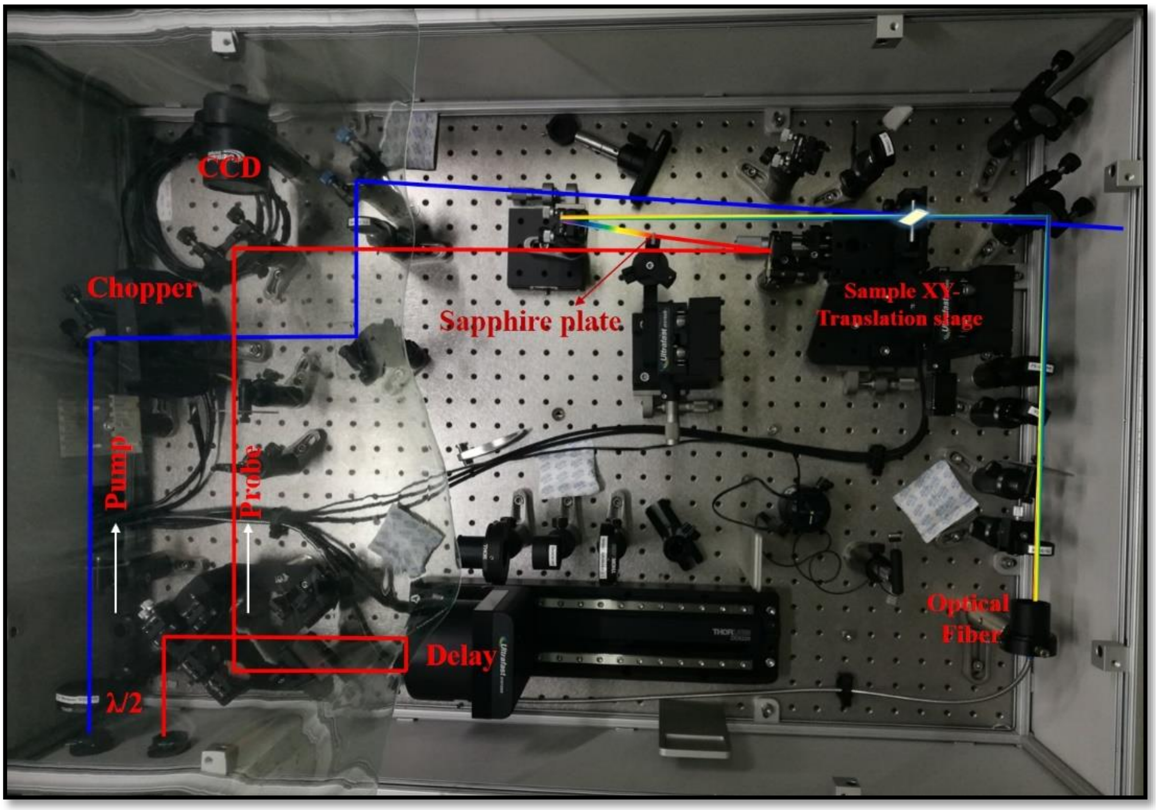

Figure 2.26 Experimental layout of the HELIOS transient absorption spectrometer.

The green signal in figure 2.27 is used by the software to determine the pump on or pump off state, i.e., the chopper phase. The transient data is collected by the following equation, $\Delta A = \log(I_0/I_{ex})$ Where I_0 is the probe intensity when the pump is blocked on the sample by chopper and I_{ex} is the intensity of the probe light when the pump is incident on the sample. The sample was kept on an XY-motorized stage to prevent continuous exposure to the sample. The transmission of the probe beam was collected using a fiber-coupled spectrometer. A set of ND filters were provided to control the input power of the two beams before and after the sample. The complete data acquisition was carried on Surface Xplorer software package, as shown in figure 2.28, which is designed on a LabView platform.

Instrument specifications

- ✓ Probe spectral range – 400 - 800 nm
- ✓ Spectral resolution - 1.5 nm
- ✓ Time window – 5.5 ns
- ✓ Intrinsic temporal resolution – 7 fs
- ✓ VIS detector – fiber-coupled multi-channel spectrometer with CMOS sensor
- ✓ Laser frequency range – up to 5kHz
- ✓ Data acquisition – Surface Xplorer software package

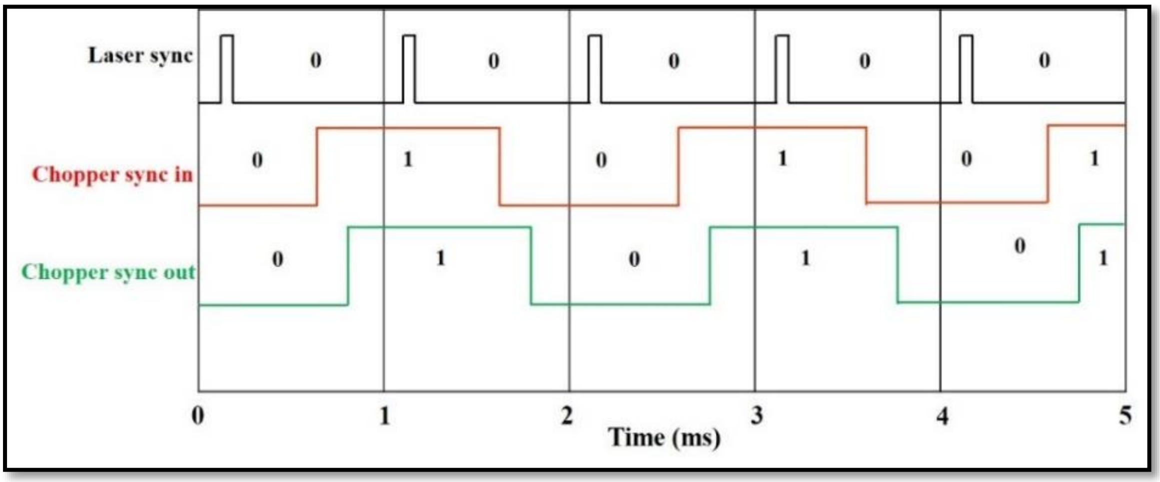

Figure 2.27 Trigger signals (black) laser sync signal (red) chopper sync signal that block every other pump pulse (green) chopper sync out signal

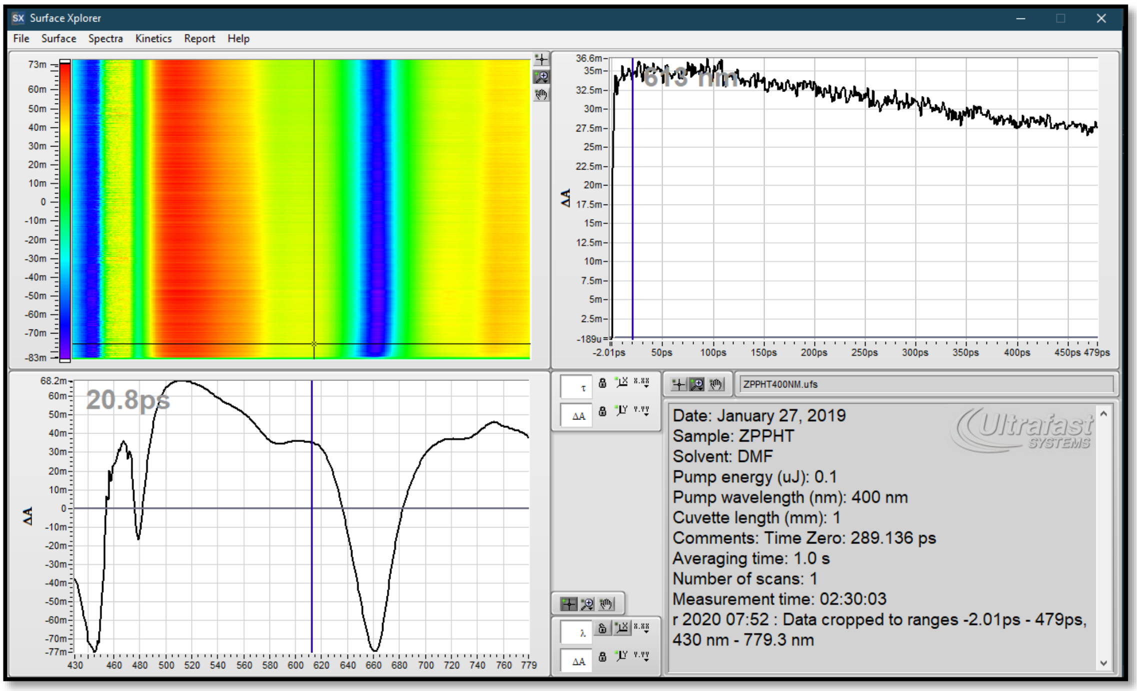

ZPPHT400NM.ufs

Date: January 27, 2019
Sample: ZPPHT
Solvent: DMF
Pump energy (uJ): 0.1
Pump wavelength (nm): 400 nm
Cuvette length (mm): 1
Comments: Time Zero: 289.136 ps
Averaging time: 1.0 s
Number of scans: 1
Measurement time: 02:30:03
r 2020 07:52 : Data cropped to ranges -2.01ps - 479ps, 430 nm - 779.3 nm

Figure 2.28 Surface Xplorer software graphical layout. The top left panel shows the ΔA(t, λ) surface; it contains a number of transient spectra at closely space probe time delays. The below-left corner shows the transient spectra at successive probe delay. The top right corner displays the individual kinetic profile with a probe delay. The lower right corner contains experimental details during the measurement.

2.8.3 Data processing

2.8.3.1 Chirp correction

In the process of probe pulse generation, the white-light continuum (WLC) is chirped, i.e., different components of the probe spectrum overlap at different times at sample. Therefore, the WLC has intrinsic group velocity dispersion (GVD).[29] The WLC before reaching to the sample which goes through the several optics (lenses and cuvettes), and this results in an increase of the GVD to several picoseconds. This can be reduced with a pair of parabolic mirrors for collimation and focusing on the sample. This can also affect the estimation of short-lived components in the investigated sample. This dispersion curve can be correctly modelled by fitting the data using a quadratic polynomial function. This can be used for numerical correction of obtained data, as shown in figure 2.29. This process can be readily performed in a surface Xplorer software whereby choosing the different points across the wavelength region the software fits them with the following equation $t_0 = a\sqrt{b.\lambda^2 - 1/c.\lambda^2 - 1} + d$ where a, b, c, d are fitting parameters, t_0 is time zero and λ is wavelength. The data is then corrected by interpolating the signal [i.e. $\Delta A_{cor}(\chi, \Delta t_{cor}) = \Delta A(\lambda, \Delta t + \delta t(\lambda))$] for each wavelength and at new time $t_{cor}=t+\delta t$.

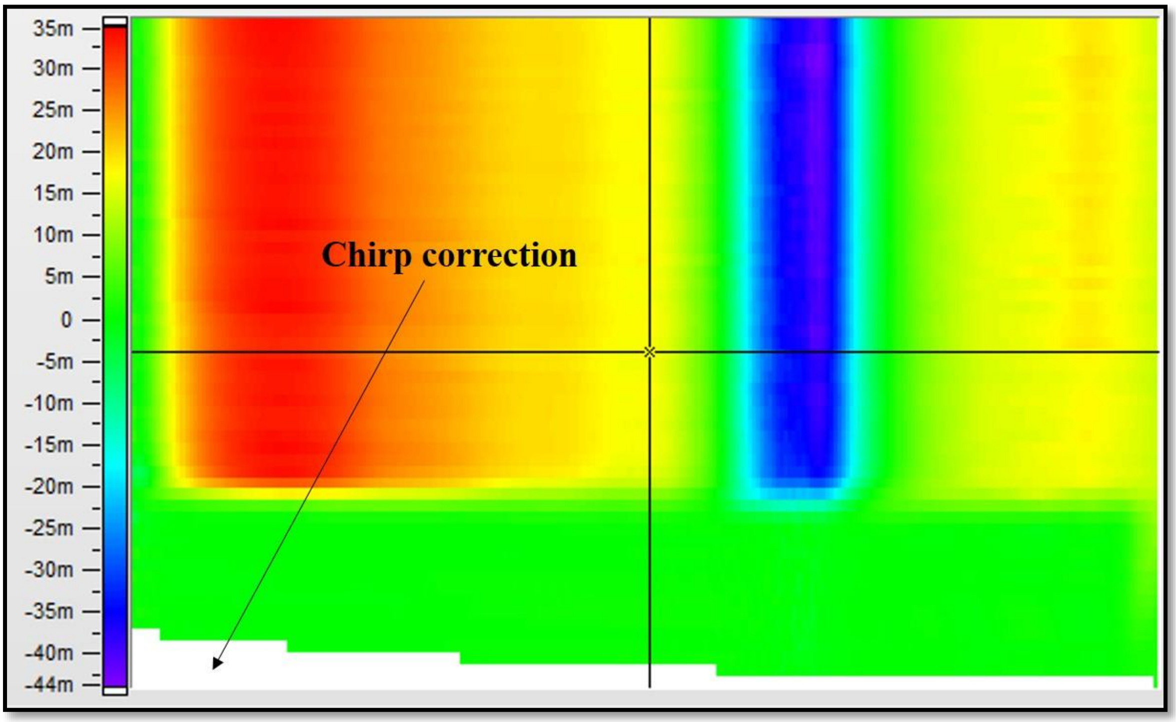

Figure 2.29 Chirp corrected 3D surface panel data.

2.8.3.2 IRF measurement

The instrument response function (IRF) is defined as the convolution of exciting laser pulse shape (usually Gaussian), and the detector response.[29, 31] IRF limits the observation of the fastest components in the experiment. In TA, IRF can be measured by frequency mixing of both pump and probe in a nonlinear crystal, or by recording the TA spectra of pure solvents CCl_4, CS_2, Water, or thin glass slide. The IRF was measured in our experiment by recording the TA spectra of pure CCl_4 (purchased from Sigma Aldrich and highly pure). In the IRF measurement, the output from OPA was kept at 500 nm, and the energy was reduced to 0.1 µJ at the sample cuvette. The TA spectra were collected from pure CCl_4 solvent in a 1-mm thick cuvette. The kinetic trace at 500 nm wavelength was fitted by using a sum of Gaussian or first two derivatives of the Gaussian function, which yielded the full width half maximum (FWHM) of 116 fs as shown in figure 2.30. Also, we have verified at different wavelength regions to attain the accuracy in IRF measurements; the FWHM values were in the range of ~110-127 fs.

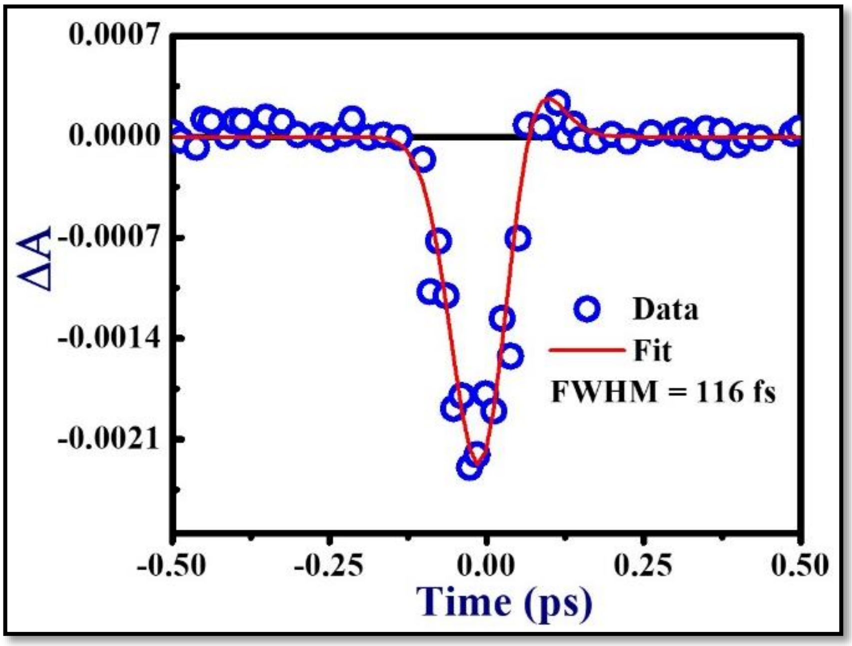

Figure 2.30 IRF measurement of Helios spectrometer in CCl_4

2.8.3.3 Global and target analysis

In TAS data, the ΔA(t, λ) spectrum contains large data points, i.e., several hundred wavelengths and corresponding time delay points. The data can be analysed in two different ways in order to extract valuable information. First, plot the TA spectra at different probe delays; this allows us to visualize the different processes involved in the reaction. Next, we take the kinetic trace of a particular wavelength; this shows the rise and decay of populations C_i. We fit the data with a model function and if the fit is good agreement with the data, the fit parameters can be used to describe the reaction.[31] The model function is defined for n number of states as a sum of exponentials,

$$\Delta A(\lambda, t) = \sum_i^n A_i \,.\, e^{-k_i t} \tag{48}$$

Where A_i is constant, and k_i is decay constant. Due to the limited response of the instrument, the above equation is convoluted with IRF, usually Gaussian shape with width σ and delay time t_0, which yields.

$$A(\lambda, t) = \sum_i^n A_i \,.\, e^{\frac{-(t-t_0)}{\tau_i}} \otimes \frac{1}{\sigma 2\sqrt{2}} e^{-\frac{t^2}{\sigma^2}} \tag{49}$$

We use the above equation to fit the kinetic response of the sample. A similar function is used in the surface Xplorer software to fit the kinetic response. We can choose a number of exponentials until the fitting matches with the experimental data. This can be visualized from $\chi^{(2)}$ value, defined as the difference between experiment (ΔA_{exp}) and theoretical fit ($A(\lambda, t)$), also called residual.

$$\chi^{(2)} \int \left| \Delta A_{exp}(\lambda, t) - A_{fit}(\lambda, t)|_{A_i \tau_i t_0 \sigma} \right|^2 dt \tag{50}$$

The second method follows global and target fitting techniques because several processes take place upon photoexcitation; the single wavelength kinetic trace will not provide significant information. Here global fitting means all the kinetic traces are fitted simultaneously with same time constants but independent amplitudes. In this thesis, the global and target analysis is performed on a graphical user interface Glotaran based on R-package TIMP.[32]

The first step of global analysis is to fit the data with adequate number of exponential decays (i.e., number of components or lifetimes). The components decay independently or parallel, resulting in decay associated difference spectra (DADS). The number of linear independent components is estimated by using singular value decomposition (SVD) (i.e., this method filters the vast data into a rather lesser number of components or spectra). SVD is a Mathematical operation that decomposes a matrix $M_{m\times n}$ into three separate matrices

$$M_{m\times n} = U_{m\times m} S_{m\times n} V_{n\times n} \tag{51}$$

Where U ($m \times m$) and V ($n \times n$) are orthogonal matrices whose columns comprise the left and right singular vectors, and S is a diagonal matrix consists of singular values with decreasing weight order. Experimentally, $M_{m\times n}$ matrix means differential absorption $\Delta A(\lambda, t)$ spectrum. Here column corresponds to the kinetic trace, and rows correspond to the differential spectrum, i.e., columns of matrix U and V are kinetic trace and spectrum. From the magnitude of singular values, the most important components n is estimated, i.e., $S_1 > S_2 > S_{ncomp} \ldots = 0$.

Apart from using independent decays, another method is used where the components decay sequentially (with increasing lifetime), also called an unbranched, unidirectional model. In this process, the components are referred to as compartments. Following photoexcitation, the first compartment gets populated and subsequently transfers to the second compartment. The second compartment decays to third and so on until it reaches to the ground state, which yields the evolution associated difference spectra (EADS), which reflects the spectral evolution as the third component rises with the lifetime of the second component and decays with a lifetime of the third component.

The final method is fitting with a complete photophysical model, which is the combination of both parallel and sequential models called kinetic analysis. When the investigated system has branching and back-reactions involved between different compartments, the so-called linear compartmental model can be used. A compartmental model involves multiple compartment excitation back-reactions and branching; thus, it allows much flexibility in modelling the data. In the compartmental model, transitions between different compartments are defined by microscopic rate constants, which constitutes the half diagonal elements of the transfer matrix K in Glotaran software. Columns in the K-matric are corresponding to the compartments. The reciprocal of the eigenvalues of this matrix are corresponds to the lifetime of each compartment. A linear compartmental modal for n_{cop} components can be described as,

$$\frac{d}{dt}c(t) = Kc(t) + j(t) \tag{52}$$

Where $c(t) = [c_1(t), c_2(t) \ldots c_{n\,comp}(t)]^T$ is the concentration of all compartments, $j(t)=i(t)[X_1\ X_2 \ldots X_l]^T$ where i(t) is described by IRF, and X_1 is input to compartment *l*. the off-diagonal elements k_{pq} of the transfer matrix K contains represents the microscopic rate constants from compartment *'q'* to *'p'*. The diagonal elements provide the total decay rates of each compartment. A graphical user interface Glotaran based on R-package TIMP is used in this thesis to analyze the TAS data.

2.9 Coherent Anti-stokes Raman Spectroscopy (CARS)

Coherent Anti-Stokes Raman spectroscopy (CARS) is an efficient technique to probe the ground state vibrational dynamics of the molecules with higher temporal and spectral resolutions in both gas and liquid phases.[33-40] CARS is a nonlinear spectroscopic technique that eliminates the less scattering cross-section of the natural Raman process. Spontaneous Raman is an incoherent process wherein the photons scatter in all the directions. In contrast, CARS is a coherent technique in which all the Raman scattered photons emerge out in one direction, similar to a laser. Coherent Raman spectroscopy is a versatile technique for imaging and characterizing the materials even with strong fluorescence background. Employment of ultrafast lasers enables the novel possibilities of time and frequency-resolved spectroscopies to probe the vibrational dynamics that occur in the time scales shorter than the molecular vibration period ~100 fs. In a femtosecond time-resolved CARS (TR-CARS) experiment, several vibrational modes of the molecules can be excited simultaneously, and the relaxation processes can be probed in real-time. TR-CARS also enables us to estimate the dephasing times and collisional relaxation times of the interested vibrational modes in solutions. Additionally, TR-CARS facilitate to probe the excited state dynamics of vibrational modes. However, the excitation of molecular vibrational modes with fs broadband pulses in CARS experiment limits the spectral resolution, and it can be eliminated by employing pulse shaping techniques [41-43] to trigger selective absorptions. The analysis of TR-CARS spectra provokes the insight on intermolecular interactions as well as the molecular structure.

Figure 2.23 shows the TR-CARS BOXCARS arrangement. The pump beam (ω_p) and stokes beam (ω_s) are overlap onto the sample and coherently excite a Raman active vibrational mode at the frequency difference of $\omega_p - \omega_s$ in the electronic ground state of the molecule. This coherence can be probed by mixing a third beam called probe ω_{pr} and scattered to generated the fourth signal at anti-stokes frequency $\omega_{as} = \omega_p - \omega_s + \omega_{pr}$ in the specific direction defined by phase-matching direction $k_{as} = k_p - k_s + k_{pr}$. The intensity of the CARS signal can be obtained by solving the wave equation of an electric filed at ω propagating in a nonlinear medium,

$$\frac{d^2E(\omega)}{dz^2} + kE(\omega) = \frac{\omega^2}{c^2\varepsilon_0}P^{(3)}(\omega) \tag{53}$$

Where c is the speed of light, n is the linear refractive index of the medium k $(=n\omega/c)$ is the propagation constant, and ε_0 is the vacuum permittivity and $P^{(3)}(\omega)$ is the nonlinear polarization at the angular frequency ω. Two laser beams of frequency ω_1 and ω_2 are incidents simultaneously then

$$P_{NL} = \frac{1}{2}\sum_{j=1}^{3} P^{(3)}(\omega)e^{-i\omega_j t} + \cdots \tag{54}$$

Here

$$\begin{aligned} P^{(3)}(\omega_1) &= \chi^{(3)}N(\omega_1)E(\omega_1)|E(\omega_2)|^2 \\ P^{(3)}(\omega_2) &= \chi^{(3)}N(\omega_2)E(\omega_2)|E(\omega_1)|^2 \\ P^{(3)}(\omega_3) &= \chi^{(3)}N(\omega_3)E(\omega_1)|E(\omega_2)|^2 \end{aligned} \tag{55}$$

Where N is the density of the molecules and $\omega_3 = 2\omega_1 - \omega_2$, while $\chi^{(3)}$ is the third-order nonlinear susceptibility, the last term can have a contribution from resonant and non-resonant processes according to Bloembergen's notation $\chi^{(3)} = \chi_R + \chi_{NR}$ where ($\chi_R=\chi' + i\chi''$). The resonant part of the nonlinear susceptibility χ_R has a contribution from rotational-vibrational resonances. The non-resonant part of $\chi^{(3)}$ has a contribution due to the electronic resonances. The $\chi^{(3)}$ is resonantly enhanced at the Raman frequency $\omega_R = \omega_p - \omega_s$. If the difference between pump and stokes frequency matches to any of the Raman frequency, the CARS will be enhanced. The principle of the CARS process is shown in figure 2.31 with two real (|0>, |1>) and two virtual energy levels (|2>, |3>). Upon pump pulse ω_p excitation, the molecule from ground state |0> will excited to a virtual state |2>. The second photon of frequency ω_{Stokes} is tuned to a transition from excited molecule to rotational-vibrational level |1>. Upon second pump photon ω_p the molecule will go to higher virtual level |3>. An anti-stokes frequency at ω_{CARS} is emitted while returning back to the ground state |0>. The rotational-vibrational selection rules of CARS and spontaneous Raman is identical. For a diatomic molecule,

$$\Delta v = 1, \quad \begin{Bmatrix} \Delta j = +2 \;\; S - branch \\ \Delta j = 0 \quad Q - bracnh \\ \Delta j = -2 \;\; O - branch \end{Bmatrix} \qquad vibrational\ CARS \tag{56}$$

$$\Delta v = 0, \quad \Delta j = \pm 2 \;\; O - S - branch \quad rotational\ CARS \tag{57}$$

where j and v are rotational and vibration quantum numbers. The vibrationally excited molecule in the Q-branch gives more signals than that in the case of O or S-branch. So, most of the CARS experiments use the very intense Q-branch.

The three input electric fields (pump/probe, stokes) mixing in Raman active medium to produce CARS signal field

$$E(z,t) = \frac{1}{2}\left[E_p(z,\omega_p)e^{i(k_p z - \omega_p t)} + E_p(z,\omega_p)e^{i(k_p z - \omega_p t)} + E_s(z,\omega_s)e^{i(k_s z - \omega_s t)} + \cdots\right] \tag{58}$$

These fields induce third-order nonlinear polarization, which is the source of the CARS signal at anti-stokes frequency ω_{as}. The nonlinear response of the material to the input fields is expressed in terms of polarization density as

$$P = \varepsilon_0 \chi^{(1)} E + \varepsilon_0 \chi^{(2)} E.E + \varepsilon_0 \chi^{(3)} E.E.E + \cdots \tag{59}$$

$$P = P^{(1)} + P^{(2)} + P^{(3)} + \cdots \tag{60}$$

Where $\chi^{(1)}$ is the linear susceptibility this term defines the absorption, refractive index, spontaneous Raman scattering process, $\chi^{(2)}$ is the second-order nonlinear susceptibility which is the source of second harmonic, sum-frequency and hyper-Raman scattering processes, this term vanishes medium with inversion symmetry (gases, liquids, plasmas, crystals with Centro symmetry). The final term $\chi^{(3)}$ is called the third-order nonlinear susceptibility exists in all media, which is a fourth rank tensor with four frequencies and polarizations, and it contains 81 (3^4) elements. In the isotropic media, this number is reduced to 3, and in the degenerate CARS ($\omega_p = \omega_{pr}$), there are only 2 elements. The intensity of the CARS signal can be calculated by using the above two equations (a, b) in a Maxwell equation which results in the average CARS signal intensity as,

$$I_{as} = \frac{\omega_{as}^2 N^2}{16\varepsilon_0^2 c^4}[\chi^{(3)}(\omega_p - \omega_s)]^2 I_p^2 I_s L^2 \frac{sin^2(\Delta kL/2)}{(\Delta kL/2)^2} \tag{61}$$

Where $\Delta k = k_p + k_{pr} - k_s - k_{as}$ is called the phase miss-match, L is the sample length, Ip, Is the intensity of pump and Stokes beams. For a perfect phase-matching $\Delta k = 0$, therefore, $k_{as} = k_p + k_{pr} - k_s$ is generated.

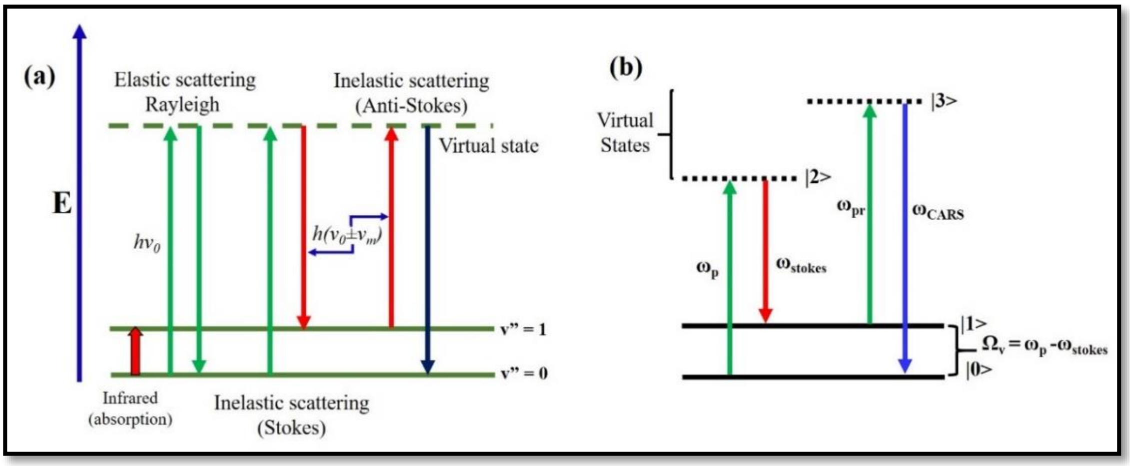

Figure 2.31 (a) Energy level representation of spontaneous Raman, (b) CARS processes.

2.9.1 Experimental details

The experimental setup for TR-CARS is illustrated in figure 2.32. A Ti: Sapphire based laser amplifier (LIBRA M/s Coherent) that delivers ultrafast pulses of central maximum 800 nm, and pulse duration of ~ 50 fs at 1 kHz repetition rate was utilized in this experiment. The output of the amplifier at 800 nm is divided into two parts in a power ratio of 20:80 using a plate beam splitter (BS1). One of the divided beams is employed as a pump to an optical parametric amplifier (OPA, TOPAS), which generates a wide range of tunable wavelengths to produce Stokes pulse of our interest. The other part of the beam from the beam splitter (20:80) is further divided into two equal parts, with the help of a 50:50 beam splitter (BS2), amongst which one part plays the role of the pump, and the remaining part is the probe. The probe beam is delayed with respect to the pump, stokes beams, and these delays are controlled by a Newport translation stage interfaced with the ESP300 Universal motion controller.

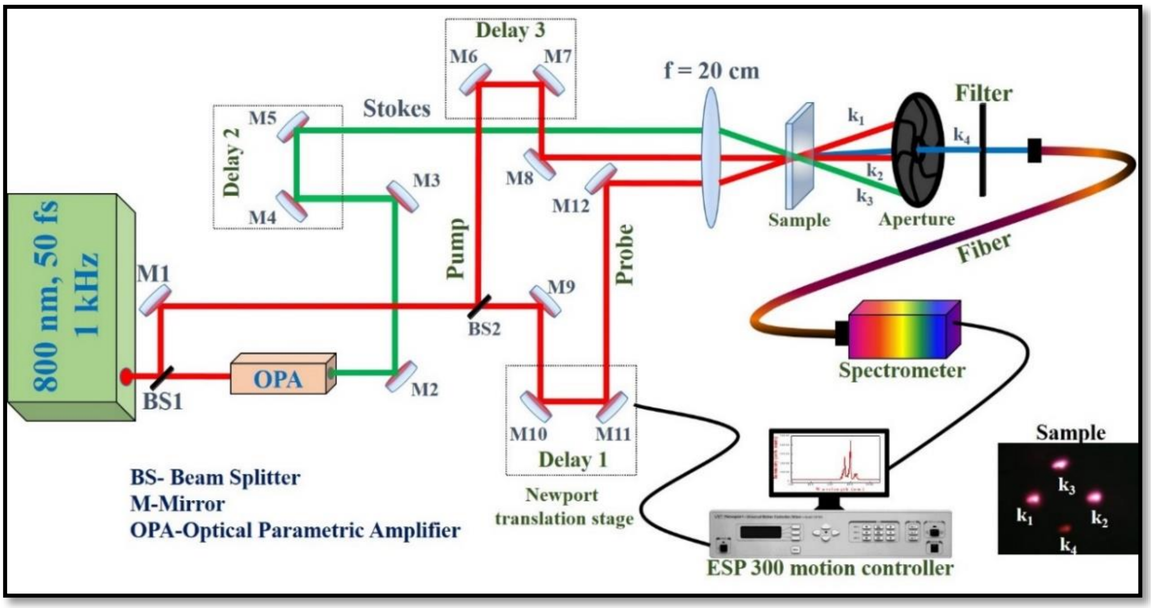

Figure 2.32 Experimental set up of femtosecond TR-CARS. Inset depicts the CARS signal recorded in BOXCARS geometry for the tetrazole sample.

The three beams (pump, Stokes, and probe) are arranged in a three-dimensional crossed beam phase matching (forward BOXCAR) configuration. The average energies of the pump, probe pulses, and the Stokes pulse from OPA are measured to be ~0.6 µJ. These three pulses are focused by a plano-convex lens of focal length ~25 cm onto a quartz cuvette (of path length ~5 mm) comprises the sample solution of our interest. Usage of a lens with longer focal length in the experiment enhances the interaction volume, and it eventually leads to a significant CARS signal generation. The wavelengths of the pump (ω_p) and probe (ω_{pr}) pulses are taken as 800 nm, whereas the wavelength of Stokes pulse from OPA is chosen to be 872 nm. Initially, the sample medium is pumped by the combination of both pump and Stokes pulses; later on, the delayed probe pulse interrogates the excited sample medium. Further, the pump and Stokes create the intramolecular coherence between the vibrational ground state and excited state that belongs to an electronic ground state. A delayed Probe pulse scatters from the transient grating formed by the excited sample medium as the CARS signal (ω_{CARS}) when the required phase-matching condition is fulfilled. TR-CARS signals by the sample at different probe delays are spatially filtered and allowed into a spectrometer (MAYA 2000, M/s Ocean Optics). The samples 6 and 8 are dissolved in acetonitrile to prepare ~1 mM solution and are taken in a 5 mm quartz cuvette and placed in the focal plane, as shown in figure 2.32.

References

1. Bridges, T.; Cheo, P., Spontaneous Self-Pulsing and Cavity Dumping in a Co2 Laser with Electro-Optic Q-Switching. *Applied Physics Letters* **1969**, *14*, 262-264.
2. Maydan, D.; Chesler, R., Q-Switching and Cavity Dumping of Nd: Yalg Lasers. *Journal of Applied Physics* **1971**, *42*, 1031-1034.
3. Paschotta, R., *Field Guide to Laser Pulse Generation*; SPIE press Bellingham, **2008**; Vol. 14.
4. Berg, N. J.; Lee, J. N. In *Acousto-Optic Signal Processing: Theory and Implementation*, New York, Marcel Dekker, Inc.(Optical Engineering. Volume 2), 1983, 496 p. No individual items are abstracted in this volume., **1983**.
5. Maldonado, T. A., Electro-Optic Modulators. *Handbook of optics* **1995**, *2*, 13.11-13.35.
6. Denker, B.; Shklovsky, E., *Handbook of Solid-State Lasers: Materials, Systems and Applications*; Elsevier, **2013**.
7. Hussain, S. A., Discovery of Several New Families of Saturable Absorbers for Ultrashort Pulsed Laser Systems. *Scientific Reports* **2019**, *9*, 1-9.
8. Weiner, A., *Ultrafast Optics*; John Wiley & Sons, **2011**; Vol. 72.
9. Brabec, T.; Spielmann, C.; Curley, P. F.; Krausz, F., Kerr Lens Mode Locking. *Optics Letters* **1992**, *17*, 1292-1294.
10. Agrawal, G. P.; Olsson, N. A., Self-Phase Modulation and Spectral Broadening of Optical Pulses in Semiconductor Laser Amplifiers. *IEEE Journal of quantum electronics* **1989**, *25*, 2297-2306.
11. Weiner, A. M., Ultrafast Optical Pulse Shaping: A Tutorial Review. *Optics Communications* **2011**, *284*, 3669-3692.
12. Fattahi, H., Regenerative Amplifiers. In *Third-Generation Femtosecond Technology*, Springer International Publishing: Cham, 2016; pp 73-86.
13. Wynne, K.; Reid, G. D.; Hochstrasser, R. M., Regenerative Amplification of 30-Fs Pulses in Ti: Sapphire at 5 Khz. *Optics letters* **1994**, *19*, 895-897.
14. Ross, I. N., Optical Parametric Amplification Techniques. In *Strong Field Laser Physics*, Brabec, T., Ed. Springer New York: New York, NY, **2009**; pp 35-59.
15. Liu, J.; Zhou, G.; Pyo, S., Parametric Gain of the Generation and the Amplification of Ultrashort Optical Pulses. *JOSA B* **1995**, *12*, 2274-2287.

16. Tatian, B., Fitting Refractive-Index Data with the Sellmeier Dispersion Formula. *Appl. Opt.* **1984**, *23*, 4477-4485.

17. Voronin, A.; Zheltikov, A., The Generalized Sellmeier Equation for Air. *Scientific reports* **2017**, *7*, 46111.

18. Raghuramaiah, M.; Sharma, A.; Naik, P.; Gupta, P.; Ganeev, R., A Second-Order Autocorrelator for Single-Shot Measurement of Femtosecond Laser Pulse Durations. *Sadhana* **2001**, *26*, 603-611.

19. Rompotis, D., A Single-Shot Nonlinear Autocorrelation Approach for Time-Resolved Physics in the Vacuum Ultraviolet Spectral Range. **2016**.

20. Sheik-Bahae, M.; Said, A. A.; Wei, T. H.; Hagan, D. J.; Van Stryland, E. W., Sensitive Measurement of Optical Nonlinearities Using a Single Beam. *IEEE Journal of Quantum Electronics* **1990**, *26*, 760-769.

21. Sheik-Bahae, M.; Said, A. A.; Van Stryland, E. W., High-Sensitivity, Single-Beam N 2 Measurements. *Optics letters* **1989**, *14*, 955-957.

22. Abrams, R. L.; Lind, R. C., Degenerate Four-Wave Mixing in Absorbing Media. *Optics letters* **1978**, *2*, 94-96.

23. Thiel, C., Four-Wave Mixing and Its Applications. *Faculty of Washington, Washington DC* **2008**.

24. Romanov, D.; Filin, A.; Compton, R.; Levis, R., Phase Matching in Femtosecond Boxcars. *Optics letters* **2007**, *32*, 3161-3163.

25. Prior, Y., Three-Dimensional Phase Matching in Four-Wave Mixing. *Appl. Opt.* **1980**, *19*, 1741_1-1743.

26. Giordmaine, J., Mixing of Light Beams in Crystals. *Physical Review Letters* **1962**, *8*, 19.

27. Eckbreth, A. C., Boxcars: Crossed-Beam Phase-Matched Cars Generation in Gases. *Applied Physics Letters* **1978**, *32*, 421-423.

28. Klug, D. R.; Rech, T.; Joseph, D. M.; Barber, J.; Durrant, J. R.; Porter, G., Primary Processes in Isolated Photosystem Ii Reaction Centres Probed by Magic Angle Transient Absorption Spectroscopy. *Chemical physics* **1995**, *194*, 433-442.

29. Berera, R.; van Grondelle, R.; Kennis, J. T., Ultrafast Transient Absorption Spectroscopy: Principles and Application to Photosynthetic Systems. *Photosynthesis research* **2009**, *101*, 105-118.

30. Lanzani, G., *The Photophysics Behind Photovoltaics and Photonics*; John Wiley & Sons, **2012**.

31. van Stokkum, I. H.; Larsen, D. S.; van Grondelle, R., Global and Target Analysis of Time-Resolved Spectra. *Biochimica et Biophysica Acta (BBA)-Bioenergetics* **2004**, *1657*, 82-104.

32. Snellenburg, J. J.; Laptenok, S. P.; Seger, R.; Mullen, K. M.; Stokkum, I. H. M. v., Glotaran: Ajava-Based Graphical User Interface for Therpackagetimp. *Journal of Statistical Software* **2012**, *49*.

33. Liu, X.; Zhang, W.; Song, Y.; Zheng, Z.; Lv, Z.; Yang, Y., Selective Excitation of Vibrational Modes and Probe for Asymmetric Intramolecular Energy Redistribution. *Physica Scripta* **2019**, *94*, 065402.

34. Wang, S.; Yang, Y.; Sun, Z.; Dlott, D. D., Fast Spectroscopy of Energy Release in Nanometric Explosives. *Chemical Physics Letters* **2003**, *368*, 189-194.

35. Namboodiri, M.; Kazemi, M. M.; Zeb Khan, T.; Materny, A.; Kiefer, J., Ultrafast Vibrational Dynamics and Energy Transfer in Imidazolium Ionic Liquids. *Journal of the American Chemical Society* **2014**, *136*, 6136-6141.

36. Zhao, Y.; Zhang, S.; Zhou, B.; Dong, Z.; Chen, D.; Zhang, Z.; Xia, Y., Spectrally Dispersed Femtosecond Cars Investigation of Vibrational Characteristics in Ethanol. *Journal of Raman Spectroscopy* **2014**, *45*, 826-829.

37. Niu, K.; Lee, S.-Y., Analysis of Time Resolved Femtosecond and Femtosecond/Picosecond Coherent Anti-Stokes Raman Spectroscopy: Application to Toluene and Rhodamine 6g. *The Journal of Chemical Physics* **2012**, *136*, 064504.

38. Wrzesinski, P. J.; Stauffer, H. U.; Kulatilaka, W. D.; Gord, J. R.; Roy, S., Time-Resolved Femtosecond Cars from 10 to 50 Bar: Collisional Sensitivity. *Journal of Raman Spectroscopy* **2013**, *44*, 1344-1348.

39. Kiefer, J.; Namboodiri, M.; Kazemi, M. M.; Materny, A., Time-Resolved Femtosecond Cars of the Ionic Liquid 1-Ethyl-3-Methylimidazolium Ethylsulfate. *Journal of Raman Spectroscopy* **2015**, *46*, 722-726.

40. Engel, S. R.; Miller, J. D.; Dedic, C. E.; Seeger, T.; Leipertz, A.; Meyer, T. R., Hybrid Femtosecond/Picosecond Coherent Anti-Stokes Raman Scattering for High-Speed Ch4/N2measurements in Binary Gas Mixtures. *Journal of Raman Spectroscopy* **2013**, *44*, 1336-1343.

41. Levitt, J. M.; Katz, O.; Silberberg, Y., Frequency-Encoded Multiplexed Cars Microscopy by Rapid Pulse Shaping. *Journal of Modern Optics* **2014**, *61*, 872-876.

42. Müller, N.; Brückner, L.; Motzkus, M., Invited Article: Coherent Raman and Mid-Ir Microscopy Using Shaped Pulses in a Single-Beam Setup. *APL Photonics* **2018**, *3*, 092406.

43. Kolesnichenko, P. V.; Tollerud, J. O.; Davis, J. A., Background-Free Time-Resolved Coherent Raman Spectroscopy (Csrs and Cars): Heterodyne Detection of Low-Energy Vibrations and Identification of Excited-State Contributions. *APL Photonics* **2019**, *4*, 056102.

Chapter 3 Ultrafast NLO Properties of Novel Perovskite Nanocrystals

Abstract

This chapter comprises the data obtained from nonlinear optical (NLO) studies of perovskite nanocrystals (CsPbBr$_3$) and zero-dimensional (0-D) perovskite (Cs$_4$PbBr$_6$) thin films achieved from colloidal nanocrystals and prepared following room temperature, open atmosphere anti-solvent precipitation method. The NLO studies were performed on the films of CsPbBr$_3$ perovskite nanocubes (NCs) and nanorods (NRs) using the Z-scan technique from 600 - 800 nm wavelength range. Large two-photon absorption cross-sections (~10^5 GM) were retrieved. Furthermore, a strong third-order NLO susceptibility (~10^{-10} esu) was observed in these films. At higher input peak intensities, a switching of the sign (both in NCs and the NRs) in the real, imaginary parts of the NLO susceptibility was observed in CsPbBr$_3$ NCs. Further, broadband NLO properties of phase pure Cs$_4$PbBr$_6$ 0-D PRM were investigated using the Z-scan and degenerate four-wave mixing (DFWM) techniques. These perovskite NCs exhibited strong multi-photon absorption properties in the near-infrared spectral regime with (a) two-photon absorption (2PA) coefficient [cross-section, σ_2 of 10^{-43}-10^{-44} cm^{4}s equivalent to ~10^6 GM] in the 500-800 nm region (b) three-photon absorption (3PA) coefficient [cross-section, σ_3 of ~10^{-73} cm^{6}s^2] in the 900-1200 nm region and (c) four-photon absorption (4PA) coefficient [cross-section, σ_4 ~10^{-100} cm^{8}s^3] in the 1300-1500 nm spectral region. These multi-photon absorption processes are explained using a simple energy/band diagram. The Cs$_4$PbBr$_6$ 0-D PRMs have demonstrated a large third order NLO susceptibility $\chi^{(3)}$ (~10^{-7} esu). The strong values of nonlinearities can possibly be attributed to the strong quantum confinement resulting from spatially isolated and exciton containing individual [PbBr$_6$]$^{4-}$ octahedron.

This chapter comprises data from the following publications:

1. **Krishnakanth, K.N.,** Seth, S., Samanta, A. and Rao, S.V., 2018. Broadband femtosecond nonlinear optical properties of CsPbBr$_3$ perovskite nanocrystals. *Optics Letters*, *43*(3), pp.603-606.
2. **Krishnakanth, K.N.,** Seth, S., Samanta, A. and Rao, S.V., 2019. Broadband ultrafast nonlinear optical studies revealing exciting multi-photon absorption coefficients in phase pure zero-dimensional Cs$_4$PbBr$_6$ perovskite films. *Nanoscale*, *11*(3), pp.945-954.

3.1 Introduction

During the last few years metal halide perovskites (MHPs) have evoked a remarkable interest resulting in a diversity of photonic[1] and opto-electronic applications such as LEDs,[2-3] lasers,[4-9] and photodetectors[10] due to their (a) broad absorption (b) tunable narrow emission united with a high photoluminescence (PL) quantum yield (QY) (c) high charge carrier mobility (d) defect tolerant behavior and (e) a reduced amount of nonradiative recombination decays.[10-13] Recently, the current technologies incorporate the MHPs into photo-detectors/amplification functionalities. The recent results suggest that there seems to be an increasing mandate of MHPs to be used in photonic technologies. Therefore, nonlinear optical (NLO) properties such as multi-photon absorption (MPA)[14-15] and saturable absorption (SA)[13, 16-17] from perovskite QDs have triggered extensive research resulting in a range of applications, for e.g. in ultrafast lasers[8,17] switching,[16] and optical data storage.[18] Among several recent literature reports, organometallic halide ($CH_3NH_3PbX_3$, where X = Br, Cl, I) perovskite NC films have been shown to possess strong third-order NLO properties ($\beta = 10^{-9}$ mW^{-1}, $n_2 = 10^{-13}$ cm^2/W) in the mid-IR spectral region.[19] A strong second harmonic generation (SHG) with type-1 phase matching along with a high laser-induced damage threshold was recently demonstrated in germanium-based hybrid perovskite materials.[20] The thickness, shape dependent optical properties of perovskite nanocrystals permit tuning the optical/NLO properties, such as two-photon absorption (2PA), SA etc. MHPs usually exhibit large 2PA cross sections, at least one or two orders of magnitude larger than traditional colloidal QDs (CdSe, CdTe).[21-22] On the other hand, all inorganic $CsPbBr_3$ perovskite NCs exhibit strong 2PA cross sections (~10^5 GM),[23,24] and stable,[25] tunable[26-27] lasing across the visible spectral regime (at room temperature) and with high-quality factors. The shape/thickness dependent variation of 2PA coefficients was also observed in the case of $CsPbBr_3$ NCs.[28] Further, organic-inorganic halide perovskites with multi-dimensional core-shell structure established superior optoelectronic and promising NLO properties such as MPA[29] and SHG.[20] A few recent reports on the MPA cross-sections of $CsPbBr_3$/$MAPbI_3$ NCs revealed 2PA cross-section values of ~10^6 GM, which are 2 orders of magnitude larger than those observed in conventional semiconductors (e.g. CdSe and CdTe) QDs. Herein we have investigated two compounds including the NLO optical properties of $CsPbBr_3$ NCs of controlled sizes and shapes [nanocubes (NCs), nanorods (NRs)] along with zero-dimensional perovskite nanomaterials. The materials were prepared using a reported method of anti-solvent precipitation at room temperature and ambient conditions.[30] All these perovskite materials are composed of metal bromide (e.g. $PbBr_6^{4-}$) octahedral units with corner shared connectivity and monovalent cations (Cs, CH_3NH_3 etc.) residing in the cuboctahedral voids. Among these, smaller NCs (size is ≤Bohr exciton diameter) fall in the quantum confinement region but their exciton binding energy is low (typically 20-50 meV) and excitons can dissociate easily at room temperature.[31] On the contrary, rhombohedral Cs_4PbBr_6 crystals are made of electronically decoupled [$PbBr_6$] octahedral units and cesium ions bridge between them.[32-34] Since, photo-excitation generates excitons in [$PbBr_6$] units, excitons are in essence confined within the individual octahedron and feature a higher binding energy.[32, 35-36] Considering the structure and electronic confinement in all three dimensions, this material is often termed as 0-dimensional perovskite-related material (0-D PRM).[36-38] The optical properties of Cs_4PbBr_6 are highly controversial and based on absence/presence of PL. This material is categorized into two forms, viz. non-fluorescent and fluorescent.[32,36-37,39] Apart from few reports in LEDs[40] and photo-detector applications[41] the use of Cs_4PbBr_6 material of both the forms is basically unexplored. Here, we have investigated a broad range of NLO studies of Cs_4PbBr_6 0-D PRM using femtosecond (fs) Z-scan and the DFWM techniques. Strong multi-photon absorption cross-sections (σ_2, σ_3, and σ_4) were observed in the near-infrared (NIR) spectral regime when compared to $CsPbBr_3$ perovskite nanocrystals (NCs). Ultrafast dephasing times were also obtained using the fs-DFWM technique in the Boxcar phase-matching geometry.[42] Non-fluorescent Cs_4PbBr_6 0-D PRM NCs demonstrated a faster response (~81 fs) compared to fluorescent (92 fs) NCs with investigations performed in the colloidal form. These strong NLO coefficients in conjunction with ultrafast response times are qualifications for any material to be used in photonic device applications.

3.2 Experimental Details

Synthesis of Cs_4PbBr_6 nanocrystals: For the synthesis of Cs_4PbBr_6 NCs, we have employed two different and popular methods i.e. for non-luminescent hot injection and for luminescent anti-solvent precipitation techniques.

Chemicals required: Octadecene (ODE, 90%, Aldrich), Cs_2CO_3 (99.9%, Aldrich), oleylamine (OLA, 70%, Aldrich), oleic acid (OA, 90%, Aldrich), hydrobromic acid (48%

in water, 99.99%, Aldrich), $PbBr_2$ (99.999%, Aldrich), dimethyl formamide (AR grade, Fisher Scientific), toluene and hexane were purchased from Finar and distilled following standard procedure. Preparation of Cs-Oleate: 0.5625 gm Cesium carbonate and 5.4 mL oleic acid was taken in a 100 mL double necked flask and degassed for one hour at 130 °C. Temperature was raised to150 °C to prepare yellowish Cs-oleate.

Non-fluorescent Cs_4PbBr_6 NCs: 0.04 gm of $PbBr_2$, 0.2 mL oleic acid, 5 mL octadecene and 1.5 mL oleylamine were mixed in a 100 mL double necked flask at 130 °C under vacuum until the solution becomes clear. The temperature of the solution was decreased to 80 °C and 0.36 mL of Cs-oleate solution was added quickly. The solution become turbid indicating the formation of nanocrystals (after 30 seconds). After the solution was quickly cooled down under water stream and centrifuged. The solid was washed with toluene repeatedly and finally dissolved in toluene for measurements.

Fluorescent Cs_4PbBr_6 NCs: 0.011 gm of $PbBr_2$ was dissolved in 1 mL of DMF solvent followed by addition of 20 μL of HBr, 0.05 mL of oleylamine and 0.1 mL of oleic acid. In a 50 mL of round bottom flask 5 mL oleic acid, 10 mL hexane and 0.2 mL of as-prepared Cs-oleate solution were added. Previously made $PbBr_2$ solution was quickly added to the RB in vigorous stirring condition. The solution immediately turned greenish white. Then it was centrifuged and purified for further spectroscopic use.

For the Z-scan measurements thin film of the NCs were prepared by drop casting the individual NC solutions and drying under vacuum. The experimental details of degenerate four-wave mixing and Z-scan techniques were discussed in chapter 2.

3.3 Results and Discussion

3.3.1 $CsPbBr_3$ NCs:

The UV-visible absorption spectrum provided the first absorption onset of NCs at 498 nm and in NRs near 510 nm. The sizes of the NCs and NRs, estimated from TEM images, were ~12±2 nm and 80±10 nm (diameter). The HR-TEM images [figure 3.1(b) and (e)] with clear lattice fringes indicate high crystallinity of the material. Complete details of characterization of these nanomaterials were summarized in an earlier work.[30] The NCs/NRs films were prepared by dropcasting the respective colloidal solution on a glass subtrate and subsequently permitting the solvent evaporation at room temperature under high vaccum [insets of figure

3.1(c) and 3.1(f)]. The thickness of the prepared films, measured using AFM, were estimated to be ~35 nm in the NCs case and ~200 nm in the NRs case. The length of the NRs was in the range of 0.5-2 μm. The absorbance (which was typically <0.1) was measured for these films at wavelengths of 600 nm, 700 nm, and 800 nm and the corresponding thickness and absorption coefficients were used for the Z-scan data analysis. The incident laser pulses were focused with a 15 cm lens and the beam waists ($2\omega_0$ at focus) were in the range of 60-70 μm. The input beam diameter was 2.5-4 mm (it changes depending on the wavelength) resulting in a slightly different Rayleigh range (Z_R) for different scans. The thickness of the samples was much less than Z_R, which satisfies the thin sample limit. The 800 nm beam was from the amplifier and has a large diameter compared to the 600 nm/700 nm beam. Therefore, this resulted in a smaller Rayleigh range in this case. Typical input energies of <0.1 μJ were used and their corresponding input peak intensities were estimated to be in the range of 20 to 30 GW/cm^2. The Z-scan measurements at 600 nm were also performed at higher peak intensities (~400 GW/cm^2). The open and closed aperture Z-scan measurements were performed at three different wavelengths of (a) 600 nm (b) 700 nm and (c) 800 nm. The transmitted light in the Z-scan experiments was collected using a photodiode (Thorlabs SM1PD2A, DEC10L/M), which was connected to a lock-in amplifier (signal recovery 7265). A motorized delay stage was used to control the sample movement along the Z-axis and all the components were synchronized using a computer based LabView program. Figure 3.2 illustrates the Z-scan results of both NCs and NRs recorded at 600 nm, 700 nm, and 800 nm. The peak intensities were estimated to be in the 20-30 GW/cm^2 range. The data obtained clearly indicate reverse saturable absorption type of behavior in both the cases and for all wavelengths investigated. The data was fitted for extracting the 2PA coefficient. The magnitudes of 2PA cross-sections were in the range of 10^4-10^5 GM. We have ensured that the contribution from the glass substrate is considered while evaluating these coefficients and found that the glass slide did not show any nonlinearity at the peak intensities used. Closed aperture Z-scan measurements [data shown in figures 3.2 (b), 2(d), 2(f), 2(h), 2(j), 2(l)] revealed the signature to be of peak-valley category suggesting the occurrence of negative nonlinearities ($n_2<0$) at all investigated wavelengths. The magnitude of n_2 was estimated to be $0.1\text{-}29\times10^{-13}$ cm^2/W at the wavelengths studied. The nonlinearity from n_2 with femtosecond excitation is attributed mainly to the bound charge carriers in such materials.[43] Table 3.1 summarizes the magnitudes of obtained 2PA cross-sections and table 3.2 reviews all the NLO coefficients achieved (for both NCs and NRs) in this study. It is evident that the

NLO coefficients of NCs were superior than those of the NRs at each wavelength. However, the n_2 [and therefore the $\chi^{(3)}$] value of the NRs at 800 nm was higher when equated to the NCs. The magnitude of $\chi^{(3)}$ was estimated to be ~10^{10} esu.

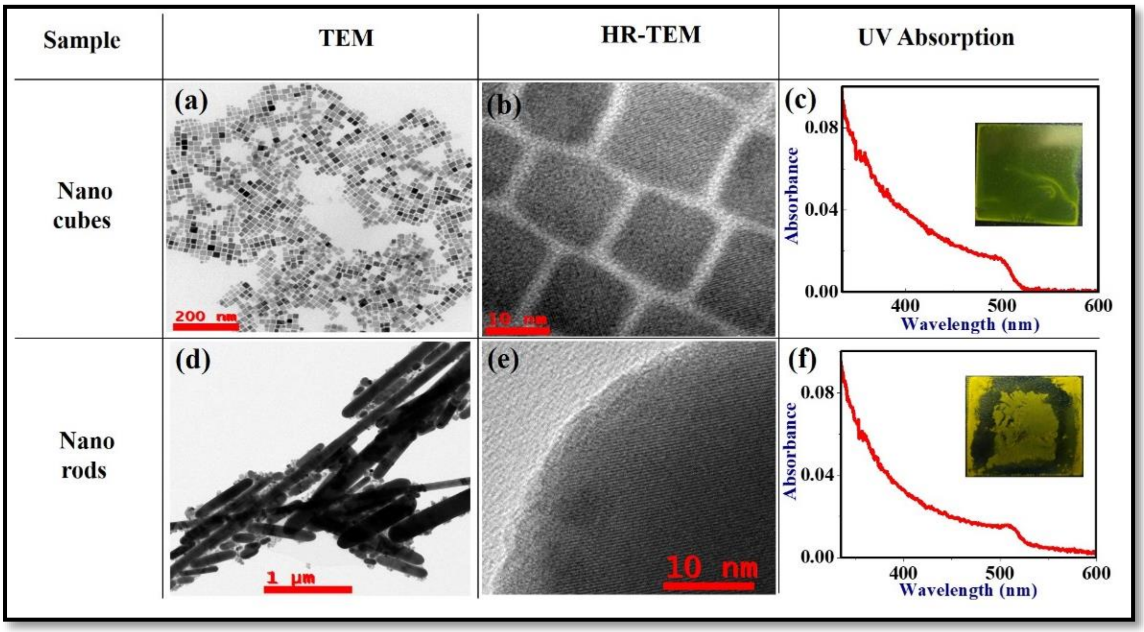

Figure 3.1 (a, d) TEM images of the nanocubes (12±2 nm) and nanorods (~80±10 nm diameter) (b, e) High-resolution TEM images of NCs and NRs (c, f) UV-visible absorption spectra of NCs and NRs. Insets depict the thin films of both compounds on a glass slide.

The large nonlinearity observed in NCs could be partially attributed to the edges (which apparently are not available in the case of NRs) where the electric field could be localized leading to large enhancements. The errors in these measurements and, hence, the NLO coefficients presented in this work arise mainly from the (a) estimation of peak intensity (b) input laser fluctuations and (b) fitting errors. The scattering was minimal in the nonlinear absorption measurements (OA Z-scan). Figures 3.3 (a)-3(d) illustrate the OA and CA Z-scan data recorded at 600 nm, but with a higher peak intensity of 400 GW/cm^2. All the samples were found to be stable at these peak intensities. This was confirmed by repeating the Z-scan measurements multiple times and over a period of thirty days. A further increase in the input peak intensities resulted in the formation of a Supercontinuum, which is detrimental for the Z-scan studies. The perovskite films of both NCs and NRs fascinatingly depicted saturable absorption (SA) behavior with a saturation intensity, I_s of ~5×10^{11} W/cm^2 in the case of NCs while an I_s of ~9.5×10^{10} W/cm^2 was obtained in the case of NRs. The peak intensity where the transition from RSA to SA occurred was estimated to be ~200 GW/cm^2.

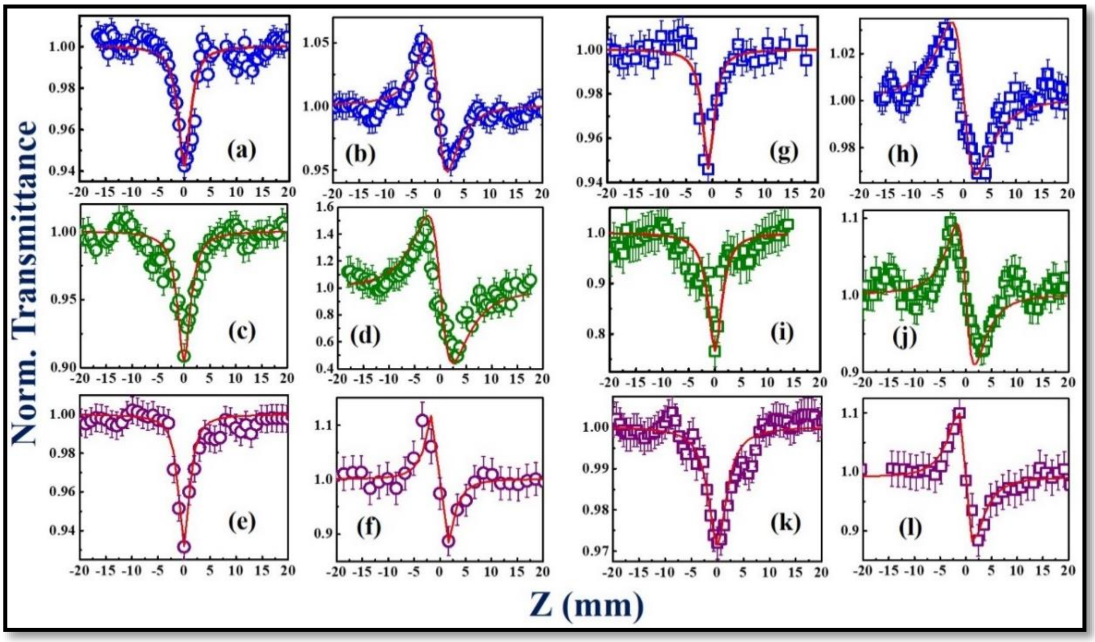

Figure 3.2 (a), (b) Open, closed aperture Z-scan traces of NCs at 600 nm (c), (d) Open, closed aperture Z-scan traces of NCs at 700 nm (e), (f) Open, closed aperture Z-scan traces of NCs at 800 nm (g), (h) Open, closed aperture Z-scan traces of NRs at 600 nm (i), (j) Open, closed aperture Z-scan traces of NRs at 700 nm (k), (l) Open, closed aperture Z-scan traces of NRs at 800 nm. Open symbols are experimental data points while the solid lines are theoretical fits.

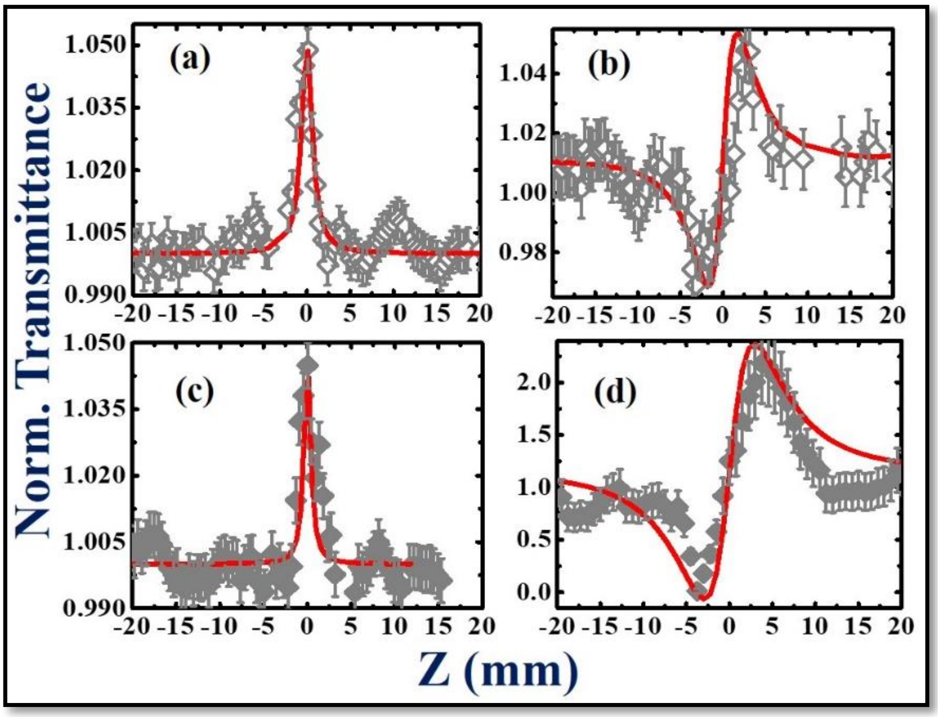

Figure 3.3 (a), (b) Open, closed aperture Z-scan data of the NCs film at 600 nm using a peak intensity of ~400 GW/cm^2 (c), (d) Open, closed aperture Z-scan data of the NRs film at 600 nm using a peak intensity of 400 GW/cm^2. Open symbols are experimental data points while the solid lines are theoretical fits.

There are a few reports in literature on the NLO studies of perovskite colloidal solutions and thin films with different morphologies, input wavelengths and pulse durations.[14, 22-23, 28, 43] The NLO coefficients obtained from the present study was compared with those and we observed ours are on par with those reported recently. Particularly, the n_2 values are barely reported and our n_2 values are superior to others. Chen et al.[44] have recently reported the size dependence (mean sizes of 4.6-11.4 nm) of the 2PA cross-sections in $CsPbBr_3$ perovskite quantum dots (QDs) and achieved a maximum $\sigma^{(2)}$ value of $1.8\pm0.1\times10^5$ GM for 9.4 nm sized QDs. They reported an increase in the $\sigma^{(2)}$ value by an order of magnitude once the QDs size changed from 5 nm to 12 nm. Compared to this, the value obtained in our case was 9.8×10^5 GM at 800 nm for 12±2 nm sized NCs, which is consistent with the data/analysis of Chen et al..[44] However, the wavelength dependent studies reported by them suggested an enhancement of ~2 times (600/700 nm when compared to 800 nm while in the present case we observed ~7 times higher $\sigma^{(2)}$ value at 800 nm when compared to 600 nm. Chen et al.[44] clearly suggested that the estimation of $\sigma^{(1)}$ is detrimental for achieving the accurate values of $\sigma^{(2)}$. Any uncertainty in the estimation of $\sigma^{(1)}$ will lead to errors in the estimation of $\sigma^{(2)}$. In their case they obtained those from femtosecond transient absorption measurements. Furthermore, their studies employed longer laser pulses (>120 fs) whereas in the present case we used ~70 fs laser pulses. Further detailed transient absorption studies will help us elucidate the different behavior observed in the present case. 2PA cross-sections mentioned here are estimated using the concentration of the solutions used for preparing the thin films. Nevertheless, there could be minor differences between the exact nanoparticle concentration in the films and the solution values used here, in which case the 2PA cross-sections will be slightly over-estimated. Interestingly, some of our NLO coefficients match well with those reported earlier.[44]

Lu et al.[45] compared the NLO coefficients of QDs of $CsPbBr_3$ and $CH_3NH_3PbBr_3$ using MHz, 130 fs pulses using the Z-scan technique. They obtained 2PA coefficients of 10^{-9} cm/W and n_2 of $2\text{-}5\times10^{-13}$ cm/W^2. However, their measurements were performed with 76 MHz pulses and thermal effects predominantly contribute to the nonlinearities resulting in enhanced values. For the peak intensities used in their studies they observed SA at 800 nm. Liu et al.[26] obtained lower values of β and n_2 for $CsPbX_3$ perovskite nanocrystals (15-29 nm sizes) compared to ours while using 396 fs pulses at 787 nm and 1 kHz repetition rate. Wang et al.[23] reported σ_2 value of ~1.2×10^5 GM for the 9 nm-sized $CsPbBr_3$ nanocrystals at 800 nm using 100 fs, 1 kHz pulses. This value is comparable to that obtained in this study. Li and co-workers[46] reported the magnitude of σ_2 to be 2.8×10^6 GM for $CsPb(I/Br)_3$ quantum dots obtained with 1030 nm excitation and longer pulses of 340 fs. Further, the sign of n_2 changed from negative to positive type and the magnitude also increased by an order. The CA Z-scan data for obtaining n_2 depicted peak-valley for all wavelengths at low pump intensities (self-defocusing phenomenon). The value of $\Delta\phi$ was ensured to be $<\pi$ in both the cases. At higher pump intensities at 600 nm self-focusing was observed and the nonlinear susceptibility is dominated by refractive index n_2 from indirect two photon optical transition. Liu et al.[14] reported SA in $(PEA)_2PbI_4$ along with 2PA saturation. They argue that due to confinement effects they expect enhanced light-matter interaction (e.g. strong exciton-phonon coupling). Such carrier confinement can lead to enhanced nonlinearities. Further, the shape effects of the NCs and the NRs also assist in the enhancement of the nonlinearity. Li et al.[17] also reported SA in CsPbBr3 perovskite quantum dots with 343 fs pulse excitation at 515 nm.

Wavelength (nm)	**Nano-cubes (σ_2)**	**Nano-rods (σ_2)**
600	2.1×10^4 GM	0.3×10^4 GM
700	3.4×10^4 GM	0.2×10^4 GM
800	9.8×10^5 GM	0.2×10^4 GM

Table 3.1 2PA cross section values at peak intensities of 20-30 GW/cm^2.

Low intensity					**High intensity**		
Sample	**n_2 (10^{-13} cm^2/W)**	**β (10^{-11}cm/W)**	**$\chi^{(3)}$ (10^{-10}esu)**	**σ_{TPA} (10^4GM)**	**n_2 (10^{-13} cm^2/W)**	**$\chi^{(3)}$ (10^{-8}esu)**	**λ**
NCs	-1.8	180	4.3	98	-	-	800 nm
NRs	-29	0.71	9.5	0.2	-	-	
NCs	-12	7.20	3.0	3.4	-	-	700 nm
NRs	-0.3	0.50	6.7	0.2	-	-	
NCs	-0.8	3.80	2.0	2.1	8.0	15.1	600 nm
NRs	-0.1	0.50	0.5	0.3	6.5	12.2	

Table 3.2 Summary of the third order nonlinear optical parameters measured at low ($2.0\text{-}3.0\times10^{10}$ W/cm^2) and high ($\sim40\times10^{10}$ W/cm^2) peak intensities.

The switch over from RSA to SA can be partly attributed to the saturation of 2PA (ground state bleaching) or trapping of the carriers in gap-states.[47] Further detailed studies are essential and will be performed in future to elucidate this transition behavior.

In summary, the NLO properties of an ambient condition synthesized colloidal $CsPbBr_3$ perovskite NCs and NRs were measured using the Z-scan technique with fs pulses. A notable change in the refractive index is observed, at higher intensities 7.3×10^{10} W/cm^2, an increase in the refractive index with a saturated absorption is apparent. The NCs demonstrated a strong nonlinear absorption coefficient of 0.1 cm/GW (at 2.4×10^{10} W/cm^2). Large 2PA cross-sections are reported which are comparable to those reported in reference [7] and in table 3.3. It is observed that $CsPbBr_3$ NCs and NRs depict a size and thickness dependent nonlinear optical properties with increasing saturation intensity at high peak intensities. The strong nonlinear absorption and switching properties of these open atmospheric prepared, cost-effective $CsPbX_3$ perovskite NCs indicate a very high potential as a futuristic material for applications such as in (a) light harvesting (b) MIR nonlinear absorbers and (c) all-optical communications.[19, 48] Such applications mainly arise because of their (i) high charge carrier mobility (ii) broad absorption (iii) narrow, tunable emission with high PL QY and (iv) long diffusion lengths.

Ref.	Perovskite	β (cm/W)	n_2 (cm^2/W)	σ_{TPA} (GM)
7	(NCs) $CsPbBr_3$	—	—	2.7×10^6
23	(NCs) $CsPbBr_3$	9.7×10^{-11}	—	1.2×10^5
49	(QDs) $CsPbBr_3$	8.5×10^{-11}	—	—
45	(QDs) $CsPbBr_3$	10^{-9}	$2\text{-}5\times10^{-13}$	—
44	(QDs) $CsPbBr_3$	—	—	$4 - 1.8\times10^5$ (670 - 800 nm)
28	(NSs) $CsPbBr_3$	$4.7\text{-}11\times10^{-9}$	—	—
26	(NCs) $CsPbCl_3$	1.4×10^{-11}	5.3×10^{-15}	—
	(NCs) $CsPbI_3$	1.5×10^{-11}	6.8×10^{-15}	—
	(NCs) $CsPbBr_3$	3.2×10^{-11}	4.7×10^{-15}	—
46	(QDs) $CsPbBr_3$	—	—	2.8×10^6 (1080 nm)

Table 3.3 Summary of the NLO coefficients of various perovskite NCs reported recently in literature.

3.3.2 Cs_4PbBr_6 Nanocrystals:

Figures 3.4(a) and 4(b) illustrate the TEM images of the as-synthesized NCs, which depict an average size of 10.5±1 nm and 20±3 nm for non-fluorescent and fluorescent cases, respectively. Non-fluorescent Cs_4PbBr_6 NCs demonstrated a sharp absorption peak near 310 nm [Figure 3.4(c)] indicating a band gap of ~4 eV. Fluorescent Cs_4PbBr_6 NCs also demonstrated a similar, intense peak near 310 nm combined with a long tail up to 500 nm and the emission peak appeared near 505 nm. Even though the origin of PL in this material is controversial, it has been proved very recently that arises due to sub-band gap trap states mediated radiative recombination.[36-38] The NLO properties were measured over a wide range of wavelengths in the visible and NIR (500 nm-1500 nm) using the fs Z-scan technique. The experiments were performed on thin films prepared by drop casting the colloidal solution onto a glass coverslip and subsequently dried under high vacuum. The thickness of the films, achieved using atomic force microscopy, was estimated to be ~40 nm in the fluorescent and ~20 nm in the non-fluorescent cases (see figure 3.5 for the data obtained).

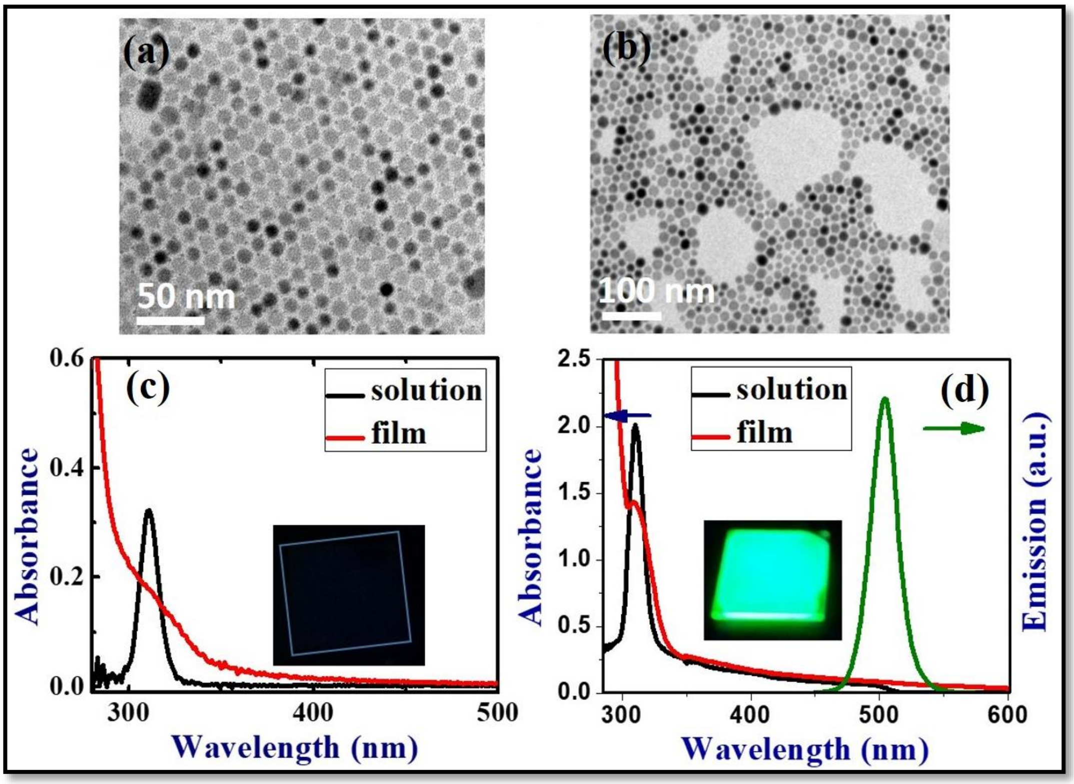

Figure 3.4 TEM images of (a) non-fluorescent (b) fluorescent Cs_4PbBr_6 NCs. (c) Absorption spectrum of non-fluorescent NCs. (d) Absorption and emission spectra of fluorescent NCs. Insets of (c) and (d) show the pictures of thin films of the corresponding samples under UV light irradiation (365 nm).

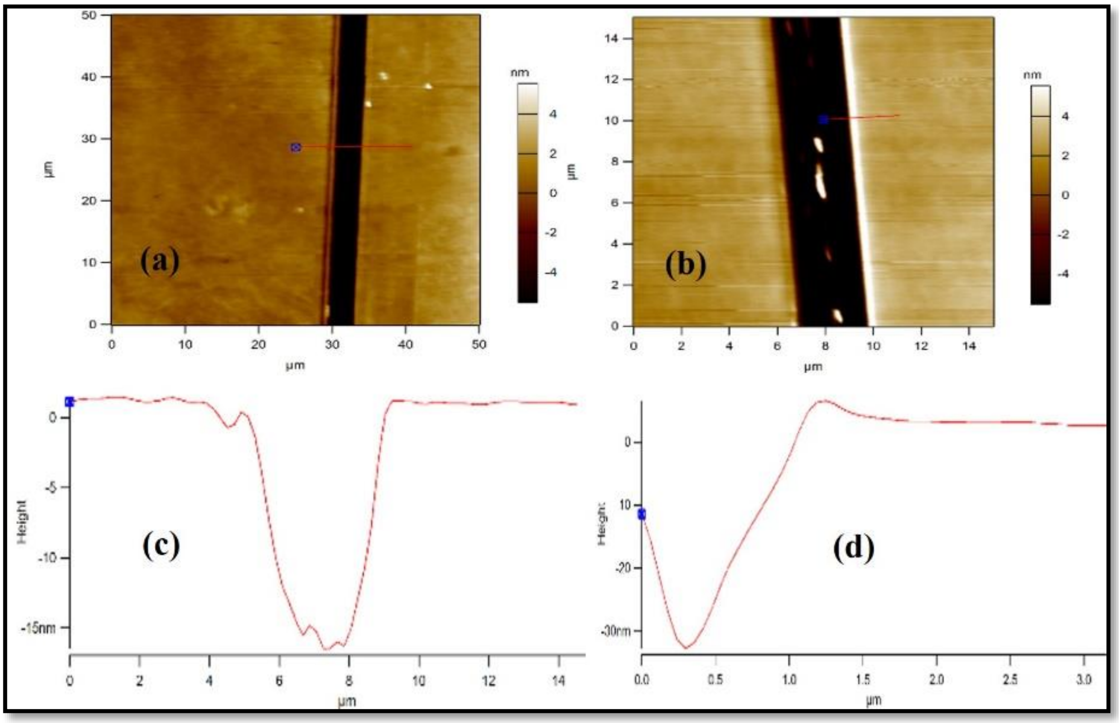

Figure 3.5 AFM data of non-fluorescent (20 nm) (a) and fluorescent (40 nm) (b) thin films.

The third-order nonlinear optical susceptibility [$\chi^{(3)}$] was measured from the real (related to the nonlinear refractive index, n_2) and imaginary (related to the nonlinear absorption coefficient, β) parts using the relations[50]

$$Re\chi^{(3)} = 2cn_0^2\varepsilon_0 n_2 \tag{1}$$

$$Im\chi^{(3)} = \frac{c^2\varepsilon_0 n_0^2\beta}{\omega} \tag{2}$$

where ω is the angular frequency of the laser beam, and ε_0, n_0 are the vacuum permittivity and linear refractive index. From the OA and CA data the NLO coefficients n_2 and β were obtained in Cs_4PbBr_6 thin films. The nonlinear transmission curves in OA and CA case were fitted using the equations 3 and 4, respectively.

$$T_{OA(nPA)} = \frac{1}{\left[1+(n-1)\beta_n L\left(\frac{I_0}{1+\left(\frac{Z}{Z_0}\right)^2}\right)^{n-1}\right]^{1/n-1}} \tag{3}$$

$$T_{CA} = 1 \pm \frac{4\Delta\phi\left(\frac{Z}{Z_0}\right)}{\left[\left(\frac{Z}{Z_0}\right)^2+9\right]\left[\left(\frac{Z}{Z_0}\right)^2+1\right]} \tag{4}$$

where L is the effective path length in the sample for tow photon absorption (2PA), three-photon absorption (3PA) and four-photon absorption (4PA) are given as

$$L_{eff} = 1 - e^{-\alpha_0 L}/\alpha_0\ ,\ L'_{eff} = 1 - e^{-2\alpha_0 L}/2\alpha_0\ ,\ L''_{eff} = 1 - e^{-3\alpha_0 L}/3\alpha_0$$

Wherein Z is the sample position, Z_0 is the Rayleigh range $Z_0 = \pi\omega_0^2/\lambda$, ω_0 is the beam waist at the focus (Z=0), I_0 is the input peak intensity. The multi-photon absorption cross-sections were obtained using the relation $\sigma_n = \frac{(\hbar\omega)^{n-1}}{N}\beta_n$, where N is the concentration of the NCs, ω is the frequency of the laser radiation. We have confirmed that the contribution from the glass substrate to the nonlinear absorption (at these peak intensities) was negligible. This was accomplished by performing the Z-scans of the glass coverslip alone and the data obtained evidently established that glass coverslip did not show any optical nonlinearity. The OA Z-scan data, illustrated in figure 3.6, was recorded for the wavelengths of 500-800 nm while the CA data is presented for the 500-900 nm range. Similarly, figure 3.7 shows the OA and CA data for 900 nm, 1100 nm, and 1200 nm. It is apparent from the data that both the films exhibited RSA behavior. This data was obtained at input peak intensities of 20-70 GW/cm^2. A strong 2PA coefficient (~10^{-8} cm/W) was retrieved from the fits to the data in the 500-800 nm spectral region. The corresponding 2PA cross-sections obtained were in the range of 10^6-10^7 GM [see tables 3.4, 3.5 for a summary of all the NLO coefficients obtained]. The obtained 2PA coefficients and cross sections are relatively stronger than some of the earlier reports[6, 16, 25, 44-45, 51-52] on perovskite NCs.

The 2PA cross sections obtained here followed the wavelength dependence as discussed by Chen et al.[44] in their work on $CsPbBr_3$. The quantum confinement arising from the isolated $PbBr_6$ octahedral could increase the local charge fields and the presence of sub-gap states generally enhances the multi-photon absorption processes. These 0-D PRM NCs exhibited strong three and four-photon absorption at NIR excitation wavelengths. From the Z-scan data presented in figure 3.9, the OA data clearly depicts a 3PA process in the 900-1200 nm spectral range and the cross-sections obtained were ~10^{-73} cm^{6}s^2. The obtained cross-sections values from phase pure Cs_4PbBr_6 0D-PRMs are higher than the $CsPbBr_3$ or $MAPbBr_3$ QDs[29] reported earlier. From the Z-scan data presented in figure 3.10, it is evident that at higher wavelengths (1300-1500 nm) four-photon absorption (4PA) process was responsible for the nonlinear absorption observed. A strong 4PA coefficient at wavelengths of 1300 nm, 1400 nm and 1500 nm with corresponding 4PA cross-sections of ~10^{-100} cm^{8}s^3 is observed. The MPA coefficients obtained for the Cs_4PbBr_6 NCs are higher compared to conventional perovskite NCs and can possibly be attributed to the strong exciton confinement in the isolated $PbBr_6$ octahedral units strengthening the light matter interactions. A relatively strong nonlinear absorption (order of magnitude higher coefficients) is observed for non-fluorescent NCs compared to the fluorescent ones. Tables 3.4 and 3.5 summarize the NLO coefficients and cross-sections of both the NCs films.

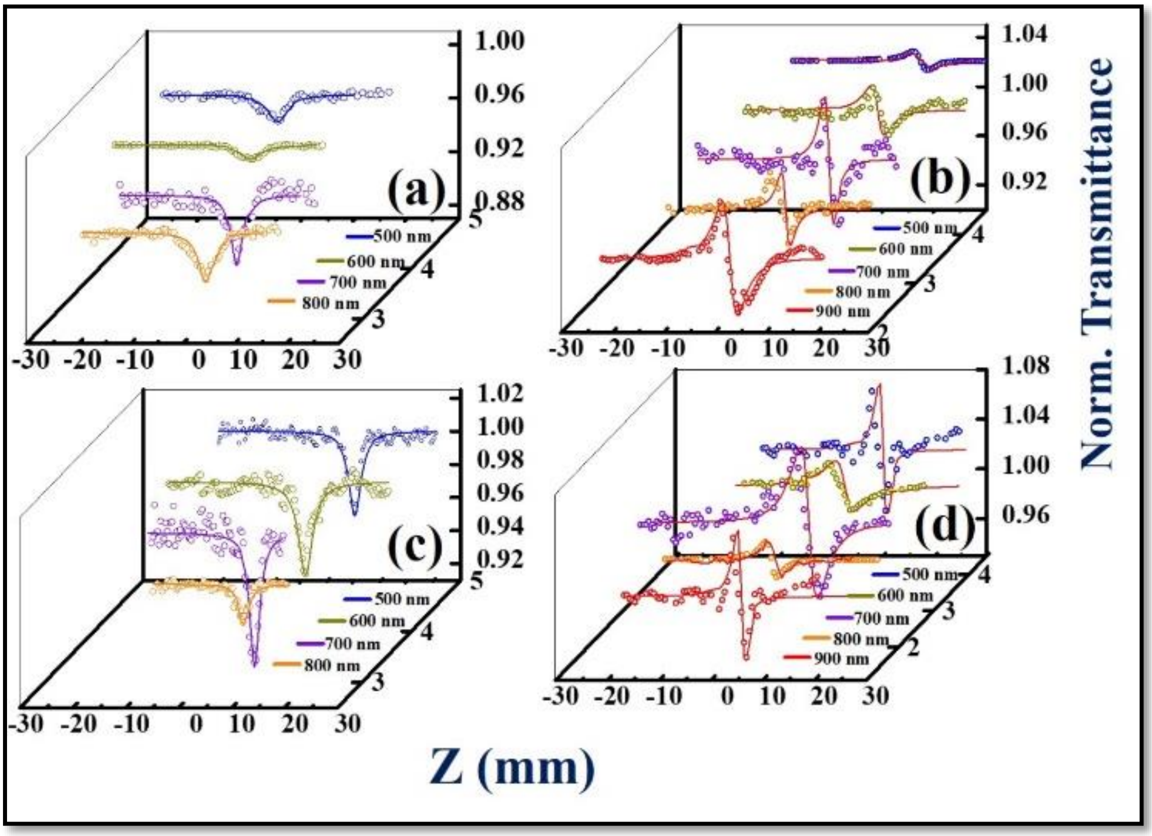

Figure 3.6 OA and CA Z-scan data of 0-D PRM in the 500-900 nm spectral region. OA and CA data of (a), (b) fluorescent and (c), (d) non-fluorescent Cs_4PbBr_6 NCs thin films. Open circles are the experimental data points while the solid lines represent the theoretical fits. OA data fitted well with 2PA equation.

The CA Z-scan measurements performed in the wavelength range of 500 nm-900 nm revealed a self-defocusing effect ($n_2 < 0$) from both the films, as illustrated in figures 3.6(b) and 6(d). The magnitude of n_2 was obtained by fitting the CA Z-scan data using equation (4) and the obtained values of n_2 were found to be ~10^{-9} cm^2/W, which are larger than many of the earlier reports on perovskite NCs.[19, 45, 52-53]

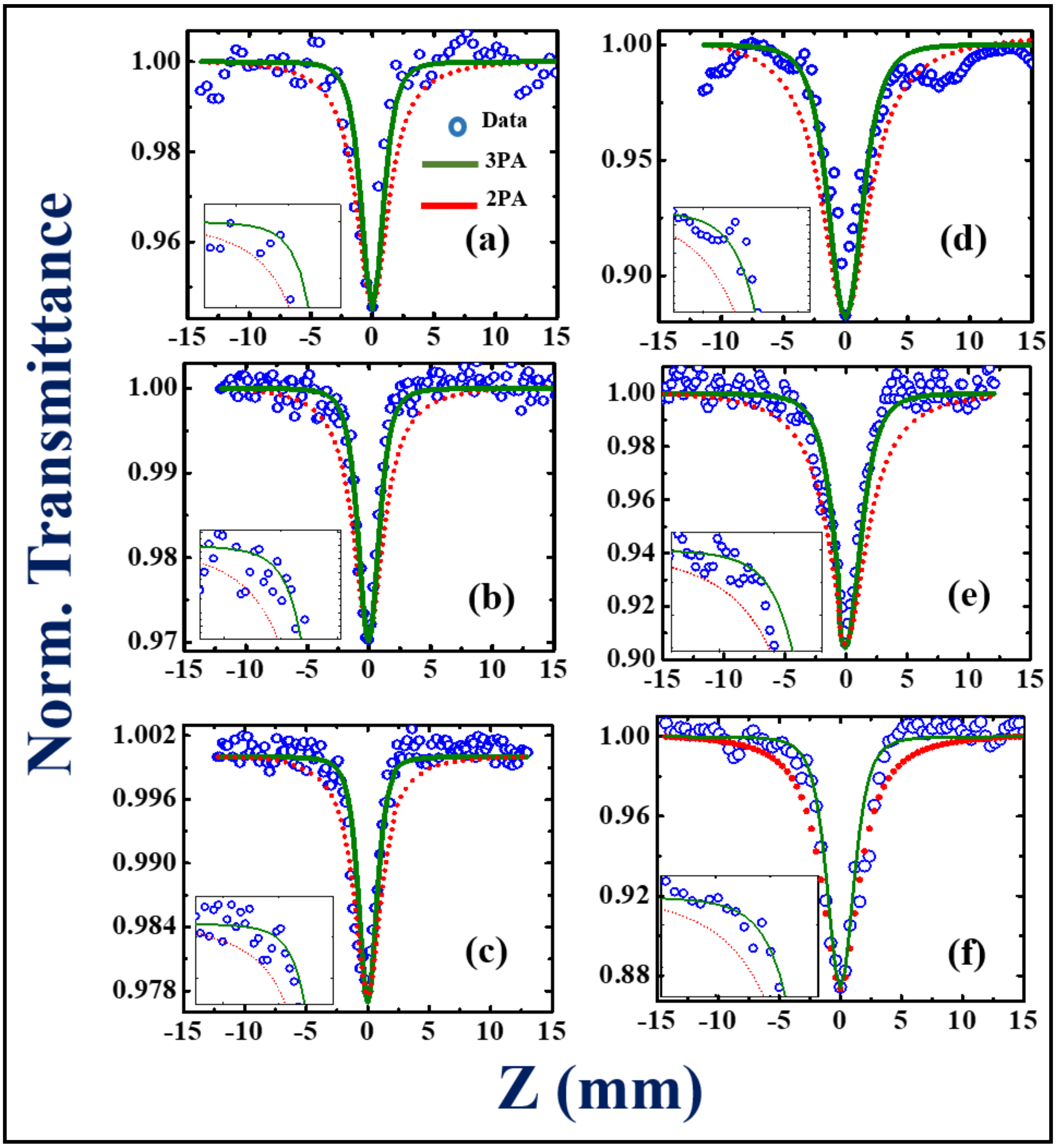

Figure 3.7 OA ZS data depicting 3PA in fluorescent (a,b,c) and non-fluorescent (d,e,f) Cs_4PbBr_6 NCs. 900 nm, 1100 nm and 1200 nm data are shown in(a,d), (b,e) and (c,f), respectively. Open circles are the experimental data points and solid lines represent the theoretical fits. Both 3PA (olive green colour, top solid curves) and 2PA (red colour, bottom dotted curves) fits are shown. Insets of each graph clearly show the difference between both the fits.

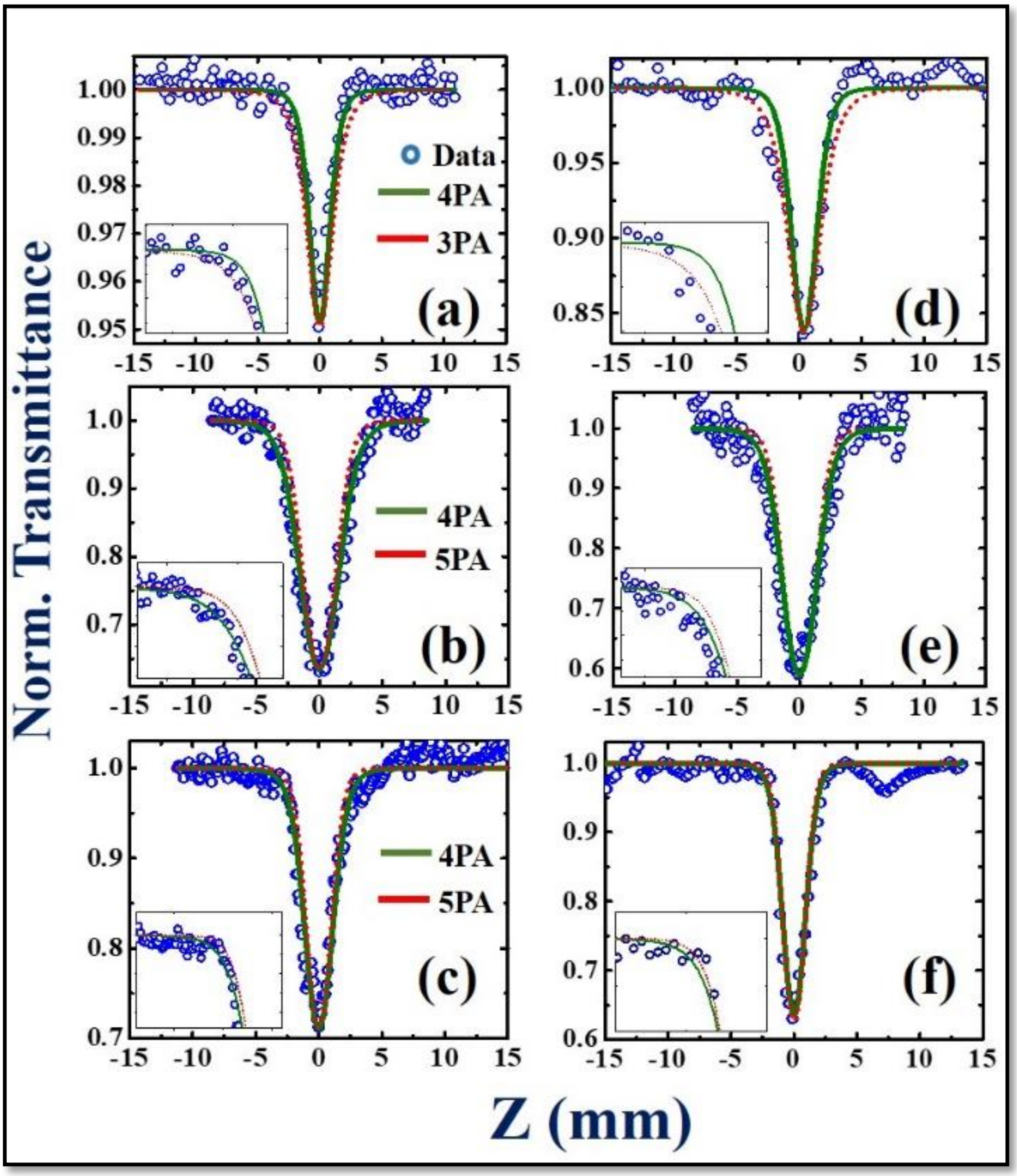

Figure 3.8 OA Z-scan data and theoretically fitted curves of (a) fluorescent (d) non-fluorescent NC films at 1300 nm, (b) fluorescent (e) non-fluorescent NC films at 1400 nm and (c) fluorescent (f) non-fluorescent NC films at 1500 nm. Open circles are the experimental data points while the solid lines are the fits. Both 4PA (olive green colour, solid curves) and 3PA (red colour, dotted curves) fits are shown in (a) and (b). Best fits were obtained for 4PA. Both 4PA (olive green colour, solid curves) and 5PA (red colour, dotted curves) fits are shown in (b), (c), (e) and (f). The best fits were obtained again for 4PA in these cases also.

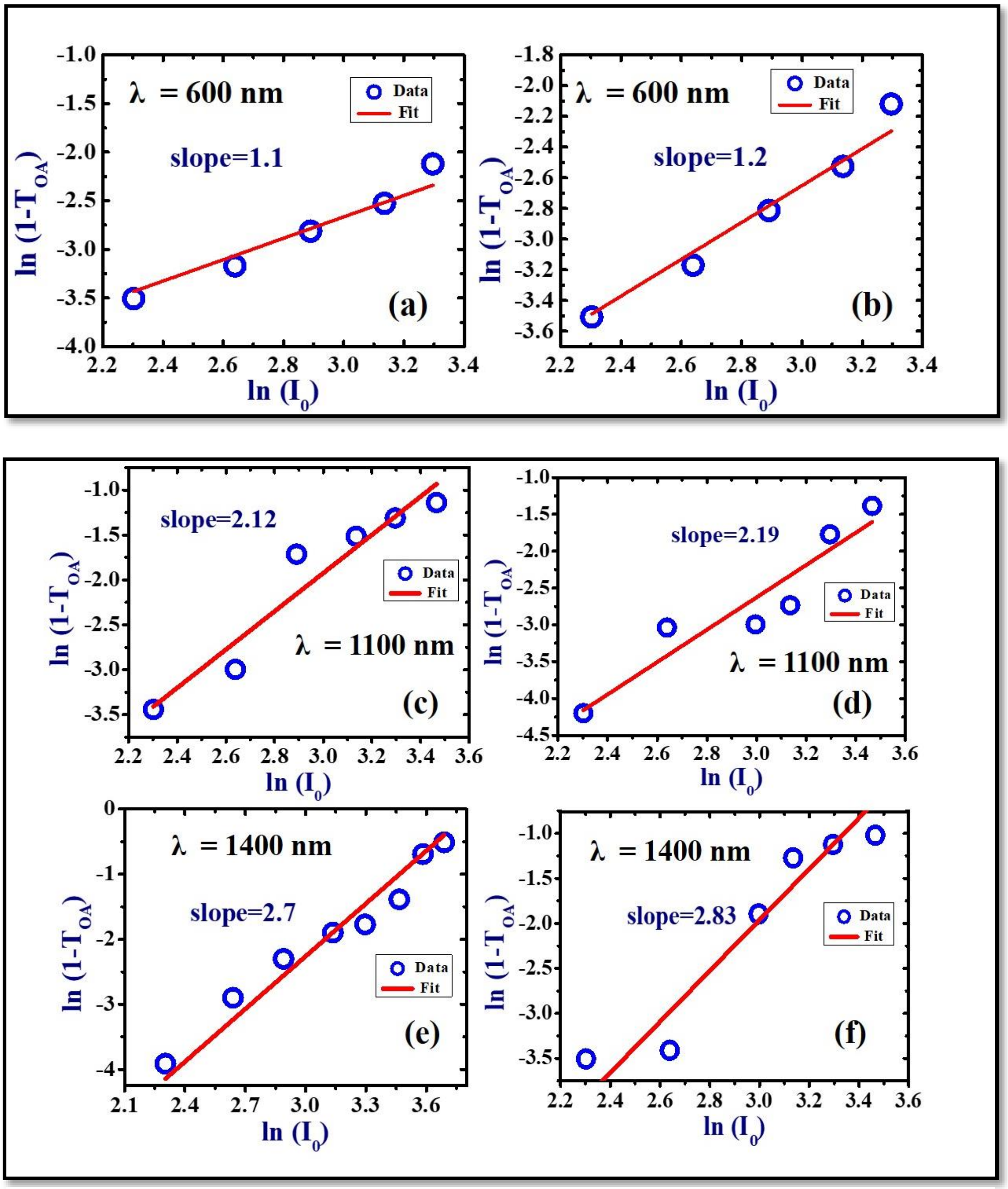

Figure 3.9 Intensity dependent plots of 2PA, 3PA and 4PA processes of (b,d.f) non-fluorescent and (a,c,e) fluorescent NCs of 0D-PRM measured at 600 nm,1100 nm and 1400 nm.

To confirm that the observed nonlinear absorption processes were indeed 2PA/3PA/4PA we performed detailed, intensity-dependent nonlinear transmission studies (see data presented in figure 3.9). For the spectral range of 500 nm-800 nm the plot of ln(I_0) versus ln(1-T_{OA}) yielded a slope close to 1 clearly suggesting the presence of 2PA.[29] For the data recorded in the spectral region of 900-1200 nm the slope was found to be close to 2, clearly suggesting the existence of 3PA process. Similarly, for the case of data obtained in 1300-1500 nm spectral range the slope was close to 3, suggesting the presence of a 4PA process.[29]

Figures 3.10(a), 10(b) depict the 4PA processes of the non-fluorescent and fluorescent NCs. Similar arguments could be extended for both 2PA and 3PA cases. Both types of NCs illustrated a band gap of ~4 eV. However, in the case of fluorescent NCs the absorbance drop was not sharp and a weak tail (until 500 nm) was observed indicating that there are a few states below the ~4 eV energy level. In thin films the absorption spectra are slightly modified in both the cases with the conduction band edge starting at ~3.1 eV in the non-fluorescent case and ~2.5 eV in the fluorescent case. This data clearly suggests the formation of few trap states (or more likely surface states) below the band gap while in the film form. An 800 nm photon has an energy corresponding to 1.55 eV. However, since these are broadband pulses (~70 fs which implies a FWHM bandwidth of 12-16 nm for a transform limited pulse) the energy has a spread around 1.55 eV (which will be 1.55±0.03 eV). The following arguments can apply for the non-fluorescent and fluorescent NCs films since:

(a) In the spectral range of 500 nm - 800 nm (in steps of 100 nm) the corresponding energies are 2.48 eV, 2.07 eV, 1.77 eV, and 1.55 eV. 2PA indicates the photons carry energy >3.1 eV, at least, which clearly takes the population from ground state (valence band in this case) to the excited state (conduction band in this case).

(b) In the spectral range of 900 nm - 1200 nm (in steps of 100 nm) the corresponding energies are 1.38 eV, 1.13 eV, and 1.03 eV. The presence of 3PA absorption indicates that the photons energy is ≥3.1 eV (a small bandwidth is associated with 1.03 eV also) which is sufficient for the transition of population from ground to the excited states.

(c) In the spectral range of 1300 nm - 1500 nm (again in 100 nm steps) the corresponding energies are 0.95 eV, 0.89 eV, and 0.83 eV. The energy of four photons i.e. 3.32 eV (1500 nm) is greater than the band gap and, therefore, confirms the presence of 4PA.

(d) Combined with an energy level diagram and the intensity-dependent Z-scan data it is apparent that the arguments indicating (a) presence of 2PA in the 500-800 nm range

(b) 3PA in the 900-1200 nm range along with (c) 4PA in the 1300-1500 nm range seems to be effective. Furthermore, we also did try fitting the obtained experimental data for 4PA in the 900-1200 nm range and 5PA in the case of1300-1500 nm data and the theoretical fits obtained were far from good (see data in figures 3.4 and 3.5). Tables 3.1, 3.2 summarize all the NLO coefficients along with the cross-sections (2PA, 3PA, 4PA) obtained. Further the $\chi^{(3)}$ values are also presented wherever applicable for both the fluorescent and non-fluorescent NCs. Figure of Merits (FOM) for both real, imaginary parts of the third order nonlinear susceptibility were calculated using [49][54]

λ (nm)	**T(%)**	**α_0 $\times 10^5(cm^{-1})$**	**β $\times 10^{-8}$(cm/W)**	**γ $\times 10^{-18}(cm^3/W^2)$**	**δ $\times 10^{-26}(cm^5/W^3)$**	**Im[$\chi^{(3)}$] $\times 10^{-11}$(esu)**	**n_2 $\times 10^{-9}(cm^2/W)$**	**Re[$\chi^{(3)}$] $\times 10^{-7}$(esu)**	**σ_2 $\times 10^6$(GM)**	**σ_3 $\times 10^{-73}(cm^6s^2)$**	**σ_4 $\times 10^{-100}(cm^8s^3)$**
500	75	7.17	4.30		-	1.53	4.17	2.37	4.30	-	-
600	80	11.1	46.0	-	-	19.6	2.84	1.61	63.7	-	-
700	85	8.10	16.0	-	-	8.0	5.42	3.08	18.9	-	-
800	87	6.04	4.60	-	-	2.29	6.09	3.46	4.76	-	-
900	85	8.10	-	7.30	-	-	3.31	1.88	-	14.8	-
1100	78	12.4	-	7.15	-	-	4.80	2.73	-	9.70	-
1200	82	9.90	-	8.40	-	-	5.20	2.96	-	9.60	-
1300	84	8.70	-	-	1.57	-	4.60	2.62	-	-	2.34
1400	87	6.95	-	-	3.33	-	4.10	2.33	-	-	3.97
1500	85	8.10	-	-	1.55	-	4.50	2.56	-	-	1.50

Table 3.4 Summary of NLO coefficients obtained from the nonfluorescent Cs_4PbBr_6 NCs films.

Table 3.5 Summary of NLO coefficients obtained from the fluorescent Cs_4PbBr_6 NCs films.

λ (nm)	T(%)	α_0 $\times10^{5}(cm^{-1})$	β $\times10^{-8}(cm/W)$	γ $\times10^{-18}(cm^3/W^2)$	δ $\times10^{-26}(cm^5/W^3)$	$Im(\chi^{(3)})$ $\times10^{-12}$(esu)	n_2 $\times10^{-9}(cm^2/W)$	$Re(\chi^{(3)})$ $\times10^{-7}$(esu)	σ_2 $\times10^{6}$(GM)	σ_3 $\times10^{-73}(cm^6s^2)$	σ_4 $\times10^{-100}(cm^8s^3)$
500	78	6.20	1.29		-	4.59	0.71	0.40	17.1	-	-
600	85	4.05	1.05	-	-	3.74	1.25	0.71	11.6	-	-
700	75	7.17	1.06	-	-	3.77	0.80	0.45	10.0	-	-
800	80	5.57	1.28	-	-	4.56	2.70	1.53	23.2	-	-
900	83	4.65	-	0.65	-	-	2.81	1.62	-	10.7	-
1100	87	3.47	-	0.72	-	-	1.20	0.68	-	7.76	-
1200	87	3.17	-	0.84	-	-	1.50	0.85	-	7.68	-
1300	90	2.62	-	-	1.32	-	2.30	1.31	-	-	15.7
1400	82	4.95	-	-	2.60	-	2.40	1.36	-	-	24.7
1500	84	4.35	-	-	1.55	-	3.20	1.82	-	-	12.0

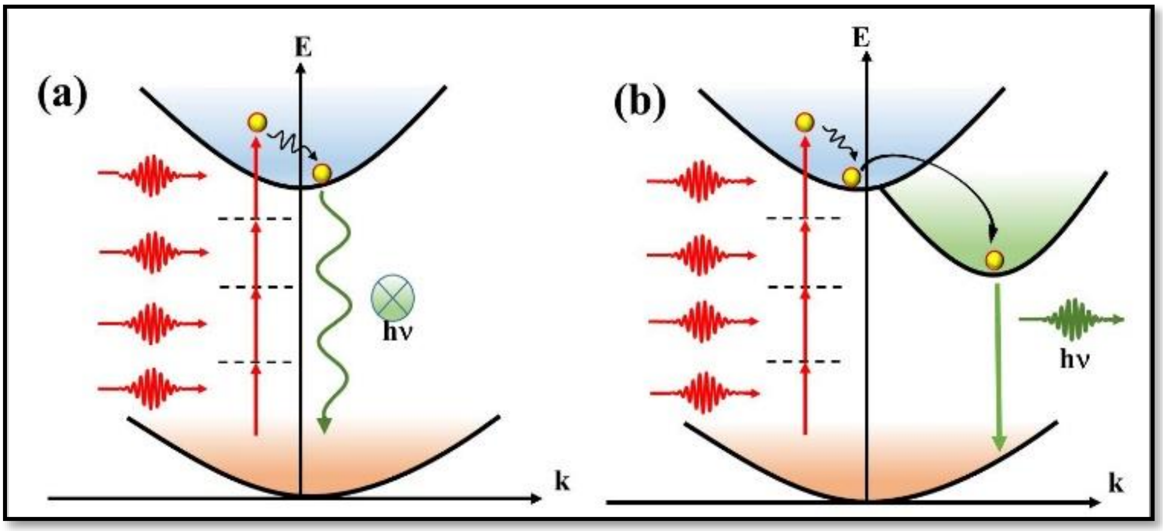

Figure 3.10 Energy level diagrams of (a) non-fluorescent and (b) fluorescent 0D-PRMs explaining the 4PA mechanism.

The CA Z-scan data obtained in the wavelength range of 1100 nm-1500 nm are presented in figures 3.11(a) and 3.11(b) for fluorescent, non-fluorescent films, respectively. The data revealed a similar self-defocusing effect ($n_2<0$) in both the films as was observed in the visible region. The magnitudes of n_2 were found to be ~10^{-9} cm^2/W. These magnitudes are superior, at least by an order of magnitude, to the values of recently reported perovskites.

The time-resolved degenerate four-wave mixing (DFWM) experiments were performed on colloidal solutions in the BOXCAR phase-matching geometry. The third order nonlinear optical susceptibility $\chi^{(3)}$ was estimated by comparing the DFWM signal with CCl_4 [$\chi^{(3)} = 4.4\times10^{-14}$esu]. The relation to calculate the $\chi^{(3)}$ is given by[42]

$$\chi^{(3)}_{Sample} = \left(\frac{n_{Sample}}{n_{ref}}\right)^2 \left(\frac{I_{Sample}}{I_{ref}}\right)^{1/2} \left(\frac{L_{ref}}{L_{Sample}}\right) \alpha L_{Sample} \left(\frac{e^{\frac{\alpha L_{Sample}}{2}}}{1-e^{-\alpha L_{Sample}}}\right) \chi^{(3)}_{ref} \tag{5}$$

'*I*' is the DFWM signal intensity while 'α' linear absorption coefficient and 'L' is sample length. In order to reduce the errors in the data from laser fluctuations we have recorded an averaged data of 1000 pulses and the obtained values of $\chi^{(3)}$ are summarized in the table 3.6. The intensity dependence of the DFWM signal amplitude clearly shows the slope of 2.9 from the data presented in figure 3.12 (b) and this clearly suggests that no higher order nonlinearities are present in our measurements performed at an input intensity of 200 GW/cm^2.

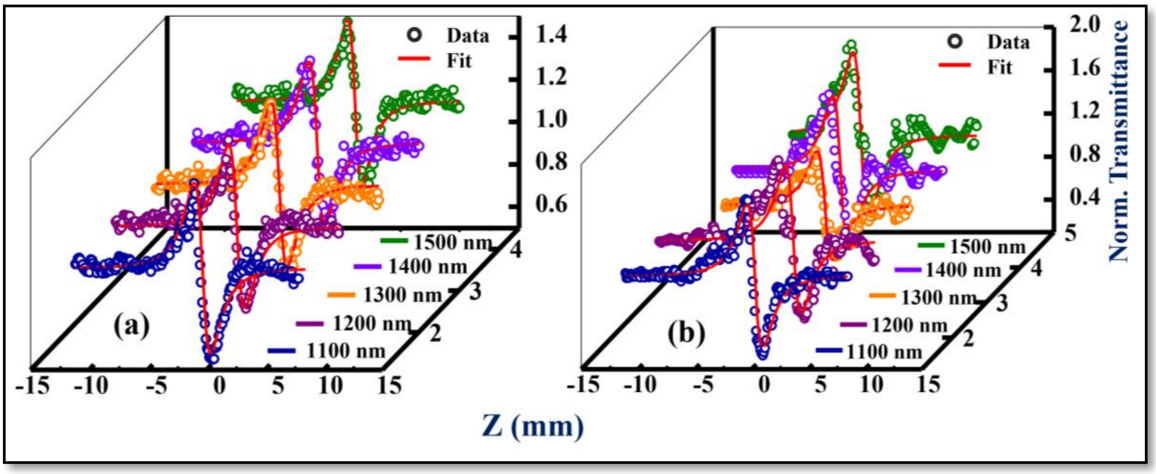

Figure 3.11 CA Z-scan measurements of (a) fluorescent and (b) Non-fluorescent Cs_4PbBr_6 NCs in the wavelength range of 1100 nm-1500 nm.

Figure 3.13 shows the time-resolved DFWM signals of the colloidal Cs_4PbBr_6 solution as a function of probe delay (ps). The transient signals were fitted with a Gaussian function and the full width at half maximum (FWHM) yielded ~131 fs for fluorescent and ~120 fs for non-fluorescent NCs. The observed transients were fitted using an exponential decay function which shows dephasing times of ~92 fs and ~81 fs for fluorescent and non-fluorescent colloidal solution. The measurements were performed at an 800 nm wavelength with~70 fs pulses (estimated to be the pulse duration at the sample position). The input pulse duration was measured by an autocorrelation technique. This fast response clearly suggests that these materials have potential for all-optical switching applications. The fast response from the non-fluorescent NCs can be attributed to large number of trap states and solvent which significantly increases the many body effects which shows fast dephasing time compared to fluorescent colloidal solution. It is to be noted here that the DFWM studies were performed in solution form initially. We also tried to perform the studies in film form. However, the DFWM signal was quite weak and a harder pumping ended damaging the films. We optimized the signal for a particular input energy (where the damage was absent) and recorded the DFWM data for thin films too. The $\chi^{(3)}$ values obtained from the DFWM data are summarized in table 3.3 (both thin films and solutions). The $\chi^{(3)}$ values obtained for the films were found to be one order of magnitude lower than those obtained with the Z-scan measurements. This can possibly be attributed to the following reasons (a) improper overlap of the beams in space and time domains leading to lower DFWM signal (b) small inhomogeneities in the films (c) more importantly, we did not consider the number of NCs (density) in DFWM measurements as was in the case of Z-scan data and analysis. Additional, detailed measurements with increasing concentrations of the NCs in thin films will be essential to quantify the $\chi^{(3)}$ magnitudes using the DFWM technique

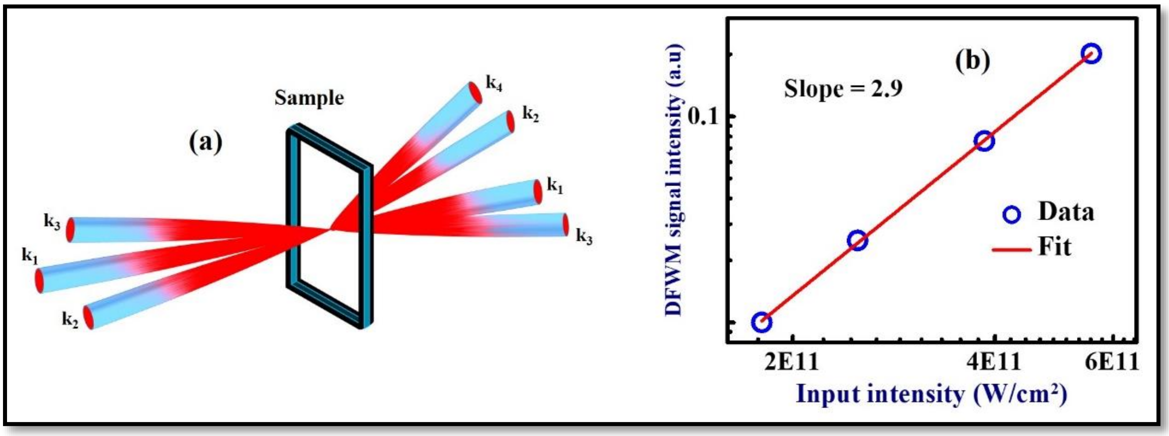

Figure 3.12 (a) BOXCAR arrangement of three input laser beams (b) Intensity-dependent DFWM signal amplitude in fluorescent NC solution in toluene.

Table 3.6 $\chi^{(3)}$ values obtained from the DFWM experiments in colloidal solution and thin films of 0D-PRM (F means fluorescent and NFL means Non-fluorescent).

Wavelength (λ)	Sample studied	$\chi^{(3)}$ (esu)
800 nm	NFL Solution	0.70×10^{-13}
800 nm	NFL Film	7.34×10^{-9}
800 nm	F Solution	0.40×10^{-13}
800 nm	F Film	5.38×10^{-9}

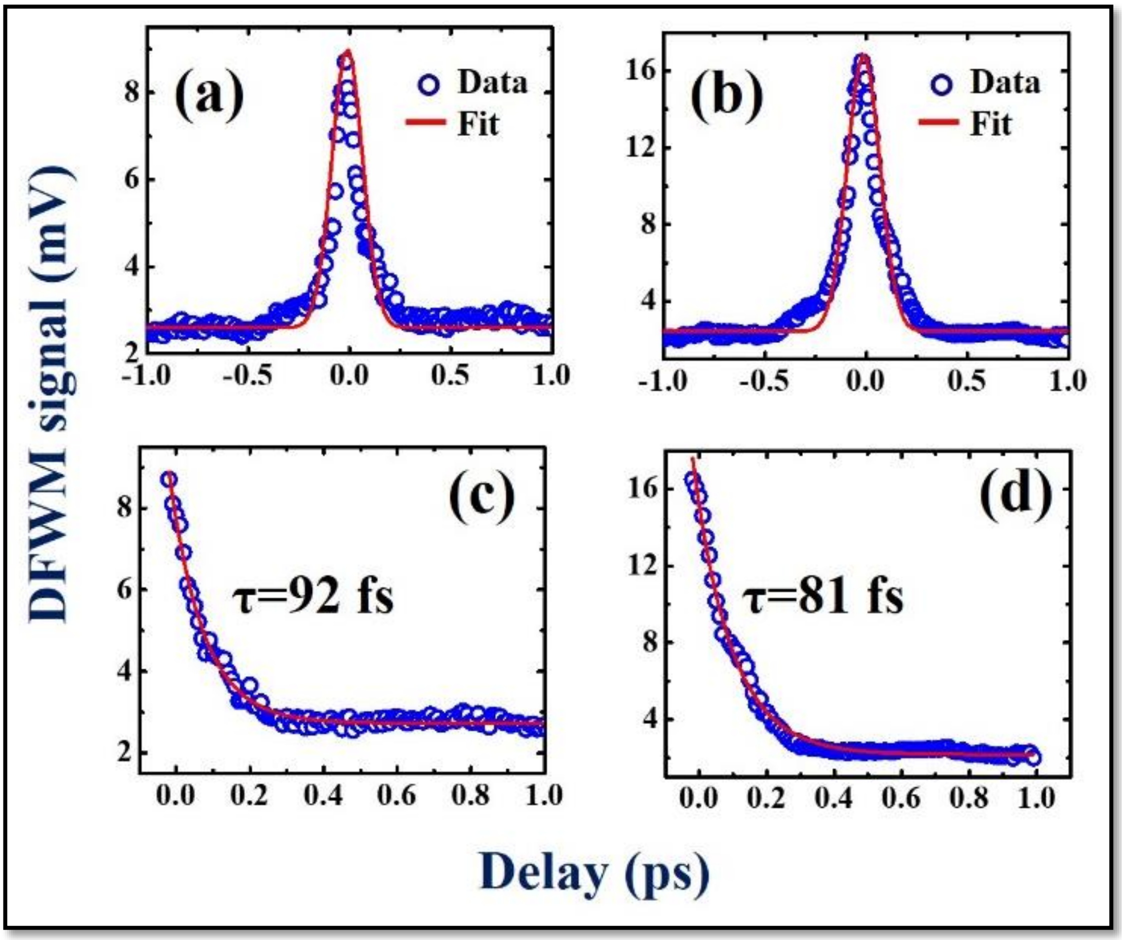

Figure 3.13 Time-resolved DFWM measurements of (a) fluorescent and (b) non-fluorescent 0D-PRM NCs. (c) and (d) illustrate the expanded view of the time-resolved data after zero delay and their corresponding exponential fits of the respective NCs.

Tables 3.7 and 3.8 summarize the 2PA, 3PA, 4PA coefficients and cross-sections obtained in the present work and those reported recently in literature. Zou et al.[55] reported 2PA in Fe doped $CsPb(Cl/Br)_3$ microwires with 140 fs, 800 nm pulses. They obtained the magnitude of 2PA coefficient of 210 cm/GW. However, they performed the measurements with 80 MHz pulses wherein thermal effects are anticipated to play a significant role. Wei et al.[49] reported 2PA coefficient of 8.5 cm/GW for a single crystal $MAPbBr_3$ studied using 300 fs, 1044 nm pulses and a repetition rate of 20.8 MHz, again where the thermal effects are expected to be predominant. Xie et al.[56] reported a very large value of 2PA coefficient of 1.15 cm/kW for $CH_3NH_3Pb_{0.75}Sn_{0.25}I_3$ perovskite thin film obtained using 400 fs pulses but, most importantly, with 43 MHz pulses. It is not apposite to compare the magnitude of coefficients obtained with fs, kHz pulses with those reported using fs, MHz repetition rate pulses since they inevitably demonstrate strong NLO coefficients. There are other reports on $CsPbBr_3$ NCs solution demonstrating a 2PA coefficient of 0.097 cm GW^{-1} at 800 nm,[23] $CsPbBr_3$ nanosheets demonstrating a 2PA coefficient of 10.94 cm GW^{-1} at 800 nm[28] and $CH_3NH_3PbBr_3$ single crystal with a value of 8.2 cm GW^{-1} at 800 nm.[51] Ganeev et al.[57] recently reported 2PA coefficients of $\sim 7\times10^{-7}$ cmW^{-1} for $CH_3NH_3PbX_3$ films with 40 fs pulses at 800 nm. Our earlier result[16] on $CsPbBr_3$ perovskite films demonstrated a best 2PA coefficient of 10^{-9} cm/W, which is at least two orders of magnitude lower compared those presented here. It is pertinent to note that the present measurements were performed at similar experimental conditions reported in reference [16] clearly suggesting the superiority of the present NCs investigated. Han and co-workers[58] have reported 800 nm, kHz repetition rate measurements of nonlinear absorption in colloidal $CsPbX_3$ quantum dots and observed 2PA coefficients of $\sim 10^{-1}$ cm/GW and the corresponding cross-sections of $\sim 10^5$ GM, which are again lower than those reported here. Saouma and co-workers[53] studied in detail the optical nonlinearity in two-dimensional organic-inorganic lead iodide perovskites wherein they argue that in conventional 2D perovskites the observed strong nonlinearities are generally associated with exciton resonances. The β values for their compounds were extracted from the NLO studies and the obtained values were 15.3 ± 2.6 cm GW^{-1} ($n = 1$), 18.4 ± 3.1 cm GW^{-1} ($n = 2$), 20.7 ± 3.5 cm GW^{-1} ($n = 3$), and 46.5 ± 8.4 cm GW^{-1} ($n = \infty$), respectively. These values are comparable (but slightly lower when compared to non-fluorescent Cs_4PbBr_6 NCs film values) the values reported in the present study. Tables 3.7-3.8 summarizes all the NLO coefficients and cross-sections of the perovskite materials reported in recent literature. Saouma and co-workers[59] again have studied the MPA properties and reported a 3PA coefficient value of $MAPbCl_3$ as ~0.05 cm^3/GW^2, which are one order of magnitude lower than those studied here. Gao and co-workers[8] investigated room temperature three-photon pumped $CH_3NH_3PbBr_3$ perovskite microlasers wherein they reported a value of 3PA coefficient of 2.26×10^{-5} cm^3/GW^2, which is orders of magnitude lower than the Cs_4PbBr_6 perovskite NC films investigated in this work. There are not many reports in literature on 3PA and 4PA of perovskites. Chen et al.[29] have reported 2PA, 3PA, 4PA, and 5PA in multi-dimensional core-shell type halide perovskite colloidal NCs. They report their measurements on (a) $CsPbBr_3$ NCs (~9 nm) (b) core-only $MAPbBr_3$ NCs (diameter of 8-9 nm) and (c) core–shell $MAPbBr_3/(OA)_2PbBr_4$ NCs (diameter of 9–10 nm). They report 2PA cross-sections of 10^6 GM in (a)-(c) in the 675-1000 nm spectral range. 3PA cross-sections of ~10^{-74} cm^6s^2 and 4PA cross-sections of 10^{-104} cm^8s^3 are also reported for these NCs. They report the “action cross-sections” defined as $\sigma_n\times\eta$, where η is the PL quantum yield. The values obtained in the present study are higher compare to their coefficients and cross-sections. However, the mechanisms for the observed large nonlinearities are completely different in each case. In their case the size effects probably played a dominant role in quantum confinement. In our case the confinement is due to the structure of the 0-D PRM NCs. It is evident from all the data presented in various tables and the comparison provided above that the NLO parameters obtained from Cs_4PbBr_6 NCs used in the present study are superior compared to recently reported perovskite NCs. We strongly believe that the strong quantum confinement of 0-D PRM probably provided a mechanism to enhance the optical nonlinearities. Further, the involvement of defect states can probably help in increasing the multi-photon absorption processes. Since fluorescent NCs are larger in size (~20 nm) as compared to the non-fluorescent ones (~10 nm), it is expected that these NCs will create more voids in the film and number of particles will be lesser than expected. This could be a reason for the obtained lower value of NLO parameters for the fluorescent NCs films. Interestingly the 4PA cross-sections of fluorescent NCs films were superior to the non-fluorescent counterparts and this behavior needs further detailed investigations. The population resides for a longer time in the excited states in the case of fluorescent NCs whereas in the non-fluorescent case it comes back to the ground state much faster. This also could possibly affect the nonlinearities observed. There are no studies reported thus far on the lifetimes of the different excited states in these novel NCs. The strong NLR values possibly arising from the effect of quantum confinement, free carries and band gap.[60-63] A complete knowledge of the excited state dynamics is indispensable to segregate and comprehend the exact reason(s) for the observed large nonlinearities. Therefore, our future endeavours will be to extend these NLO studies to the mid-infrared spectral region and investigate the whole excited state dynamics in these NC films by using the technique of transient absorption spectroscopy in both the visible and near-IR spectral ranges.

Material	Excitation	β (cm/W)	n_2 (cm^2/W)	σ_2 (GM)	Ref.
(QDs) CsPbBr$_3$	800 nm, 1 kHz, 100 fs	8.5×10^{-11}	-	-	49
(QDs) CsPbBr$_3$	800 nm,76 MHz, 130 fs	10^{-9}	$2\text{-}5\times10^{-13}$	-	45
(QDs) CsPbBr$_3$	800 nm,1 kHz, 120 fs	-	-	1.8×10^{5} 4.0×10^{5} (670 nm)	44
CsPbBr$_3$ (NCs)	800 nm,1 kHz, 90 fs	-	-	2.7×10^{6}	6
CsPbI$_3$ (NCs) (NCs) CsPbBr$_3$ (NCs) CsPbBr$_3$	787 nm,1 kHz, 386 fs	3.2×10^{-11}	6.8×10^{-15}	-	26
	787 nm,1 kHz, 386 fs	9.7×10^{-11}	4.7×10^{-15}	-	
	800 nm, 1 kHz, 100 fs	9.7×10^{-11}	-	1.2×10^{5}	
(QDs) CsPbBr$_3$	1 kHz, 340 fs	-	-	2.8×10^{6} 1080 nm	46
MAPbBr$_3$ NCs in toluene (8-9 nm size, sphere)	675-1000 nm, 50 fs, 1kHz	-	-	4.8–6.2×10^{5} ($\sim8.0\times10^{5}$ at 800 nm)	29
MAPbBr$_3$/(OA)2PbBr4 NCs in toluene (9-10 nm, spheres)	675-1000 nm, 50 fs, 1kHz	-	-	3.3–4.0×10^{5} ($\sim5.0\times10^{6}$ at 800 nm)	
CsPbBr$_3$ NCs in toluene (~ 9 nm, cube)	675-1000 nm, 50 fs, 1kHz	-	-	~9.7–1.3×10^{5} ($\sim1.1\times10^{6}$ at 800 nm)	
CsPbBr$_3$ NCs in toluene (~ 9 nm, cubes)	800 nm, 100 fs, 1 kHz	-	-	2.7×10^{6}	
Mn-doped CsPbCl$_3$ NCs (11.7±1.8 nm)	720 nm, fs pulses	-	-	$\sim3.18\times10^{5}$	24

$CH_3NH_3PbBr_3$ films	mid-IR, 2.8 ps, 32.3 MHz		$\sim10^{-8}$	-	19
$CH_3NH_3PbBr_3$	1044 nm, 300 fs, 20.8 MHz	8.5×10^{-9}	-	-	64
CsPbBr3 NCs Thin film	600-800 nm 1 kHz, 70 fs	1.8×10^{-9}	$\sim10^{-9}$	$\sim9.8\times10^{5}$	16
$CH_3NH_3Pb_{0.75}Sn_{0.25}I_3$ (thin film)	1535 nm, 400 fs, 43 MHz	1.15×10^{6}	-	-	56
Fe-doped $CsPbX_3$	800 nm, 140 fs, 80 MHz	201×10^{-9}	-	-	55
$CH_3NH_4PbBr_3$	800 nm,100 fs	8.6×10^{-9}	-	-	51
Cs_4PbBr_6 0D-PRM	70 fs, 1 kHz 500-1500 nm	$\sim10^{-7}$	$\sim10^{-9}$	10^{7}	This work

Table 3.7 Comparison of the 2PA coefficients and cross-sections of the halide perovskite NCs with the literature values.

Material	**Excitation Parameters**	**γ (cm^3/GW^2)**	**σ_3 (10^{-74} cm^6s^2 $photon^2$)**	**σ_4 (10^{-104} cm^8s^3 $photon^3$)**	**Ref.**
$MAPbCl_3$	1064 nm, 30 ps, 50 Hz	0.05 ± 0.01	-	-	59
$CH_3NH_3PbBr_3$	100 fs, 1 kHz, 1240 nm	2.26×10^{-5}	-	-	8
$MAPbBr_3$	1050-2000 nm, 50 fs, 1 kHz	-	0.33±0.05–2.7±0.4	0.036±0.005–3.0±0.5	29
$MAPbBr_3$/ $(OA)_2PbBr_4$	1050-2000 nm, 50 fs; 1kHz	-	2.5±0.4–22±3	0.21±0.03–24±4	
$CsPbBr_3$	1050-2000 nm, 50 fs, 1kHz	-	0.38±0.06–8.0±1.0	0.07±0.01–7.0±1.0	
Cs_4PbBr_6 0D-PRM	70 fs, 1 kHz, 500-1500nm	$6\text{-}8\times10^{-19}$	70-148	$12\text{-}37.8\times10^{3}$	This work

Table 3.8 Comparison of the 3PA/4PA coefficients and cross-sections of the halide perovskite NCs with the literature values.

3.4 Conclusions

- The NLO properties of an ambient condition synthesized colloidal $CsPbBr_3$ perovskite NCs and NRs and zero-dimensional Cs_4PbBr_6 perovskite NCs were investigated over a wide range of wavelengths 600-800 nm for $CsPbBr_3$ and (500-1500 nm) for Cs_4PbBr_6 NCs using the Z-scan and DFWM techniques by femtosecond pulse excitation.
- For $CsPbBr_3$ NCs a notable change in the refractive index is observed, at higher intensities 7.3×10^{10} W/cm^2, an increase in the refractive index with a saturated absorption is evident. The NCs demonstrated strong nonlinear absorption coefficient of 0.1 cm/GW (at 2.4×10^{10} W/cm^2).
- Large 2PA cross-sections are reported which are comparable to those reported in table 3.3, 3.7-3.8. It is observed that $CsPbBr_3$ NCs and NRs depict a size and thickness dependent nonlinear optical properties with increasing saturation intensity at high peak intensities.
- The strong nonlinear absorption and switching properties of these open atmospheric cost effective $CsPbX_3$ perovskite NCs indicate high potential to be a future material for light harvesting, mid-infrared nonlinear absorbers and all-optical communications. In case of Cs_4PbBr_6 Both the NCs (fluorescent and non-fluorescent) exhibited superior nonlinearities in the 500-1500 nm spectral region with non-fluorescent NCs exhibiting slightly stronger 2PA, 3PA coefficients and cross-sections than their fluorescent counterparts.
- We believe the observed superior NLO parameters are due to the strong confinement effects with a high dipole moment. The magnitude of 2PA, 3PA, and 4PA cross sections were estimated to be ~10^{-43}-10^{-44} cm^{4}s, ~10^{-73} cm^{6}s^2 and ~10^{-100} cm^{8}s^3, respectively, and these are found to be superior to many recently reported NLO coefficients of on perovskite NCs. DFWM experimental data on zero-dimensional NCs suggested a fast response (~92 fs and ~81 fs) in colloidal solutions, which is a prerequisite in photonic switching devices.
- The strong multi-photon absorption coefficients along with the cross-sections at near-IR wavelengths render these NLO materials suitable for next-generation multi-photon based imaging and photonic/optoelectronic device applications.

References

1. Qi, X.; Zhang, Y.; Ou, Q.; Ha, S. T.; Qiu, C.-W.; Zhang, H.; Cheng, Y.-B.; Xiong, Q.; Bao, Q., Photonics and Optoelectronics of 2d Metal-Halide Perovskites. *Small* **2018**, *14*, 1800682.
2. Dohner, E. R.; Jaffe, A.; Bradshaw, L. R.; Karunadasa, H. I., Intrinsic White-Light Emission from Layered Hybrid Perovskites. *Journal of the American Chemical Society* **2014**, *136*, 13154-13157.
3. Li, X.; Wu, Y.; Zhang, S.; Cai, B.; Gu, Y.; Song, J.; Zeng, H., Quantum Dots: $CsPbX_3$ quantum Dots for Lighting and Displays: Room-Temperature Synthesis, Photoluminescence Superiorities, Underlying Origins and White Light-Emitting Diodes (Adv. Funct. Mater. 15/2016). *Advanced Functional Materials* **2016**, *26*, 2584-2584.
4. Jiang, G.; Miao, L.; Yi, J.; Huang, B.; Peng, W.; Zou, Y.; Huang, H.; Hu, W.; Zhao, C.; Wen, S., Ultrafast Pulse Generation from Erbium-Doped Fiber Laser Modulated by Hybrid Organic–Inorganic Halide Perovskites. *Applied Physics Letters* **2017**, *110*, 161111.
5. Li, P., et al., Two-Dimensional Ch3nh3pbi3 Perovskite Nanosheets for Ultrafast Pulsed Fiber Lasers. *ACS Applied Materials & Interfaces* **2017**, *9*, 12759-12765.
6. Fu, Y.; Zhu, H.; Stoumpos, C. C.; Ding, Q.; Wang, J.; Kanatzidis, M. G.; Zhu, X.; Jin, S., Broad Wavelength Tunable Robust Lasing from Single-Crystal Nanowires of Cesium Lead Halide Perovskites ($CsPbX_3$, X = Cl, Br, I). *ACS Nano* **2016**, *10*, 7963-7972.
7. Xu, Y., et al., Two-Photon-Pumped Perovskite Semiconductor Nanocrystal Lasers. *Journal of the American Chemical Society* **2016**, *138*, 3761-3768.
8. Gao, Y.; Wang, S.; Huang, C.; Yi, N.; Wang, K.; Xiao, S.; Song, Q., Room Temperature Three-Photon Pumped $CH_3NH_3PbBr_3$ Perovskite Microlasers. *Scientific Reports* **2017**, *7*.
9. Yakunin, S.; Protesescu, L.; Krieg, F.; Bodnarchuk, M. I.; Nedelcu, G.; Humer, M.; De Luca, G.; Fiebig, M.; Heiss, W.; Kovalenko, M. V., Low-Threshold Amplified Spontaneous Emission and Lasing from Colloidal Nanocrystals of Caesium Lead Halide Perovskites. *Nature Communications* **2015**, *6*.

10. Ramasamy, P.; Lim, D.-H.; Kim, B.; Lee, S.-H.; Lee, M.-S.; Lee, J.-S., All-Inorganic Cesium Lead Halide Perovskite Nanocrystals for Photodetector Applications. *Chemical Communications* **2016**, *52*, 2067-2070.
11. Protesescu, L.; Yakunin, S.; Bodnarchuk, M. I.; Krieg, F.; Caputo, R.; Hendon, C. H.; Yang, R. X.; Walsh, A.; Kovalenko, M. V., Nanocrystals of Cesium Lead Halide Perovskites ($CsPbX_3$, X = Cl, Br, and I): Novel Optoelectronic Materials Showing Bright Emission with Wide Color Gamut. *Nano Letters* **2015**, *15*, 3692-3696.
12. Wehrenfennig, C.; Eperon, G. E.; Johnston, M. B.; Snaith, H. J.; Herz, L. M., High Charge Carrier Mobilities and Lifetimes in Organolead Trihalide Perovskites. *Advanced Materials* **2013**, *26*, 1584-1589.
13. Kang, J.; Wang, L.-W., High Defect Tolerance in Lead Halide Perovskite $CsPbX_3$. *The Journal of Physical Chemistry Letters* **2017**, *8*, 489-493.
14. Liu, W.; Xing, J.; Zhao, J.; Wen, X.; Wang, K.; Lu, P.; Xiong, Q., Giant Two-Photon Absorption and Its Saturation in 2d Organic-Inorganic Perovskite. *Advanced Optical Materials* **2017**, *5*, 1601045.
15. Manzi, A.; Tong, Y.; Feucht, J.; Yao, E.-P.; Polavarapu, L.; Urban, A. S.; Feldmann, J., Resonantly Enhanced Multiple Exciton Generation through Below-Band-Gap Multi-Photon Absorption in Perovskite Nanocrystals. *Nature Communications* **2018**, *9*.
16. Krishnakanth, K. N.; Seth, S.; Samanta, A.; Rao, S. V., Broadband Femtosecond Nonlinear Optical Properties of $CsPbBr_3$ Perovskite Nanocrystals. *Optics Letters* **2018**, *43*, 603.
17. Li, J.; Dong, H.; Xu, B.; Zhang, S.; Cai, Z.; Wang, J.; Zhang, L., $CsPbBr_3$ Perovskite Quantum Dots: Saturable Absorption Properties and Passively Q-Switched Visible Lasers. *Photonics Research* **2017**, *5*, 457.
18. Náfrádi, B.; Szirmai, P.; Spina, M.; Lee, H.; Yazyev, O. V.; Arakcheeva, A.; Chernyshov, D.; Gibert, M.; Forró, L.; Horváth, E., Optically Switched Magnetism in Photovoltaic Perovskite $CH_3NH_3(Mn{:}Pb)I_3$. *Nature Communications* **2016**, *7*.
19. Yi, J.; Miao, L.; Li, J.; Hu, W.; Zhao, C.; Wen, S., Third-Order Nonlinear Optical Response of $CH_3NH_3PbI_3$ Perovskite in the Mid-Infrared Regime. *Optical Materials Express* **2017**, *7*, 3894.
20. Stoumpos, C. C.; Frazer, L.; Clark, D. J.; Kim, Y. S.; Rhim, S. H.; Freeman, A. J.; Ketterson, J. B.; Jang, J. I.; Kanatzidis, M. G., Hybrid Germanium Iodide Perovskite

Semiconductors: Active Lone Pairs, Structural Distortions, Direct and Indirect Energy Gaps, and Strong Nonlinear Optical Properties. *Journal of the American Chemical Society* **2015**, *137*, 6804-6819.

21. Li, X., et al., All Inorganic Halide Perovskites Nanosystem: Synthesis, Structural Features, Optical Properties and Optoelectronic Applications. *Small* **2017**, *13*, 1603996.
22. Bai, T.; Dong, N.; Cheng, H.; Cheng, Q.; Wang, J.; Chen, Y., $CH_3NH_3PbI_3$ Perovskite:Poly(N-Vinylcarbazole) Blends for Broadband Optical Limiting. *RSC Advances* **2017**, *7*, 1809-1813.
23. Wang, Y.; Li, X.; Zhao, X.; Xiao, L.; Zeng, H.; Sun, H., Nonlinear Absorption and Low-Threshold Multiphoton Pumped Stimulated Emission from All-Inorganic Perovskite Nanocrystals. *Nano Letters* **2015**, *16*, 448-453.
24. He, T.; Li, J.; Ren, C.; Xiao, S.; Li, Y.; Chen, R.; Lin, X., Strong Two-Photon Absorption of Mn-Doped $CsPbCl_3$ Perovskite Nanocrystals. *Applied Physics Letters* **2017**, *111*, 211105.
25. Pan, J., et al., Air-Stable Surface-Passivated Perovskite Quantum Dots for Ultra-Robust, Single- and Two-Photon-Induced Amplified Spontaneous Emission. *The Journal of Physical Chemistry Letters* **2015**, *6*, 5027-5033.
26. Liu, S.; Chen, G.; Huang, Y.; Lin, S.; Zhang, Y.; He, M.; Xiang, W.; Liang, X., Tunable Fluorescence and Optical Nonlinearities of All Inorganic Colloidal Cesium Lead Halide Perovskite Nanocrystals. *Journal of Alloys and Compounds* **2017**, *724*, 889-896.
27. Liu, Z.; Yang, J.; Du, J.; Hu, Z.; Shi, T.; Zhang, Z.; Liu, Y.; Tang, X.; Leng, Y.; Li, R., Robust Subwavelength Single-Mode Perovskite Nanocuboid Laser. *ACS nano* **2018**, *12*, 5923-5931.
28. Zhang, J.; Jiang, T.; Zheng, X.; Shen, C.; Cheng, X. a., Thickness-Dependent Nonlinear Optical Properties of $CsPbBr_3$ Perovskite Nanosheets. *Optics Letters* **2017**, *42*, 3371.
29. Chen, W.; Bhaumik, S.; Veldhuis, S. A.; Xing, G.; Xu, Q.; Grätzel, M.; Mhaisalkar, S.; Mathews, N.; Sum, T. C., Giant Five-Photon Absorption from Multidimensional Core-Shell Halide Perovskite Colloidal Nanocrystals. *Nature Communications* **2017**, *8*.

30. Seth, S.; Samanta, A., A Facile Methodology for Engineering the Morphology of $CsPbX_3$ Perovskite Nanocrystals under Ambient Condition. *Scientific Reports* **2016**, *6*.

31. D'Innocenzo, V.; Grancini, G.; Alcocer, M. J. P.; Kandada, A. R. S.; Stranks, S. D.; Lee, M. M.; Lanzani, G.; Snaith, H. J.; Petrozza, A., Excitons Versus Free Charges in Organo-Lead Tri-Halide Perovskites. *Nature Communications* **2014**, *5*.

32. Zhang, Y.; Saidaminov, M. I.; Dursun, I.; Yang, H.; Murali, B.; Alarousu, E.; Yengel, E.; Alshankiti, B. A.; Bakr, O. M.; Mohammed, O. F., Zero-Dimensional Cs_4PbBr_6 Perovskite Nanocrystals. *The Journal of Physical Chemistry Letters* **2017**, *8*, 961-965.

33. Akkerman, Q. A.; Abdelhady, A. L.; Manna, L., Zero-Dimensional Cesium Lead Halides: History, Properties, and Challenges. *The Journal of Physical Chemistry Letters* **2018**, *9*, 2326-2337.

34. Yin, J.; Maity, P.; De Bastiani, M.; Dursun, I.; Bakr, O. M.; Brédas, J.-L.; Mohammed, O. F., Molecular Behavior of Zero-Dimensional Perovskites. *Science Advances* **2017**, *3*, e1701793.

35. Saidaminov, M. I.; Almutlaq, J.; Sarmah, S.; Dursun, I.; Zhumekenov, A. A.; Begum, R.; Pan, J.; Cho, N.; Mohammed, O. F.; Bakr, O. M., Pure Cs_4PbBr_6: Highly Luminescent Zero-Dimensional Perovskite Solids. *ACS Energy Letters* **2016**, *1*, 840-845.

36. De Bastiani, M., et al., Inside Perovskites: Quantum Luminescence from Bulk Cs_4PbBr_6 Single Crystals. *Chemistry of Materials* **2017**, *29*, 7108-7113.

37. Seth, S.; Samanta, A., Photoluminescence of Zero-Dimensional Perovskites and Perovskite-Related Materials. *The Journal of Physical Chemistry Letters* **2017**, *9*, 176-183.

38. Seth, S.; Samanta, A., Fluorescent Phase-Pure Zero-Dimensional Perovskite-Related Cs_4PbBr_6 Microdisks: Synthesis and Single-Particle Imaging Study. *The Journal of Physical Chemistry Letters* **2017**, *8*, 4461-4467.

39. Almutlaq, J.; Yin, J.; Mohammed, O. F.; Bakr, O. M., The Benefit and Challenges of Zero-Dimensional Perovskites. *The Journal of Physical Chemistry Letters* **2018**, *9*, 4131-4138.

40. Xu, J. et al., Imbedded Nanocrystals of $CsPbBr_3$ in Cs_4PbBr_6 : Kinetics, Enhanced Oscillator Strength, and Application in Light-Emitting Diodes. *Advanced Materials* **2017**, *29*, 1703703.
41. Tong, G.; Li, H.; Zhu, Z.; Zhang, Y.; Yu, L.; Xu, J.; Jiang, Y., Enhancing Hybrid Perovskite Detectability in the Deep Ultraviolet Region with Down-Conversion Dual-Phase ($CsPbBr_3$– Cs_4PbBr_6) Films. *The journal of physical chemistry letters* **2018**, *9*, 1592-1599.
42. Kumar, R. S. S.; Rao, S. V.; Giribabu, L.; Rao, D. N., Ultrafast Nonlinear Optical Properties of Alkyl Phthalocyanines Investigated Using Degenerate Four-Wave Mixing Technique. *Optical Materials* **2009**, *31*, 1042-1047.
43. Kalanoor, B. S.; Gouda, L.; Gottesman, R.; Tirosh, S.; Haltzi, E.; Zaban, A.; Tischler, Y. R., Third-Order Optical Nonlinearities in Organometallic Methylammonium Lead Iodide Perovskite Thin Films. *ACS Photonics* **2016**, *3*, 361-370.
44. Chen, J., et al., Size- and Wavelength-Dependent Two-Photon Absorption Cross-Section of $CsPbBr_3$ Perovskite Quantum Dots. *The Journal of Physical Chemistry Letters* **2017**, *8*, 2316-2321.
45. Lu, W.-G.; Chen, C.; Han, D.; Yao, L.; Han, J.; Zhong, H.; Wang, Y., Nonlinear Optical Properties of Colloidal $CH_3NH_3PbBr_3$ and $CsPbBr_3$ quantum Dots: A Comparison Study Using Z-Scan Technique. *Advanced Optical Materials* **2016**, *4*, 1732-1737.
46. Li, J.; Zhang, S.; Dong, H.; Yuan, X.; Jiang, X.; Wang, J.; Zhang, L., Two-Photon Absorption and Emission in $CsPb(Br/I)_3$ cesium Lead Halide Perovskite Quantum Dots. *CrystEngComm* **2016**, *18*, 7945-7949.
47. Seth, S.; Mondal, N.; Patra, S.; Samanta, A., Fluorescence Blinking and Photoactivation of All-Inorganic Perovskite Nanocrystals $CsPbBr_3$ and $CsPbBr_2I$. *The Journal of Physical Chemistry Letters* **2016**, *7*, 266-271.
48. Wang, Y.; Li, X.; Nalla, V.; Zeng, H.; Sun, H., Solution-Processed Low Threshold Vertical Cavity Surface Emitting Lasers from All-Inorganic Perovskite Nanocrystals. *Advanced Functional Materials* **2017**, *27*, 1605088.
49. Wei, K.; Xu, Z.; Chen, R.; Zheng, X.; Cheng, X.; Jiang, T., Temperature-Dependent Excitonic Photoluminescence Excited by Two-Photon Absorption in Perovskite $CsPbBr_3$ Quantum Dots. *Optics Letters* **2016**, *41*, 3821.

50. Sheik-Bahae, M.; Said, A. A.; Wei, T. H.; Hagan, D. J.; Van Stryland, E. W., Sensitive Measurement of Optical Nonlinearities Using a Single Beam. *IEEE Journal of Quantum Electronics* **1990**, *26*, 760-769.
51. Walters, G.; Sutherland, B. R.; Hoogland, S.; Shi, D.; Comin, R.; Sellan, D. P.; Bakr, O. M.; Sargent, E. H., Two-Photon Absorption in Organometallic Bromide Perovskites. *ACS Nano* **2015**, *9*, 9340-9346.
52. Li, J.; Ren, C.; Qiu, X.; Lin, X.; Chen, R.; Yin, C.; He, T., Ultrafast Optical Nonlinearity of Blue-Emitting Perovskite Nanocrystals. *Photonics Research* **2018**, *6*, 554.
53. Saouma, F. O.; Stoumpos, C. C.; Wong, J.; Kanatzidis, M. G.; Jang, J. I., Publisher Correction: Selective Enhancement of Optical Nonlinearity in Two-Dimensional Organic-Inorganic Lead Iodide Perovskites. *Nature Communications* **2017**, *8*.
54. Dong, N.; Li, Y.; Zhang, S.; McEvoy, N.; Zhang, X.; Cui, Y.; Zhang, L.; Duesberg, G. S.; Wang, J., Dispersion of Nonlinear Refractive Index in Layered WS_2 and WSe_2 Semiconductor Films Induced by Two-Photon Absorption. *Optics Letters* **2016**, *41*, 3936.
55. Zou, S.; Yang, G.; Yang, T.; Zhao, D.; Gan, Z.; Chen, W.; Zhong, H.; Wen, X.; Jia, B.; Zou, B., Template-Free Synthesis of High-Yield Fe-Doped Cesium Lead Halide Perovskite Ultralong Microwires with Enhanced Two-Photon Absorption. *The Journal of Physical Chemistry Letters* **2018**, *9*, 4878-4885.
56. Xie, Y.; Fan, J.; Liu, C.; Chi, S.; Wang, Z.; Yu, H.; Zhang, H.; Mai, Y.; Wang, J., Giant Two-Photon Absorption in Mixed Halide Perovskite $CH_3NH_3Pb_{0.75}Sn_{0.25}I_3$ Thin Films and Application to Photodetection at Optical Communication Wavelengths. *Advanced Optical Materials* **2018**, *6*, 1700819.
57. Ganeev, R. A.; Rao, K. S.; Yu, Z.; Yu, W.; Yao, C.; Fu, Y.; Zhang, K.; Guo, C., Strong Nonlinear Absorption in Perovskite Films. *Optical Materials Express* **2018**, *8*, 1472.
58. Han, Q.; Wu, W.; Liu, W.; Yang, Q.; Yang, Y., Two-Photon Absorption and Upconversion Luminescence of Colloidal $CsPbX_3$ Quantum Dots. *Optical Materials* **2018**, *75*, 880-886.
59. Saouma, F. O.; Park, D. Y.; Kim, S. H.; Jeong, M. S.; Jang, J. I., Multiphoton Absorption Coefficients of Organic–Inorganic Lead Halide Perovskites

$CH_3NH_3PbX_3$ (X = Cl, Br, I) Single Crystals. *Chemistry of Materials* **2017**, *29*, 6876-6882.

60. Kriso, C.; Stein, M.; Haeger, T.; Pourdavoud, N.; Gerhard, M.; Rahimi-Iman, A.; Riedl, T.; Koch, M., Nonlinear Refraction in $CH_3NH_3PbBr_3$ Single Crystals. *Optics Letters* **2020**, *45*, 2431-2434.
61. J. Varma, S.; Cherusseri, J.; Li, J.; Kumar, J.; Barrios, E.; Thomas, J., Quantum Dots of Two-Dimensional Ruddlesden–Popper Organic–Inorganic Hybrid Perovskite with High Optical Limiting Properties. *AIP Advances* **2020**, *10*, 045130.
62. Suárez, I.; Vallés-Pelarda, M.; Gualdrón-Reyes, A. F.; Mora-Seró, I.; Ferrando, A.; Michinel, H.; Salgueiro, J. R.; Pastor, J. P. M., Outstanding Nonlinear Optical Properties of Methylammonium-and $CsPbX_3$ (X= Br, I, and Br–I) Perovskites: Polycrystalline Thin Films and Nanoparticles. *Apl Materials* **2019**, *7*, 041106.
63. Jin, M.; Liang, X.; Zhang, H.; Liu, J.; Shao, G.; Xiang, W.; Song, Y., A Promising Optical Limiting Material: Tunable Third-Order Nonlinear Optical Properties of Robust $CsPbX_3$ (X= Cl/Br, Br) Nanocrystals Glasses. *Journal of the European Ceramic Society* **2020**.
64. Wei, T.-C.; Mokkapati, S.; Li, T.-Y.; Lin, C.-H.; Lin, G.-R.; Jagadish, C.; He, J.-H., Nonlinear Optics: Nonlinear Absorption Applications of $CH_3NH_3PbBr_3$ Perovskite Crystals (Adv. Funct. Mater. 18/2018). *Advanced Functional Materials* **2018**, *28*, 1870122.

Intentional blank page

Chapter 4 Ultrafast Electron Dynamics and Third-order NLO Properties of Laser Fabricated Au and $Ag_{50}Au_{50}$ Nanoparticles

Abstract

Gold and gold-silver nanoparticles (NPs) were achieved using ultrashort pulse laser ablation in liquids technique. The surface plasmon dynamics of these gold and gold-silver alloy NPs at excitation wavelengths of 400 nm and 800 nm were explored using the technique of femtosecond (~70 fs) transient absorption (TA) spectroscopy. With 400 nm photoexcitation, the dynamics demonstrated a plasmon photo-bleach signal along with a transient absorption in the wings of bleach spectra. With 800 nm photoexcitation, $Ag_{50}Au_{50}$ alloy NPs demonstrated a fast electron thermalization time (~150 fs). A slower decay of positive absorption (TA spectra) from alloy NPs was observed when compared to the pure Au NPs. Both the NPs demonstrated a rapid initial electron thermalization and displayed similar time scales for the electron-phonon relaxation. The third-order nonlinear optical (NLO) properties of these NPs were measured using the standard Z-scan technique with fs, kHz pulses at 800 nm. It was observed that the alloy NPs possessed comparatively large value of third-order NLO susceptibility $\chi^{(3)}$ (~10^{-11} esu) compared to the pure gold NPs, finding applications in fields such as bio-medical and photonic devices.

This chapter comprises data from the following publication:

1. Ultrafast excited-state dynamics and femtosecond nonlinear optical properties of laser fabricated Au and $Ag_{50}Au_{50}$ nanoparticles. **K N Krishnakanth**, B Chandu, MSS Bharathi, SSK Raavi, S Venugopal Rao **Optical Materials** 95 (2019), 109239.

4.1 Introduction

Metal and metal alloy nanoparticles (NPs) and/or colloids have fascinating physical, electrical, optical properties depending on their (a) shape (b) size and (c) surrounding environmental (dielectric) parameters. This has a created a tremendous interest because of their potential in applications such as catalytic reactions, plasmonic lasers.[1-3] The ultrafast nonlinear optical (NLO) properties of gold (Au), silver (Ag), and gold-silver (Au-Ag) alloy NPs have also attracted a substantial interest in several fields for a variety of device applications.[4-5] Au and Ag NPs exhibit the surface plasmon (SP) modes in the visible spectral region arising from the oscillations of conduction electrons. The position of plasmon peak mainly depends on the size, shape of the NPs. With an increase in the size, the peak shifts towards the red spectral region and broadens.[6-7] The advantage of doping metal nanoparticles with semiconductors is that it can substantially tune the plasmon band over the visible and near-infrared spectral regions. Another advantage being the metal NPs are excellent light absorbers and can possibly create highly excited electron/hole pairs. Consequently, these hot charge carriers are utilized in photo-catalysis, solar energy conversion applications.[8-9] The surface plasmon resonance (SPR) of metal NPs is the reason for many optical properties, mainly the nonlinear absorption which can make the metal NPs be appiled in different photonic applications sucha as opticallimiters, switching and optical memories. Ultrafast relaxation processes of electrons in the metal nanostructures which involve localized SPs has been demonstrated to be an important aspect for developing high-performance optical switching materials and devices based.[10-16] The electron dynamics as well as the third-order NLO properties of metal, metal-alloy NPs are well studied[14-20] using different spectroscopic techniques in exploration of unique optoelectronic, switching device applications.[11-13, 17] There are a few research reports on the investigations of the electron dynamics in Au, Au-Ag alloy NPs using transient absorption spectroscopy (TAS) technique employing femtosecond (fs) pulses.[13, 18-19 20-26]

The geometry of the NPs and the corresponding electron dynamics (in the excited states) seem to influence the NLO properties.[27-28] Subsequent to the input laser pulse excitation, the electrons relax through different processes such as (a) internal thermalization by electron-electron collision followed by (b) electron-phonon coupling arising from external thermalization.[20-22] The non-thermal (or non-Fermi) electron distribution following laser excitation above the Fermi level has been investigated by various techniques.[9, 24-25] Electron thermalization dynamics after intraband/interband excitations in mixed metal NPs are largely not investigated. Recently, Zhang and co-workers[10] investigated the interband and intraband contributions to the localized SP plasmon oscillations in pure Au NPs. Their data suggested a red-shifted induced LSPR feature with 400 nm excitation. When pumped above the threshold energy (2.38 eV), an induced electronic transition from the ‘5d’ band to the ‘6sp’ band (conduction) takes place resulting in a transient increase of electron population in the conduction band was observed. The excited 5d electrons then relaxed to a ‘6sp’ band with a time delay of 1 ps has been observed.[10] In this work, we have thoroughly investigated the electron thermalization dynamics of both Au and $Ag_{50}Au_{50}$ NPs using fs transient absorption spectroscopy. These NPs were achieved using the technique of ultrafast laser ablation in liquid (ULAL) technique. We observed a fast internal thermalization of non-Fermi electron distribution in Au and $Ag_{50}Au_{50}$ NPs. The measured decay times confirm the faster response from $Ag_{50}Au_{50}$ alloy nanoparticles compared to pure Au NPs. Furthermore, the third order nonlinear optical (NLO) properties were also measured using the Z-scan technique at 800 nm wavelength with femtosecond, kHz pulses.

4.2 Experimental Details

4.2.1 Au and Ag-Au Nanoparticles Fabrication

Gold and silver-gold NPs were fabricated using the technique of fs laser ablation of the bulk targets ($Au/Ag_{50}Au_{50}$) immersed in the liquid. The bulk targets of Au and $Ag_{50}Au_{50}$ (locally purchased with a purity of 99% and thickness of 1 mm) were immersed in distilled water (DW) and irradiated by ultrafast laser pulses from a fs amplifier (800 nm, 1 kHz, ~50 fs). The input laser pulses were focused on to the target using a plano-convex lens (focal length of 100 mm), which was placed in 5 ml of DW. The height of covered liquid layer above the surface of target was estimated to be 6 mm. During the ablation process, the target was translated using an X-Y motorized stage which was computer-controlled. The stage velocities used were 0.1 mm/s in both the directions of X and Y. The experiments were performed with an input pulse energy of 500 µJ. The estimated spot size on the target surface was ~100 µm. Post fabrication, all the NPs were collected in air-tightened glass bottles (to avoid moisture) and stored at the room temperature. The NPs UV-visible absorption studies were performed using a Perkin Elmer Lambda 750 spectrometer in the wavelength range of 250 nm-1000 nm. Morphological studies of the generated NPs were achieved using a high-resolution transmission electron microscope (HRTEM) along with selected area diffraction patterns (SAED). The NP compositions and line map images were obtained by field emission scanning electron microscope (FESEM) and energy dispersive X-ray spectroscopy (EDX) techniques. Femtosecond transient absorption measurements were performed using a transient absorption spectrometer (HELIOS) based on a femtosecond laser system. The complete experimental details are discussed in chapter 2. The energy of the pump laser kept at 1 µJ-2 µJ. The transmitted probe beam was focused on to an optical fiber connected to a spectrometer/CCD combination. We have measured the contributions from water/cuvette in all the measurements and found them to be negligible.

4.3 Results and Discussion

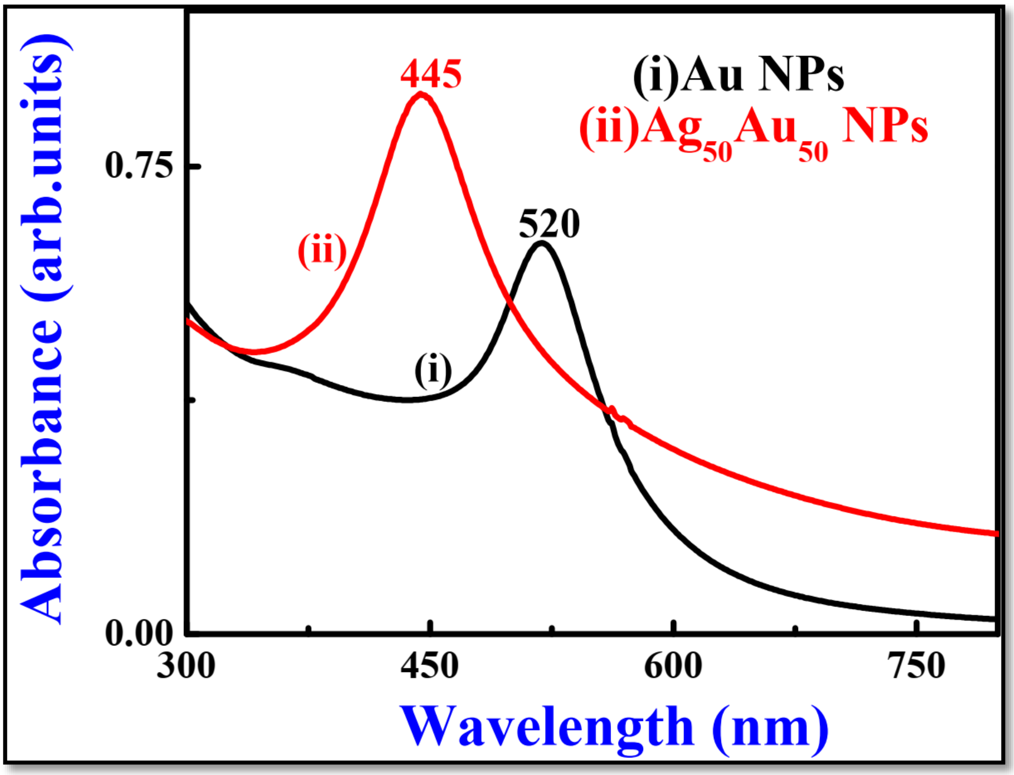

Figure 4.1 UV-Visible absorption spectra of the as-fabricated NPs (i) Au (ii) $Au_{50}Ag_{50}$ obtained in DW using fs laser ablation with a pulse energy of 500 µJ.

Figure 4.1 illustrates the UV-Visible absorption spectra of the as-fabricated NPs (in DW) obtained using fs ablation. As is evident from data illustrated in the figure 4.1, a single plasmon peak was observed in the vicinity of 445 nm for $Ag_{50}Au_{50}$ NPs, clearly indicating that there were no core-shell NPs in the obtained colloidal solutions. We generally expect two plasmon bands if there were any core-shell type of NPs in contrast with the Ag-Au bimetallic NPs.

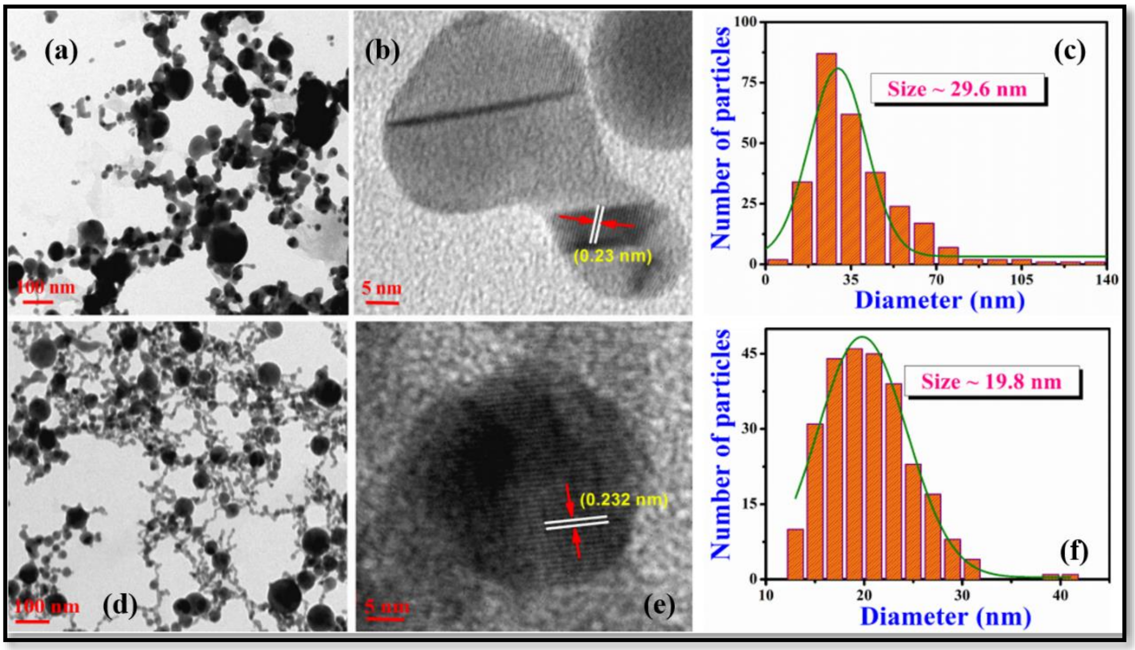

Figure 4.2 TEM, HRTEM and size distribution images of as-fabricated NPs (a, b, and c) Au, (d, e and f) $Ag_{50}Au_{50}$, respectively. Inset of (b) and (e) shows their corresponding lattice parameters of Au and $Ag_{50}Au_{50}$ NPs, respectively.

From figure 4.1 data it is also evident that the observed absorption maxima at 520 nm demonstrating the formation of spherical Au NPs. Furthermore, the observed plasmon band for bimetallic NPs was located exactly in region between that of the pure Ag and Au NPs, which is in excellent agreement with most of the earlier reports data. In one of our earlier reports, we had clearly demonstrated a smooth tuning of the bimetallic NPs plasmon bond while changing the proportion of Au (in alloy) in other laser ablation experiments.[29-30] The morphological data and crystallographic phases of as-fabricated NPs were obtained from the TEM and HRTEM data analysis, respectively. Figures 4.2(a) and 4.2(b) illustrate the TEM, HRTEM micrographs of the obtained Au NPs. Most of the obtained NPs had spherical shape with a few interconnected structures. The NPs diameters were estimated to be in 10-140 nm range. Figure 4.2(b) inset shows the interplanar spacing of Au NPs (of 0.23 nm), which corresponds to the Miller plane (111). Figures 4.2(d), 4.2(e) illustrate the TEM, HRTEM images of $Ag_{50}Au_{50}$ NPs wherein the diameters were estimated to be in the 15-50 nm range. Inset of figure 4.2(e) depicts the lattice plane separation of 0.232 nm for $Ag_{50}Au_{50}$ NPs, which is attributed to the Miller plane (111). Moreover, the $Ag_{50}Au_{50}$

interplanar separation was found to be comparable to the pure Ag and Au phases due to the similar lattice constants of Ag and Au [a = 4.09 Å for Ag; a = 4.08 Å for Au]. The NPs mean size was estimated by counting more than 250 particles using the image-J software. The obtained mean sizes were estimated to be ~29.6 nm and ~19.8 nm for Au NPs [figure 4.2(c)] and $Ag_{50}Au_{50}$ NPs [figure 4.2(f)], respectively.

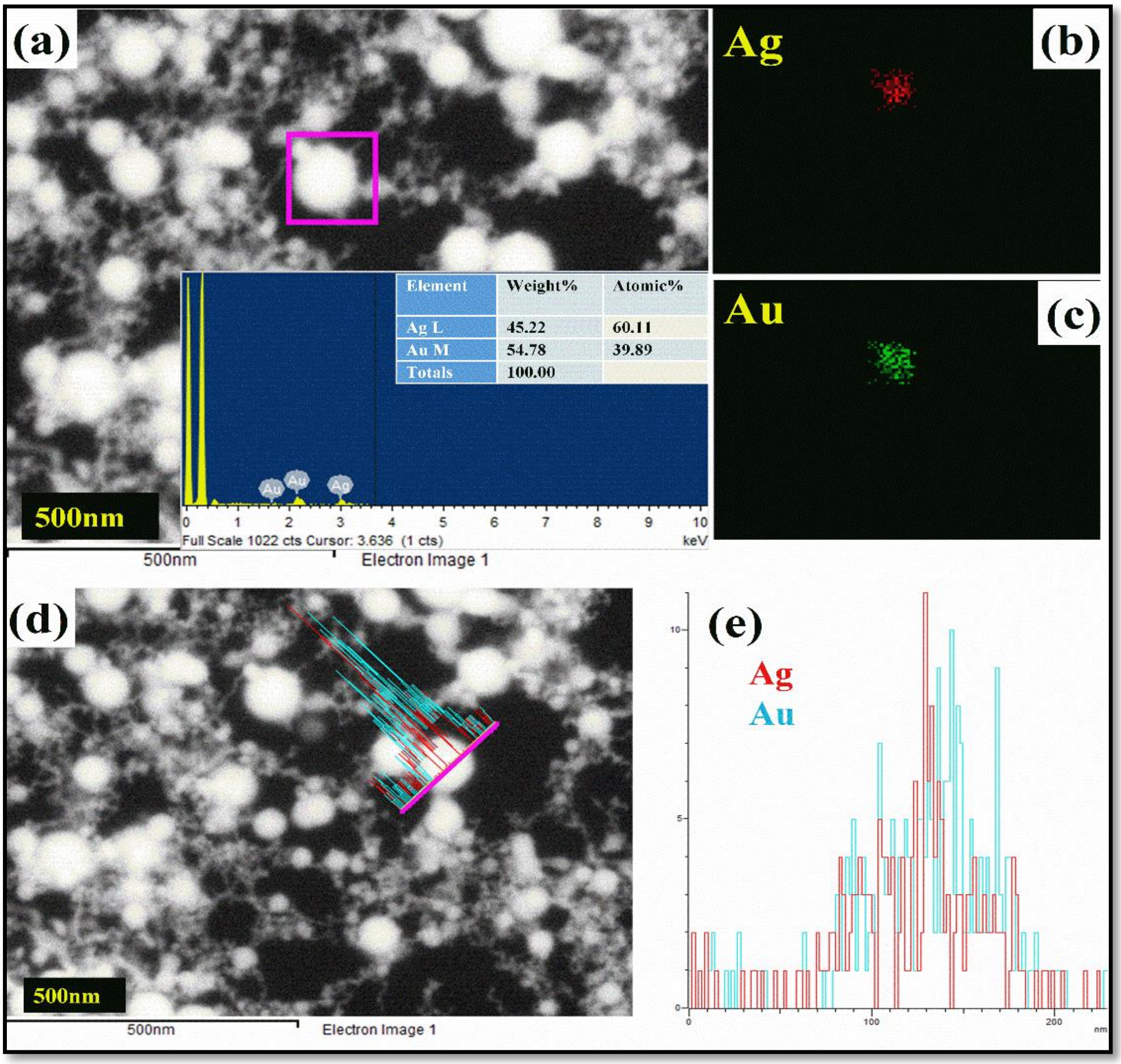

Element	Weight%	Atomic%
Ag L	45.22	60.11
Au M	54.78	39.89
Totals	100.00	

Figure 4.3 (a) FESEM image of $Ag_{50}Au_{50}$ NPs with a single map of NP (pink color box) and inset demonstrating the EDS spectra (b) EDS map of Ag (c) EDS map of Au (d) Line profile of the $Ag_{50}Au_{50}$ particle indicating the presence of Ag and Au (e) Intensity distribution of both the atoms, Ag and Au.

Further, the FESEM-EDX mapping was accomplished on an $Ag_{50}Au_{50}$ single particle to identify the distribution/composition of both atoms present. Figure 4.3(a) illustrates the EDS map on the single particle ($Ag_{50}Au_{50}$ NP) presented with rectangular box (pink color) and parts (b) and (c) of figure 4.3 established the presence of both atoms [Ag (representing the red one), Au (representing the green one)]. The EDX spectra presented in the inset of figure 4.4(a) clearly demonstrates the presence of individual Ag and Au atoms and their composition with weight percentages of 45.2% and 54.7%, respectively. Figures 4.3(d), 4.3(e) depict the data from a line scan on single NP, clearly signifying the particle comprised of both Ag and Au atoms. The formation of bimetallic NPs during laser ablation of any alloy target can be understood as follows. When an intense, focused fs pulse interacts with the target (in the presence of a liquid) extremely high temperatures/pressures are created at the target-liquid interface. During the laser irradiation atoms and/or ions will be ejected through the vaporization followed by the formation of cohort of dense metal atoms (Ag and Au) near the focal spot. The ejected metal atoms will subsequently aggregate and generate the bimetallic NPs due to a strong interaction between the individual metal atoms and the solvent/metal. Therefore, the formed bimetallic NPs will usually be homogeneous owing to the thermodynamically favorable mixing process at any proportion.[31]

4.3.1 Transient absorption

Figures 4.4(a) and 4.4.(b) illustrate the TA spectra of Au while (c) and (d) illustrate that of $Ag_{50}Au_{50}$ NPs at different probe delay times. Subsequent to the laser excitation photo-bleach of the plasmonic band and a transient absorption spectrum at the wings of the bleached spectrum was observed. As we further increased the time delay between pump, probe pulses we observed a decay in the transient absorption spectra while the bleach spectrum recovered. However, with 400 nm excitation, pure Au NPs illustrated a negative band centered near 525 nm, which could possibly be due to the depletion of plasmon electrons. Another positive band at >600 nm could be accredited to absorption of thermally excited non-equilibrium electrons distribution near Fermi level. Near the intraband excitation (i.e. 800 nm wavelength) the positive absorption band at >600 nm disappeared [clearly seen in the figure 4.4(b) data] suggesting the oscillation of conduction band electrons. In the case of $Ag_{50}Au_{50}$ NPs, an intense photo-bleach spectrum was observed near ~450 nm and a photo-induced absorption at >500 nm wavelengths with both intraband and interband excitations.

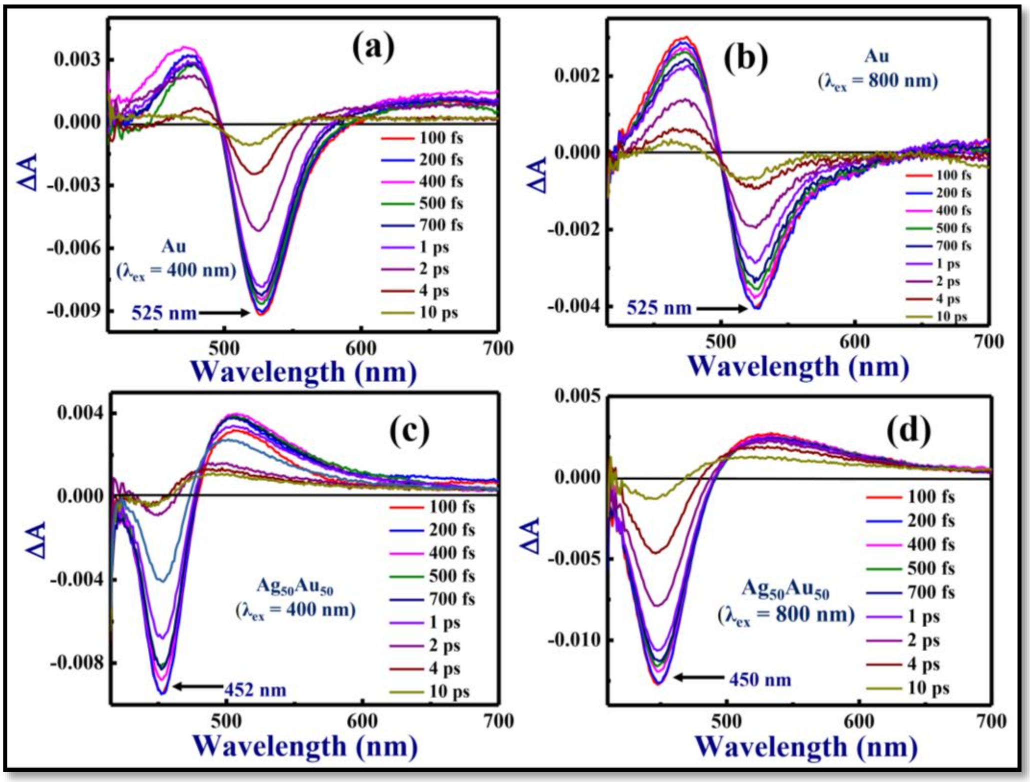

Figure 4.4 Transient absorption spectra of (a, b) Au and (c, d) Au-Ag NPs in DW pumped at 400 nm and 800 nm wavelength and the insets show their corresponding kinetic spectra of surface plasmon.

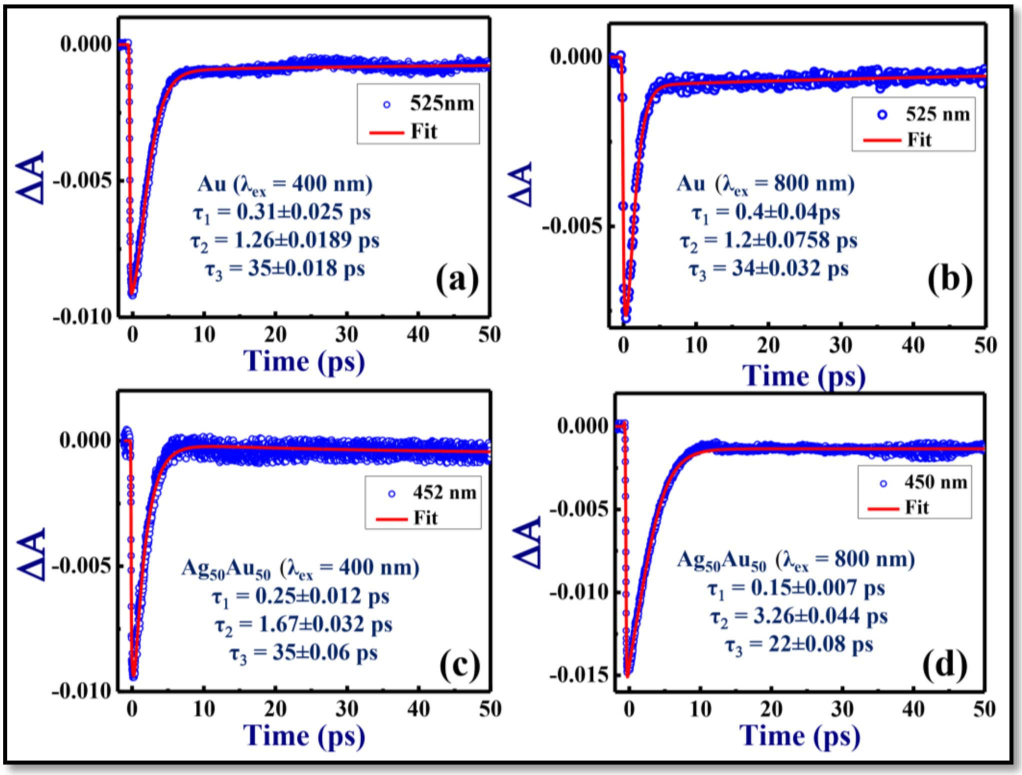

Figure 4.5 The intrinsic Plasmon bleach recovery of (a, b) Au and (c, d) $Ag_{50}Au_{50}$ NPs. Open circles are the experimental data points while the solid curves are theoretical fits.

The representative kinetics of the photo-bleached plasmonic bands was fitted using a tri-exponential function given by $(A(\lambda, t) = \sum_i^n A_i \, . \, e^{\frac{-(t-t_0)}{\tau_i}} \otimes \frac{1}{\sigma 2\sqrt{2}} e^{-\frac{t^2}{\sigma^2}})$ convolved with a Gaussian-shaped instrument response function (IRF). Three lifetimes/constants were required to satisfactorily fit the transient kinetic data of both Au and $Ag_{50}Au_{50}$ NPs. The data obtained from the fits to the experimental data is summarized in Table 4.1. With both 400 nm, 800 nm excitation $Ag_{50}Au_{50}$ NPs exhibited a faster response in comparison with pure Au NPs and is apparent from the figure 4.5 data. The obtained three lifetimes were ascribed to the (a) internal electron-electron (b) electron-phonon and (c) phonon-phonon scattering mechanisms, respectively.[32-35] It is evident that the positive absorption above 600 nm, referred to as the interband excitation induced plasmon (EIP),[10] decayed slowly (~3.5 ps) when compared to the intrinsic plasmon peak. As we further increased the time delay to 20 ps the intrinsic plasmon (IP) peak was found to be blue shifted by 8 nm with 400 nm pumping, possibly due to the influence of EIP on IP.

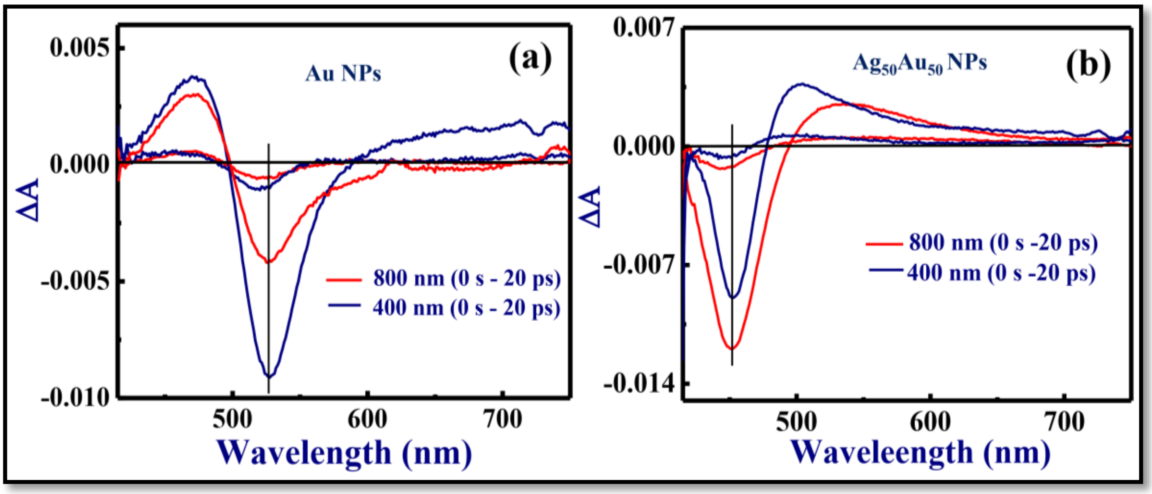

Figure 4.6 Transient absorption spectra of (a) Au and (b) $Au_{50}Ag_{50}$ NPs at delay increasing from 0 and 20 ps for 400 nm and 800 nm pump wavelength.

The TA spectra of Au and $Ag_{50}Au_{50}$ alloy NPs at 400 nm, 800 nm excitations are presented in figures 4.6(a) and 4.6(b). The $Ag_{50}Au_{50}$ alloy NPs data depicted an intrinsic plasmon photo-bleach peak near 450 nm along with a positive absorption EIP like process above 490 nm. The photo-bleach (PB) spectra band was observed to be broader with 800 nm excitation when compared to that of the data obtained with 400 nm excitation. The positive peak decayed faster at interband excitation with retreived lifetimes of 1.94 ps and 7.6 ps. The electron dynamic processes of the bleached plasmonic band illustrated a faster electron–electron scttering compared to that of pure Au Nps (figure 4.5). From the figure 4.6(b) data we observed that with an increase in delay, the bleached plasmonic band recovered with decreasing positive abosrption while no change in the resonant bleached spectrum was observed.

Time constants	**Au (λ_{ex} = 400 nm)**	**Au (λ_{ex} = 800 nm)**	**$\mathrm{Ag_{50}Au_{50}}$ (λ_{ex} = 400 nm)**	**$\mathrm{Ag_{50}Au_{50}}$ (λ_{ex} = 800 nm)**
τ_1	0.31±0.03 ps	0.4±0.04ps	0.25±0.01 ps	0.15±0.01 ps
τ_2	1.26±0.02 ps	1.2±0.08 ps	1.67±0.03 ps	3.26±0.04 ps
τ_3	35±0.02 ps	34±0.03 ps	35±0.06 ps	22±0.08 ps

Table 4.1 Individual decay constants of Au and $\mathrm{Ag_{50}Au_{50}}$ with intraband (800 nm) and Interband (400 nm) excitation.

4.3.2 NLO Studies

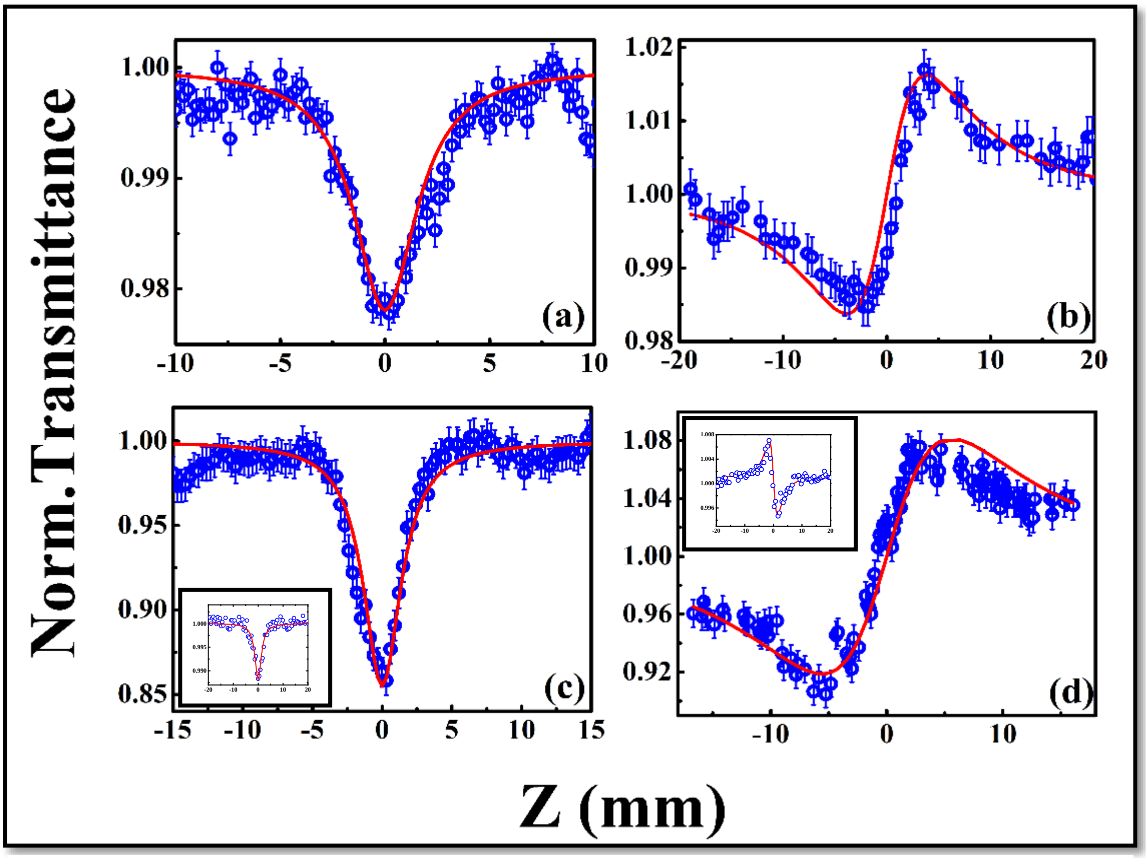

Figure 4.7 Open (a) and (c), closed (b) and (d) aperture Z-scan curves for laser ablated Au and $\mathrm{Ag_{50}Au_{50}}$ NPs, respectively. Insets of (c) and (d) illustrate the solvent (water) NLO response. Open circles are the experimental data points while the solid curves are theoretical fits.

The NLO properties of synthesized Au, $Ag_{50}Au_{50}$ NPs third-order were investigated using the standard Z-scan technique with 800 nm fs pulses. The complete experimental details can be found in the experimental chapter.[36] Figures 4.7(a)-(d) illustrate the open and closed aperture Z-scan data of Au and $Ag_{50}Au_{50}$ NPs measured at an input peak intensity of 40 GW/cm^2. Figures 4.7(a), (c) illustrate the open aperture Z-scan curves obviously depicting a reverse saturable absorption (RSA) type of behavior for all the NPs. The obtained data were fitted using the standard two-photon absorption (2PA) equation.[36] The estimated values of β were 0.4×10^{-12} and 5.0×10^{-12} m/W for Au and $Ag_{50}Au_{50}$ NPs, respectively. From the obtained 2PA values $Ag_{50}Au_{50}$ alloy NPs clearly shows stronger NLO coefficients compared to pure Au NPs.

Figures 4.7(b) and 4.7(d) illustrate the closed aperture Z-scan curves for Au and $Ag_{50}Au_{50}$ NPs, respectively. The data manifests the self-focusing effect and the data were again fitted using the standard equations.[36] The normalized transmittance data depicted a valley followed by a peak clearly suggesting that the sample possessed a positive nonlinearity. The obtained values of n_2 were 3.2×10^{-20} m^2/W and 1.6×10^{-19} m^2/W for Au and Ag-Au alloy NPs, respectively. Because of the errors in fluctuations of laser power and estimation of beam waist along with fitting procedures a ~10% error bar was considered to represent the errors in analysis. Ganeev et al. recently investigated the NLO properties of Ag NPs prepared by laser ablation in various liquids and calculated the nonlinear coefficients to be 3×10^{-9} cm/W at 397.5 nm and 8×10^{-9}cm/W at 795 nm.[37-38] Further, they have also studied the NLO coefficients of Au NPs[11] and the magnitudes were found to be 8×10^{-14} m^2/W and 1.7×10^{-10} m/W.[39] The NLO coefficients obtained from the present study are summarized in table 4.2. The NLO coefficients of the metal colloids mainly depend on the metal (size and shape), matrix and the plasmon resonance. Further, the dimensional reduction of the conduction electrons and the interband/intraband transitions (which leads to bleaching of the plasmon band) certainly determine the absorption properties.[40-42] Recently, Palpant et al.[43] demonstrated the influence of pulse duration on the absorption cross section of the gold nanorods which shows the increase in absorption cross section with sub picosecond pulses. Here, the obtained NLO parameters have contributions both from the metal NPs and the solvent (water) and the obtained NLO coefficients are relatively similar to the differently synthesized metal NPs.[11, 44-46] Apart from the oxide layer formation on laser ablated NPs in liquid the mechanism of LAL are robust and chemical free, which can be used for optical limiting (OL), saturable absorbers and biological applications. Sánchez-Dena et.al.[47] have investigated the size dependence of NLO response of Au NPs with size 14.2 nm, 13.4 nm and 5.1 nm using 6 ps laser pulses at 532 nm, and they have showed a size dependence nonlinear absorption and size independent nonlinear refraction with increasing size. Additionally, Mostafavi et al.[48] have demonstrated a size-dependent NLO response of Au NPs. Their data suggested that the OL strength increased with sizes increasing from 15 nm to 25 nm. However, they observed that with a further increase in size, the OL performance decreased for NPs (especially with sizes above 50 nm). Therefore, when the size of the Au NPs is less than or equal to the surface layer of NPs the absorption induced (nonlinear) scattering is higher. Hence, the absorbed energy is transferred from NPs to the solvent leading to the formation of solvent bubbles and, consequently, the OL will be more effective. When the size is larger than the surface layer of NPs, the absorbed energy will transfer to core of NPs so the less transfer of energy to solvent which makes the OL weaker in larger NPs.[47-48] In case of Au NPs the overlap of Interband absorption and SPR absorption decreases the plasmon excitation. But, in case of Ag NPs the interband absorption (which is below 300 nm) is far from the SPR absorption (which is near 400 nm). Therefore, the plasmon excitation is expected to be efficient in Ag NPs when compared to Au NPs.[49-52] The NLO properties of these NPs arise mainly from the (a) free carrier absorption (b) plasmon bleaching and (c) migration of NPs at higher intensities. However, more detailed studies are essential to understand and isolate these effects in different metal NPs, which can be achieved using high repetition rate laser pulses and different pulse durations (ns to fs).

NPs	**β (m/W)**	**n_2 (m²/W)**	**χ^{I} (m²/V²)**	**$\chi^{(I)}$ (m²/V²)**	**$\chi^{(3)}$ (m²/V²)**	**$\chi^{(3)}$ (esu)**
Au	0.4×10^{-12}	3.2×10^{-20}	3.0×10^{-22}	2.7×10^{-22}	4.0×10^{-22}	2.8×10^{-14}
$Ag_{50}Au_{50}$	5.0×10^{-12}	1.6×10^{-19}	1.5×10^{-21}	3.0×10^{-21}	3.3×10^{-21}	2.4×10^{-13}
Water	8.1×10^{-14}	2.2×10^{-21}	2.1×10^{-23}	4.9×10^{-25}	2.1×10^{-23}	1.5×10^{-15}

Table 4.2 NLO coefficients of the Au and $Ag_{50}Au_{50}$ alloy NPs obtained at 800 nm wavelength using fs Z-scan data.

4.4 Conclusions

1. We have successfully synthesized the Au, $Au_{50}Ag_{50}$ composite NPs with an average diameter of 10-20 nm using fs LAL process.
2. The electron-electron relaxation times were obtained for $Ag_{50}Au_{50}$ alloy NPs had a fast response at both inter and intraband excitation.
3. Both the NPs had similar electron-phonon relaxation times, which suggests a homogeneity in the composite material.
4. The obtained electron dynamics from these NPs exhibited faster response when compared to other studies on gold and Au-Ag nanocomposite materials.[25-27]
5. The third-order NLO susceptibility of alloy NPs had stronger values compared to pure Au NPs (measured at 800 nm).
6. The tunability of the plasmonic band along with the fast response of these nanocomposite materials qualifies them for use in optical switching devices, biological imaging applications.
7. We could not, however, study the properties of pure Ag NPs due to their absorption in the UV region. Those studies were not possible with our experimental conditions due to the lack of an excitation source.

References

1. Li, Y.; Lan, J. Y.; Liu, J.; Yu, J.; Luo, Z.; Wang, W.; Sun, L., Synthesis of Gold Nanoparticles on Rice Husk Silica for Catalysis Applications. *Industrial & Engineering Chemistry Research* **2015**, *54*, 5656-5663.
2. Sung, K.-M.; Mosley, D. W.; Peelle, B. R.; Zhang, S.; Jacobson, J. M., Synthesis of Monofunctionalized Gold Nanoparticles by Fmoc Solid-Phase Reactions. *Journal of the American Chemical Society* **2004**, *126*, 5064-5065.
3. Suchomel, P.; Kvitek, L.; Prucek, R.; Panacek, A.; Halder, A.; Vajda, S.; Zboril, R., Simple Size-Controlled Synthesis of Au Nanoparticles and Their Size-Dependent Catalytic Activity. *Scientific Reports* **2018**, *8*.
4. Heilweil, E. J.; Hochstrasser, R. M., Nonlinear Spectroscopy and Picosecond Transient Grating Study of Colloidal Gold. *The Journal of Chemical Physics* **1985**, *82*, 4762-4770.
5. Bloemer, M. J.; Haus, J. W.; Ashley, P. R., Degenerate Four-Wave Mixing in Colloidal Gold as a Function of Particle Size. *Journal of the Optical Society of America B* **1990**, *7*, 790.
6. Kerker, M., *The Scattering of Light and Other Electromagnetic Radiation: Physical Chemistry: A Series of Monographs*; Academic press, 2013; Vol. 16.
7. Bohren, C. F.; Huffman, D. R., *Absorption and Scattering of Light by Small Particles*; Wiley, 1998.
8. Rana, A.; Gupta, N.; Lochan, A.; Sharma, G. D.; Chand, S.; Kumar, M.; Singh, R. K., Charge Carrier Dynamics and Surface Plasmon Interaction in Gold Nanorod-Blended Organic Solar Cell. *Journal of Applied Physics* **2016**, *120*, 063102.
9. Hartland, G. V.; Besteiro, L. V.; Johns, P.; Govorov, A. O., What's So Hot About Electrons in Metal Nanoparticles? *ACS Energy Letters* **2017**, *2*, 1641-1653.
10. Zhang, X.; Huang, C.; Wang, M.; Huang, P.; He, X.; Wei, Z., Transient Localized Surface Plasmon Induced by Femtosecond Interband Excitation in Gold Nanoparticles. *Scientific Reports* **2018**, *8*.
11. Zhang, Y.-x.; Wang, Y.-h., Nonlinear Optical Properties of Metal Nanoparticles: A Review. *RSC Advances* **2017**, *7*, 45129-45144.
12. Ren, M.; Jia, B.; Ou, J.-Y.; Plum, E.; Zhang, J.; MacDonald, K. F.; Nikolaenko, A. E.; Xu, J.; Gu, M.; Zheludev, N. I., Nanostructured Plasmonic Medium for

Terahertz Bandwidth All-Optical Switching. *Advanced Materials* **2011**, *23*, 5540-5544.

13. Lin, Y.; Zhang, X., Ultrafast Multipolar Plasmon for Unidirectional Optical Switching in a Hemisphere-Nanoshell Array. *Advanced Optical Materials* **2017**, *5*, 1601088.
14. Guzelturk, B.; Utterback, J. K.; Coropceanu, I.; Kamysbayev, V.; Janke, E. M.; Zajac, M.; Yazdani, N.; Cotts, B. L.; Park, S.; Sood, A., Nonequilibrium Thermodynamics of Colloidal Gold Nanocrystals Monitored by Ultrafast Electron Diffraction and Optical Scattering Microscopy. *ACS Nano* **2020**, *14*, 4792-4804.
15. Zhou, M.; Zhong, J.; Wang, S.; Guo, Q.; Zhu, M.; Pei, Y.; Xia, A., Ultrafast Relaxation Dynamics of Luminescent Rod-Shaped, Silver-Doped Ag X Au25–X Clusters. *The Journal of Physical Chemistry C* **2015**, *119*, 18790-18797.
16. Jiang, J.; Wu, T.; Gao, Y. In *Size-Dependent Nonlinear Absorption Properties and Ultrafast Dynamics of Ag Nanoparticles*, AOPC 2019: Nanophotonics, International Society for Optics and Photonics: 2019; p 113360M.
17. Takeda, Y.; Plaksin, O. A.; Lu, J.; Kishimoto, N., Optical Switching Performance of Metal Nanoparticles Fabricated by Negative Ion Implantation. *Nuclear Instruments and Methods in Physics Research Section B: Beam Interactions with Materials and Atoms* **2006**, *242*, 194-197.
18. Voisin, C.; Del Fatti, N.; Christofilos, D.; Vallée, F., Ultrafast Electron Dynamics and Optical Nonlinearities in Metal Nanoparticles. *The Journal of Physical Chemistry B* **2001**, *105*, 2264-2280.
19. Averitt, R. D.; Westcott, S. L.; Halas, N. J., Ultrafast Electron Dynamics in Gold Nanoshells. *Physical Review B* **1998**, *58*, R10203-R10206.
20. Elsayed-Ali, H. E.; Juhasz, T.; Smith, G. O.; Bron, W. E., Femtosecond Thermoreflectivity and Thermotransmissivity of Polycrystalline and Single-Crystalline Gold Films. *Physical Review B* **1991**, *43*, 4488-4491.
21. Wright, O. B., Ultrafast Nonequilibrium Stress Generation in Gold and Silver. *Physical Review B* **1994**, *49*, 9985-9988.
22. Schoenlein, R. W.; Lin, W. Z.; Fujimoto, J. G.; Eesley, G. L., Femtosecond Studies of Nonequilibrium Electronic Processes in Metals. *Physical Review Letters* **1987**, *58*, 1680-1683.

23. Sun, C. K.; Vallée, F.; Acioli, L. H.; Ippen, E. P.; Fujimoto, J. G., Femtosecond-Tunable Measurement of Electron Thermalization in Gold. *Physical Review B* **1994**, *50*, 15337-15348.
24. Fann, W. S.; Storz, R.; Tom, H. W. K.; Bokor, J., Direct Measurement of Nonequilibrium Electron-Energy Distributions in Subpicosecond Laser-Heated Gold Films. *Physical Review Letters* **1992**, *68*, 2834-2837.
25. Fujimoto, J. G.; Liu, J. M.; Ippen, E. P.; Bloembergen, N., Femtosecond Laser Interaction with Metallic Tungsten and Nonequilibrium Electron and Lattice Temperatures. *Physical Review Letters* **1984**, *53*, 1837-1840.
26. Johns, P.; Beane, G.; Yu, K.; Hartland, G. V., Dynamics of Surface Plasmon Polaritons in Metal Nanowires. *The Journal of Physical Chemistry C* **2017**, *121*, 5445-5459.
27. Hua, Y.; Chandra, K.; Dam, D. H. M.; Wiederrecht, G. P.; Odom, T. W., Shape-Dependent Nonlinear Optical Properties of Anisotropic Gold Nanoparticles. *The Journal of Physical Chemistry Letters* **2015**, *6*, 4904-4908.
28. Karam, T. E.; Smith, H. T.; Haber, L. H., Enhanced Photothermal Effects and Excited-State Dynamics of Plasmonic Size-Controlled Gold–Silver–Gold Core–Shell–Shell Nanoparticles. *The Journal of Physical Chemistry C* **2015**, *119*, 18573-18580.
29. Podagatlapalli, G. K.; Hamad, S.; Rao, S. V., Trace-Level Detection of Secondary Explosives Using Hybrid Silver–Gold Nanoparticles and Nanostructures Achieved with Femtosecond Laser Ablation. *The Journal of Physical Chemistry C* **2015**, *119*, 16972-16983.
30. Byram, C.; Soma, V. R., 2,4-Dinitrotoluene Detected Using Portable Raman Spectrometer and Femtosecond Laser Fabricated Au–Ag Nanoparticles and Nanostructures. *Nano-Structures & Nano-Objects* **2017**, *12*, 121-129.
31. Lee, I.; Han, S. W.; Kim, K., Production of Au–Ag Alloy Nanoparticles by Laser Ablation of Bulk Alloys. *Chemical Communications* **2001**, 1782-1783.
32. Link, S.; Burda, C.; Wang, Z. L.; El-Sayed, M. A., Electron Dynamics in Gold and Gold–Silver Alloy Nanoparticles: The Influence of a Nonequilibrium Electron Distribution and the Size Dependence of the Electron–Phonon Relaxation. *The Journal of Chemical Physics* **1999**, *111*, 1255-1264.

33. Ahmadi, T. S.; Logunov, S. L.; El-Sayed, M. A., Picosecond Dynamics of Colloidal Gold Nanoparticles. *The Journal of Physical Chemistry* **1996**, *100*, 8053-8056.
34. Zarick, H. F.; Boulesbaa, A.; Talbert, E. M.; Puretzky, A.; Geohegan, D.; Bardhan, R., Ultrafast Excited-State Dynamics in Shape- and Composition-Controlled Gold–Silver Bimetallic Nanostructures. *The Journal of Physical Chemistry C* **2017**, *121*, 4540-4547.
35. Du, L. C.; Xi, W. D.; Zhang, J. B.; Matsuzaki, H.; Furube, A., Electron Transfer Dynamics and Yield from Gold Nanoparticle to Different Semiconductors Induced by Plasmon Band Excitation. *Chemical Physics Letters* **2018**, *701*, 126-130.
36. Krishnakanth, K. N.; Seth, S.; Samanta, A.; Venugopal Rao, S., Broadband Ultrafast Nonlinear Optical Studies Revealing Exciting Multi-Photon Absorption Coefficients in Phase Pure Zero-Dimensional Cs4pbbr6 Perovskite Films. *Nanoscale* **2019**, *11*, 945-954.
37. Ganeev, R. A.; Baba, M.; Ryasnyansky, A. I.; Suzuki, M.; Kuroda, H., Characterization of Optical and Nonlinear Optical Properties of Silver Nanoparticles Prepared by Laser Ablation in Various Liquids. *Optics Communications* **2004**, *240*, 437-448.
38. Ganeev, R. A.; Suzuki, M.; Baba, M.; Ichihara, M.; Kuroda, H., Low- and High-Order Nonlinear Optical Properties of Au, Pt, Pd, and Ru Nanoparticles. *Journal of Applied Physics* **2008**, *103*, 063102.
39. Philip, R.; Chantharasupawong, P.; Qian, H.; Jin, R.; Thomas, J., Evolution of Nonlinear Optical Properties: From Gold Atomic Clusters to Plasmonic Nanocrystals. *Nano Letters* **2012**, *12*, 4661-4667.
40. Dengler, S.; Kübel, C.; Schwenke, A.; Ritt, G.; Eberle, B., Near- and Off-Resonant Optical Limiting Properties of Gold–Silver Alloy Nanoparticles for Intense Nanosecond Laser Pulses. *Journal of Optics* **2012**, *14*, 075203.
41. Karavanskii, V. A.; Simakin, A. V.; Krasovskii, V. I.; Ivanchenko, P. V., Nonlinear Optical Properties of Colloidal Silver Nanoparticles Produced by Laser Ablation in Liquids. *Quantum Electronics* **2004**, *34*, 644-648.
42. Pan, H.; Chen, W.; Feng, Y. P.; Ji, W.; Lin, J., Optical Limiting Properties of Metal Nanowires. *Applied Physics Letters* **2006**, *88*, 223106.

43. Hou, X.; Djellali, N.; Palpant, B., Absorption of Ultrashort Laser Pulses by Plasmonic Nanoparticles: Not Necessarily What You Might Think. *ACS Photonics* **2018**, *5*, 3856-3863.
44. Novak, J. P.; Brousseau, L. C.; Vance, F. W.; Johnson, R. C.; Lemon, B. I.; Hupp, J. T.; Feldheim, D. L., Nonlinear Optical Properties of Molecularly Bridged Gold Nanoparticle Arrays. *Journal of the American Chemical Society* **2000**, *122*, 12029-12030.
45. Majles Ara, M. H.; Dehghani, Z.; Sahraei, R.; Daneshfar, A.; Javadi, Z.; Divsar, F., Diffraction Patterns and Nonlinear Optical Properties of Gold Nanoparticles. *Journal of Quantitative Spectroscopy and Radiative Transfer* **2012**, *113*, 366-372.
46. Ahmadi, N.; Poursalehi, R.; Kirilyuk, A.; Moravvej-Farshi, M. K., Effect of Gold Plasmonic Shell on Nonlinear Optical Characteristics and Structure of Iron Based Nanoparticles. *Applied Surface Science* **2019**, *479*, 114-118.
47. Sánchez-Dena, O.; Mota-Santiago, P.; Tamayo-Rivera, L.; Crespo-Sosa, A.; Oliver, A.; Reyes-Esqueda, J. A., Size- and Shape-Dependent Nonlinear Optical Response of Au Nanoparticles Embedded in Sapphire. In *Nonlinear Optics*, OSA: 2013.
48. Francois, L.; Mostafavi, M.; Belloni, J.; Delouis, J.-F.; Delaire, J.; Feneyrou, P., Optical Limitation Induced by Gold Clusters. 1. Size Effect. *The Journal of Physical Chemistry B* **2000**, *104*, 6133-6137.
49. Gurudas, U.; Brooks, E.; Bubb, D. M.; Heiroth, S.; Lippert, T.; Wokaun, A., Saturable and Reverse Saturable Absorption in Silver Nanodots at 532 Nm Using Picosecond Laser Pulses. *Journal of Applied Physics* **2008**, *104*, 073107.
50. Sun, Y.-P.; Riggs, J. E.; Rollins, H. W.; Guduru, R., Strong Optical Limiting of Silver-Containing Nanocrystalline Particles in Stable Suspensions. *The Journal of Physical Chemistry B* **1999**, *103*, 77-82.
51. Gao, Y.; Wu, W.; Kong, D.; Ran, L.; Chang, Q.; Ye, H., Femtosecond Nonlinear Absorption of Ag Nanoparticles at Surface Plasmon Resonance. *Physica E: Low-dimensional Systems and Nanostructures* **2012**, *45*, 162-165.
52. Zheng, C.; Ye, X.; Cai, S.; Wang, M.; Xiao, X., Observation of Nonlinear Saturable and Reverse-Saturable Absorption in Silver Nanowires and Their Silica Gel Glass Composite. *Applied Physics B* **2010**, *101*, 835-840.

Chapter 5 Ultrafast NLO Studies and Excited-state Dynamics of Soret-Band Excited D-π-D Porphyrins

Abstract

This chapter discusses the results obtained from ultrafast nonlinear optical (NLO) measurements and studies of excited-state dynamics of organic materials. These studies were performed in three diverse porphyrin molecules, which were designed in a D-π-D fashion (phenothiazine-porphyrin-phenothiazine) and possessing two different central metal ions [Zn(II), Cu(II)]. We have performed an extensive target analysis of the femtosecond (fs) transient absorption data obtained. The study conveyed the right exited state/species spectra of each process, and we could get respective lifetimes along with microscopic rate constants of each of the excited states. The obtained lifetime values were in the range of 0.25-33 ps: associated with relaxation with the S_n; 0.9-62 ps: associated with relaxation with Hot S_1 (to S_1); 1.5-6.2 ns: associated with relaxation from S_1; and finally, 1-1.25 μs: associated with relaxation from T_1 states. Furthermore, we observed that the third-order NLO coefficients [two-photon absorption (TPA), nonlinear refractive index (n_2)] of CPPHT and ZPPHT exhibited superior values compared to HPPHT obtained with ~50 fs, 1 kHz pulses at 800 nm. The magnitude of the TPA coefficients of the studied molecules was compared with some of the recently reported porphyrin molecules and was found to be more significant. The time-resolved degenerate four-wave mixing (DFWM) measurements confirmed a large magnitude plus an ultrafast response of the nonlinearity in these molecules, suggesting potential photonic and all-optical switching applications.

This chapter comprises data from the following publication:

1. "Femtosecond Transient Absorption Studies of Soret-Band Excited D-π-D Porphyrin Molecules and Third-order Nonlinear Optical Properties" **Katturi Naga Krishnakanth**, Govind Reddy, Chinmoy Biswas, Sai Santosh Kumar Raavi, Giribabu Lingamallu, Venugopal Rao Soma, *Optical Materials*, **107,** 110041, 2020.

5.1 Introduction

Porphyrins, phthalocyanines are organic molecules possessing fantastic chemical and thermal stabilities.[1-3] Alteration of the macrocyclic structure of porphyrins can significantly affect their chemical, physical, optical, and optoelectronic properties.[3-6] As a consequence, several research groups have been aiming to utilize porphyrins in artificial photo-devices such as photonic devices,[7] molecular switches,[8] and dye-sensitized solar cells (DSCs) for solar energy conversion.[5, 9, 10] Metalloporphyrins (MPs) have gained attention due to their functional universality, stability, and ease of chemical modification.[9] MPs have also been used as versatile substrates in various light-driven chemical reactions,[11,12] enabling the inter/intramolecular energy redistribution.[13] MPs have also been demonstrated as promising materials for the conversion of solar energy into electric energy in SCs.[14] Moreover, π-conjugated 2D organic molecules (e.g., phthalocyanines, porphyrins) demonstrated superior nonlinear optical (NLO) properties compared to other organic materials.[15-16] The optical properties of porphyrin molecules can be modulated simply by varying the central metal ion or the surrounding environment.[17-18] There exists great flexibility in modulating physicochemical attributes by synthetic substitutions on planar π-conjugated porphyrin ring and central metal ion, which can be incorporated into donor-acceptor assemblies. In general, donor-π-acceptor porphyrin systems possess good light-harvesting properties for solar cells and also have higher thermal stability and favorable electrical properties.[13,19] By changing the donor-π-acceptor design as sensitizers for DSSC applications to the donor-π-donor approach, porphyrins can be potential candidates as hole-transporting materials for optoelectronic applications.[20] The electron transfer dynamics is essential in many processes and has been a great research area relevant to solar energy conversion, information storage, catalysis, and NLO processes. Therefore, understanding the molecular level dynamics in an ultrafast time scale is important for fundamental science and applications of such molecules. Apart from this, the NLO properties of porphyrins have been studied extensively for their tremendous applications in many fields such as optical limiting, optical switching, storage, imaging, etc. arising mainly from the delocalized π-electrons. Incorporation of the metal ion into the porphyrin system helps the generation of a large number of delocalized π-electrons. Generally, organic molecules with electron donor and acceptor groups, which are connected to a large π-electron conjugation, demonstrate strong third-order NLO properties. The MPs offer a large change in ground and excited state dipole moments in response to a given electric field intensity, which is the fundamental reason behind the observed strong optical nonlinearities.[6,8,21] However, the applications of porphyrins are mostly associated with electronic transitions taking place in a broad spectral range, primarily from the Q-band transitions. Hence, it is crucial to study the excited state dynamics of porphyrins.[22-25] Particularly, the excited-state absorption (ESA) such as excited singlet or triplet absorption properties are subject to several investigations owing to their importance in applications such as all-optical switching and optical limiting.[26-27] It is also important to understand the excited state dynamics in porphyrin moieties because the nonlinear transmission properties of these molecules depend on the excited state energy transfer processes. Various time-resolved spectroscopic techniques such as time-resolved fluorescence by frequency upconversion and transient absorption (TA) are generally used to investigate the excited state dynamics and motion of vibrational wave packets in real-time. Herein, we report the results from the transient absorption studies and third-order NLO measurements of three phenothiazine-porphyrin-phenothiazine derivatives (D-π-D) porphyrin molecules [28] namely

- 3,3’-((10,20-bis(2,6-bis(octyloxy)phenyl)porphyrin-5,15-diyl)-bis(ethyne-2,1-diyl))bis(10-octyl-10H-phenothiazine) [hereafter referred to as **HPPHT**]

- 3,3’-((10,20-bis(2,6-bis(octyloxy)phenyl)porphyrin-5,15-diyl)-bis(ethyne-2,1-diyl))bis(10-octyl-10H-phenothiazine)-Cu [hereafter referred to as **CPPHT**] and

- 3,3’-((10,20-bis(2,6-bis(octyloxy)phenyl)porphyrin-5,15-diyl)bis-(ethyne-2,1-diyl))bis(10-octyl-10H-phenothiazine)-Zn(II) [hereafter referred to as **ZPPHT**].

Further, the conjugation effect on the third-order NLO coefficients is also discussed. The excited-state lifetimes, accomplished through fs transient absorption studies, have been investigated in detail. Additionally, the mechanisms of third-order NLO absorption and refraction effects are also examined. The superior NLO coefficients (TPA coefficients along with cross-sections and n_2) combined with the fast response times obtained for these molecules suggest these can be used in potential photonic applications (e.g., optical limiting, bio-imaging, all-optical signal processing).

5.2 Experimental Details

5.2.1 Synthesis

Both the starting materials 3-ethynyl-10-octyl-10*H*-phenothiazine (PTZ-E) and 5,15-bis(2,6-bis(octyloxy)phenyl)-10,20-dibromoporphyrin (Por-Br2) were synthesized following the methods reported in literature.[28] The free-base derivative (HPPHT) was obtained by Sonogashira coupling between PTZ-E and Por-Br2 using a Pd catalyst and the corresponding metallo derivatives were achieved by inserting metal into the porphyrin cavity. All three porphyrins were characterized using (a) elemental analysis(b) ^1H NMR and (c) MALDI-MS techniques. The obtained data and analysis confirmed the proposed molecular structures (Figures 5.1-5.6).

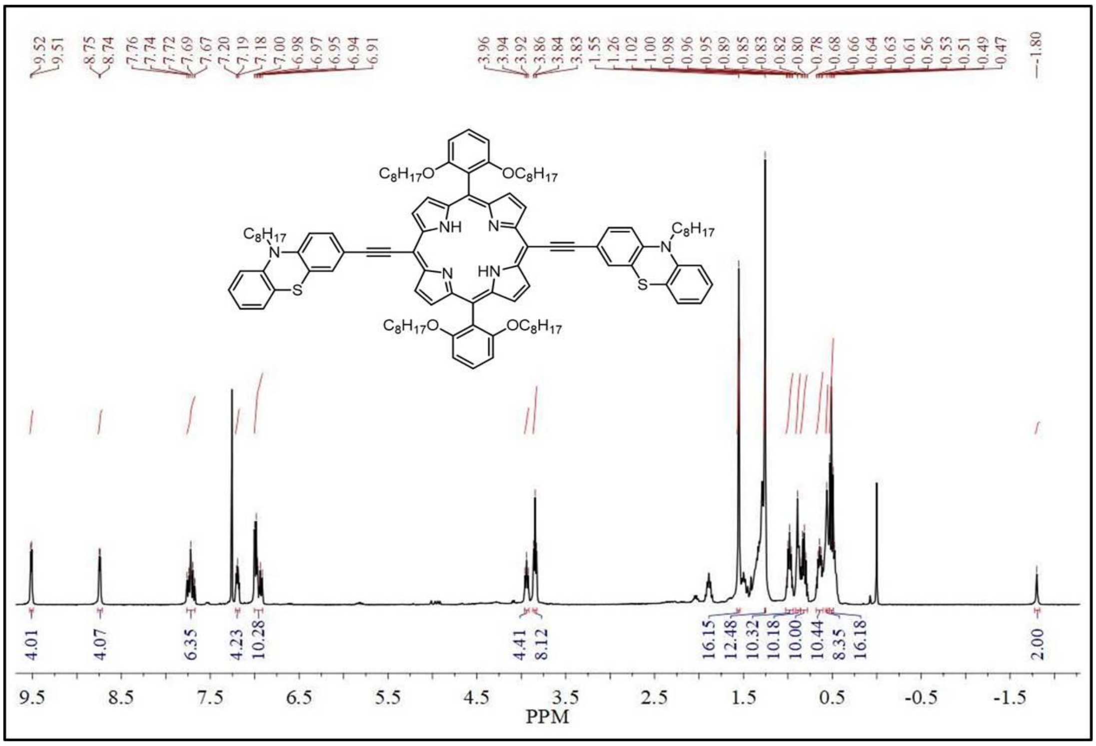

Figure 5.1 ^1H NMR spectra of HPPHT in $CDCl_3$.

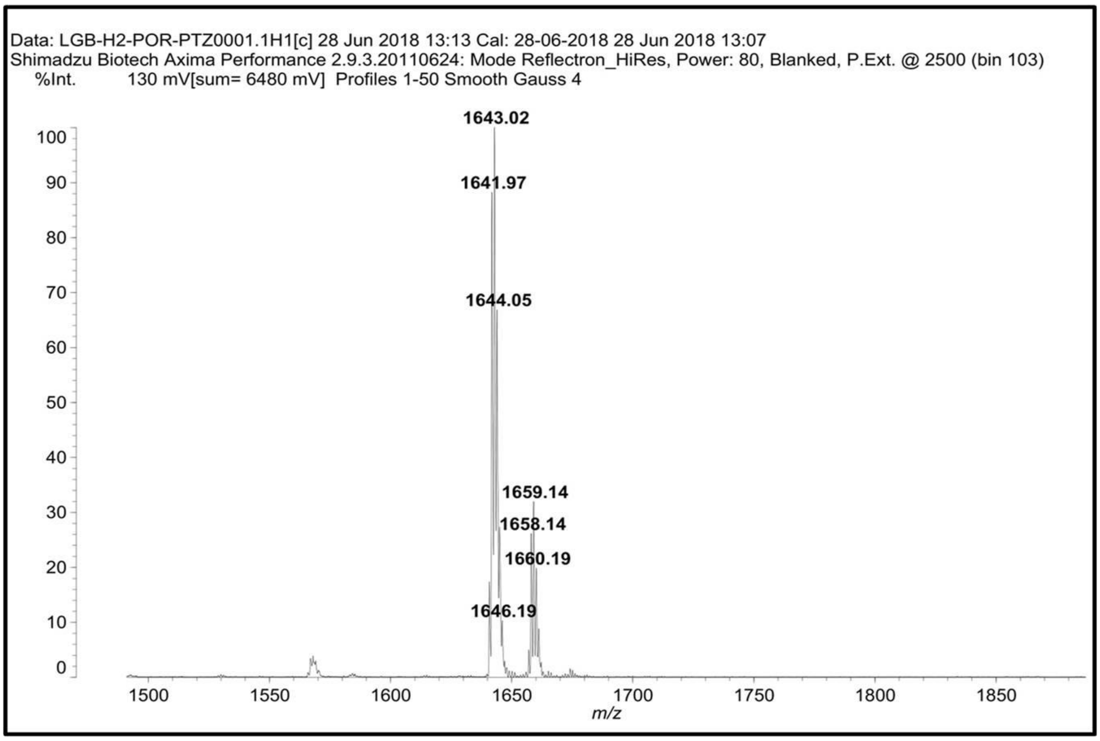

Figure 5.2 MALDI-TOF of the HPPHT.

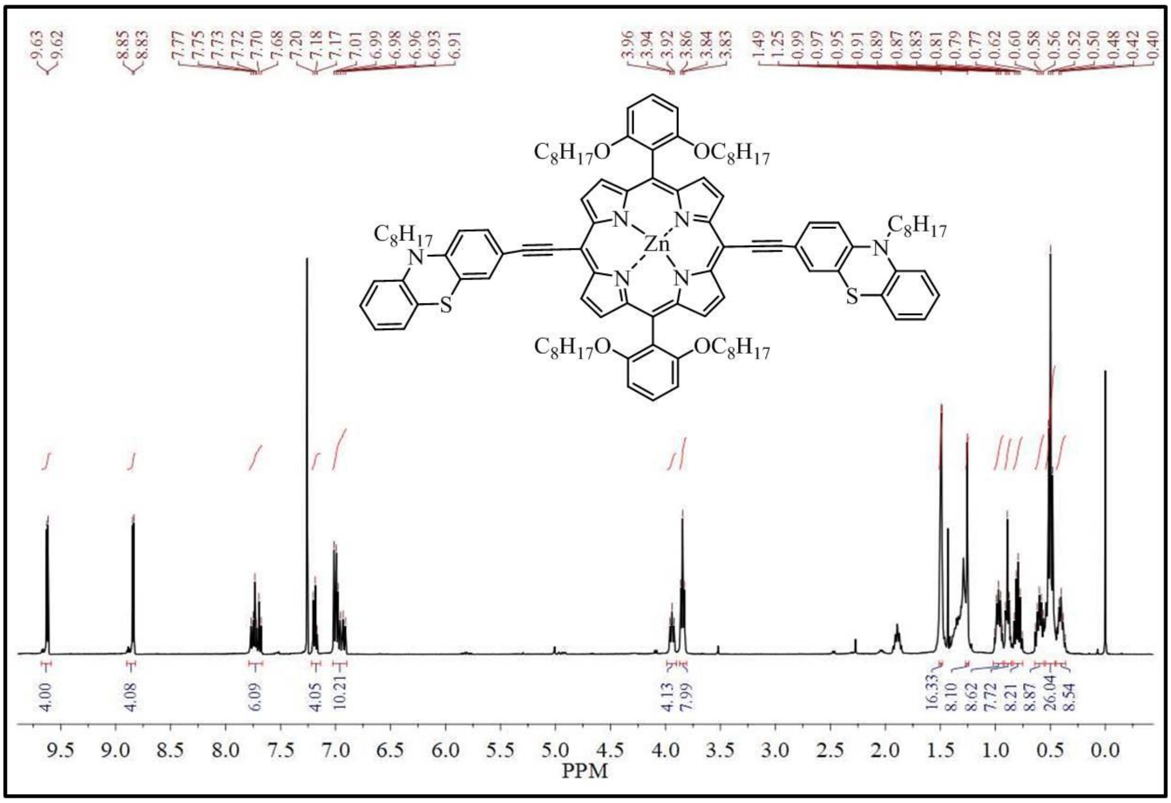

Figure 5.3 ^{1}H NMR spectra of ZPPHT in $CDCl_3$.

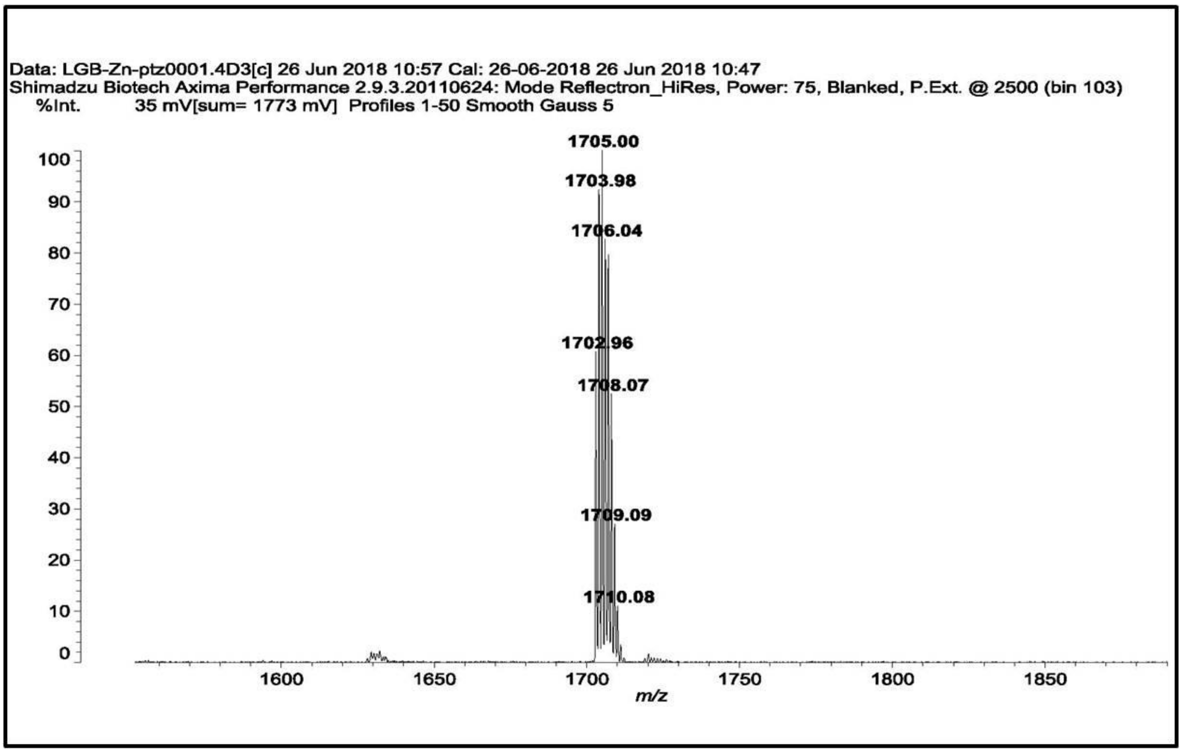

Figure 5.4 MALDI-TOF of the ZPPHT.

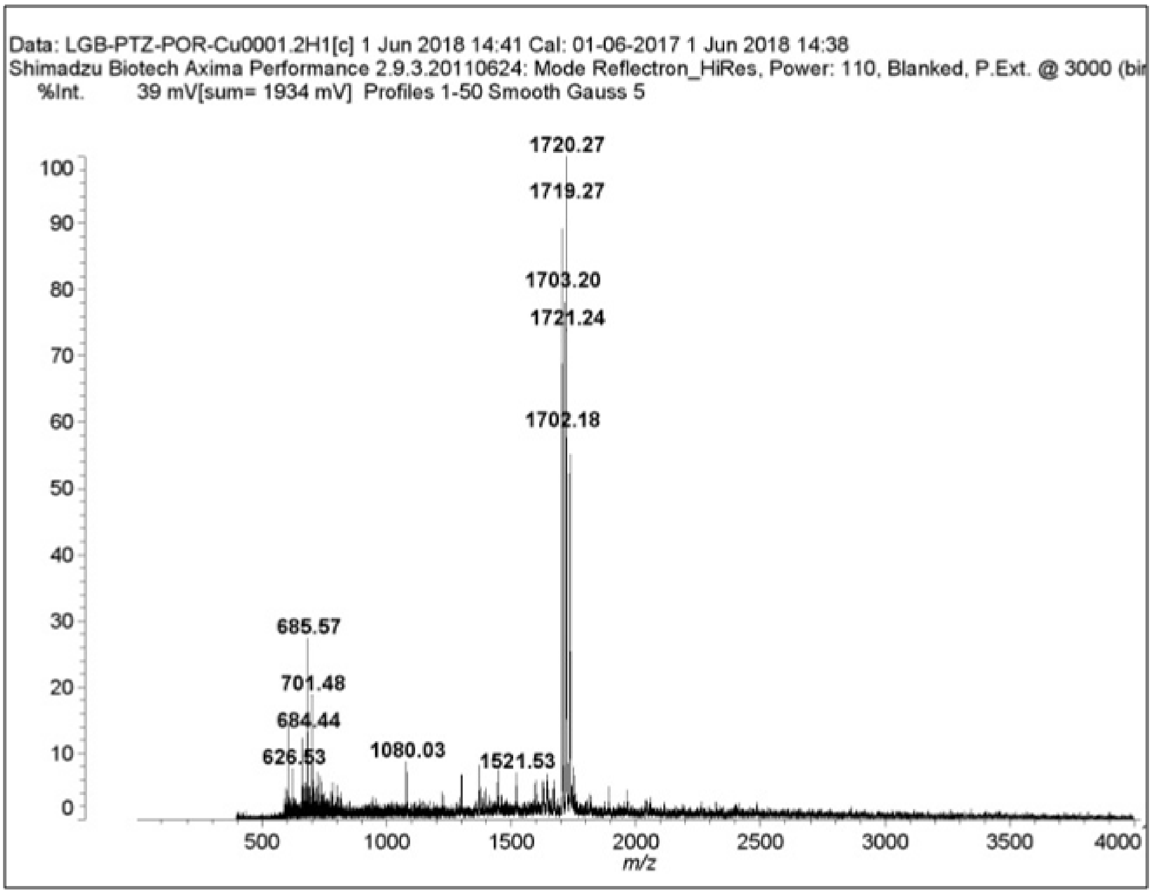

Figure 5.5 MALDI-TOF of the CPPHT.

Synthesis of 3,3’-((10,20-bis(2,6-bis(octyloxy)phenyl)porphyrin-5,15-diyl)-bis(ethyne-2,1-diyl))bis(10-octyl-10H-phenothiazine) [**HPPHT**]: We have adopted a slightly modified approach compared to that reported in the literature. Por-Br2 (0.500 g, 0.42 mmol) was dissolved in a mixture of 10 ml triethylamine (TEA) and 10 ml of dry tetrahydrofuran (THF) under an inert atmosphere. The resulting solution was purged with N_2 gas for ~15 minutes followed by the addition of CuI (0.020 g), and Tetrakis(triphenylphosphine)palladium(0) [$Pd(PPh_3)_4$] (0.10 g), which were heated to 60^oC. Subsequently, 3-ethyl-10-octyl-10H-phenothiazine (PtZ-E) (0.42 g, 1.25 mmol)) was dissolved in 3 ml of THF and added slowly with the help of a syringe, and a spontaneous colour change (brown to green) was observed. The progress of the reaction was monitored by TLC until all the starting materials were consumed. Later the reaction mixture was brought down to room temperature (RT) and the solvent was removed through rotary evaporation. Then the obtained crude material was dissolved in DCM, filtered and dried over anhydrous Na_2SO_4. The solvent removed and obtained solid was subjected to silica gel column chromatography Hexane: DCM (3:1 v/v) and recrystalized with methanol/DCM yielded 81% as reddish-green powder. Anal. Calcd. For $C_{108}H_{132}N_6O_4S_2$ % (1641.98): C, 78.98; H, 8.10; N,5.12. Found; C, 79.03; H, 8.19; N, 5.13. MALDI-TOF: m/z $[M]^+$calcd. For $C_{108}H_{132}N_6O_4S_2$, 1641.98; found, 1641.97. ^1H NMR (400 MHz, CDCl3) δ 9.50 (d, J = 4.6 Hz, 4H), 8.72 (d, J = 4.3 Hz, 4H), 7.76 – 7.67 (m, 6H), 7.20 – 7.18 (m, 4H), 7.00 – 6.91 (m, 10H), 3.94 (t, J = 7.0 Hz, 4H), 3.82 (t, J = 6.2 Hz, 8H), 1.55 (s, 16H), 1.24 (s, 12H), 1.02 – 0.95 (m, 10H), 0.89 (s, 10H), 0.80 (dt, J = 14.7, 7.3 Hz, 10H), 0.62 (dt, J = 14.0, 7.0 Hz, 10H), 0.54 (s, 8H), 0.50 (dd, J = 14.6, 7.4 Hz, 16H), -1.82 (s, 2H).

3,3’-((10,20-bis(2,6-bis(octyloxy)phenyl)porphyrin-5,15-diyl)-bis(ethyne-2,1-diyl))bis(10-octyl-10H-phenothiazine)-Cu [**CPPHT**] :150 mg (0.06 mmol) of HPPHT was dissolved in 30 ml of chloroform. To this, 90 mg (0.45 mmol) of copper acetate (dissolved in 30 ml of methanol) was added. The resultant reaction mixture was refluxed until change in absorption spectra (~2 h) and the solvent was removed to obtain the crude product. By using column chromatography, the crude product was purified with (9:1 v/v) Hexane: THF, and recrystallized from methanol to obtain CPPHT in 87% yield as a green powder. Anal. Calcd. For $C_{108}H_{130}N_6O_4S_2Cu$% (1701.89): C,76.13; H,7.69; N,4.93; Found C,76.10; H,7.86; N,4.91. MALDI-TOF: m/z $[M]^+$calcd. (1701.89): For $C_{108}H_{130}N_6O_4S_2Cu$; found, 1702.18.

3,3'-((10,20-bis(2,6-bis(octyloxy)phenyl)porphyrin-5,15-diyl)bis-(ethyne-2,1-diyl))bis(10-octyl-10H-phenothiazine)-Zn(II) [**ZPPHT**]: We have adopted a similar procedure for CPPHT but one difference is that we have used zinc acetate instead of copper acetate. Yield: 90%. Anal. Calcd. For $C_{108}H_{130}N_6O_4S_2Zn$% (1702.89): C,76.05; H,7.68; N,4.93; Found C,76.10; H,7.58; N,4.88. MALDI-TOF: m/z $[M]^+$calcd. (1702.89): For $C_{108}H_{130}N_6O_4S_2$; found, 1702.96. ^1H NMR (400 MHz, $CDCl_3$) δ 9.62 (d, J = 4.6 Hz, 4H), 8.84 (d, J = 4.6 Hz, 4H), 7.72 (dt, J = 23.1, 8.4 Hz, 6H), 7.19 (t, J = 7.1 Hz, 4H), 7.01 – 6.91 (m, 10H), 3.94 (t, J = 7.2 Hz, 4H), 3.84 (t, J = 6.4 Hz, 8H), 1.49 (s, 16H), 1.25 (s, 8H), 1.02 – 0.93 (m, 8H), 0.89 (t, J = 6.9 Hz, 8H), 0.84 – 0.75 (m, 8H), 0.60 (dt, J = 14.6, 7.1 Hz, 8H), 0.50 (t, J = 7.3 Hz, 26H), 0.46 – 0.40 (m, 8H).

Highly pure solvent DMF was used to prepare the dilute solutions (12 µM concentration) to avoid any accumulation effects. The steady-state UV-visible absorption and photoluminescence (PL) emission measurements were performed using a Perkin Elmer make spectrophotometer. Femtosecond transient absorption (TAS) analyses were performed using a commercial transient absorption spectrometer and the complete details of these experiments are presented in chapter 2.

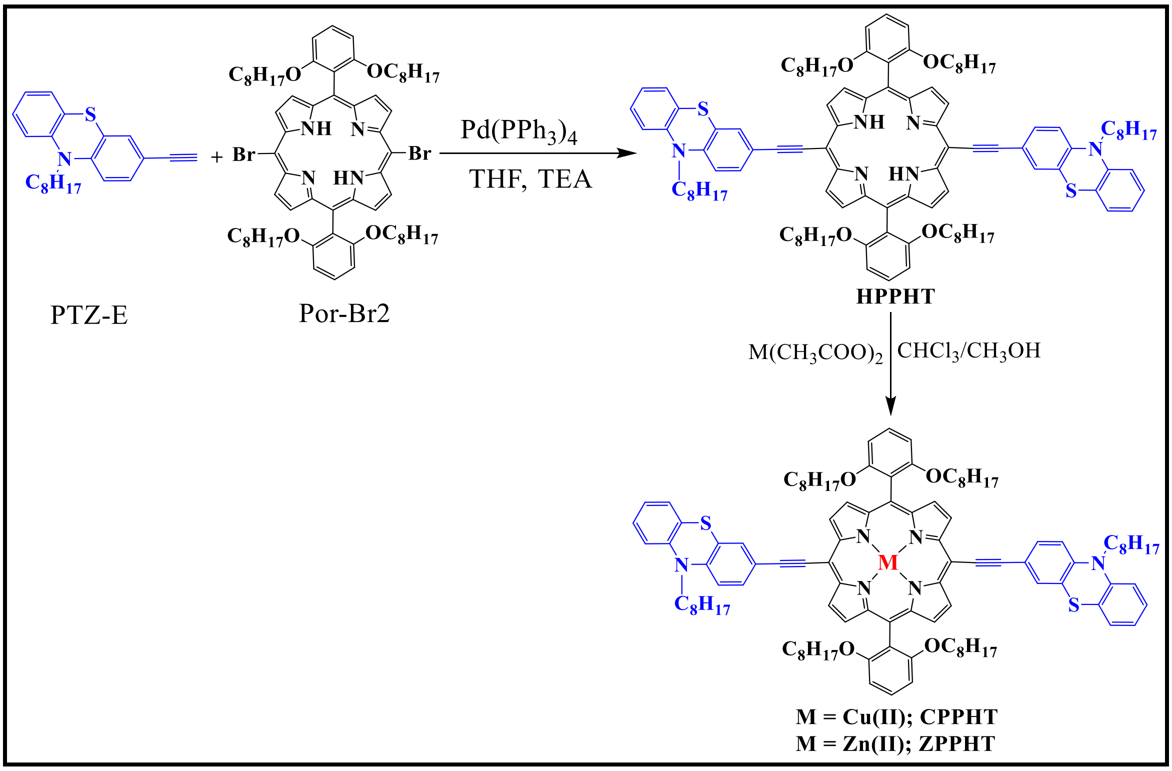

Figure 5.6 Synthetic scheme of porphyrin systems investigated in the present study.

5.3 Results and Discussions

5.3.1 UV-Visible Absorption and Emission Measurements

The steady-state absorption spectrum of the three investigated porphyrin molecules HPPHT, CPPHT, and ZPPHT (dissolved in DMF) are shown in figure 5.7. The intense peak near 458 nm, termed as the Soret (S_2) band, is attributed to $a_2(\pi)/b_1(\pi^*)$ electronic transition. ZPPHT illustrated a sharp Soret absorption with a redshift compared to CPPHT and HPPHT at 463 nm, probably due low energy gap between highest occupied molecular orbital (HOMO) to lowest occupied molecular orbital (LUMO).[28]

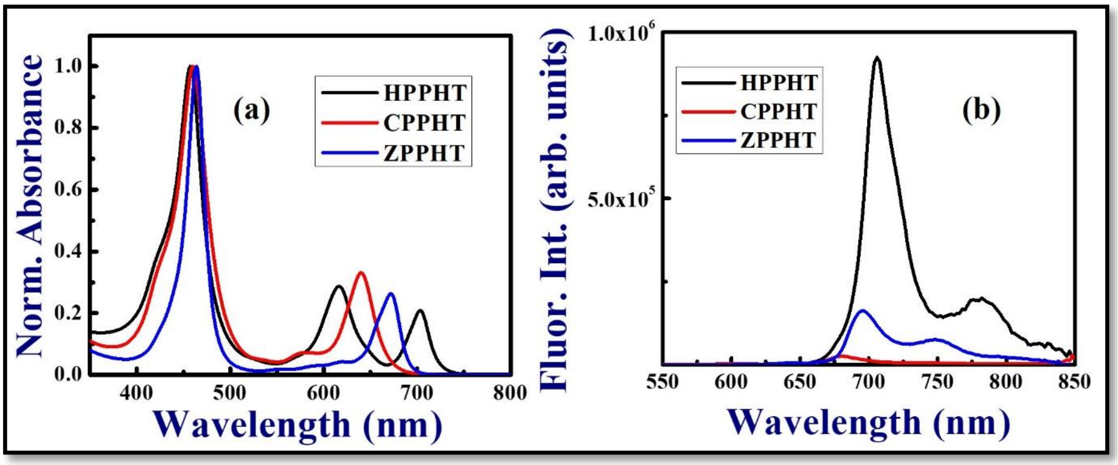

Figure 5.7 (a) absorption and (b) emission spectra of studied porphyrin molecules in DMF. CPPHT depicted a weak emission compared to the other two molecules.

Sample	Absorption (nm) [ε M^{-1} cm^{-1}]		Emission (nm)	Radiative Lifetimes (ns)
	Soret band	Q-band		
HPPHT	458 [491500]	617 [132500] 703 [88000]	705, 781	6.2 [28]
CPPHT	458 [343100]	640 [107011]	678	1.5 [unpublished]
ZPPHT	463 [452450]	673 [104292]	695, 748	1.8 [28]

Table 5.1 Summary of the steady-state absorption and emission peaks of three porphyrins measured in DMF (ε is the extinction coefficient).

The absorption peaks in the spectral region above 550 nm are due to $a_2(\pi)/b_2(\pi^*)$ electronic transitions, assigned to the first excited state (S_1) having two bands. The peaks at 703 and 617 nm are due to the origins of two non-degenerate electronic transitions (Q_x and Q_y) of the free base porphyrin. The steady-state emission spectra of porphyrin molecules dissolved in DMF solvent were recorded with 450 nm excitation. The strongest emission was observed from HPPHT and which demonstrated a smaller stokes shift from the Q-band absorption edge. The photophysical parameters of the investigated molecules obtained from steady-state measurements are summarized in table 5.1.

5.3.2 Transient Absorption Studies

The excited-state properties of the synthesized molecules were investigated using fs TAS experiments using 400 nm as the pump for photoexcitation of the Soret band and the probing in the spectral region of 480 nm to 780 nm. Figure 5.8 shows the transient absorption (TA) spectra of HPPHT, CPPHT, and ZPPHT dissolved in DMF solvent (concentration of 80 μM) at increasing probe delays varying from 100 fs to 2 ns. From the absorption data (figure 5.2) it is evident the porphyrin molecules have strong Soret band absorption at ~458 nm possessing strong molar extinction coefficients than for other wavelengths of the spectra. Due to the limitation of the probe spectral range the lower spectral region of GSB from S_2 could not be recorded. The obtained TA spectra of CPPHT and ZPPHT revealed two distinct areas i) photo-induced absorption (PIA) in the spectral range of 480-605 nm and >670 nm ii) ground state bleach ($GSB_{Q\text{-band}}$) from 605-650 nm overlapped with stimulated emission (SE). The contribution of SE for the molecules was observed at 705 nm, 680 nm and 695 nm for HPPHT, CPPHT, and ZPPHT, respectively. The PIA of ZPPHT with a maximum near 520 nm illustrated a long-lived TA signal, which might be due to the long lifetime of the triplet state. Similarly, for other molecules of CPPHT and HPPHT, the PIA maximum was at 510 nm, and decays were faster compared to ZPPHT. Among these, the free-base porphyrin HPPHT exhibited a quicker decay time (<1 ns).

The obtained TA spectra displayed different time evolutions at different spectral regions owing to several processes occurring post photoexcitation such as (a) ground state bleaching (GSB) (b) excited-state absorption (ESA) and (c) stimulated emission (SE). An in-depth analysis of the fs transient absorption spectra was obtained by performing the global and target analysis based on a compartmental model[29] as illustrated in figure 5.9 and using the Surface Xplorer (Ultrafast systems) and Glotaran software.[30]

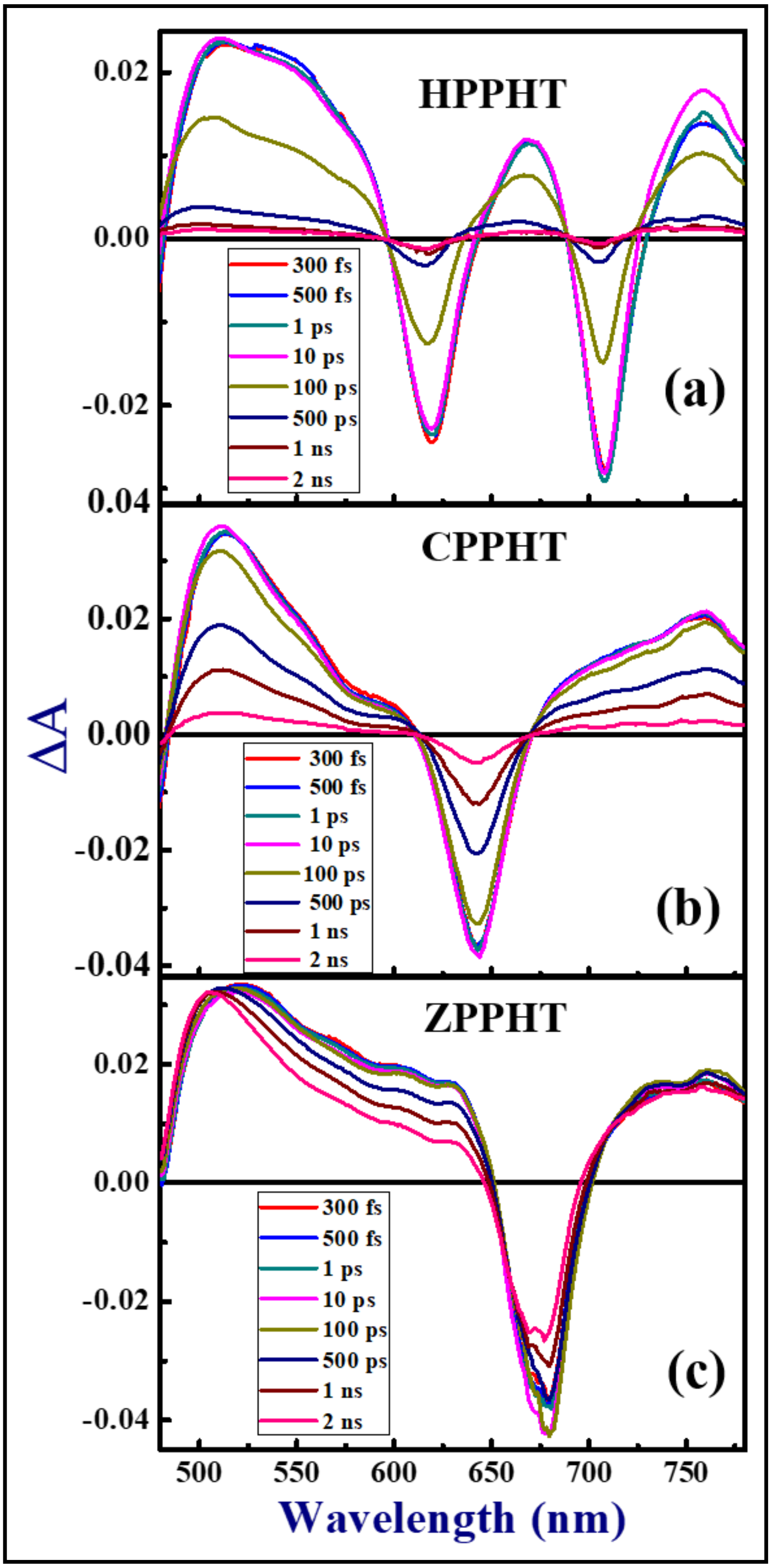

Figure 5.8 fs-TAS spectra of three different porphyrins in solution phase at different delay times at 400 nm photoexcitation for (a) HPPHT (b) CPPHT and (c) ZPPHT.

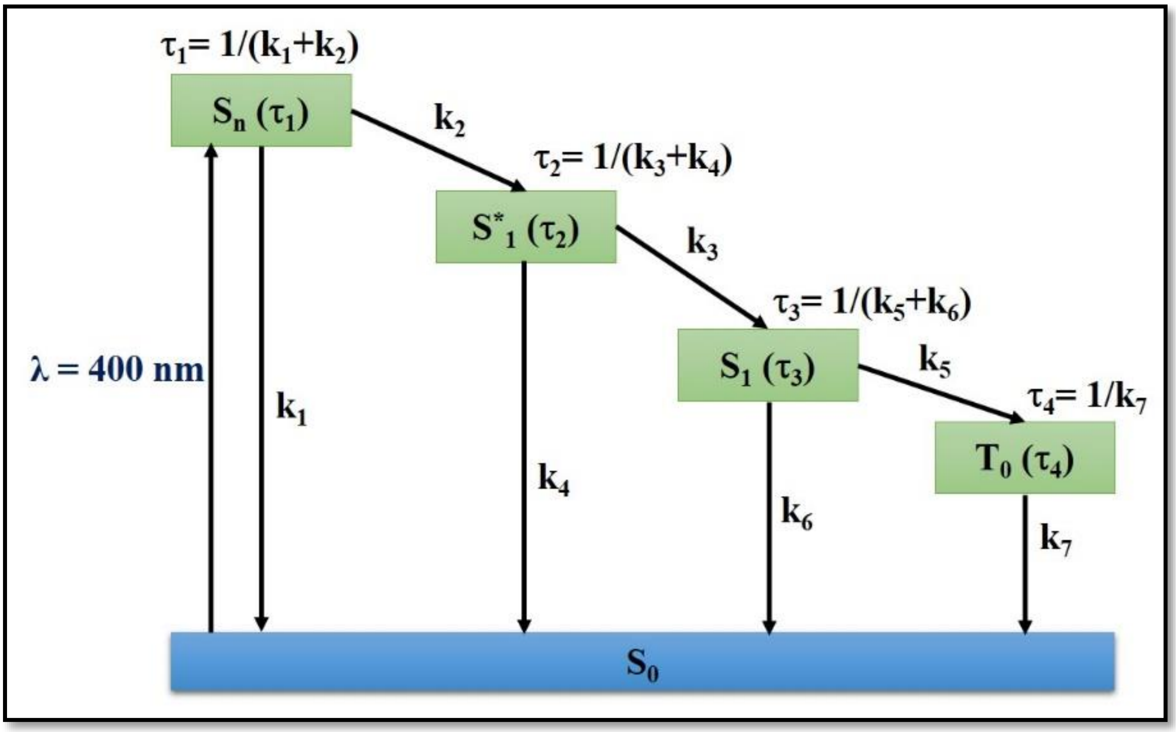

Figure 5.9 Schematic of the target model used to fit TA spectra of synthesized porphyrins after 400 nm photoexcitation.

First, the TA spectra were globally fitted using a parallel and sequential model, which yielded both the decay associated difference spectra (DADS) and evolution associated decay spectra (EADS). Both DADS and EADS provide information on the growth of difference spectra along with different microscopic rate constants. The obtained time constants from the parallel and sequential models were used to estimate the species associated difference spectra (SADS) in the target analysis (a combination of parallel and sequential model), which contained all the possible branching routes with specific rate constants, i.e., the decay of compartments and transfer of population between the compartments. Figure 5.10 presents the kinetics of ZPPHT from the TA spectra after global analysis obtained at different probe wavelengths. The scattered points represent the experimental data, while the solid lines represent the theoretical fits obtained from target analysis. We observed an excellent agreement between the experiments and the theoretically fitted data. The characteristic wavelengths were chosen at different portions of the TA spectra corresponding to ground state bleach and photoinduced absorption process. The obtained time constants from the fits are summarized in table 5.2.

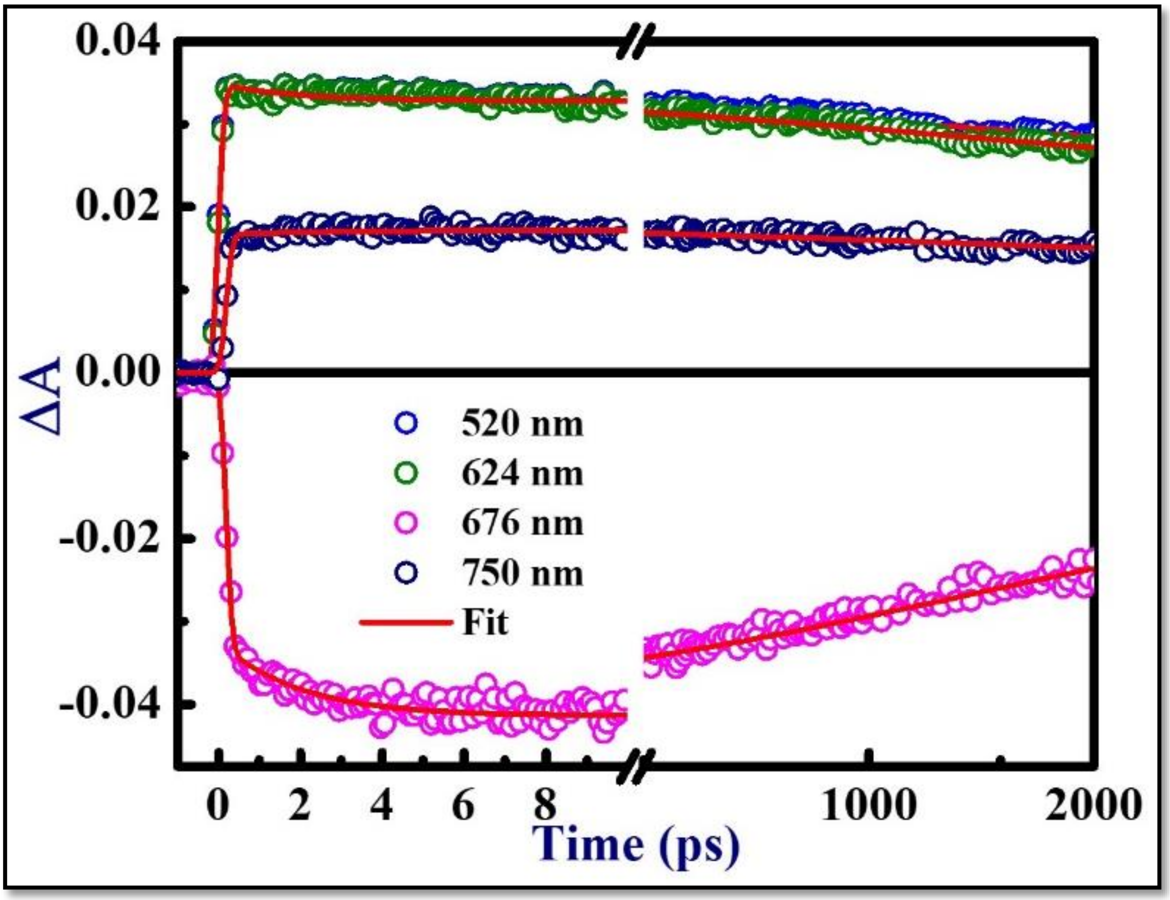

Figure 5.10 Kinetics of ZPPHT at selected probe wavelengths after target analysis. Open symbols represent data points from experiments, and the solid lines represent theoretical fits.

Lifetime and decay parameters	**HPPHT**	**CPPHT**	**ZPPHT**	**Microscopic rate constants**		
				HPPHT	**CPPHT**	**ZPPHT**
τ_1 = 1/ (k_1+ k_2)	333 fs	250 fs	500 fs	k_1=(1.66 ps)$^{-1}$ k_2=(416 fs)$^{-1}$	k_1=(1.25 ps)$^{-1}$ k_2=(312 fs)$^{-1}$	k_1=(2.5 ps)$^{-1}$ k_2=(625 fs)$^{-1}$
τ_2 = 1/ (k_3+ k_4)	142 ps	20 ps	50 ps	k_3=(158 ps)$^{-1}$ k_4=(1.42 ns)$^{-1}$	k_3=(22 ps)$^{-1}$ k_4=(200 ps)$^{-1}$	k_3=(55.5 ps)$^{-1}$ k_4=(500 ps)$^{-1}$
τ_3 = 1/ (k_5+ k_6)	6.2 ns	1.5 ns	1.8 ns	k_5=(8.9 ns)$^{-1}$ k_6=(20.8 ns)$^{-1}$	k_5=(2.16 ns)$^{-1}$ k_6=(5.05 ns)$^{-1}$	k_5=(2.57 ns)$^{-1}$ k_6=(6 ns)$^{-1}$
τ_4 = 1/ (k_7)$^{-1}$	1.01 μs	0.1 μs	1.23 μs	k_7= (1.01 μs)$^{-1}$	k_7=(0.1 μs)$^{-1}$	k_7=(1.23 μs)$^{-1}$

Table 5.2 Summary of the kinetic parameters of three porphyrin molecules obtained from global and target analysis of fs-TA data (τ_3 value was obtained from the TCSPC measurements[28]). The error in the obtained rate constants is estimated to be less than one percent.

The TA spectra were collected up to a delay of 2 ns and, consequently, the T_0 spectra cannot be estimated precisely from this data. Therefore, the lowest excited state (S_1) lifetime was fixed with a time constant that was obtained from time-correlated single-photon counting (TCSPC) data,[28] and the T_0 lifetime was set to be in the range of 1-2 µs. Under these assumptions, the experimental data fitted well, and the rate constants obtained in this manner are summarized in table 5.2. The goodness of the fits is clearly shown in figure 5.10. The estimated species associated difference spectra of ZPPHT and respective population time profiles are shown in figure 5.11. The first SADS1 spectra is attributed to the S_n state, with lifetimes of 250 fs (HPPHT), 333 fs (CPPHT), and 500 fs (ZPPHT). This first lifetime τ_1 corresponds to the internal conversion from S_n states (population transfer) to S_1 hot state (highest vibrational state of S_1). The second lifetime τ_2 = 142 ps, 20 ps, and 50 ps correspond to the vibrational relaxation from S_1 hot states to thermally relaxed S_1 state with corresponding SADS2 spectra depicted in figure 5.11. The third lifetime τ_3 = 6.2 ns, 1.5 ns, and 1.8 ns is assigned to the combination of radiative relaxation from S_1 state to the S_0 state as well as intersystem crossing to the lowest triplet state T_0 with SADS3 spectra. Finally, the SADS4 spectra and lifetime τ_4 = 1.01 µs, 0.1 µs, and 1.23 µs can be recognized with the T_0 state with an excited state absorption peak at 505 nm. The microscopic rate constants pertaining to each state obtained from the detailed analysis are summarized in table 5.2.

Figure 5.11 illustrates the depopulation of the excited state (S_n) SADS1 spectra occurring through two different channels: first, 20% of the population decays through radiative process to ground state with 2.5 ps $(k_1)^{-1}$ time constant. Secondly, the remaining population from the SADS1 goes to the S_1 hot state via internal conversion with a time constant of 625 fs $(k_2)^{-1}$. Here k_1, k_2 correspond to rate constants of kinetics with $\tau_1 = 1/(k_1+k_2)^{-1}$ and its value was calculated to be 500 fs. From SADS2, 90% of the population was found on decaying in non-radiative pathways from S_1 hot state to thermally relaxed S_1 state through vibrational relaxation with a time constant of 55.5 ps $(k_3)^{-1.}$ In contrast, the remaining population decays through radiative pathway from S_1 hot state to ground state with time constant of 500 ps $(k_4)^{-1}$. The lifetime of the S_1 hot state was determined to be 50 ps from $\{\tau_2 = 1/(k_3+k_4)^{-1}\}$. Next, 30% of the population of SADS3 decayed by a radiative process to ground state with a time constant of 6 ns $(k_6)^{-1}$, the lifetime of SADS3 was constrained to be the value obtained from TCSPC of 1.8 ns from $\{\tau_3 = 1/(k_5+k_6)^{-1}\}$

and remaining population undergoes ISC to the lowest triplet state T_0 with a time constant of 2.57 ns $(k_5)^{-1}$. Finally, SADS4 very slowly decayed to ground state from T_0, with a time constant arbitrarily set to 1.23 μs from $\{\tau_4 = (1/\ k_7)^{-1}\}$ due to the limitation in detection window of our setup. Similar values of these parameters were obtained for the other two porphyrin molecules, HPPHT and CPPHT, and the data is listed in table 5.2. Figure 5.12 illustrates the TA spectra at 300 fs and 2 ns probe delay with an excellent agreement with global analysis fitting.

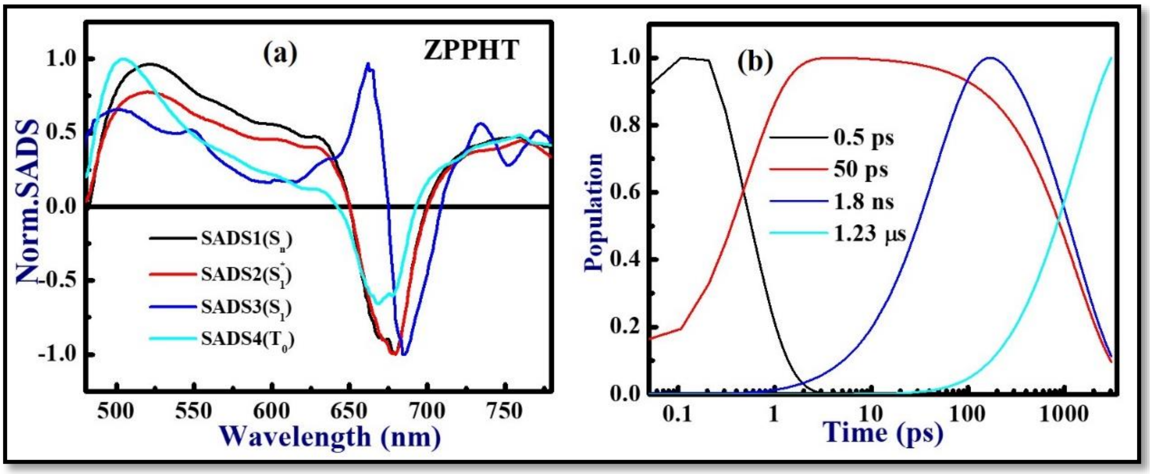

Figure 5.11 (a) Estimated species associated spectra and (b) population decay profiles of respective species/states of ZPPHT. The inset shows the enlarged view of population profiles up to 20 ps. At 400 nm photoexcitation.

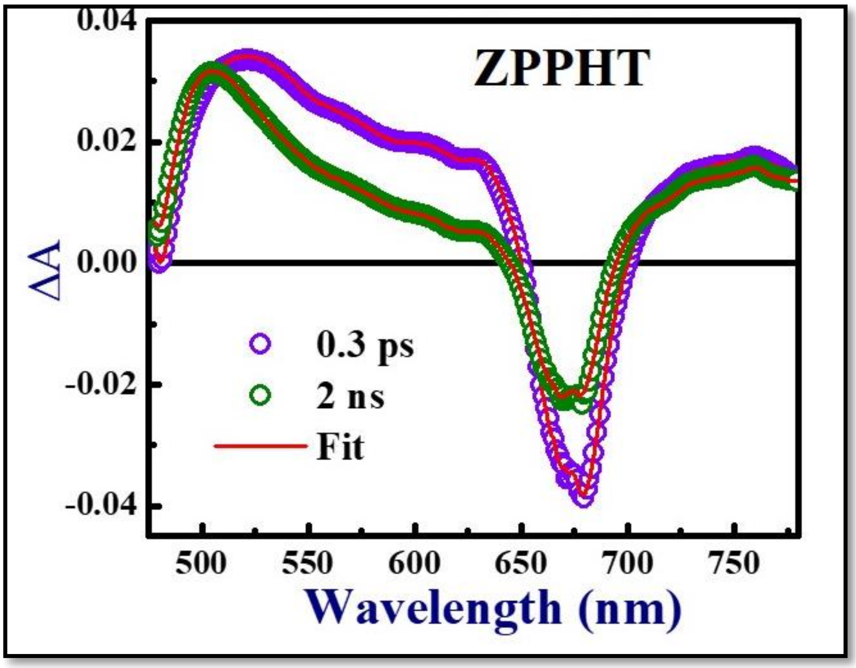

Figure 5.12 Fs-TAS spectra of ZPPHT at 0.3 ps and 2 ns probe delay with global analysis. Solid lines are theoretical fits while the open symbols are the experimental data (400 nm photoexcitation).

From the data presented in table 5.2, it is evident that both ZPPHT and HPPHT porphyrin molecules revealed longer relaxation times significantly compared to the CPPHT. This could possibly be attributed to either a higher triplet quantum yield (through intersystem crossing) or a reduction in the radiative lifetime in the case of ZPPHT due to the incorporation of Zinc in HPPHT.[28] The obtained rate constants were found to be consistent with that reported in recent literature,[23-25] thus representing the utility and reliability of the analysis scheme used for these new porphyrin moieties. A similar analysis was performed for the other two molecules of HPPHT and CPPHT, and the data is shown in figures 5.13-5.14.

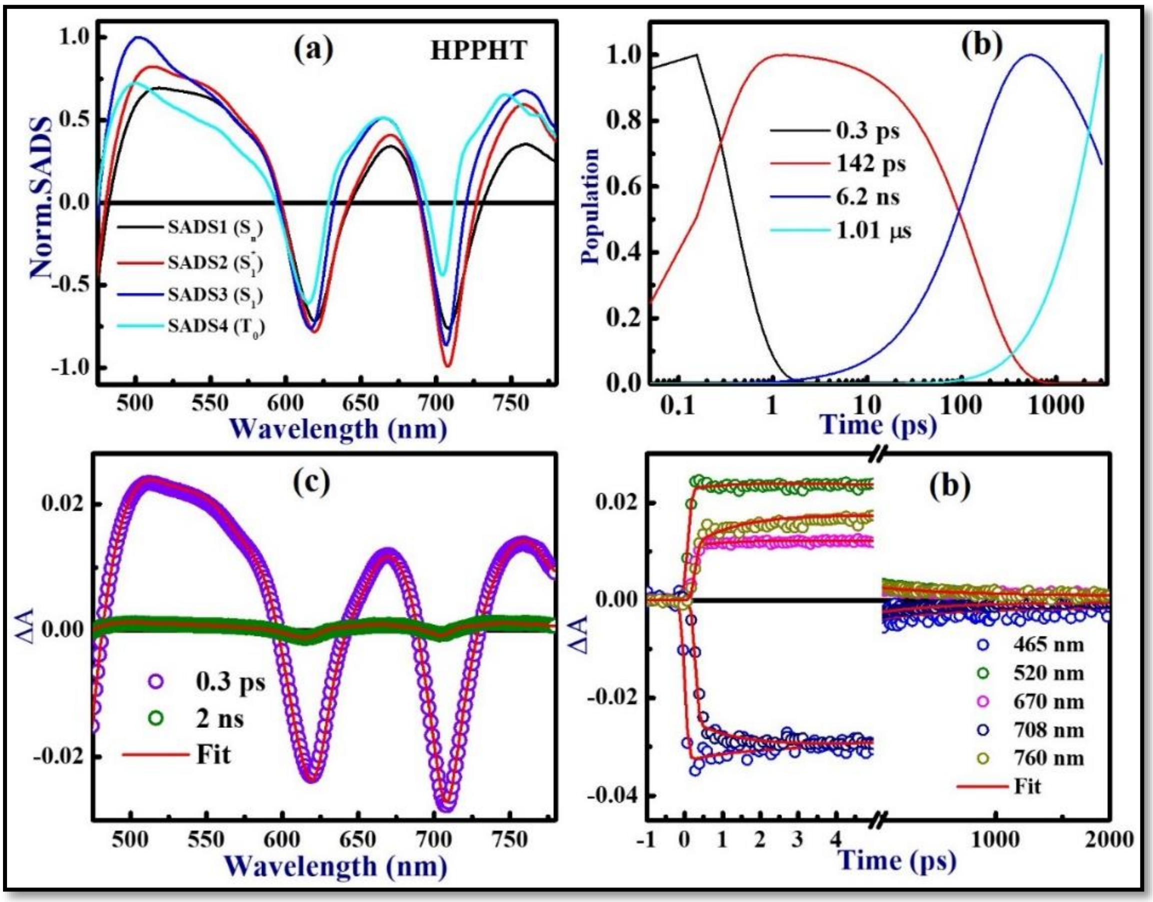

Figure 5.13 (a) SADS spectra (b) population decay profiles (c) shows the goodness of fits at probe delay of 0.3 ps and 2 ns of TA spectra (d) decay of different wavelength with global fitting of the TA spectra of HPPHT. (Open symbols are experimental data were solid lines shows the fits).

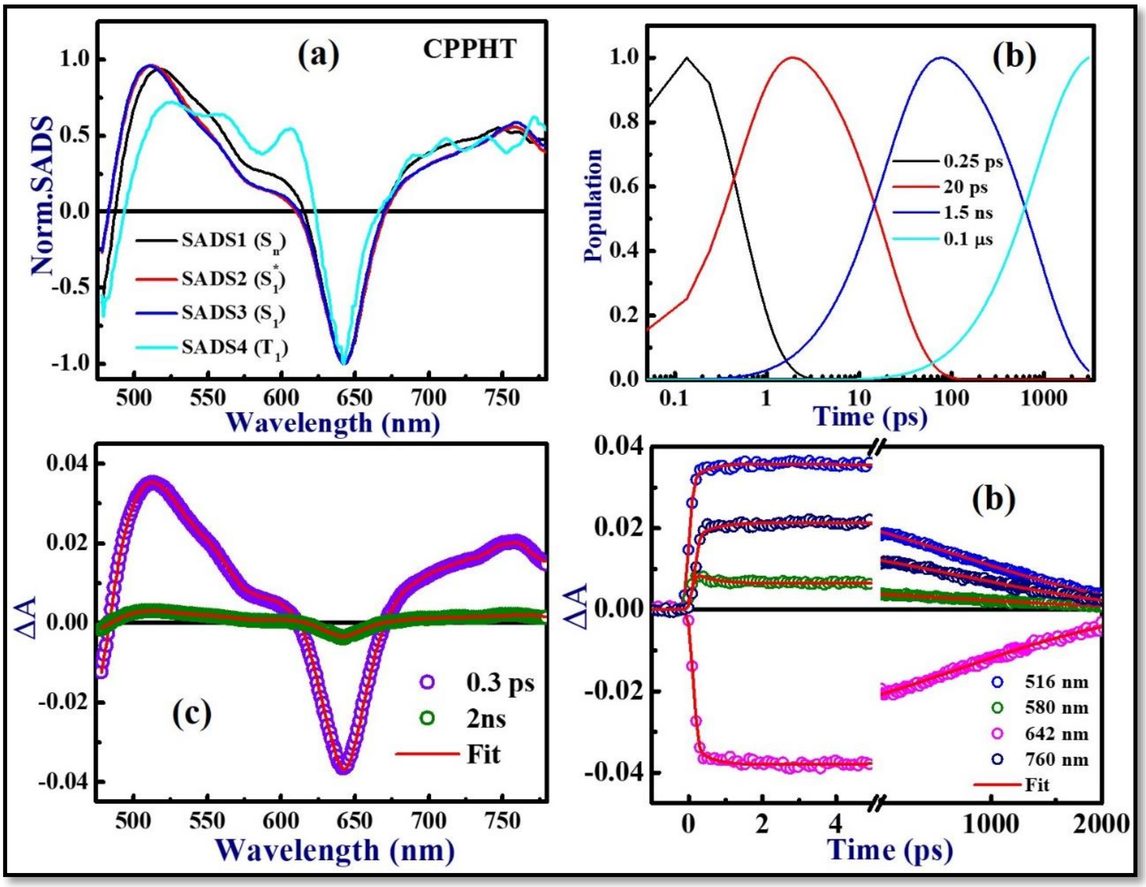

Figure 5.14 (a) SADS spectra (b) population decay profiles (c) shows the goodness of fits at probe delay of 0.3 ps and 2 ns of TA spectra (d) decay of different wavelength after global fitting of the TA spectra of CPPHT. (Symbols are experimental data were solid lines shows the fits).

5.3.3 NLO studies

5.3.3.1 Z-scan data analysis

The NLO properties of these novel porphyrins were deliberated using the standard Z-scan technique at the input peak intensity of ~160 GW/cm^2. The open aperture (OA) Z-scan curves confirmed the presence of reverse saturable absorption (RSA) type of behavior as illustrated in figure 5.15 data. The origin of RSA can be due to either the excited state absorption or two-photon absorption. The obtained OA curves were fitted using a standard two-photon absorption equation,[31] and the obtained NLO parameters are summarized in table 5.3. Metal doped porphyrins depict strong NLO coefficients and this improvement depends on several factors such as (a) central metal ion (b) intramolecular charge transfer and (c) expanded π-conjugated system of these molecules. The closed aperture (CA) Z-scan transmission data confirmed the presence of self-focusing behavior (positive refractive index n_2>0). The CA data were again fitted to a standard equation.[31] The magnitudes of the NLO coefficients obtained from our molecules were compared with some of the recently reported molecules.[18, 32-40] Terazima and co-workers[18] reported n_2 values of 10^{-15} cm^2/W for their porphyrin oligomers obtained with ps laser pulses at 800 nm. The n_2 values were found to be increasing linearly with the number of porphyrin units, and the meso substitution of porphyrin units displayed enhanced two-photon absorption values (2.1-7×10^{-11} cm/W). Ahn et al.[38] investigated the TPA behavior from expanded porphyrin arrays by altering the dihedral angle. They recorded 2PA cross-section values $\sigma^{(2)}$ of ~10^3 GM with fs pulse excitation at a repetition rate of 240 kHz. Further, they found stronger 2PA and more prolonged exited state absorption from the aromatic hexaphyrin compared to antiaromatic hexaphyrin owing to the extended aromaticity. Recently, an increase/decrease of the excited state lifetime and extension of π-electron conjugation have been linked to increased 2PA cross-section values in different porphyrin moieties are reported.[32-33] Ogawa and co-workers[40] observed strong 2PA from the butadiyne-linked bisporphyrin system by designing donor/acceptor molecules connected to a π-conjugation symmetrically or asymmetrically, and they have found an increased $\sigma^{(2)}$ with a magnitude of ~3.7-76×10^2 GM with fs laser pulse excitation at a wavelength of 817 nm. Similar studies were performed by Odom et al.,[41] wherein they observed the strong electronic coupling between (D-π-D) bisporphyrin motifs enhancing the 2PA values (~6.9- 9.7×10^3 GM) measured with 170 fs at 887 nm, arising from the several transitions due to a large number of low-lying excited states. Sheng et al.[42] have shown D-π-A structures with asymmetric porphyrin possess large 2PA cross-section values compared to asymmetric analogues, and they have demonstrated a large 2PA cross-section of 6.1×10^5 GM from pyrenyl substituted porphyrins. Mikhaylov and co-workers[43] also have reported a large 2PA cross-section values (~10^5 GM) from self-assembled butadiyne Zn-porphyrin nanostructures due to the efficient π-conjugation arising from axial oriented π-orbitals. Hisaki et al.[44] reported a large 2PA cross-section values of 9620 GM from doubly β-to-β butadiyne-bridged diporphyrins arising from the rigid planar structure. Yoon et al.[45] have observed a strong 2PA property correlation from hexaporphyrin molecules with a larger number of π-electrons and rectangular rigid structures possessing increased polarizability along the molecular direction. They have reported 2PA cross-section values of 2600-3100 GM with fs excitation.

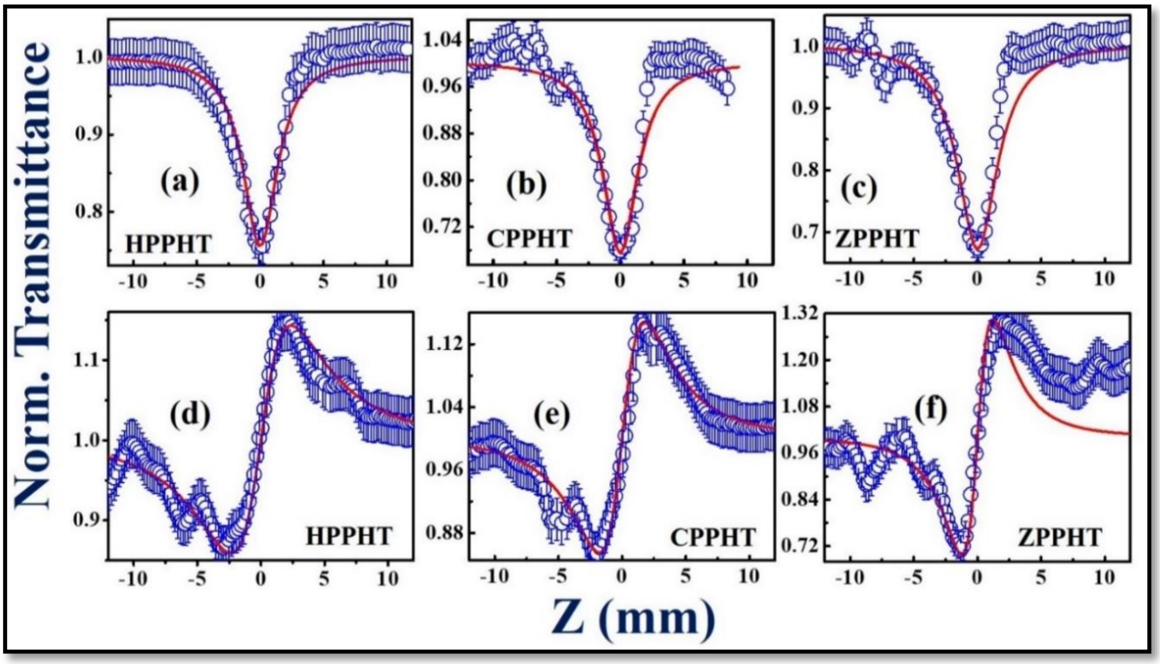

Figure 5.15 (a)-(c) Open aperture Z-scan data (d)-(f) closed aperture Z-scan data of HPPHT, CPPHT, ZPPHT, respectively, recorded at 800 nm with fs pulses and at 1 kHz repetition rate.

Sample	**β $\times 10^{-13}$ (m/W)**	**n_2 $\times 10^{-19}$ (m^2/W)**	**$\sigma_{(2)}$ $\times 10^{3}$ (GM)**	**$\chi^{(R)}$ $\times 10^{-21}$ (m^2/V^2)**	**$\chi^{(I)}$ $\times 10^{-22}$ (m^2/V^2)**	**$\chi^{(3)}$ $\times 10^{-21}$ (m^2/V^2)**	**$\chi^{(3)}$ $\times 10^{-13}$ (esu)**
HPPHT	1.0	5.8	0.82	6.3	0.7	6.3	4.5
CPPHT	6.5	6.0	5.4	5.7	4.0	5.7	4.1
ZPPHT	4.4	13	3.6	120	2.6	12	8.8

Table 5.3 Summary of the NLO coefficients of porphyrins investigated in the present study and obtained using the Z-scan technique at 800 nm.

Several factors are expected to influence the 2PA values of porphyrin macrocycles such as (a) delocalization of the conjugated π-electrons (b) symmetry of the molecule (c) length of π-conjugation and (d) directionality, playing crucial roles in the obtained enhanced 2PA values.[41-46] From the obtained NLO coefficients, we observed that metal doped porphyrin moieties exhibited stronger 2PA cross-section values than free-base porphyrin (HPPHT), possibly because of the substantial excited state population as seen from the TA Spectra. It has earlier been proved that porphyrins with different central metals demonstrated superior nonlinearities compared to the free-base porphyrins. The obtained

TPA cross-section values in the present case were found to be either on par or superior compared to some of the recently reported porphyrin molecules (table 5.4). Therefore, we firmly believe that these molecules will find applications in optical limiting and TPA-based bio-imaging. The error bars in the NLO coefficients were capped at ±5%, predominantly due to errors in the estimation of input peak intensities and variations in the input laser pulse energy. There could also be fitting errors.

Compound	Laser parameters	β (cm/GW)	$\sigma^{(2)}$ (GM)	Solvent	Ref.
Butadiyne-Linked Bisporphyrin (5D)	887 nm, 170 fs, 1 kHz	-	7600	$CHCl_3$	40
Bis(Porphyrin)-Substituted Squaraine	775 nm, 140 fs, 1 kHz	-	53000	DCM	41
A_3B type porphyrin 1	800 nm, 170 fs, 1 kHz	0.148	610000	$CHCl_3$	42
(c-P12)2·(DABCO)12 (nanostructures)	900-1600 nm, 100 fs, 1 kHz	-	170000	Toluene	43
2Zn	800 nm, 100 fs, 5 kHz	-	9620	Toluene	44
[26] [28] hexaphyrins	1200 nm,130 fs, 5 kHz	-	2600-3100	Toluene	45
bisporphyrin dimer 3	800-875 nm, 70 fs, 1 kHz	-	530000	Chloroform	46
PtTBP(CO2Bu)8	800 nm, 150 fs, 80 MHz	-	500	DMA	47
monozincbisporphyrin 7D	887 nm, 120 fs, 1 kHz	-	7600	$CHCl_3$	48
H_2TTP	800 nm, 100 fs, 1 kHz	-	25	Toluene	49
NiTCTMP	800 nm, 2 ps, 1 kHz	0.0052	53690	Chloroform	50
DPP-ZnP-ZnP-DPP	910 nm, 120 fs, 80 MHz	-	4300	DCM	51
DPP–ZnP porphyrin	900 nm, 100 fs, 80 MHz	-	4000	DCM	52
meso–meso,β–β,β–β triply linked porphyrin tape (4)	2.3 μm, 130 fs, 5 kHz	-	41200	Toluene	53
$(OMe)_2TPC$	Nanosecond, 1064 nm	-	67.6	CS_2	54
H2TPYRP, H2TPHEP	800 nm, 170 fs, 1 kHz	-	42600 13600	Chloroform	55
5,16-Di-(4-bromophenyl)-	800 nm,	-	29	DCM	56

tetraoxa[22]porphyrin(2.1.2.1)	50 fs, 1 kHz		
D-π-D porphyrins	800 nm, 50 fs, 1 kHz	820 5400 3600	Present work

Table 5.4 Summary of 2PA cross-section values from recent works on different porphyrin molecules.

5.3.3.2 DFWM Data and Analysis

The DFWM experiments were performed at 800 nm using five different input energies (the same concentrations used for Z-scan measurements were utilized for the DFWM measurements). Figures 5.16(a), (c), and (e) data illustrate the cubic dependency of the DFWM signals confirming the presence of a third-order NLO process. Carbon tetrachloride (CCl_4) solvent was used as a reference with a $\chi^{(3)}$ value of 4.4×10^{-14} esu, and the $\chi^{(3)}$ of the investigated molecules was calculated following a standard procedure.[31] The obtained NLO coefficients from the DFWM studies and Z-scan studies matched well in the orders of magnitude. The obtained $\chi^{(3)}$ values were significantly higher compared to the free-base porphyrin molecule. Many researchers have investigated the NLO properties of diverse porphyrin moieties with sub-picosecond pulses.[32-33,56] The time-resolved DFWM data of all the porphyrin molecules are shown in figures 5.16(b), (d), and (e). The exponential decay of the time-resolved DFWM signal (fitted to an exponential decay), as shown in figure 5.16, confirmed the origin of nonlinearity, which is mainly due to pure electronic contribution. The n_2 values were calculated using the following equation $n_2\ (cm^2/W) = \left(\frac{0.0395}{n_0^2}\right)\chi^{(3)}$ esu. Metal doped porphyrin molecules depicted higher n_2 values when compared to the free-base porphyrin HPPHT (see table 5.5).

Molecule	$\chi^{(3)}$ (esu)	n_2 (cm^2/W)
HPPHT	5.13×10^{-14}	1.00×10^{-15}
CPPHT	6.87×10^{-14}	1.33×10^{-15}
ZPPHT	7.69×10^{-14}	1.49×10^{-15}

Table 5.5 Summary of the NLO coefficients obtained from the DFWM technique measured at 800 nm with ~70 fs pulses.

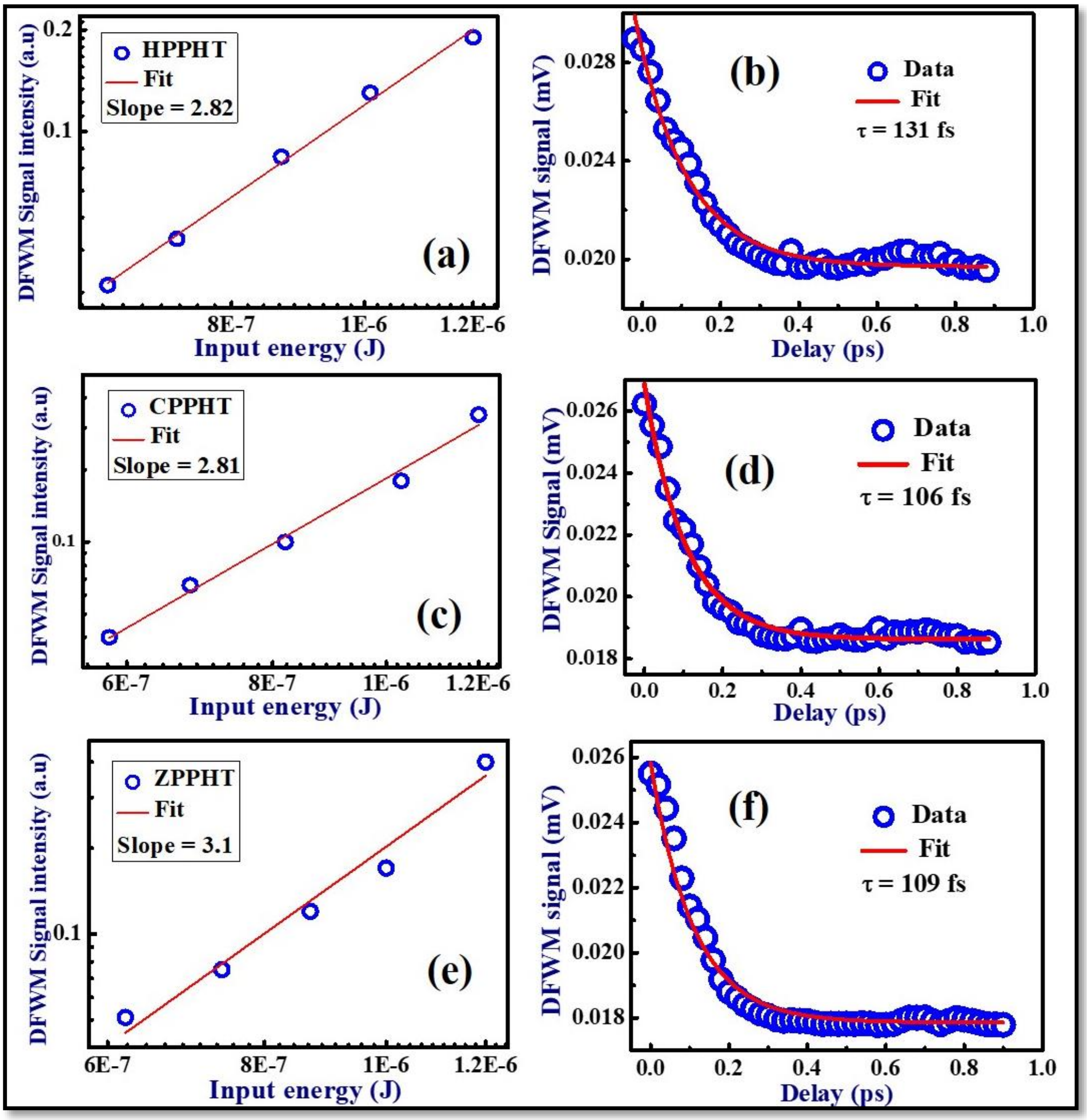

Figure 5.16 (a) Cubic dependency of the DFWM signal. Here a.u. stands for arbitrary units. (b) time-resolved DFWM signal profile of ZPPHT.

The obtained NLO coefficients and their magnitudes were found to be similar or higher in magnitude than few of the recently reported porphyrin/metalloporphyrin molecules. Recently, Narendran et al.[37] have reported $\chi^{(3)}$ values of *meso*-tetrakis porphyrin complexes with magnitudes of 10^{-12} esu obtained using ns pulses. Rao and co-workers[35] reported a $\chi^{(3)}$ value of 10^{-9} esu from benzoporphyrins with ps laser pulses. Rao and co-workers[36] have recently published $\chi^{(3)}$ values of ~10^{-12} esu from tetraphenyl porphyrins obtained with a continuous wave laser at 671 nm. Kumar et al.[32] extensively studied a few alkyl phthalocyanines using the DFWM experiments with ~100 fs pulses and have reported a highest $\chi^{(3)}$ of 4.31×10^{-14} esu. Biswas and co-workers reported DFWM measurements with 70 fs pulses for quinoxalines molecules with highest $\chi^{(3)}$ values of 4.35×10^{-14} esu.[58] The investigated porphyrin molecules from the present study have demonstrated strong $\chi^{(3)}$ values and ultrafast response time. Therefore, we firmly believe that these molecules will find applications in areas such as all-optical switching, optical limiting.

5.4 Conclusions

In this work, a thorough photophysical investigation and the ultrafast NLO studies of three novel porphyrins (HPPHT, CPPHT, and ZPPHT) have been performed.

- Femtosecond transient absorption spectroscopic studies elucidated the evolution of excited state photo-processes various photophysical processes. By performing a thorough global and target analysis of the TAS data, helps to estimated different rate constants for various photophysical processes such as IC from S_n-S_1 (k_2) hot found to be in the range of ~ (300-600 fs)$^{-1}$and vibrational cooling from S_1 hot - S_1 (k_3) state happens in the range of ~ (22 - 158 ps)$^{-1}$.
- From S_1 the population relaxed to the ground state upon the radiative process as well as the lowest triplet state T_0 with nanosecond time scale.
- The NLO properties of synthesized porphyrins were investigated using the fs Z-scan and DFWM experimental techniques.
- The obtained NLO coefficients were found to be stronger in the case of the ZPPHT molecule when compared to the other two molecules.
- The two-photon absorption cross-sections were found to be in the range of 820-5400 GM, significantly superior to some of the recently reported organic moieties.
- We firmly believe that these molecules have the potential for various optoelectronics and photonics applications.

References

1. Higuchi, T.; Uzu, S.; Hirobe, M., Synthesis of a Highly Stable Iron Porphyrin Coordinated by Alkylthiolate Anion as a Model for Cytochrome P-450 and Its Catalytic Activity in Oxygen-Oxygen Bond Cleavage. *Journal of the American Chemical Society* **1990**, *112*, 7051-7053.
2. Vicente, M. G. H.; Jaquinod, L.; Smith, K. M., Oligomeric Porphyrin Arrays. *Chemical Communications* **1999**, 1771-1782.
3. Arnold, L.; Müllen, K., Modifying the Porphyrin Core — a Chemist's Jigsaw. *Journal of Porphyrins and Phthalocyanines* **2011**, *15*, 757-779.
4. Di Carlo, G.; Caramori, S.; Casarin, L.; Orbelli Biroli, A.; Tessore, F.; Argazzi, R.; Oriana, A.; Cerullo, G.; Bignozzi, C. A.; Pizzotti, M., Charge Transfer Dynamics in Β- and Meso-Substituted Dithienylethylene Porphyrins. *The Journal of Physical Chemistry C* **2017**, *121*, 18385-18400.
5. Mahmood, A.; Hu, J.-Y.; Xiao, B.; Tang, A.; Wang, X.; Zhou, E., Recent Progress in Porphyrin-Based Materials for Organic Solar Cells. *Journal of Materials Chemistry A* **2018**, *6*, 16769-16797.
6. Senge, M. O.; Fazekas, M.; Notaras, E. G. A.; Blau, W. J.; Zawadzka, M.; Locos, O. B.; Ni Mhuircheartaigh, E. M., Nonlinear Optical Properties of Porphyrins. *Advanced Materials* **2007**, *19*, 2737-2774.
7. Imahori, H.; Fukuzumi, S., Porphyrin- and Fullerene-Based Molecular Photovoltaic Devices. *Advanced Functional Materials* **2004**, *14*, 525-536.
8. O'Neil, M. P.; Niemczyk, M. P.; Svec, W. A.; Gosztola, D.; Gaines, G. L.; Wasielewski, M. R., Picosecond Optical Switching Based on Biphotonic Excitation of an Electron Donor-Acceptor-Donor Molecule. *Science* **1992**, *257*, 63-65.
9. Reddy, G.; Devulapally, K.; Islavath, N.; Giribabu, L., Metallated Macrocyclic Derivatives as a Hole - Transporting Materials for Perovskite Solar Cells. *The Chemical Record* **2019**.
10. Higashino, T.; Imahori, H., Porphyrins as Excellent Dyes for Dye-Sensitized Solar Cells: Recent Developments and Insights. *Dalton Transactions* **2015**, *44*, 448-463.
11. Ghann, W.; Chavez-Gil, T.; Goede, C. I.; Kang, H.; Khan, S.; Sobhi, H.; Nesbitt, F.; Uddin, J., Photophysical, Electrochemical and Photovoltaic Properties of

Porphyrin-Based Dye Sensitized Solar Cell. *Advances in Materials Physics and Chemistry* **2017**, *07*, 148-172.

12. Daphnomili, D.; Landrou, G.; Prakash Singh, S.; Thomas, A.; Yesudas, K.; K, B.; Sharma, G. D.; Coutsolelos, A. G., Photophysical, Electrochemical and Photovoltaic Properties of Dye Sensitized Solar Cells Using a Series of Pyridyl Functionalized Porphyrin Dyes. *RSC Advances* **2012**, *2*, 12899.
13. Arpaçay, P.; Maity, P.; El-Zohry, A. M.; Meindl, A.; Akca, S.; Plunkett, S.; Senge, M. O.; Blau, W. J.; Mohammed, O. F., Controllable Charge-Transfer Mechanism at Push–Pull Porphyrin/Nanocarbon Interfaces. *The Journal of Physical Chemistry C* **2019**, *123*, 14283-14291.
14. Imahori, H.; Umeyama, T., Porphyrin-Modified Electrodes for Solar Energy Conversion. *Journal of Porphyrins and Phthalocyanines* **2009**, *13*, 1063-1068.
15. Clavian, L. M.; Rajesh Kumar, P. C.; Anil Kumar, K. V.; Rao, D. N.; Shihab, N. K.; Ganesh, S., Enhanced Third Order Optical Nonlinearity in Ultrathin Amorphous Film of Tetraphenyl-Porphyrin in Picosecond Regime. *Optics & Laser Technology* **2019**, *119*, 105642.
16. Bharati, M. S. S.; Bhattacharya, S.; Suman Krishna, J. V.; Giribabu, L.; Venugopal Rao, S., Femtosecond, Broadband Nonlinear Optical Studies of a Zinc Porphyrin and Zinc Phthalocyanine. *Optics & Laser Technology* **2018**, *108*, 418-425.
17. Wan, Y.; Xue, Y.; Sheng, N.; Rui, G.; Lv, C.; He, J.; Gu, B.; Cui, Y., Solvent Effects on the Fluorescence and Effective Three-Photon Absorption of a Zn(Ii)-[Meso-Tetrakis(4-Octyloxyphenyl)Porphyrin]. *Optics & Laser Technology* **2018**, *102*, 47-53.
18. Terazima, M.; Shimizu, H.; Osuka, A., The Third-Order Nonlinear Optical Properties of Porphyrin Oligomers. *Journal of Applied Physics* **1997**, *81*, 2946-2951.
19. Krishna, N. V.; Krishna, J. V. S.; Singh, S. P.; Giribabu, L.; Han, L.; Bedja, I.; Gupta, R. K.; Islam, A., Donor-Π–Acceptor Based Stable Porphyrin Sensitizers for Dye-Sensitized Solar Cells: Effect of Π-Conjugated Spacers. *The Journal of Physical Chemistry C* **2017**, *121*, 6464-6477.
20. Kang, S. H.; Lu, C.; Zhou, H.; Choi, S.; Kim, J.; Kim, H. K., Novel Π-Extended Porphyrin-Based Hole-Transporting Materials with Triarylamine Donor Units for High Performance Perovskite Solar Cells. *Dyes and Pigments* **2019**, *163*, 734-739.

21. Chen, L.; Hu, R.; Xu, J.; Wang, S.; Li, X.; Li, S.; Yang, G., Third-Order Nonlinear Optical Properties of a Series of Porphyrin-Appended Europium(Iii) Bis(Phthalocyaninato) Complexes. *Spectrochimica Acta Part A: Molecular and Biomolecular Spectroscopy* **2013**, *105*, 577-581.
22. Yu, H.-Z.; Baskin, J. S.; Zewail, A. H., Ultrafast Dynamics of Porphyrins in the Condensed Phase: Ii. Zinc Tetraphenylporphyrin†. *The Journal of Physical Chemistry A* **2002**, *106*, 9845-9854.
23. Venkatesh, Y.; Venkatesan, M.; Ramakrishna, B.; Bangal, P. R., Ultrafast Time-Resolved Emission and Absorption Spectra of Meso-Pyridyl Porphyrins Upon Soret Band Excitation Studied by Fluorescence up-Conversion and Transient Absorption Spectroscopy. *The Journal of Physical Chemistry B* **2016**, *120*, 9410-9421.
24. Zhang, J.; Pápai, M.; Hirsch, A.; Jennings, G.; Kurtz, C. A.; Møller, K. B.; Lomoth, R.; Gosztola, D.; Zhang, X.; Canton, S. E., Elucidating the Ultrafast Dynamics of Photoinduced Charge Separation in Metalloporphyrin-Fullerene Dyads across the Electromagnetic Spectrum. *The Journal of Physical Chemistry C* **2016**, *120*, 19537-19546.
25. Kumar, P. H.; Venkatesh, Y.; Siva, D.; Ramakrishna, B.; Bangal, P. R., Ultrafast Relaxation Dynamics of 5, 10, 15, 20-Meso-Tetrakis Pentafluorophenyl Porphyrin Studied by Fluorescence up-Conversion and Transient Absorption Spectroscopy. *The Journal of Physical Chemistry A* **2015**, *119*, 1267-1278.
26. Wang, C.; Shi, G.; Zhu, Z.; Luo, S.; Sun, W.; Jiao, W.; Gao, R.; Fan, G.; Song, Y., Ultrafast Dynamics and Third-Order Nonlinear Optical Response of Meso-(2-Thienyl)Porphyrin Derivatives. *Optical Materials* **2020**, *100*, 109621.
27. Enescu, M.; Steenkeste, K.; Tfibel, F.; Fontaine-Aupart, M.-P., Femtosecond Relaxation Processes from Upper Excited States of Tetrakis(N-Methyl-4-Pyridyl)Porphyrins Studied by Transient Absorption Spectroscopy. *Physical Chemistry Chemical Physics* **2002**, *4*, 6092-6099.
28. Reddy, G.; Katakam, R.; Devulapally, K.; Jones, L. A.; Della Gaspera, E.; Upadhyaya, H. M.; Islavath, N.; Giribabu, L., Ambient Stable, Hydrophobic, Electrically Conductive Porphyrin Hole-Extracting Materials for Printable Perovskite Solar Cells. *Journal of Materials Chemistry C* **2019**, *7*, 4702-4708.

29. van Stokkum, I. H.; Larsen, D. S.; van Grondelle, R., Global and Target Analysis of Time-Resolved Spectra. *Biochimica et Biophysica Acta (BBA)-Bioenergetics* **2004**, *1657*, 82-104.

30. Snellenburg, J. J.; Laptenok, S. P.; Seger, R.; Mullen, K. M.; Stokkum, I. H. M. v., Glotaran: Ajava-Based Graphical User Interface for Therpackagetimp. *Journal of Statistical Software* **2012**, *49*.

31. Krishnakanth, K. N.; Seth, S.; Samanta, A.; Venugopal Rao, S., Broadband Ultrafast Nonlinear Optical Studies Revealing Exciting Multi-Photon Absorption Coefficients in Phase Pure Zero-Dimensional Cs4PbBr6 Perovskite Films. *Nanoscale* **2019**, *11*, 945-954.

32. Kumar, R. S. S.; Rao, S. V.; Giribabu, L.; Rao, D. N., Femtosecond and Nanosecond Nonlinear Optical Properties of Alkyl Phthalocyanines Studied Using Z-Scan Technique. *Chemical Physics Letters* **2007**, *447*, 274-278.

33. Kumar, R. S. S.; Rao, S. V.; Giribabu, L.; Rao, D. N., Ultrafast Nonlinear Optical Properties of Alkyl Phthalocyanines Investigated Using Degenerate Four-Wave Mixing Technique. *Optical Materials* **2009**, *31*, 1042-1047.

34. Rao, A. S.; Dar, M. H.; Venkatramaiah, N.; Venkatesan, R.; Sharan, A., Third Order Optical Nonlinear Studies and Its Use to Estimate Thickness of Sandwiched Films of Tetra-Phenyl Porphyrin Derivatives. *Journal of Nonlinear Optical Physics & Materials* **2016**, *25*, 1650039.

35. Rao, D. V. G. L. N.; Aranda, F. J.; Roach, J. F.; Remy, D. E., Third-Order, Nonlinear Optical Interactions of Some Benzporphyrins. *Applied Physics Letters* **1991**, *58*, 1241-1243.

36. Rao, S. V.; Srinivas, N. K. M. N.; Rao, D. N.; Giribabu, L.; Maiya, B. G.; Philip, R.; Kumar, G. R., Studies of Third-Order Optical Nonlinearity and Nonlinear Absorption in Tetra Tolyl Porphyrins Using Degenerate Four Wave Mixing and Z-Scan. *Optics Communications* **2000**, *182*, 255-264.

37. Siji Narendran, N. K.; Soman, R.; Arunkumar, C.; Chandrasekharan, K., Third-Order Nonlinear Optical Investigations of Meso-Tetrakis(2,3,5,6-Tetrafluoro-N,N-Dimethyl-4-Anilinyl)Porphyrin and Its Metal Complexes. *Spectrochimica Acta Part A: Molecular and Biomolecular Spectroscopy* **2015**, *136*, 838-844.

38. Ahn, T. K.; Kwon, J. H.; Kim, D. Y.; Cho, D. W.; Jeong, D. H.; Kim, S. K.; Suzuki, M.; Shimizu, S.; Osuka, A.; Kim, D., Comparative Photophysics of [26]- and

[28]Hexaphyrins(1.1.1.1.1.1): Large Two-Photon Absorption Cross Section of Aromatic [26]Hexaphyrins(1.1.1.1.1.1). *Journal of the American Chemical Society* **2005**, *127*, 12856-12861.

39. Suslick, K. S.; Chen, C. T.; Meredith, G. R.; Cheng, L. T., Push-Pull Porphyrins as Nonlinear Optical Materials. *Journal of the American Chemical Society* **1992**, *114*, 6928-6930.
40. Ogawa, K.; Ohashi, A.; Kobuke, Y.; Kamada, K.; Ohta, K., Strong Two-Photon Absorption of Self-Assembled Butadiyne-Linked Bisporphyrin. *Journal of the American Chemical Society* **2003**, *125*, 13356-13357.
41. Odom, S. A., et al., Synthesis and Two-Photon Spectrum of a Bis(Porphyrin)-Substituted Squaraine. *Journal of the American Chemical Society* **2009**, *131*, 7510-7511.
42. Sheng, N.; Liu, D.; Wu, J.; Gu, B.; Wang, Z.; Cui, Y., Donor-Π-Acceptor Type Porphyrins with Large Two-Photon Absorption Cross Section. *Dyes and Pigments* **2015**, *119*, 116-121.
43. Mikhaylov, A.; Kondratuk, D. V.; Cnossen, A.; Anderson, H. L.; Drobizhev, M.; Rebane, A., Cooperative Enhancement of Two-Photon Absorption in Self-Assembled Zinc-Porphyrin Nanostructures. *The Journal of Physical Chemistry C* **2016**, *120*, 11663-11670.
44. Hisaki, I.; Hiroto, S.; Kim, K. S.; Noh, S. B.; Kim, D.; Shinokubo, H.; Osuka, A., Synthesis of Doubly β-to-β 1,3-Butadiyne-Bridged Diporphyrins: Enforced Planar Structures and Large Two-Photon Absorption Cross Sections. *Angewandte Chemie International Edition* **2007**, *46*, 5125-5128.
45. Yoon, Z. S., et al., Nonlinear Optical Properties and Excited-State Dynamics of Highly Symmetric Expanded Porphyrins. *Journal of the American Chemical Society* **2006**, *128*, 14128-14134.
46. Raymond, J. E.; Bhaskar, A.; Goodson, T.; Makiuchi, N.; Ogawa, K.; Kobuke, Y., Synthesis and Two-Photon Absorption Enhancement of Porphyrin Macrocycles. *Journal of the American Chemical Society* **2008**, *130*, 17212-17213.
47. Esipova, T. V.; Rivera-Jacquez, H. J.; Weber, B.; Masunov, A. E.; Vinogradov, S. A., Two-Photon Absorbing Phosphorescent Metalloporphyrins: Effects of π-Extension and Peripheral Substitution. *Journal of the American Chemical Society* **2016**, *138*, 15648-15662.

48. Ogawa, K.; Ohashi, A.; Kobuke, Y.; Kamada, K.; Ohta, K., Two-Photon Absorption Properties of Self-Assemblies of Butadiyne-Linked Bis(Imidazolylporphyrin). *The Journal of Physical Chemistry B* **2005**, *109*, 22003-22012.
49. Kruk, M.; Karotki, A.; Drobizhev, M.; Kuzmitsky, V.; Gael, V.; Rebane, A., Two-Photon Absorption of Tetraphenylporphin Free Base. *Journal of Luminescence* **2003**, *105*, 45-55.
50. Swain, D.; Rana, A.; Panda, P. K.; Venugopal Rao, S., Strong Two-Photon Absorption Properties and Ultrafast Pump-Probe Studies of Novel Porphyrin Derivatives. *Chemical Physics Letters* **2014**, *610-611*, 310-315.
51. Schmitt, J.; Heitz, V.; Jenni, S.; Sour, A.; Bolze, F.; Ventura, B., π-Extended Porphyrin Dimers as Efficient near-Infrared Emitters and Two-Photon Absorbers. *Supramolecular Chemistry* **2017**, *29*, 769-775.
52. Alam, M. M.; Bolze, F.; Daniel, C.; Flamigni, L.; Gourlaouen, C.; Heitz, V.; Jenni, S.; Schmitt, J.; Sour, A.; Ventura, B., π-Extended Diketopyrrolopyrrole–Porphyrin Arrays: One- and Two-Photon Photophysical Investigations and Theoretical Studies. *Physical Chemistry Chemical Physics* **2016**, *18*, 21954-21965.
53. Nakamura, Y.; Jang, S. Y.; Tanaka, T.; Aratani, N.; Lim, J. M.; Kim, K. S.; Kim, D.; Osuka, A., Two-Dimensionally Extended Porphyrin Tapes: Synthesis and Shape-Dependent Two-Photon Absorption Properties. *Chemistry - A European Journal* **2008**, *14*, 8279-8289.
54. Greco, J. A.; Shima, S.; Wagner, N. L.; McCarthy, J. R.; Atticks, K.; Brückner, C.; Birge, R. R., Two-Photon Spectroscopy of the Q-Bands of Meso-Tetraphenyl-Porphyrin and -Chlorin Framework Derivatives. *The Journal of Physical Chemistry C* **2015**, *119*, 3711-3724.
55. Sheng, N.; Gu, B.; Ren, B.; Zhang, J.; Wang, Y.; Wang, J.; Sha, J., A Series of Polycyclic Aromatic Hydrocarbon-Substituted Metal-Free Porphyrins: Substituent Effect on Two-Photon Absorption Property. *Dyes and Pigments* **2017**, *142*, 116-120.
56. Makhal, K.; Arora, S.; Kaur, P.; Goswami, D.; Singh, K., Third-Order Nonlinear Optical Response and Ultrafast Dynamics of Tetraoxa [22] Porphyrin (2.1. 2.1) S. *Journal of Materials Chemistry C* **2016**, *4*, 9445-9453.

57. Raavi, S. S. K.; Biswas, C., Femtosecond Pump-Probe Spectroscopy for Organic Photovoltaic Devices. In *Digital Encyclopedia of Applied Physics*, Wiley-VCH Verlag GmbH & Co. KGaA: 2019; pp 1-49.

58. Biswas, C.; Krishnakanth, K. N.; Lade, J. J.; Chaskar, A. C.; Tripathi, A.; Chetti, P.; Soma, V. R.; Raavi, S. S. K., Linear and Femtosecond Nonlinear Optical Properties of Soluble Pyrrolo[1,2-a] Quinoxalines. *Chemical Physics Letters* **2019**, *730*, 638-642.

Chapter 6 Ultrafast Photophysical and NLO Properties of Free Base and Axially Substituted Phosphorus (V) Corroles

Abstract

In continuation of the work presented in chapter 5, we present results from our investigations of ultrafast photophysical processes, and third-order nonlinear optical properties of newly synthesized donor-acceptor (D-A) based free-base [$(C_6F_5)_3$] and phosphorus [P-$(OH)_2(C_6F_5)_3$] corroles in the present chapter. The global analysis of the femtosecond (fs) transient absorption data based on a compartmental model revealed the corresponding lifetimes of several photophysical processes such as (a) internal conversion (τ_{IC}) in the 260-280 fs range (b) vibrational relaxation (τ_{VR}) in the 2.5-5ps range and (c) nonradiative relaxation times (τ_{nr}) in the 4.15-7.6 ns range and finally (d) triplet lifetimes in the range of 25-50 µs. The nonlinear absorption [two-photon absorption (TPA)] measurements were performed using fs, kHz pulse Z-scan technique at wavelengths of 600 nm and 800 nm. From this data, we retrieved the TPA coefficients and cross-section values (which were found to be in the range of ~10^2 GM). Degenerate four-wave mixing (DFWM) measurements illustrated a large third-order nonlinear optical susceptibility $\chi^{(3)}$ with a magnitude of 6.9×10^{-14} esu and instantaneous (sub-picosecond) response. The time-resolved DFWM data suggests the contribution of only a pure electronic contribution to the nonlinearity of these corroles. The discoveries from this study may help further to extend the capability of corroles as NLO materials for photonic applications.

This chapter comprises data from the following publication:

1. **Katturi, N.K.,** Balahoju, S.A., Ramya, A.R., Biswas, C., Raavi, S.S.K., Giribabu, L. and Soma, V.R., Ultrafast photophysical and nonlinear optical properties of novel free base and axially substituted phosphorus (V) corroles. *Journal of Molecular Liquids*, **311,** 113308, (2020).

6.1 Introduction

Unique, organic molecules possessing stable and reliable optical/nonlinear optical (NLO) properties are a prerequisite for diverse applications in photonics, bio-imaging, photovoltaic, and photocatalysis.[1-3] Notably, organic molecules possessing large π-conjugation, specially corroles with donor-acceptor (D-A) systems, are suitable for many applications, mainly photovoltaics[4-8] and frequency up-conversion[9] due to close structural similarities of natural photosynthetic pigments.[10-12] They have also demonstrated strong NLO properties arising from a sizeable π-electron conjugation and de-localization.[13-18] Organic molecules with π-bond conjugation are known to show intense dipole moments and create a delocalized distribution of electric charges due to intramolecular charge transfer (ICT) resulting in high electrical polarization, which is advantageous for significant NLO response.[19-24] A few research reports on natural photosynthetic phenomena of D-A systems based corroles have been reported in the literature.[25-29] Such D-A systems have been designed by altering the local position of metal ion in the corrole macrocycle. For example, the substitution could be either at the axial or the meso-phenyl location. In the tetrapyrrolic family, corroles are new chromophores (that are similar to porphyrinoids) and possess 18 π–electron aromaticity, identical to that of porphyrins. Corrole ring consists of four (4) nitrogen atoms at the core and 19 carbons atoms in the molecule. When compared to porphyrins, corroles have attractive properties such as (a) stability (b) higher fluorescence yields (c) intense absorption in the red region of the optical band (d) lower oxidation potentials and (e) significant stoke shifts. In corroles, the three central nitrogen atoms can stabilize the higher oxidation states of different metals, which make them suitable materials for applications in a variety of different fields such as artificial photosynthesis and biomedical applications.[9,30] By attaching the various metals/transition metals to the corrole macrocycle, it is possible to tune the optical properties. This tuning is possible because of a change in the energy gap of the molecular orbitals, which can be potentially used for biomedical imaging and sensing.[31-35] Efficient photo-induced electron transfer (PET) and triplet photosensitization can be achieved by donor-acceptor based molecular systems with longer relaxation times.[4,36-38] PET is the fundamental process in photosynthesis and different artificial photo-devices. The triplet photosensitizers should have efficient intersystem crossing to achieve triplet excited states. This is possible by adding the metal/transition metal to the corrole macrocycle provided high fluorescence quantum yields.[9, 39-43] Liu and co-workers[44] have performed a comparative study of the excited state dynamics of Al, Ga corroles wherein they found from their studies that corroles are planar rigid frameworks with large Frank-Condon vibration states possessing large S_2 displacements compared to metalloporphyrins. They recorded lifetimes of the S_2 states to be ~520 fs and ~280 fs for Al(tpfc)(py) corrole and Ga(tpfc)(py) corrole, respectively. Raavi and co-workers[45] recently presented a systematic photophysical investigation on a series of Phosphorous (P-TTC) and Germanium (Ge-TTC) based corroles dissolved in toluene occurring in the femtosecond to microsecond time scales and concluded that Ge-TTC had superior triplet state properties compared to P-TTC. Therefore, understanding these ultrafast photophysical processes, especially in newly designed and developed molecules, is essential for the development of new systems, enabling them to find potential applications. On the other hand, the NLO properties of corroles have evoked tremendous interest due to their highly conjugated π-electron distribution compared to porphyrins. Several authors have investigated the NLO behavior of different corroles, and they found significant NLO coefficients[16,46] in comparison with porphyrins. Although the NLO properties of corroles are found to be superior to porphyrins, very few reports are found in NLO activity. In general, for an efficient NLO application (e.g. optical switching), the material should possess high nonlinear refractive index n_2 values with an instantaneous response. In this work, we have synthesized a novel free-base and axially substituted phosphorus corroles. The investigation of their photophysical process and third-order NLO properties/responses were studied in the solution phase. The transient absorption studies depicted long triplet decay times in the case of phosphorus corrole and strongly excited state absorption behavior. We observed significantly strong NLO coefficients and TPA cross-sections (~190 GM) along with Kerr-type nonlinear refractive index (n_2 ~10^{-15} cm^2/W) from these synthesized corroles.

6.2 Experimental Details

6.2.1 Synthesis

Synthesis of 5,10,15-tris(pentafluorophenyl)corrole (C_6F_5-Corrole) and phosphorous complex of C_6F_5-Corrole (P-$(OH)_2(C_6F_5)_3$-Corrole) have been reported in literature [47-48]. The steady-state UV absorption and emission spectra were obtained by using the PerkinElmer spectrophotometer and Fluorolog (M/s HORIBA). The samples were dissolved in a pure DMF to prepare the diluted solutions of ~ 25 µM concentration. The prepared samples are filled in a 1-cm quartz cuvette and kept sealed for all the measurements. The measurements were performed at room temperature. The fluorescence spectra were recorded at 410 nm excitation, and the spectra were obtained in the 300–750 nm spectral range.

6.3 Results and Discussions

6.3.1 Steady-state absorption and emission spectra

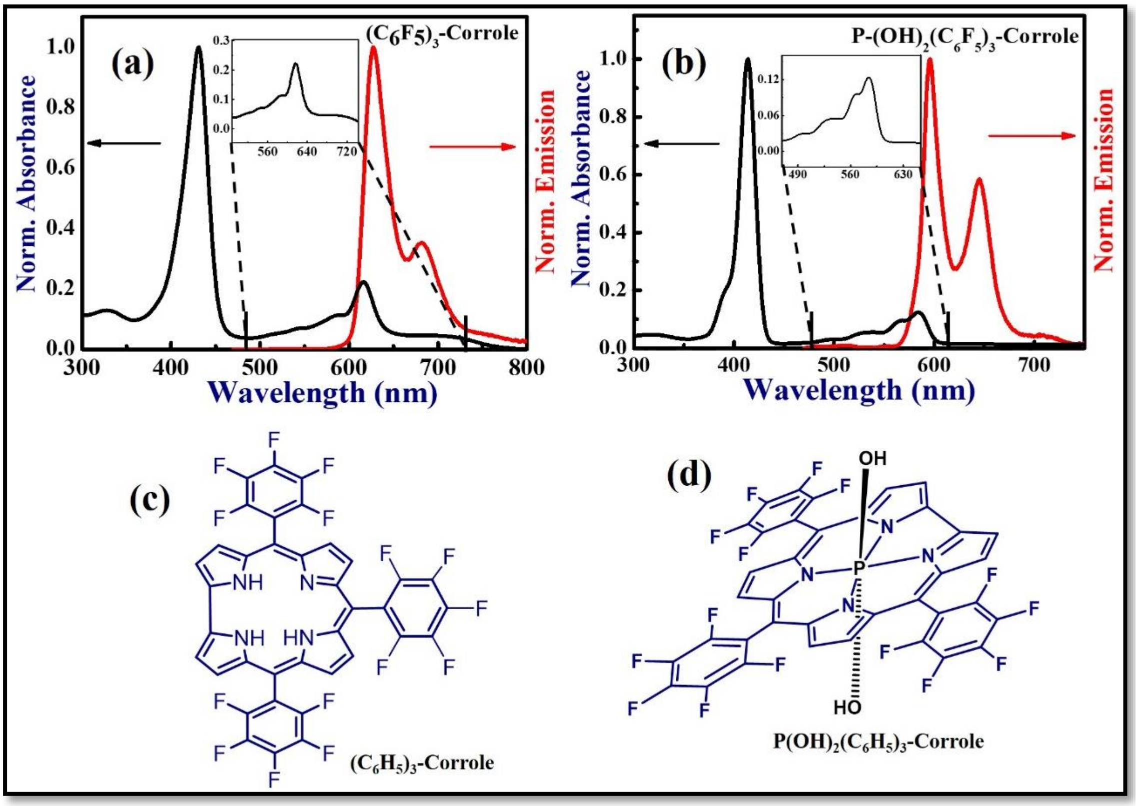

Figure 6.1 Absorption and emission spectra of (a) $(C_6H_5)_3$-Corrole and (b) P-$(OH)_2(C_6F_5)_3$-Corrole in DMF solvent (c) and (d) Molecular structure of the title molecules investigated in the present study.

The steady-state absorption spectra of two corroles $(C_6F_5)_3$-Corrole and P-$(OH)_2(C_6F_5)_3$-Corrole are shown in figures 6.1(a) and 6.1(b) (black curves). An intense peak [Soret band (S_2)] near 430 nm for the free-base corrole was observed, which arises mainly due to the π-π* electronic transitions from the ground state to the second excited state (S_2). The Soret band of phosphorus corrole was observed with a blue shift at 410 nm. The inset displays the magnified view of the Q-band absorption due to the π-π* transition from the ground state to the first excited state (S_1). The steady-state emission spectra of the synthesized corroles were recorded at 410 nm excitation, as shown in figures 6.1(a) and 6.1(b) (red curves). The photophysical parameters and DFT studies were reported in our earlier work,[49] with the corresponding molecular structure are shown in figures 6.1(c) and 6.1(d). The energies of

HOMO-LUMO were 5.80 eV, and 2.88 eV and 5.32 eV and 2.79 eV for phosphorus(V) corrole and C_6F_5-corrole respectively,[49-50] and the fluorescence quantum yields are found to be Φ=0.53 and Φ=0.14 in phosphorus(V) corrole and C_6F_5-corrole with singlet excited state lifetime of 3.6 ns and 3.7 ns in solution state (dichloromethane).[29, 49]

6.3.2 Transient Absorption Measurements

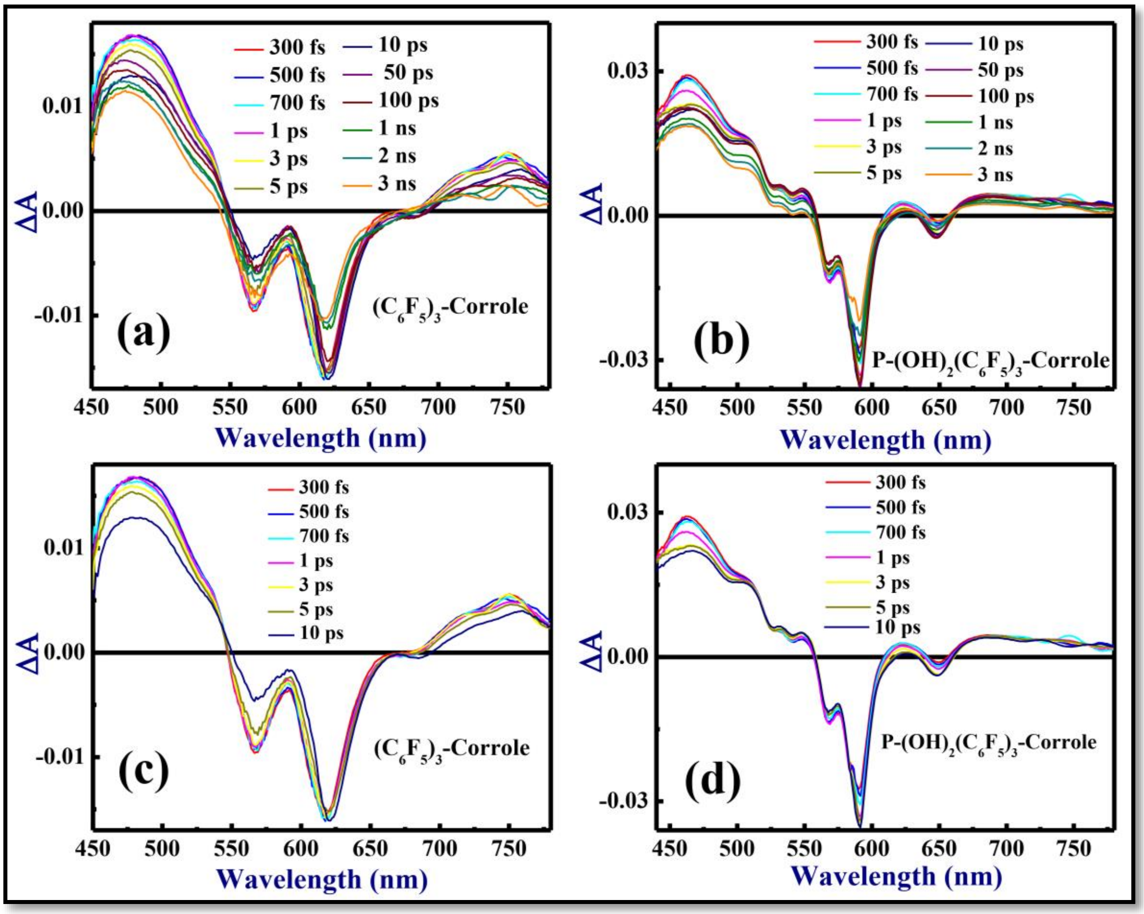

Figure 6.2 fs-TA spectra of (a) $(C_6F_5)_3$-Corrole and (b) $P-(OH)_2(C_6F_5)_3$-Corroleat different probe delays and TA spectra of (c) $(C_6F_5)_3$-Corrole and (d) $P-(OH)_2(C_6F_5)_3$-Corrole at a shorter time scale up to 10 ps.

The femtosecond (fs) transient absorption (TA) measurements were performed at Soret band photoexcitation with 400 nm wavelength. The TA spectra were measured up to 3 ns delay from 450- 780 nm wavelength range. Figures 6.2(a)-(b) depict the transient absorption spectra of the C_6F_5-Corrole and $P-(OH)_2(C_6F_5)_3$-Corrole recorded in DMF solvent. The phosphorus corrole exhibited a strong photobleach signal at 590 nm compared to free-base corrole indicating with slow recovery due to the possible formation of long-lived photo-excited species perhaps resulting from a higher triplet yield. The TA spectra illustrated three different absorption peaks upon photoexcitation I) photo-induced absorption band in the spectral range 450-550 nm due to excited state absorption including the formation of triplet-triplet state absorption II) a negative signal in the spectral range of 556-615 nm due to S_0 ground state bleach (GSB) with Q-band vibrational features and III) stimulated emission peak near 647 nm for phosphorus corrole and 685 nm for free base corrole. A closer look into the TA spectra of phosphorus corrole up to 10 ps, data of which is shown in figures 6.2(c)-(d), revealed various processes:

i. After the photoexcitation with 400 nm positive bands at 465 nm and 714 nm and negative bands at 590 nm and 566 nm are instantaneously formed, and the positive groups are assigned to singlet excited state absorption whereas the negative signals to ground state bleach
ii. The bleach maximum at 590 nm of phosphorus corrole increases up to 50ps, and the Q vibrational band at 570 nm stays up to 1 ps time scale
iii. The stimulated emission peak near 645 nm, that continues to increase up to 100 ps and after that starts decaying which is due to the relaxation of singlet relaxed excited state [figures 6.2(a)-(b)].

In the case of free base corrole, the SE band near 685 nm decayed within 1 ns and the bleach maximum at 620 nm increased up to 10 ps. On a 10 ps time scale, a blue shift in the spectra shown in figures 6.2(c)-(d), is evident from both the spectra. After that, it was observed to start decaying continuously. This represents the two different species spectra before and after a 10 ps time scale, which could be due to the vibrational relaxation to the S_1 excited state at that time scale. The longer decay of the bleach signal due to the loss of excited state absorption confirms the formation of triplet states, as seen in figures 6.2(a) and 6.2(b).

Understanding the ultrafast photophysical process by single wavelength analysis is difficult due to the overlapping of different photo-processes. Therefore, global analysis based on target model was performed on both the spectra free-base and phosphorus corrole to get a comprehensive picture of the various photo-processes involved such as A) internal conversion (from the lowest vibrational states of S_n to the highest vibrational states of S_1) B) vibrational relaxation (within the S_1 state) C) nonradiative relaxation [including the intersystem crossing (S_1 states to T_1 states) and (S_1 states to S_0 states) and D) triplet decay

(T_0-S_0) wherein the population from T_0 states relaxes to ground state S_0. Figure 6.3 shows the TA kinetic profiles along with fittings at selected wavelengths for phosphorus corrole and free-base corrole obtained after the target analysis. The displayed wavelengths represent different photo-processes after photoexcitation at 400 nm. The kinetics of phosphorus corrole at Q-band at 590 nm (GSB) did not decay even after 3 ns, which suggests the formation of long-lived excited species. The kinetics of the SE band maxima at 648 nm decayed within ~2 ns in the case of phosphorus corrole, whereas in the case of free-base corrole kinetics of the SE band at 683 nm completely decayed within 1 ns suggesting the formation of triplet states at these time scales. A kinetic analysis based on a compartmental scheme was implemented by using a photophysical model, as shown in figure 6.4, which helped us to estimate the spectra of excited species providing corresponding species associated difference spectra (SADS) and microscopic rate constants of individual species shown in figure 6.5.

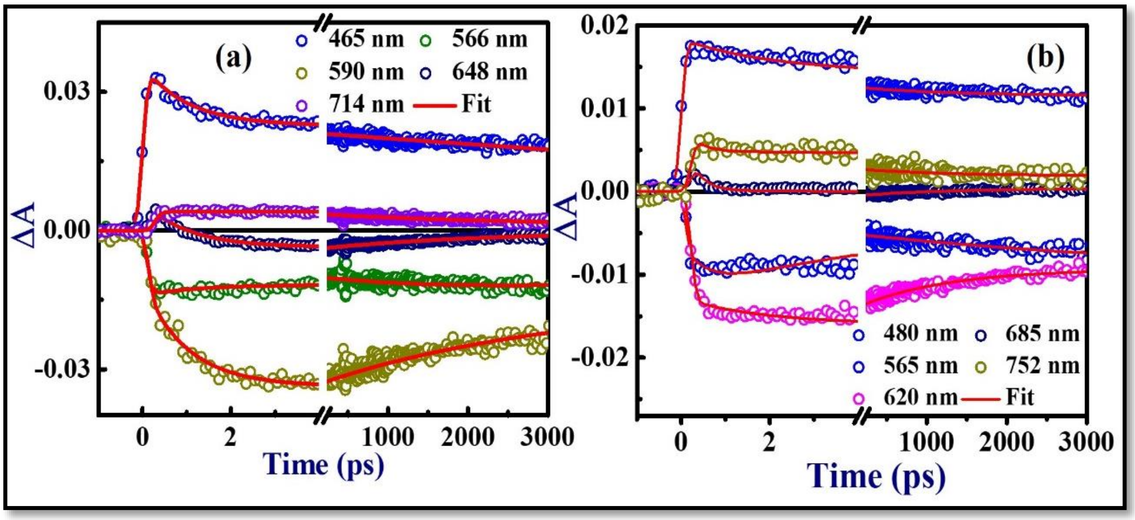

Figure 6.3 TA kinetics of (a) $(C_6F_5)_3$-Corrole and (b) P-$(OH)_2(C_6F_5)_3$-Corroleat selected wavelengths scattered points are experiential data while the solid lines are theoretical fits.

Sample	k_{IC} $10^{12}\ s^{-1}$ (τ_{IC})	k_{VR} $10^{12}\ s^{-1}$ (τ_{VR})	k_r $10^{9}\ s^{-1}$ (τ_r)	k_{nr} $10^{9}\ s^{-1}$ (τ_{nr})	k_{T0} $10^{4}\ s^{-1}$ (τ_{T0})
C_6F_5-Corrole	3.5 (280 fs)	0.2 (5.0 ps)	0.0392 (25.5 ns)	0.2622 (4.15 ns)	2 (50 µs)
P-$(OH)_2(C_6F_5)_3$-Corrole	3.8 (260 fs)	0.4 (2.5 ps)	0.1484 (6.7 ns)	0.1316 (7.6 ns)	4 (25 µs)

Table 6.1 Estimated photophysical parameters of the corroles investigated obtained from the global analysis. The values in the parenthesis indicate the relevant lifetimes.

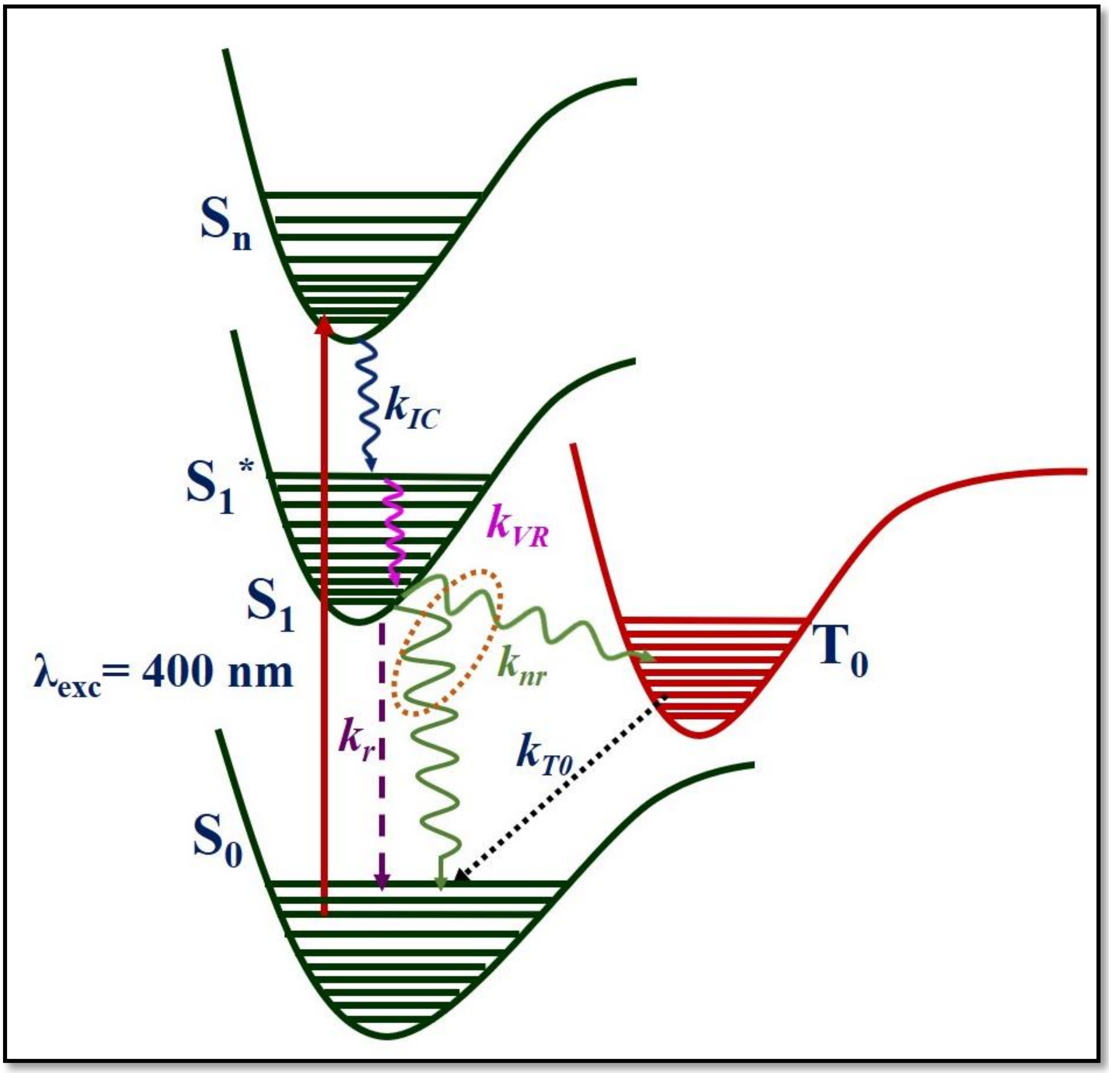

Figure 6.4 Schematic of the representative energy band model taken for global analysis.

Figure 6.5 shows the target analysis for the phosphorus corrole and free-base corrole TA spectra with respective SADS (left) and population (right) decay profiles. From the target analysis of the phosphorus corrole TA spectra based on the photophysical model (figure 6.4), we estimated the internal conversion (IC) rate (S_n to S_1^* states) as $k_{IC} = 3.8\times10^{12}$ s^{-1} corresponding to a lifetime of 260 fs, vibrational relaxation (VR) rate (from S_1^* to S_1 states) constant as $k_{VR} = 4\times10^{11}$ s^{-1} corresponding to a lifetime of 2.5 ps and triplet relaxation from T_0 to S_0 with life time estimated to be 25 µs. The lifetime of S_1 state was fixed using the value obtained from the TCSPC measurements, which was 3.6 ns. We used $\tau_{TCSPC} = [1/(k_r + k_{nr})]$ wherein 'τ_{TCSPC}' is the lifetime obtained from measurements and k_r being the radiative decay rate and k_{nr} being the nonradiative decay rate (the population from S_1 state can come down to the ground state of S_0 directly or through T_0 (via ISC).[29, 54] From S_1 state 53% of population goes radiatively to the ground state with 6.7 ns lifetime (obtained from fluorescence quantum yield), and the remaining 47% is transferred to non-radiatively with a 7.6 ns lifetime constant. In case of free-base corrole the life time of S_1 state was obtained as 3.7 ns, where 14% population from S_1 state goes radiatively to S_0 with a lifetime of 25.5 ns and 86% of population is transferred non-radiatively to the ground state with a lifetime of 4.15 ns. We have obtained an excellent agreement between the theoretical fits and the experimental TA data.

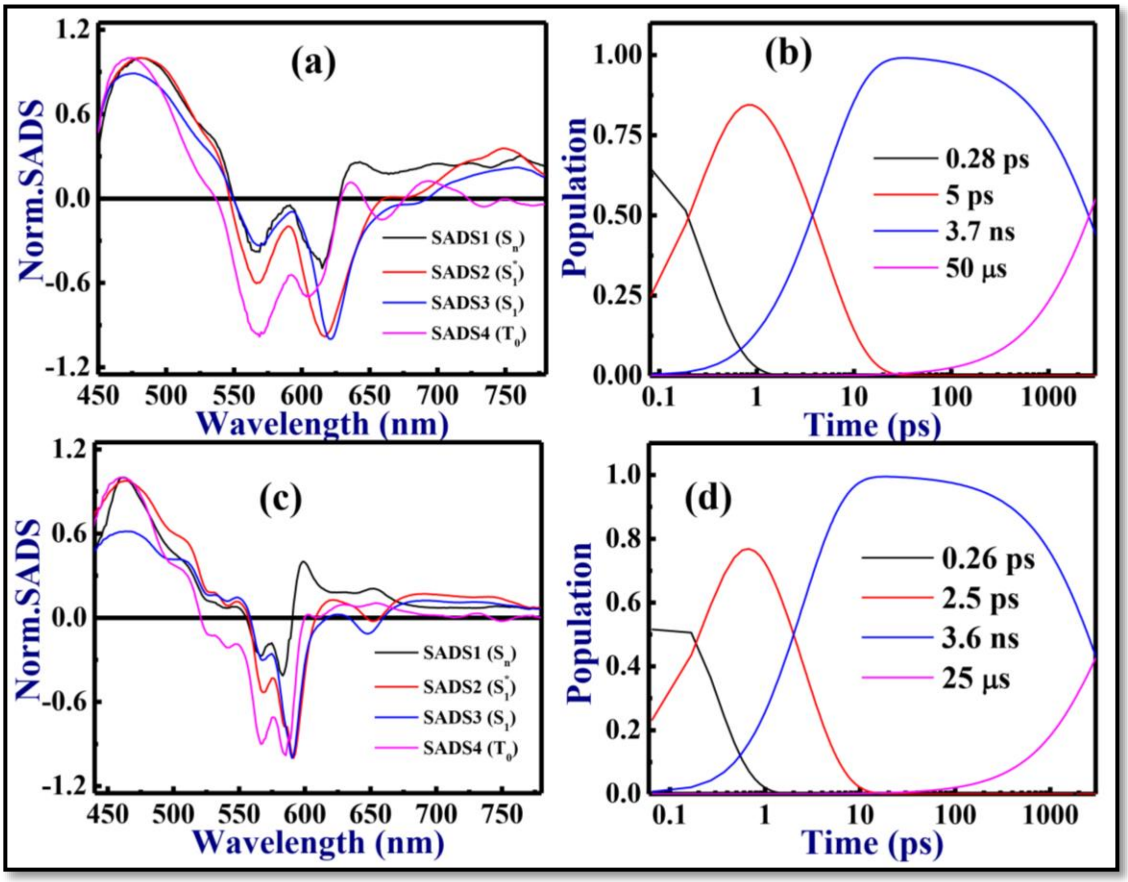

Figure 6.5 SADS (left) and concentration profiles (right) of (a, c) $(C_6F_5)_3$-Corrole and (b, d) P-$(OH)_2(C_6F_5)_3$-Corrole.

Figure 6.6 demonstrates a significant overlap (good agreement) of the TA data (represented by the scattered points) and theoretical fit (represented by solid lines) at 0.3 ps and 3 ns probe delay times of the synthesized corroles. Table 6.1 summarizes the estimated photophysical parameters from the target analysis. The errors in the lifetimes were expected to be <1%. Figures 6.5(a) and 6.5(c) illustrate the SADS spectra of two corroles and individual population decay profiles while figures 6.5(b) and 6.5(d) show the population of different excited states after photoexcitation with a wavelength of 400 nm. The SADS spectra of corroles bring the distinction between different processes, the SADS1 (left) corresponds to the formation of higher excited state S_n and SADS 2, and 3 represents the vibrational hot S_1^*states and relaxed S_1 state. The SADS4 could be due to the relaxation of the triplet state.

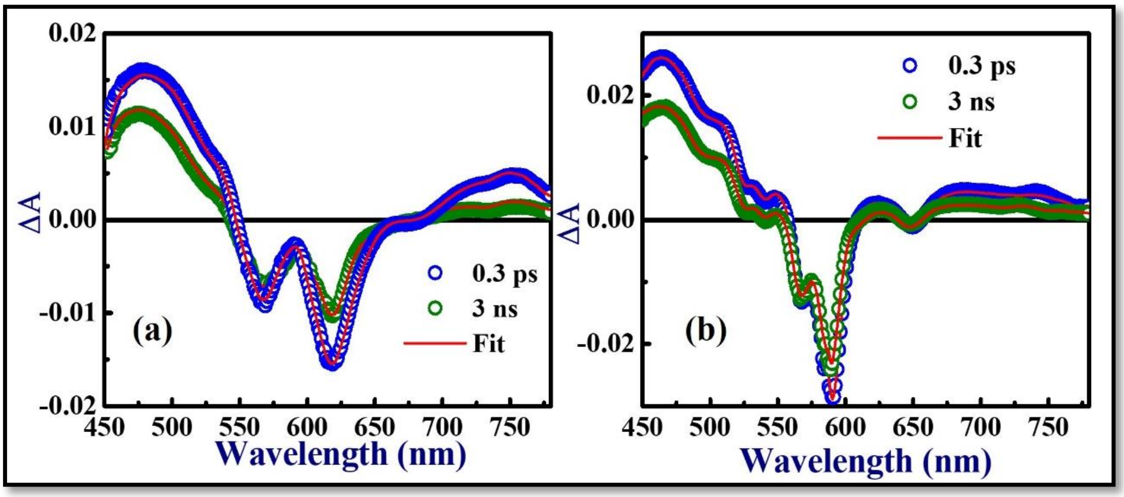

Figure 6.6 fs-TA spectra of (a) $(C_6F_5)_3$-Corrole and (b) P-$(OH)_2(C_6F_5)_3$-Corroleat a pump−probe delay of 0.3ps and 3 ns depicting an excellent agreement of the global fitting (solid line) with the experimental data (circles).

6.3.3 Nonlinear Optical Properties

6.3.3.1 Z-Scan data and analysis

The third-order NLO properties of synthesized Corrole were investigated at 600 nm and 800 nm wavelength by using a 50 fs laser pulses using a Z-scan technique with an input intensity of ~50 GW/cm^2. All the measurements were performed in a solution phase at room temperature with solution processing concentration ~0.1 mM in pure DMF. From the obtained Z-scan transmission curves, two-photon absorption coefficient (β) and nonlinear refractive index (n_2) and corresponding third-order nonlinear susceptibility $\chi^{(3)}$ were extracted. The open aperture (OA) transmission curves show the reverse saturable absorption behavior, as shown in the data presented in figures 6.7 and 6.8. The OA transmission curves were fitted using a standard two-photon absorption equation (1),

$$T_{OA(nPA)} = \frac{1}{\left[1+(n-1)\beta_n L\left(\frac{I_0}{1+\left(\frac{Z}{Z_0}\right)^2}\right)^{n-1}\right]^{1/n-1}} \tag{1}$$

$$T_{CA} = 1 \pm \frac{4\Delta\phi\left(\frac{Z}{Z_0}\right)}{\left[\left(\frac{Z}{Z_0}\right)^2+9\right]\left[\left(\frac{Z}{Z_0}\right)^2+1\right]} \tag{2}$$

where L is the effective path length of the sample $L_{eff} = 1 - e^{-\alpha_0 L}/\alpha_0$, Z_0 is the Rayleigh range $Z_0 = \pi\omega_0^2/\lambda$, ω_0 is the beam waist at focus (Z=0), I_0 is the peak intensity.

The two-photon absorption (TPA) cross-sections were obtained from $\sigma_n = \frac{(\hbar\omega)^{n-1}}{N}\beta_n$ (n=2) where ω is input laser frequency, and N is the concentration of the sample. The obtained NLO coefficients are listed in table 6.2. The errors in the NLO coefficients are estimated to be <5% arising predominantly from input peak intensity estimation. Phosphorus corrole exhibited a strong two-photon absorption coefficient (4.6×10^{-13}cm/W) compared to free-base corrole, possibly due to the effect of phosphorous ion.[16, 49, 51] The TPA cross-section values were found to be stronger compared to some of the recently reported molecules.[16-17, 46, 51-53] Figures 6.7 (b)-(d) and 6.8 (b)-(d) illustrate the closed aperture Z-scan curves. The valley followed by a peak signature suggests positive n_2 and a self-focusing behavior with a magnitude of $\sim10^{-15}$ cm^2/W. We measured the nonlinearity of the solvent also and found that the solute plus solvent nonlinearity was higher than that of solvent nonlinearity alone. It is pertinent to mention here that the n_2 measured was for the solutions prepared with typical mM concentrations. One needs to prepare thin solid films using these molecules or doped them into glasses to ascertain the actual magnitude of the solute nonlinearity. Further, there is a finite probability of laser pulses heating up the solvent, thereby resulting in thermal contribution to the overall nonlinearity. However, since the pulse duration is extremely short, and the input pulse energies are too low, we believe that the thermal contribution in this case could be minimal and may require further experiments to quantify that.

The TPA in D-A systems is usually accompanied by a charge transfer process between donor and acceptor molecules such as metal and transition metal ions.[53] Rao et al.[13] recently reported that TPA coefficients from tritolylcorrole (TTC) and triphenylcorrole (TPC) are in the range of 10^{-13} cm/W, using ~40 fs laser pulses at 800 nm. Further, Anusha et al.[51] reported the TPA coefficient from germanium-substituted TTC (GeTTC) and phosphorus substituted TTC (PTTC) corroles with a magnitude of $\sim10^{-12}$ cm/W using ~2 ps pulses again at 800 nm. Garai and co-workers[17] have thoroughly investigated the NLO properties of trans-A_2B-corroles, and they reported values of TPA (β) coefficients and nonlinear refractive index (n_2) values of 10^{-13} cm/W and $\sim10^{-14}$ cm^2/W obtained using 250 fs pulses at 80 MHz at 1064 nm. Recently, Yadav etal.[46] studied the NLO activity of push-pull trans-A2B corroles with ~150 fs pulses but at MHz repetition rate (femtosecond oscillator pulses). They found strong nonlinear coefficients by two-electron withdrawing groups at *meso* position.

Rebane et al.[16] have recenrly demonstrated TPA cross-section values of 60-130 GM (~70 fs,1 kHz repetition rate laser pulses) in *meso*-substituted A3 corroles, and they found that the cross-section values depended on electron accepting capability of the substituents. The axially substituted phosphorus corrole has more robust NLO activity compared to free-base corrole, possibly due to minimization of aggregation. Organic molecules-based donor-acceptor systems can have significant dipole moments by altering the donor or acceptor ions providing strong π-conjugation, and may produce intense electronic polarization. The enhancement of the obtained NLO coefficients from the phosphorus(V)corrole could be attributed to its strong electron withdrawing nature from the pentafluorophenyl group and possibly a strong intramolecular charge transfer between phosphorus and pentafluorophenyl group which creates the large dipole moments. The TPA coefficients and corresponding TPA cross-section values suggest that the synthesized corroles can find applications in two-photon absorption-based bio-imaging, photonics, and optical switching devices.

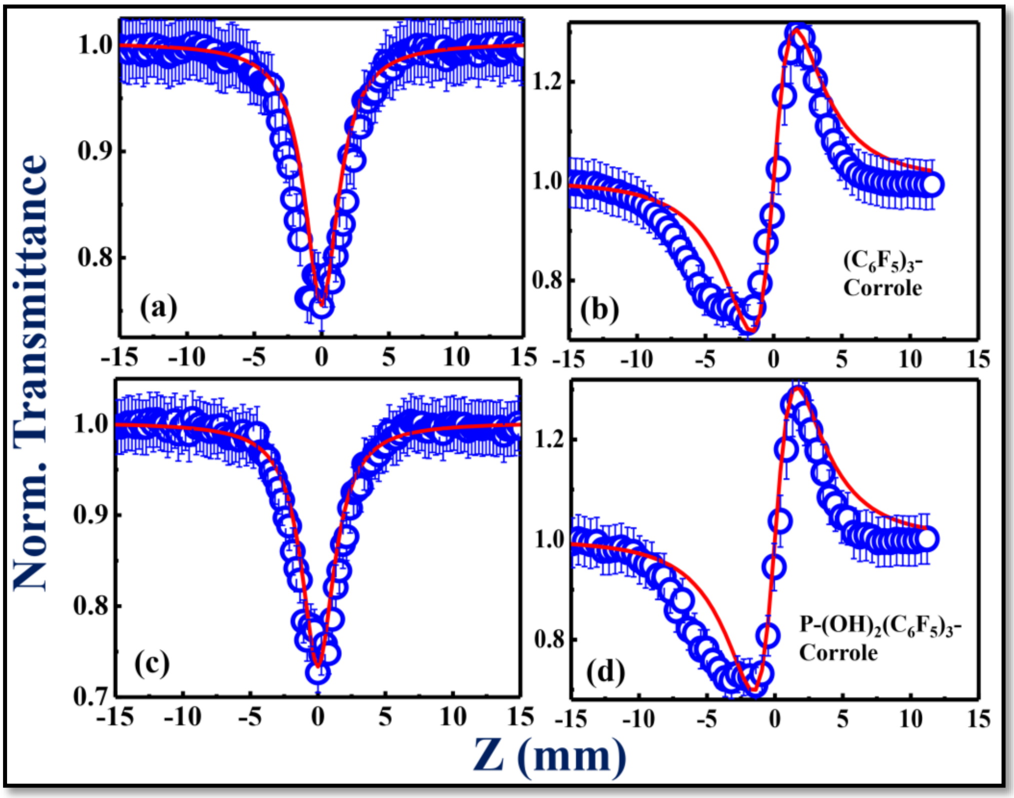

Figure 6.7 (a)-(c) Open aperture Z-scan data (d)-(d) closed aperture Z-scan data of (C_6F_5)$_3$-Corrole and P-(OH)$_2$(C_6F_5)$_3$-Corrole, recorded at 600 nm with 50 fs, 1 kHz pulses.

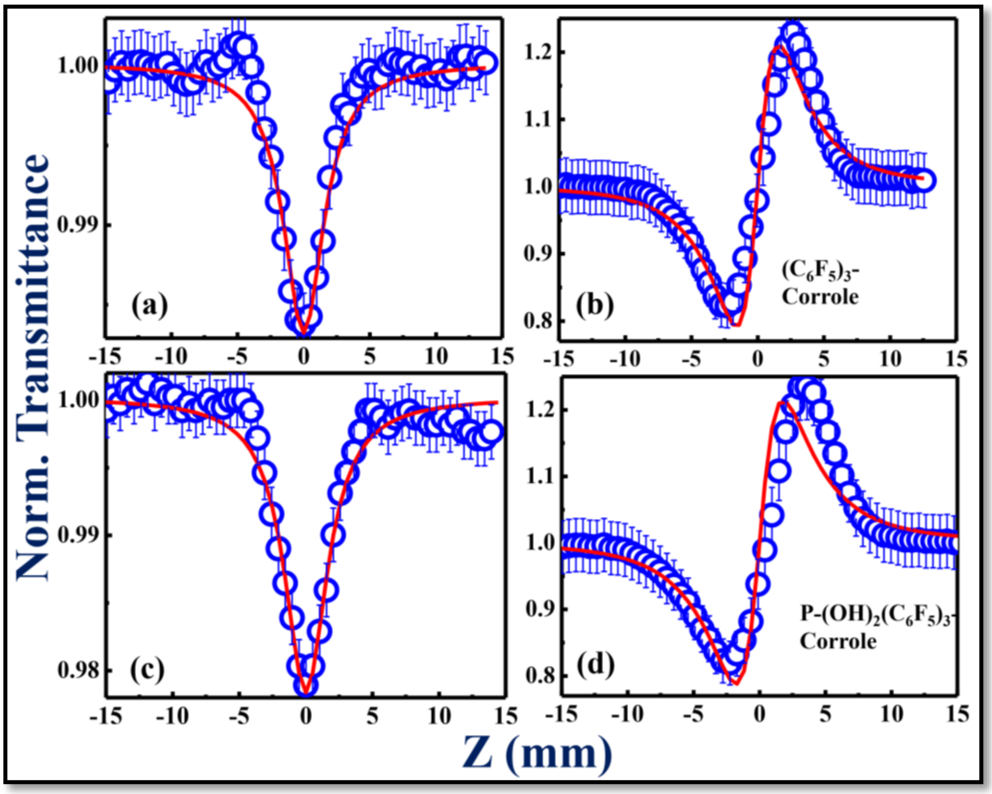

Figure 6.8 (a)-(c) Open aperture Z-scan data (d)-(d) closed aperture Z-scan data of $(C_6F_5)_3$-Corrole and P-$(OH)_2(C_6F_5)_3$-Corrole, recorded at 800 nm with 50 fs, 1 kHz pulses.

Sample	λ nm	α_2 cm/W $\times10^{-13}$	$\sigma_{(TPA)}$ GM	n_2 cm^2/W $\times10^{-15}$	$\chi^{(R)}$ m^2/v^2 $\times10^{-21}$	$\chi^{(I)}$ m^2/v^2 $\times10^{-24}$	$\chi^{(3)}$ m^2/v^2 $\times10^{-21}$	$\chi^{(3)}$ esu $\times10^{-13}$
P-$(OH)_2(C_6F_5)_3$-Corrole	800	4.6	190	2.3	2.5	3.2	2.50	1.80
C_6F_5-Corrole		3.2	130	1.4	1.5	2.2	1.50	1.10
P-$(OH)_2(C_6F_5)_3$-Corrole	600	4.4	181	2.0	2.15	2.3	2.14	1.54
C_6F_5-Corrole		2.5	103	2.1	2.25	1.3	2.24	1.61

Table 6.2 Summary of the NLO coefficients of corroles obtained using the Z-scan technique at 800 nm.

6.3.3.2 DFWM Data Analysis

The DFWM experiments were performed at 800 nm in the forward BOXCAR-geometry. Figures 6.9(a)-(c) illustrate the cubic dependence of the DFWM signal on the input energy, confirming the presence of a third-order NLO process. The measurements were performed in the solution phase (~0.1 mM concentration and dissolved in DMF) indicates the nonlinearity acts as Kerr-like fashion (with a slope of ~3.04). DFWM is an efficient technique to obtain the overall magnitude of $\chi^{(3)}$ since the effect of linear scattering does not contribute to the signal, as in the case of the Z-scan technique. DFWM, however, provides the time response of the optical nonlinearity in addition to the magnitude. Z-scan measurements have contributions occasionally from linear scattering, sample imperfections, and laser beam shape. Thus, DFWM experiments are a better choice to measure the absolute magnitude of third-order nonlinearity when the sample possesses scattering or other issues. A pure solvent [Carbontetrachloride (CCl_4)] was utilized as a reference with $\chi^{(3)} = 4.4\times10^{-14}$ esu and the third-order nonlinear susceptibility $\chi^{(3)}$ was calculated using the standard procedure.[54] We have noticed a slightly higher value of $\chi^{(3)}$ in phosphorus corrole compared to the free-base corrole. The $\chi^{(3)}$ values were 6.2×10^{-14} esu and 6.9×10^{-14} esu for $(C_6F_5)_3$-Corrole and P-$(OH)_2(C_6F_5)_3$-Corrole, respectively. A $\chi^{(3)}$of 4 $\times10^{-14}$ esu was obtained from the pure solvent (DMF) measured at the same experimental conditions. The $\chi^{(3)}$ values obtained in the DFWM and Z-scan experiments vary slightly (by a factor of 2-2.5) and this could possibly be attributed to the stringent alignment in DFWM experiments wherein we perhaps have underestimated the value and have slightly overestimated the values in the Z-scan experiments owing to errors in the peak intensity measurements.

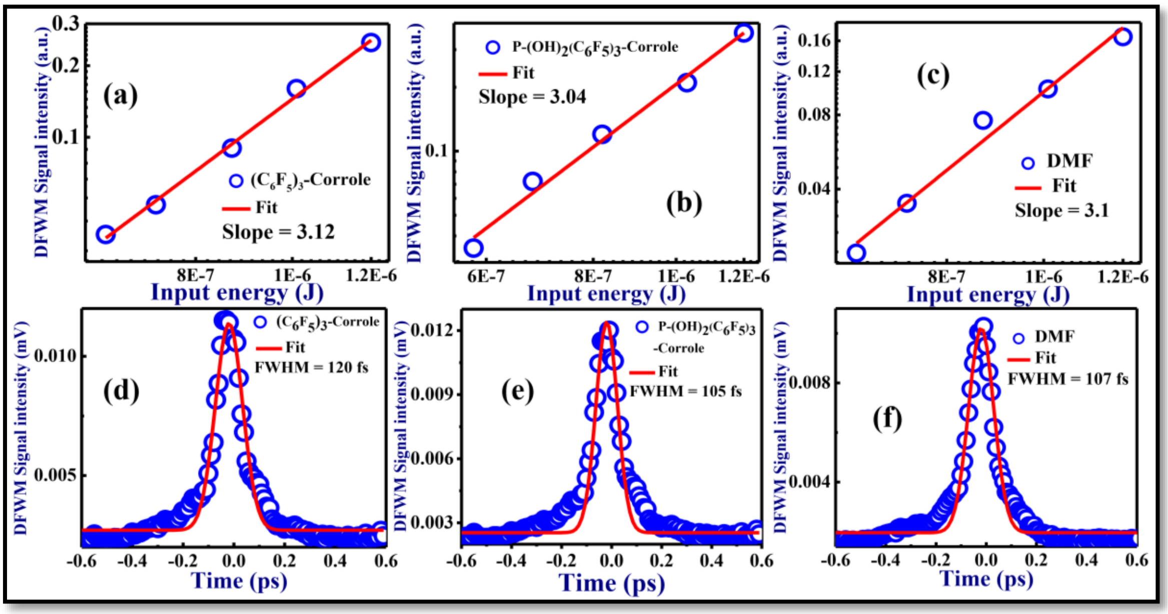

Figure 6.9 Cubic dependency of the DFWM signal on input energy and time-resolved DFWM signal profiles of (a, d) $(C_6F_5)_3$-Corrole, (b, e) P-$(OH)_2(C_6F_5)_3$-Corrole and (e, f) DMF solvent.The solid line is theoretical fits, and scattered points are experimental data.

The time-resolved DFWM signal was recorded as a function of probe delay, and the signal was found to be nearly symmetric about the zero delay. The TR-DFWM signal was fitted to a Gaussian function. The full-width half maxima (FWHM) of ~110 fs confirmed the instantaneous response, which suggests the pure electronic contribution (Kerr effect) to the nonlinearity as shown in the data of figures 6.9(d)-(f). The obtained $\chi^{(3)}$ values are similar or higher in magnitude than some of the reported works on metal-based organic moieties such as metallophthalocyanines and porphyrins.[55-56] The fast response and strong magnitude of $\chi^{(3)}$ suggest these molecules can find applications in all-optical switching and optical limiting.

6.4 Conclusions

Detailed photophysical investigations and the ultrafast NLO studies of two axially substituted phosphorus P-$(OH)_2(C_6F_5)_3$-Corrole and free-base $(C_6F_5)_3$-Corroles have been performed successfully. Femtosecond transient absorption spectroscopic measurements elucidated the evolution of various photophysical processes. With the specific target analysis of the TA spectra, we estimated rate constants for IC, VR, nonradiative, and triplet relaxation. From the analyzed TAS data, we noticed that phosphorus corrole displayed strong excited and triplet state properties compared to the free-base corrole. The third-order NLO properties of these novel corroles were explored using the Z-scan, DFWM techniques/experiments with fs, kHz pulses. The obtained NLO coefficients were found to be stronger in both the corroles compared to some of the recently reported corrole molecules. The TPA cross-sections were found to be considerably large (30-190 GM) compared to some of the recently published data obtained from organic moieties based on donor-acceptor systems. The closed aperture measurements confirmed a positive nonlinearity, suggesting self-focusing behavior with a magnitude of 2.3×10^{-15} cm^2/W (measured for 25 μM concentration solutions). The transient absorption measurements of donor-acceptor P-$(OH)_2(C_6F_5)_3$-Corrole confirmed a fast excited-state nonradiative relaxation or energy transfer, which can possibly assist in enhancing the nonlinear optical response in these molecules. DFWM measurements established reasonably large $\chi^{(3)}$ values in the range of $6.2\text{-}6.9\times10^{-14}$ esu (in solution). Time-resolved DFWM depicted an instantaneous response of $\chi^{(3)}$, which confirmed the presence of a pure electronic nonlinearity. We believe that these synthesized molecules have strong potential for various optoelectronics and photonics applications.

References

1. Castet, F.; Rodriguez, V.; Pozzo, J.-L.; Ducasse, L.; Plaquet, A.; Champagne, B., Design and Characterization of Molecular Nonlinear Optical Switches. *Accounts of Chemical Research* **2013**, *46*, 2656-2665.
2. Alemayehu, A. B.; Day, N. U.; Mani, T.; Rudine, A. B.; Thomas, K. E.; Gederaas, O. A.; Vinogradov, S. A.; Wamser, C. C.; Ghosh, A., Gold Tris(Carboxyphenyl)Corroles as Multifunctional Materials: Room Temperature near-Ir Phosphorescence and Applications to Photodynamic Therapy and Dye-Sensitized Solar Cells. *ACS Applied Materials & Interfaces* **2016**, *8*, 18935-18942.
3. Aviv, I.; Gross, Z., Corrole-Based Applications. *Chemical Communications* **2007**, 1987.
4. D'Souza, F.; Ito, O., Photosensitized Electron Transfer Processes of Nanocarbons Applicable to Solar Cells. *Chem. Soc. Rev.* **2012**, *41*, 86-96.
5. Mishra, R.; Basumatary, B.; Singhal, R.; Sharma, G. D.; Sankar, J., Corrole-Bodipy Dyad as Small-Molecule Donor for Bulk Heterojunction Solar Cells. *ACS Appl Mater Interfaces* **2018**, *10*, 31462-31471.
6. Lu, J.; Liu, S.; Wang, M., Push-Pull Zinc Porphyrins as Light-Harvesters for Efficient Dye-Sensitized Solar Cells. *Frontiers in Chemistry* **2018**, *6*.
7. Reddy, G.; Katakam, R.; Devulapally, K.; Jones, L. A.; Della Gaspera, E.; Upadhyaya, H. M.; Islavath, N.; Giribabu, L., Ambient Stable, Hydrophobic, Electrically Conductive Porphyrin Hole-Extracting Materials for Printable Perovskite Solar Cells. *Journal of Materials Chemistry C* **2019**, *7*, 4702-4708.
8. Raavi, S. S. K.; Biswas, C., Femtosecond Pump-Probe Spectroscopy for Organic Photovoltaic Devices. In *Digital Encyclopedia of Applied Physics*, Wiley-VCH Verlag GmbH & Co. KGaA: 2019; pp 1-49.
9. Mahammed, A.; Chen, K.; Vestfrid, J.; Zhao, J.; Gross, Z., Phosphorus Corrole Complexes: From Property Tuning to Applications in Photocatalysis and Triplet–Triplet Annihilation Upconversion. *Chemical Science* **2019**, *10*, 7091-7103.
10. Kc, C. B.; Lim, G. N.; Nesterov, V. N.; Karr, P. A.; D'Souza, F., Phenothiazine-Bodipy-Fullerene Triads as Photosynthetic Reaction Center Models: Substitution and Solvent Polarity Effects on Photoinduced Charge Separation and Recombination. *Chemistry* **2014**, *20*, 17100-12.

11. González-Rodríguez, D.; Bottari, G., Phthalocyanines, Subphthalocyanines and Porphyrins for Energy and Electron Transfer Applications. *Journal of Porphyrins and Phthalocyanines* **2009**, *13*, 624-636.
12. Gust, D.; Moore, T. A.; Moore, A. L., Mimicking Photosynthetic Solar Energy Transduction. *Accounts of Chemical Research* **2001**, *34*, 40-48.
13. Rao, S. V.; Srinivas, N. K. M. N.; Rao, D. N.; Giribabu, L.; Maiya, B. G.; Philip, R.; Kumar, G. R., Studies of Third-Order Optical Nonlinearity and Nonlinear Absorption in Tetra Tolyl Porphyrins Using Degenerate Four Wave Mixing and Z-Scan. *Optics Communications* **2000**, *182*, 255-264.
14. Jadhav, T.; Maragani, R.; Misra, R.; Sreeramulu, V.; Rao, D. N.; Mobin, S. M., Design and Synthesis of Donor–Acceptor Pyrazabole Derivatives for Multiphoton Absorption. *Dalton Transactions* **2013**, *42*, 4340.
15. Wojciechowski, A.; Raposo, M. M. M.; Castro, M. C. R.; Kuznik, W.; Fuks-Janczarek, I.; Pokladko-Kowar, M.; Bureš, F., Nonlinear Optoelectronic Materials Formed by Push–Pull (Bi)Thiophene Derivatives Functionalized with Di(Tri)Cyanovinyl Acceptor Groups. *Journal of Materials Science: Materials in Electronics* **2014**, *25*, 1745-1750.
16. Rebane, A.; Drobizhev, M.; Makarov, N. S.; Koszarna, B.; Tasior, M.; Gryko, D. T., Two-Photon Absorption Properties of Meso-Substituted A3-Corroles. *Chemical Physics Letters* **2008**, *462*, 246-250.
17. Garai, A.; Kumar, S.; Sinha, W.; Purohit, C. S.; Das, R.; Kar, S., A Comparative Study of Optical Nonlinearities of Trans-A2b-Corroles in Solution and in Aggregated State. *RSC Advances* **2015**, *5*, 28643-28651.
18. Hamad, S.; Tewari, S. P.; Giribabu, L.; Rao, S. V., Picosecond and Femtosecond Optical Nonlinearities of Novel Corroles. *Journal of Porphyrins and Phthalocyanines* **2012**, *16*, 140-148.
19. Wen, L.; Fang, Y.; Yang, J.; Han, Y.; Song, Y., Third-Order Nonlinear Optical Properties and Ultrafast Excited-State Dynamics of Benzothiazolium Salts: Transition in Absorption and Refraction under Different Time Regimes. *Dyes and Pigments* **2018**, *156*, 26-32.
20. Wen, L.; Fang, Y.; Yang, J.; Han, Y.; Song, Y., Comparison of Third-Order Nonlinear Optical Properties of Benzothiazolium Salt and Neutral Benzothiazole Derivative:

Broadband Absorption Response and Transient Dynamic Analysis. *Dyes and Pigments* **2019**, *168*, 28-35.

21. Xie, Q.; Shao, Z.; Zhao, Y.; Yang, L.; Wu, Q.; Xu, W.; Li, K.; Song, Y.; Hou, H., Novel Photo-Controllable Third-Order Nonlinear Optical (Nlo) Switches Based on Azobenzene Derivatives. *Dyes and Pigments* **2019**, 107599.
22. Xu, W.; Wang, W.; Li, J.; Wu, Q.; Zhao, Y.; Hou, H.; Song, Y., Two-Photon Absorption Property and Excellent Optical Limiting Response of Three Schiff Base Derivatives with Large Conjugated System. *Dyes and Pigments* **2019**, *160*, 1-8.
23. Zhai, G.; Wu, X.; Jin, P.; Song, T.; Xiao, J.; Song, Y., Synthesis, Optoelectronic Properties and Third-Order Nonlinear Optical Behaviors of the Functionalized Acene Derivatives. *Dyes and Pigments* **2018**, *155*, 93-99.
24. Yang, Y.; Wu, X.; Jia, J.; Shen, L.; Zhou, W.; Yang, J.; Song, Y., Investigation of Ultrafast Optical Nonlinearities in Novel Bis-Chalcone Derivatives. *Optics & Laser Technology* **2020**, *123*, 105903.
25. Giribabu, L.; Kandhadi, J.; Kanaparthi, R. K., Phosphorus(V)Corrole- Porphyrin Based Hetero Trimers: Synthesis, Spectroscopy and Photochemistry. *Journal of Fluorescence* **2013**, *24*, 569-577.
26. Kandhadi, J.; Yeduru, V.; Bangal, P. R.; Giribabu, L., Corrole-Ferrocene and Corrole-Anthraquinone Dyads: Synthesis, Spectroscopy and Photochemistry. *Phys Chem Chem Phys* **2015**, *17*, 26607-20.
27. Ngo, T. H., et al., Engaging Copper(Iii) Corrole as an Electron Acceptor: Photoinduced Charge Separation in Zinc Porphyrin-Copper Corrole Donor-Acceptor Conjugates. *Chemistry* **2016**, *22*, 1301-12.
28. Tasior, M.; Gryko, D. T.; Shen, J.; Kadish, K. M.; Becherer, T.; Langhals, H.; Ventura, B.; Flamigni, L., Energy- and Electron-Transfer Processes in Corrole−Perylenebisimide−Triphenylamine Array. *The Journal of Physical Chemistry C* **2008**, *112*, 19699-19709.
29. Ding, T.; Alemán, E. A.; Modarelli, D. A.; Ziegler, C. J., Photophysical Properties of a Series of Free-Base Corroles. *The Journal of Physical Chemistry A* **2005**, *109*, 7411-7417.
30. D'Souza, F.; Chitta, R.; Ohkubo, K.; Tasior, M.; Subbaiyan, N. K.; Zandler, M. E.; Rogacki, M. K.; Gryko, D. T.; Fukuzumi, S., Corrole−Fullerene Dyads: Formation of

Long-Lived Charge-Separated States in Nonpolar Solvents. *Journal of the American Chemical Society* **2008**, *130*, 14263-14272.

31. Teo, R. D.; Hwang, J. Y.; Termini, J.; Gross, Z.; Gray, H. B., Fighting Cancer with Corroles. *Chemical Reviews* **2016**, *117*, 2711-2729.
32. Aviv-Harel, I.; Gross, Z., Aura of Corroles. *Chemistry - A European Journal* **2009**, *15*, 8382-8394.
33. Buckley, H. L.; Chomitz, W. A.; Koszarna, B.; Tasior, M.; Gryko, D. T.; Brothers, P. J.; Arnold, J., Synthesis of Lithium Corrole and Its Use as a Reagent for the Preparation of Cyclopentadienyl Zirconium and Titanium Corrole Complexes. *Chemical Communications* **2012**, *48*, 10766.
34. Agadjanian, H.; Ma, J.; Rentsendorj, A.; Valluripalli, V.; Hwang, J. Y.; Mahammed, A.; Farkas, D. L.; Gray, H. B.; Gross, Z.; Medina-Kauwe, L. K., Tumor Detection and Elimination by a Targeted Gallium Corrole. *Proceedings of the National Academy of Sciences* **2009**, *106*, 6105-6110.
35. Capuano, R.; Pomarico, G.; Paolesse, R.; Di Natale, C., Corroles-Porphyrins: A Teamwork for Gas Sensor Arrays. *Sensors (Basel)* **2015**, *15*, 8121-30.
36. Borisov, S. M.; Alemayehu, A.; Ghosh, A., Osmium-Nitrido Corroles as Nir Indicators for Oxygen Sensors and Triplet Sensitizers for Organic Upconversion and Singlet Oxygen Generation. *Journal of Materials Chemistry C* **2016**, *4*, 5822-5828.
37. Barber, J.; Tran, P. D., From Natural to Artificial Photosynthesis. *Journal of The Royal Society Interface* **2013**, *10*, 20120984.
38. Balaban, T. S., Tailoring Porphyrins and Chlorins for Self-Assembly in Biomimetic Artificial Antenna Systems. *Accounts of Chemical Research* **2005**, *38*, 612-623.
39. Nardis, S.; Mandoj, F.; Stefanelli, M.; Paolesse, R., Metal Complexes of Corrole. *Coordination Chemistry Reviews* **2019**, *388*, 360-405.
40. Mahammed, A.; Gross, Z., Corroles as Triplet Photosensitizers. *Coordination Chemistry Reviews* **2019**, *379*, 121-132.
41. Stensitzki, T.; Yang, Y.; Berg, A.; Mahammed, A.; Gross, Z.; Heyne, K., Ultrafast Electronic and Vibrational Dynamics in Brominated Aluminum Corroles: Energy Relaxation and Triplet Formation. *Structural Dynamics* **2016**, *3*, 043210.
42. Pomarico, E.; Pospisil, P.; Bouduban, M. E.; Vestfrid, J.; Gross, Z.; Záliš, S.; Chergui, M.; Vlček, A. N., Photophysical Heavy-Atom Effect in Iodinated Metallocorroles:

Spin–Orbit Coupling and Density of States. *The Journal of Physical Chemistry A* **2018**, *122*, 7256-7266.

43. Yang, Y.; Jones, D.; von Haimberger, T.; Linke, M.; Wagnert, L.; Berg, A.; Levanon, H.; Zacarias, A.; Mahammed, A.; Gross, Z., Assignment of Aluminum Corroles Absorption Bands to Electronic Transitions by Femtosecond Polarization Resolved Vis-Pump Ir-Probe Spectroscopy. *The Journal of Physical Chemistry A* **2012**, *116*, 1023-1029.
44. Liu, X.; Mahammed, A.; Tripathy, U.; Gross, Z.; Steer, R. P., Photophysics of Soret-Excited Tetrapyrroles in Solution. Iii. Porphyrin Analogues: Aluminum and Gallium Corroles. *Chemical Physics Letters* **2008**, *459*, 113-118.
45. Raavi, S. S.; Yin, J.; Grancini, G.; Soci, C.; Rao, S. V.; Lanzani, G.; Giribabu, L., Femtosecond to Microsecond Dynamics of Soret-Band Excited Corroles. *J Phys Chem C Nanomater Interfaces* **2015**, *119*, 28691-28700.
46. Yadav, P.; Anand, T.; Moram, S. S. B.; Bhattacharya, S.; Sankar, M.; Rao, S. V., Synthesis and Femtosecond Third Order Nonlinear Optical Properties of Push-Pull Trans- a 2 B-Corroles. *Dyes and Pigments* **2017**, *143*, 324-330.
47. Liang, X.; Mack, J.; Zheng, L. M.; Shen, Z.; Kobayashi, N., Phosphorus(V)-Corrole: Synthesis, Spectroscopic Properties, Theoretical Calculations, and Potential Utility for in Vivo Applications in Living Cells. *Inorg Chem* **2014**, *53*, 2797-802.
48. Ghosh, A.; Ravikanth, M., Synthesis, Structure, Spectroscopic, and Electrochemical Properties of Highly Fluorescent Phosphorus (V)–Meso-Triarylcorroles. *Chemistry–A European Journal* **2012**, *18*, 6386-6396.
49. Achary, B. S.; Ramya, A. R.; Nanubolu, J. B.; Seetharaman, S.; Lim, G. N.; Jang, Y.; D'Souza, F.; Giribabu, L., Axially Substituted Phosphorous(V) Corrole with Polycyclic Aromatic Hydrocarbons: Syntheses, X-Ray Structures, and Photoinduced Energy and Electron Transfer Studies. *New Journal of Chemistry* **2018**, *42*, 8230-8240.
50. Fujino, K.; Hirata, Y.; Kawabe, Y.; Morimoto, T.; Srinivasan, A.; Toganoh, M.; Miseki, Y.; Kudo, A.; Furuta, H., Confusion and Neo-Confusion: Corrole Isomers with an Nnnc Core. *Angewandte Chemie International Edition* **2011**, *50*, 6855-6859.
51. Anusha, P. T.; Swain, D.; Hamad, S.; Giribabu, L.; Prashant, T. S.; Tewari, S. P.; Rao, S. V., Ultrafast Excited-State Dynamics and Dispersion Studies of Third-Order

Optical Nonlinearities in Novel Corroles. *The Journal of Physical Chemistry C* **2012**, *116*, 17828-17837.

52. Swain, D.; Singh, V. K.; Krishna, N. V.; Giribabu, L.; Rao, S. V., Optical, Electrochemical, Third-Order Nonlinear Optical, and Excited State Dynamics Studies of Thio-Zinc Phthalocyanine. *Journal of Porphyrins and Phthalocyanines* **2014**, *18*, 305-315.
53. Humphrey, J. L.; Kuciauskas, D., Charge Transfer Enhances Two-Photon Absorption in Transition Metal Porphyrins. *Journal of the American Chemical Society* **2006**, *128*, 3902-3903.
54. Krishnakanth, K. N.; Seth, S.; Samanta, A.; Venugopal Rao, S., Broadband Ultrafast Nonlinear Optical Studies Revealing Exciting Multi-Photon Absorption Coefficients in Phase Pure Zero-Dimensional Cs4pbbr6 Perovskite Films. *Nanoscale* **2019**, *11*, 945-954.
55. Kumar, R. S. S.; Rao, S. V.; Giribabu, L.; Rao, D. N., Ultrafast Nonlinear Optical Properties of Alkyl Phthalocyanines Investigated Using Degenerate Four-Wave Mixing Technique. *Optical Materials* **2009**, *31*, 1042-1047.
56. Rao, S. V.; Naga Srinivas, N. K. M.; Rao, D. N.; Giribabu, L.; Maiya, B. G.; Philip, R.; Kumar, G. R., Excited State Dynamics in Tetra Tolyl Porphyrins Studied Using Degenerate Four Wave Mixing with Incoherent Light and Ps Pulses. *Optics Communications* **2001**, *192*, 123-133.

Intentional blank page

Chapter 7 Femtosecond Transient Absorption and Coherent Anti-Stokes Raman Spectroscopic Studies of Nitro/Nitrogen Rich Aryl-Tetrazole Derivatives

Abstract

Femtosecond Coherent anti-Stokes Raman Spectroscopy (CARS) and transient absorption (TA) experiments were performed on amino and nitro substituted tetrazole derivatives to comprehend the intramolecular vibrational redistribution (IVR) dynamics (via vibrational couplings) and the complete excited state dynamics. The present study is advantageous in enhancing the applications of energetic materials since the nitro substituted tetrazole derivative demonstrated energetic properties those comparable with the secondary explosives such as RDX and TNT. Fourier transforms of the recorded CARS transients revealed the possible IVR mechanisms in tetrazole-N-(hetero)aryl derivatives. Further, the coherent vibrational decay times estimated from the CARS transients were in the range of 120 fs to 200 fs. From the kinetic analysis of the femtosecond transient absorption data a possible relaxation mechanism from excited electronic states to ground state is discussed. The nitro substituted tetrazole derivative, due to its high contents of nitrogen, has demonstrated a faster relaxation from upper excited states compared to amino substituted tetrazole derivative and its significance is discussed.

This chapter contains data from the following work submitted for publication

1. Ultrafast Coherent Anti-Stokes Raman Spectroscopic Studies of Nitro/Nitrogen Rich Aryl-Tetrazole Derivatives., **Naga Krishnakanth Katturi**, Sarang Dev G, Nagarjuna Kommu, Gopala Krishna Podagatlapalli, Venugopal Rao Soma, (**Chemical Physics Letters**, Under Revision, 2020).

7.1 Introduction

The invention of ultrafast lasers brought novel possibilities of probing and understanding the ultrafast phenomena such as electronic and vibrational dynamics in both excited/ground state of a variety of molecules.[1-5] Energetic materials (EMs) store enormous energy in the chemical form that can be easily converted to kinetic energy by molecular decomposition and thus retrieved chemical energy can be used in industrial and military applications.[5] Excited-state dynamics of the energetic materials provide an insight into the molecular decomposition mechanisms for different ignition processes, such as heat, shock and compression waves etc..[6-8] It was reported that compression of the material at a pressure of 30 GPa or above could induce an electronic excitation nearly equal to the lowest singlet excited states of EMs (2-2.5 ev).[8-9] The detailed investigation of electronic, chemical and structural changes of the excited states of EMs enables us to comprehend the behaviour of EMs at the molecular level. The velocity of the detonation wave in an explosive is about 10 km/s. This means at molecular dimensions, the time it takes to go over is about 100 fs. To equip the energy needed for a sustained detonation wave, some molecular processes must be efficient to release energy within the molecular transit time. Therefore, excitation of EMs by UV laser pulses provides an effective means of studying the excited state decomposition of these materials. Consequently, great research was performed to understand the reaction mechanisms to advance the inherent properties of EMs along with the enhanced safety measures.[10-16] The non-radiative transitions of the excited states of the molecules produce local heating that causes to form hotspots which initiate the chain reactions in EMs.[17] Further, it was stated that infrared (IR) photons play a prominent role in the generation of such hotspots.[18] In the microscopic view, the heat or shock front can be viewed as the superposition of molecular vibrations of chemical bonds and as the series of phonons. Under the influence of shock waves, the EMs experience a series of energy transfer processes before the disruption of their bonds. When an EM is influenced by a shock wave, initially, a number of phonons will be generated and later, the low-frequency vibrational modes will be excited through phonon-vibron coupling known as multi-phonon up-pumping.[19-20]

The vibrational energy transfer takes place from one vibrational mode to another mode which is called as intramolecular vibrational redistribution (IVR). During the IVR, distributed energies localized in one or a few chemical bonds results in the dissociation and it initiates the ignition[11]. Therefore, IVR can directly affect the vibrational energy transfer and breaking of chemical bonds in EMs. However, the visualization of ultrafast coherent phenomenon such as IVR is tedious since it involves the coupling of several vibrational modes.[21] In this context, excitation and relaxations of vibrational modes in EMs are usually performed with UV or IR excitation and these processes happens in fs domain. The EMs can be excited to higher states with UV illumination and this leads to decomposition.[22-23] Documented outcomes reveal that the ground electronic, vibrational states of EMs have been recognized to be prominent in the energy transferring processes.

Nitro-substituted arene compounds are very important in the field of defence and civilian applications due to their extended energetic properties.[24] However, the well-known polynitro arenes such as TNT, TATB, Picric acid etc. exhibit moderate performance.[25] Recently, it was reported that the derivatives of azole substituted polynitro-arenes enhance densities and performance.[26] Especially, the substitution of azoles such as triazole or tetrazole improves the positive heat of formation due to the presence of higher amounts of nitrogen.[27-30] In this context, Kommu et al. reported that the tetrazole substituted polynitro-arene derivatives exhibit superior energetic properties than TNT.[31] In this regard, Coherent anti-Stokes Raman spectroscopy (CARS) is an efficient technique to probe the ground state vibrational dynamics of the molecules with higher temporal and spectral resolutions in both gas and liquid phases.[32-39] CARS is a nonlinear spectroscopic technique that eliminates the low scattering cross-section of the natural Raman process. Spontaneous Raman is an incoherent process wherein the photons scatter in all the directions. In contrast, CARS is a coherent technique in which all the Raman scattered photons emerge out in one direction similar to a laser. Coherent Raman spectroscopy is a versatile technique for imaging and characterizing the materials even with strong fluorescence background. Employment of ultrafast lasers enables the novel possibilities of time and frequency-resolved spectroscopies to probe the vibrational dynamics that occur in the time scales shorter than molecular vibration period ~100 fs. In a femtosecond time-resolved CARS (TR-CARS) experiment, several vibrational modes of the molecules can be excited simultaneously, and the relaxation processes can be probed in real-time. TR-CARS also enables us to estimate the dephasing times and collisional relaxation times of the interested vibrational modes in solutions.

Additionally, TR-CARS facilitate to investigate the excited state dynamics of vibrational modes. However, the excitation of molecular vibrational modes with fs broadband pulses in CARS experiment limits the spectral resolution and this can be eliminated by employing pulse shaping techniques [40-42] to trigger selective absorptions. The analysis of TR-CARS spectra provokes the insight on intermolecular interactions as well as the molecular structure. To understand the molecular dynamics of the complex and nitrogen-rich EMs (tetrazole-N-(hetero) aryl derivatives namely 2,6-dinitro-4-(1H-tetrazole-1-yl)aniline ($C_7H_5N_7O_4$) and 1-(3,4,5-trinitrophenyl)-1H-tetrazole($C_7H_3N_7O_6$) femtosecond TR-CARS has been employed. To avoid the ambiguity in the description of the recorded TR CARS data, of two nitro substituted molecules, 2,6-dinitro-4-(1H-tetrazole-1-yl)aniline ($C_7H_5N_7O_4$) and 1-(3,4,5-trinitrophenyl)-1H-tetrazole($C_7H_3N_7O_6$) are labelled as 6 and 8, respectively. Furthermore, to understand the complete process of excited state decomposition of EMs, the topography of excited-state potential surfaces is also an important parameter.[8] The conical intersections due to the crossing of excited potential surfaces play an essential role in the exited electronic state process of EMs. Moreover, the nonradiative relaxation processes of excited states can lead to the formation of hotspots which can initiate the chain reaction of EMs.[9] The excited state decomposition happens in a sub-picosecond time scale, which can be probed by using an ultrafast pump-probe technique.[11-15, 19] The dynamical and spectral properties of high energy materials are rarely studied due to their absorption which lies in the UV region for most of the explosives. Direct optical excitation can initiate the excited state decomposition in high energy materials, thus understanding this process may have implications of developing novel EMs for optical initiation.[16] From the quantum chemical theory and data from time-resolved spectroscopies suggest the potential energy surfaces of electronic excited and ground states have a crucial role in photochemical pathways in EMs and can give insight into the probing of conical intersection and transition sates.[17-18] The initial decomposition product after UV excitation from nitrated explosives is found to be NO molecule due to the ultrafast internal conversion from the excited electronic state to ground state in the presence of conical intersection is reported.[8, 15] In continuation of efforts in understanding the excited state dynamics of EMs, we have performed femtosecond (fs) transient absorption studies on 6 and 8.[20] The structure of tetrazole derivatives conserves more energy than other azole derivatives and exhibits a high positive heat of formation and excellent detonation performance.

7.2 Experiments

The synthesis procedures of amino (6) and nitro (8) substituted tetrazole derivatives were reported elsewhere.[31] The compounds 6 and 8 were dissolved in acetonitrile to prepare ~1 mM solution which are used for all the measurements. The UV-Visible absorption spectra were collected using a Shimadzu model 1700 spectrophotometer and fluorescence spectra is collected using a Fluorolog-3 spectrofluorometer (HORIBA) at 400 nm wavelength excitation. The experimental details of Coherent Anti-stokes Raman and transient absorption spectroscopic techniques are discussed and presented in detail in chapter 2.

7.3 Results and Discussion

7.3.1 Raman studies

The spontaneous Raman spectra (Horiba LabRAM HR –Evolution, at 785 nm exciting line) of samples 6 and 8 are shown in figure 7.1 and the corresponding Raman modes with their labels are provided in table 7.1. The theoretical calculations were performed with Gaussian software using functional B3LYP6-331G(DP) for the peak assignments. It is found that the experimental and calculated results agreed well.

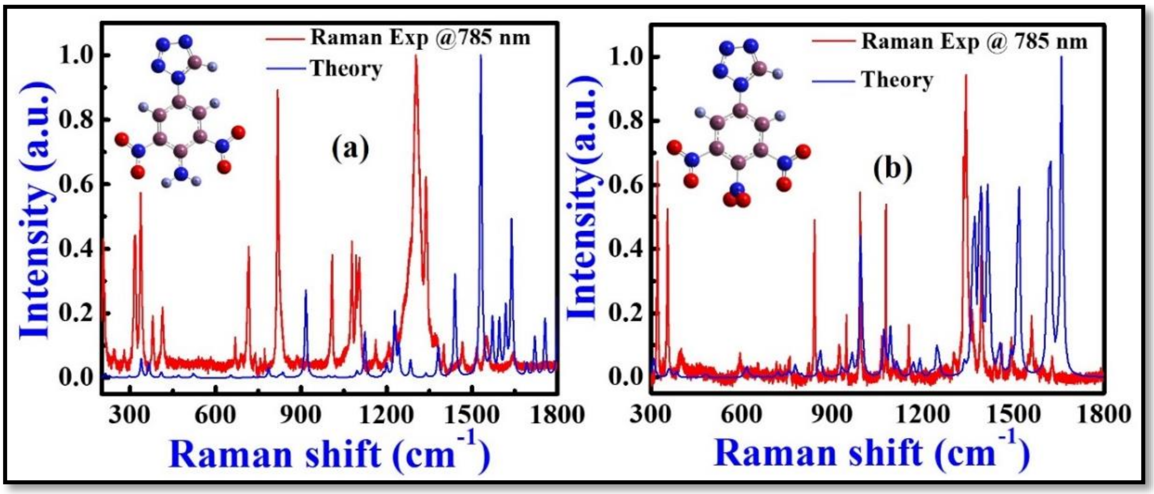

Figure 7.1 Experimental and theoretical Spontaneous Raman spectra of compounds (a) 6 and (b) 8.

Table 7.1 Experimental and theoretical Raman modes and their labels for compound 6 and 8.

Experiment compound 6	**Theory**	**Labelling**	**Experiment compound 8**	**Theory**	**Labelling**
(υ_1) 720	711	H-N-H twisting	**(υ_1) 821**	796	C-H rocking, C=C=C wagging
(υ_2) 773	786	Ring elongation (Benzene)	**(υ_2) 841**	854	C-H wagging
(υ_3) 818	822	Ring deformation, NO_2 scissoring, N=N-N wagging	**(υ_3) 920**	914	C-H wagging
(υ_4) 920	916	Ring elongation, NO_2 scissoring, C=N stretching	**(υ_4) 946**	941	C-H wagging
(υ_5) 1006	1007	C-H wagging (tetrazole ring)	**(υ_5) 992**	994	N=N-N stretching (Tetrazole ring)
(υ_6) 1076	1071	C-H wagging (Benzene ring)	**(υ_6) 1077**	1073	C=H stretching, C-N stretching, N=N-N stretching, C-H rocking
(υ_7) 1109	1104	C-H wagging (Benzene ring)	**(υ_7) 1154**	1166	C-H rocking, ring elongation (Benzene ring)
(υ_8) 1207	1201	C-H rocking (Tetrazole and Benzene rings)	**(υ_8) 1302**	1338	N=N stretching, C=C=C asymmetric stretch
(υ_9) 1231	1228	C-N stretching, C-H rocking (Tetrazole and Benzene rings)	**(υ_9) 1335**	1338	N=N stretching, C=C=C asymmetric stretch
(υ_{10}) 1337	1338	N-N stretching, C-H wagging	**(υ_{10}) 1363**	1363	N=N stretching, C=C=C asymmetric stretch
(υ_{11}) 1374	1381	N-N stretching, C-H wagging	**(υ_{11}) 1460**	1453	C-H rocking, C=C stretching, C=N stretching
(υ_{12}) 1401	1389	H-N-H rocking, N=O stretching, C-H wagging	**(υ_{12}) 1493**	1492	C=N stretching, C=C stretching
(υ_3) 1466	1440	C=N stretching, ring stretching (Benzene), C-H rocking	**(υ_{13}) 1630**	1632	NO_2 asymmetric stretching, C=C=C asymmetric stretching (Benzene ring deformation)

(υ_4) 1517	1531	H-N-H scissoring, C=N stretching, C=C=C symmetric stretching, N=N stretching	**(υ_{14}) 1574**	1612	O=N=O asymmetric stretching, C=C=C asymmetric stretching
(υ_{15}) 1551	1558	C=C asymmetric stretching, NH_2 wagging, C-H wagging, N=O stretching	**(υ_{15}) 1628**	1632	O=N=O asymmetric stretching, C=C=C asymmetric stretching

7.3.2 Time-Resolved CARS

Figures 7.2(a), (b) illustrate the time and frequency-resolved CARS spectra of sample 6 and 8 respectively. The data is illustrated in a contour map at each probe delay, varying from -300 fs to 800 fs with a frequency range of 750-1850 cm^{-1}. The 2D contour plots showcase the complex nature of CARS signal with spectral features in the frequency domain and oscillation features in the time domain. These are confirmed by the vibrational modes in the frequency domain and Fourier transform of the transient CARS traces compound 6 and compound 8. The frequency-resolved CARS spectra at 200 fs, as illustrated in figures 7.2(c) and (d), are evidently free from the non-resonant background as around the zero delay. The loss of spectral resolution due to femtosecond pulse probing is evident from figures 7.2(c) and (d) since several vibrational modes are simultaneously excited and overlapped with each other. Figures 7.2(e) and (f) depict the CARS signal along with the pump and Stokes spectra, which confirm the blue-shifted CARS signal. Figures 7.3 and 7.4 illustrate the time-resolved CARS (TR-CARS) signals for sample 6 investigated at 818 cm^{-1}, 1337 cm^{-1}, 1466 cm^{-1} and sample 8 investigated at 843 cm^{-1}, 1393 cm^{-1}, 1461 cm^{-1}, respectively. The TR-CARS signals have different features such as the non-resonant electronic background around zero delay, exponential decay arising from the population relaxation, and the oscillation which corresponds to the vibrational coupling. The TR-CARS trace has been fitted with a single exponential function that yields the coherent vibrational decay time ~120-200 fs. Negative exponential fitting was carried out (Figures 7.3 and figure 7.4) and error bars were kept in the traces to represent 5% error in the data points which can be attributed to the pulse to pulse energy fluctuations caused by the laser amplifier of rep rate 1 kHz. The Fourier transform of the resonant TR-CARS trace reveals the vibrational couplings between different vibrational modes with beat frequencies listed in table 7.2.

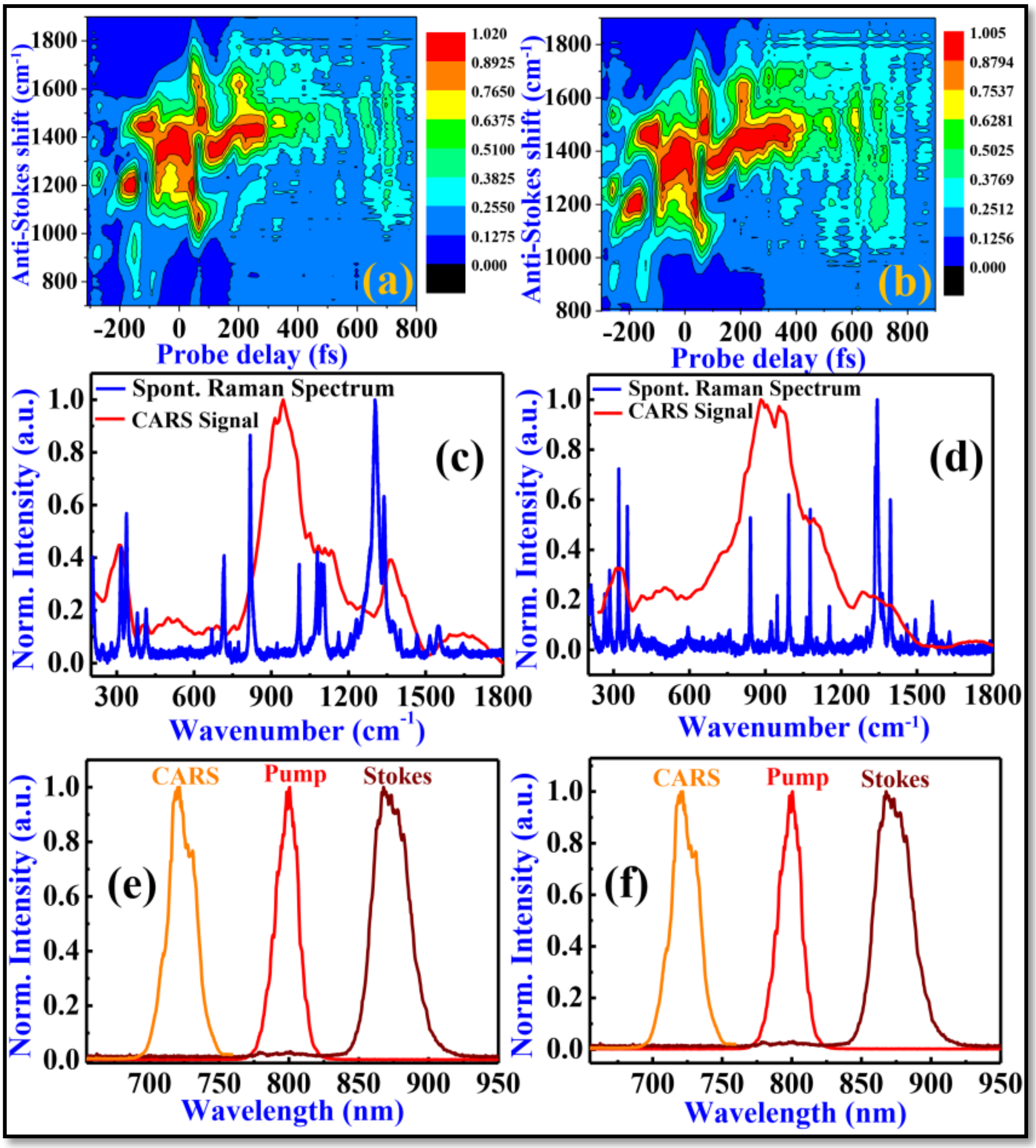

Figure 7.2 Time-resolved CARS signal of compound (a) 6 and (b) 8showing beat structure. Spontaneous Raman (blue) and CARS signal (red) of (c) 6 and (d) 8 (e,f) CARS signal, pump, and Stokes beams for compound 6 and 8 respectively.

Due to the intramolecular vibrational mode interferences, quantum beats can be observed. Quantum beats can be obtained due to the coherent evolution of the quantum wavefunctions of the single molecule. Unlike vibrational polarization beats which are due to intermolecular vibrational mode interferences, quantum beats are the consequence of intra molecular vibrational mode interferences. The occurrence of vibrational polarization beats or quantum beats certainly depends on the fact that how the molecular medium is probed. If the probe pulses energy density is above the dissociation threshold energy of the molecule under consideration, then vibrational polarization beats can be seen with shorter life times.

With probe pulse energies below the threshold, CARS polarization is long-lived and, consequently, the contribution from different vibrational states will be cancelled out, due to which vibrational polarization beats may not be seen in the spectrum. Though we believe the observed oscillations are quantum beats, in principle one cannot ignore the occurrence of vibrational polarization beats those fall under the coherent excitation of the other molecule outside the targeted molecule". Additionally, we cannot deny the possibility of the oscillations those arises due to the interference of molecular vibrational modes with the solvent modes of vibration.[43]

In the present study, pump and stokes wavelengths utilized were ~800 nm, ~872 nm, respectively. The corresponding wavenumber difference is 1033 cm^{-1}. When tetrazole-N-(hetero)aryl derivatives dissolved in acetonitrile (ACN) are simultaneously excited by two pulses, the selective vibrational modes in the proximity of 1033 cm^{-1} are expected to be excited (parent modes). But it is evident from the data presented in figures 7.3(c) and figure 7.3(b) the other modes [daughter modes] far away from the direct excitation region (1033 cm^{-1}) were observed. This is possible only when there is an intramolecular vibrational coupling and hence the possibility of the intramolecular vibrational energy re-distribution among parent and daughter modes. The relaxation pathways are investigated by the probe pulse and the obtained quantum beats. The coherent excitation of the targeted mode relaxes through the IVR process because of the coupling of the neighbouring vibrational modes of a molecule. Based on the above-mentioned arguments, we could approve the occurrence of IVR in the present time resolved CARS studies of tetrazoles (samples 6 and 8). The intramolecular vibrational relaxation (IVR) and their pathways of relaxations can be understood from the vibrational couplings since they arise from the coupling of vibrational modes of tetrazole derivatives. From table 7.2, the vibrational couplings between several modes participating in the IVR process can be visualized as coupling of one mode with two or more vibrational modes. For instance, in sample 6 the modes υ_7, υ_8, and υ_{14}, and sample 8, υ_1, υ_3, υ_4, υ_7, and υ_{12} modes which are corresponding to the benzene ring and the tetrazole ring of the molecules. These vibrational modes might participate (energy transfer process in IVR). [44-45] The vibrational modes which are interacting with only one vibrational mode such as υ_1-υ_6, υ_9-υ_{13}, υ_{15}, υ_{16} in 6 and υ_2, υ_5, υ_6, υ_8-υ_{11},υ_{13}-υ_{15} in 8 are corresponding to the C-H, C-N, C=C and NO_2 stretching vibrational modes of tetrazole and benzene rings, these modes might be involve in the initial decomposition process. These vibrational modes might participate in the initial molecular decomposition of tetrazole derivatives. The vibrational modes which are very active in interacting with other vibrational modes have a significant tendency to transfer energy through IVR. Yu et al.[46] reported on the IVR in RDX molecules using multiplex CARS technique. According to them, the low-frequency vibrational modes such as phonon modes are the doorways of energy transfer from outside to the inside of RDX molecule.

Beat frequency (cm^{-1}) of 6	Contributing modes (cm^{-1})	Beat frequency (cm^{-1}) of 8	Contributing modes (cm^{-1})
26	(υ_1) 715 and 740 (υ_2)	20	(υ_1) 821 and 840 (υ_2)
46	(υ_3) 773 and 820 (υ_4)	52	(υ_1) 821 and 870 (υ_3)
60	(υ_5) 758 and 820 (υ_4)	48	(υ_1) 821 and 870 (υ_3)
20	(υ_6) 1079 and 1103 (υ_7)	125	(υ_3) 870 and 992 (υ_4)
52	(υ_7)1103 and 1161(υ_8)	95	(υ_7) 1302 and 1394 (υ_{11})
99	(υ_7) 1103 and 1208 (υ_9)	146	(υ_9) 1342 and 1493 (υ_{12})
33	(υ_{10}) 1303 and 1338 (υ_{11})	182	(υ_6) 1153 and 1335 (υ_8)
46	(υ_8) 1161 and 1208 (υ_9)	233	(υ_8) 1335 and 1574 (υ_{14})
93	(υ_{12}) 1374 and 1466 (υ_{14})	363	(υ_4) 992 and 1363 (υ_{10})
26	(υ_{12}) 1374 and 1401 (υ_{13})	85	(υ_{13}) 1549 and 1628 (υ_{15})
58	(υ_{14}) 1466 and 1517 (υ_{15})	194	(υ_7) 1302 and 1493 (υ_{12})
87	(υ_{14}) 1466 and 1551 (υ_{16})	306	(υ_4) 992 and 1302 (υ_7)
139	(υ_8) 1161 and 1303 (υ_{10})	370	(υ_4) 992 and 1363 (υ_{10})
--	--	423	(υ_5) 1063 and 1493 (υ_{12})

Table 7.2 Possible vibrational coupling between the different vibrational modes of tetrazole derivatives.

Further, the vibrational modes which are mostly involved in IVR are found to carry the vibrational energy to the higher frequency states in IVR. In the multi-phonon up-pumping the low frequency vibrational modes which match to the frequency of phonon are the energy portals from outside to inside of the molecules.

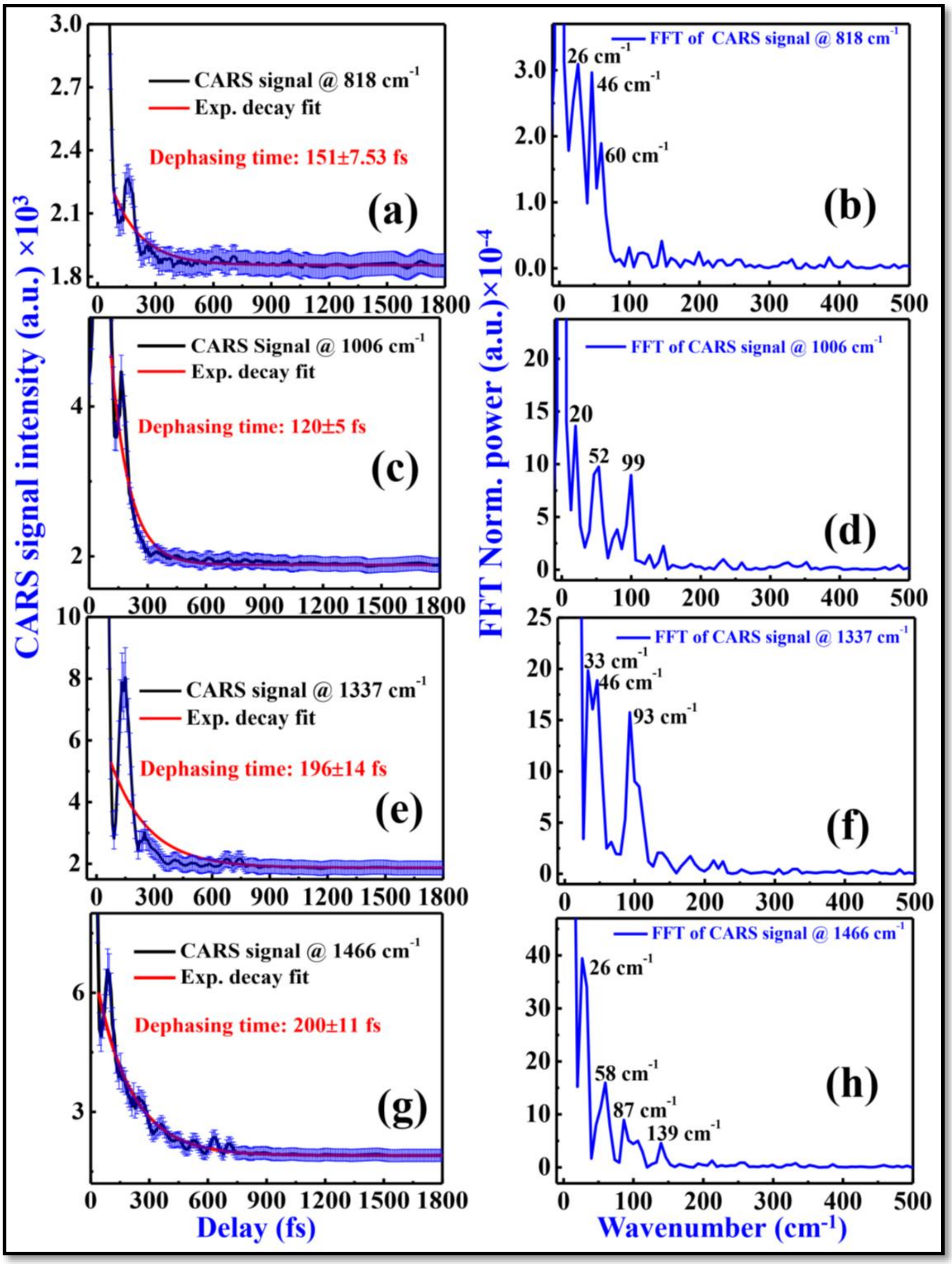

Figure 7.3 (a, c, e, g) TR-CARS signal and their corresponding fast Fourier transforms (b, d, f, h) for the 818 cm^{-1}, 1006 cm^{-1}, 1337 cm^{-1} and 1466 cm^{-1} modes, respectively obtained for sample 6. An exponential decay fitting was employed and error bars represent 5% error in the data which can be attributed to the pulse to pulse energy fluctuations caused by the laser amplifier (1 kHz repetition rate).

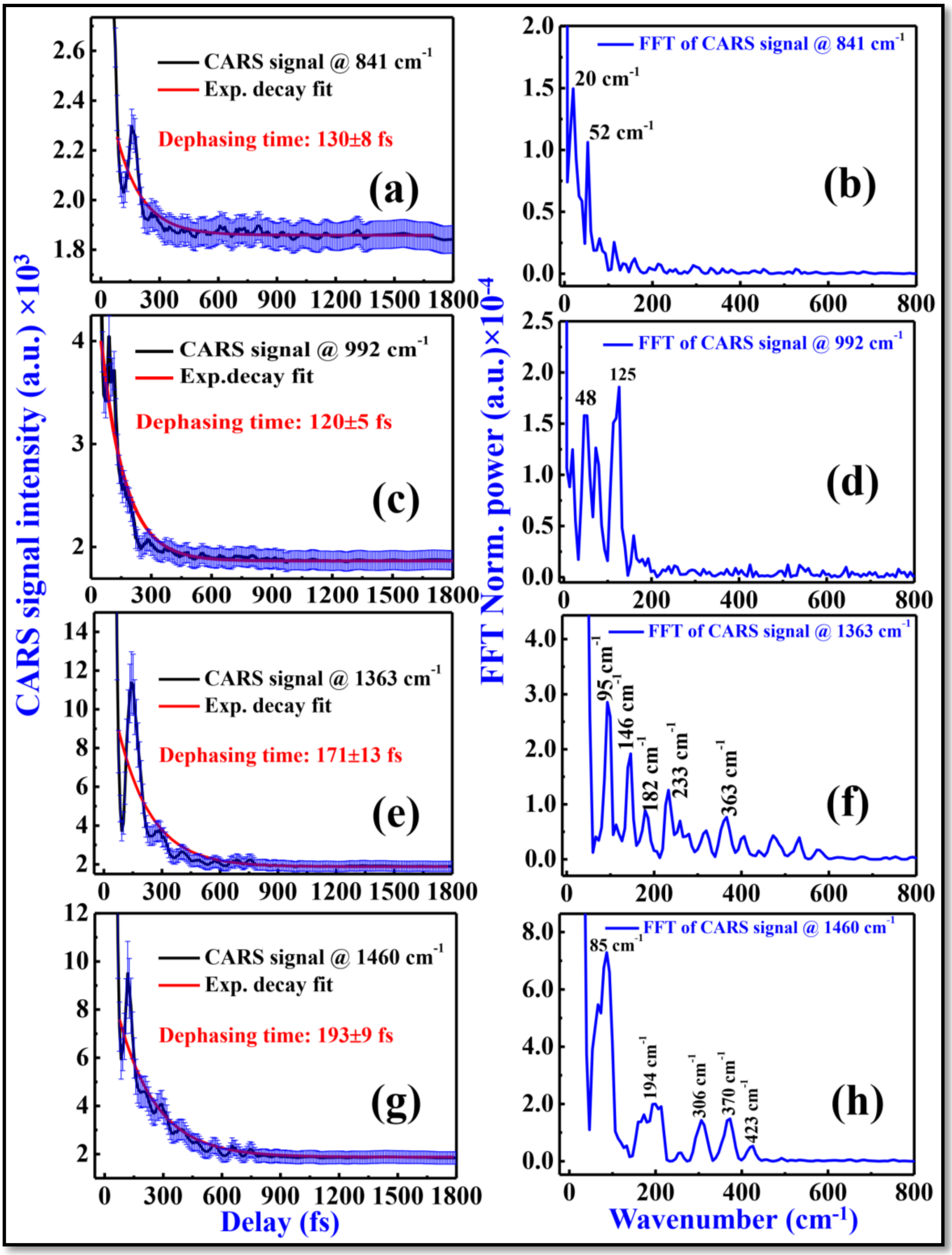

Figure 7.4 (a, c, e, g) TR-CARS signal and their corresponding fast Fourier transforms (b, d, f, h) at 841 cm^{-1}, 992 cm^{-1}, 1363 cm^{-1} and 1460 cm^{-1} modes, respectively, obtained for sample 8. An exponential decay fitting was employed and error bars represent 5% error in the data which can be attributed to the pulse to pulse energy fluctuations caused by the laser amplifier (1 kHz repetition rate).

Comparison of the exponential decay trends of TR-CARS traces demonstrates that the sample 8 exhibit a faster decay than sample 6. The reason behind this could be the presence of an extra NO_2 group in sample 8, attempting a faster IVR. From figures 7.3 and 7.4 it is evident that the low energy modes those corresponding to the C-H vibrations exhibiting faster dephasing times compared to higher energy vibrational modes, Consequently, the C-H vibrational modes could be excited first upon photoexcitation and causing an initial chemical reaction. Since we are not using extremely short laser pulses (shorter than 10 fs), selective excitation may be possible with the laser pulses utilized in the present experiment. Consequently, we believe that the probe pulses (~70 fs) might provide a significant spectral resolution and, hence, the measured decay time scales are approximated to a significant accuracy. However with time and frequency resolved CARS these effects can be minimized.[47] Several vibrational modes will participate in the IVR processes mainly in polyatomic molecules (explosives) in order to track IVR high temporal resolution, broadband excitation capability and coherent detection capability are a prerequisite. It was evident from the existing literature that the Raman modes of ACN are 380 cm^{-1}, 918 cm^{-1}, 1376 cm^{-1}, 1440 cm^{-1}, 2249 cm^{-1}, 2942 cm^{-1}. Additionally, we did not observe any solvent effects in these measurements. We recorded the CARS trace of pure acetonitrile (ACN) alone and could not see any Raman signatures of ACN vibrational modes. In principle, we must get the Raman signatures of the ACN those fall in the wavenumber window of 1033 cm^{-1}, though we repeated the experiment number of times. Recorded signature of the solvent was like noise without having any Raman peaks as shown in the figure 7.5 (a). Moreover, the pump (800 nm), Stokes (872 nm) beam wavelengths both are far from the absorption maximum 320-380 nm of the ACN solvent. We feel that the selected pump wavelengths are not in resonance with ACN absorption and perhaps this resulted in no Raman signatures for the pure solvent. Further, the intensity dependent CARS signal with a slope of 2.1 ensures the CARS process as shown in figure 7.5 (b).

Moreover, the relationship between IVR and solvent assisted vibrational energy transfer (VET) is so complex to understand even for simple molecules too. The molecules under the present study are novel tetrazoles require an extensive study to claim on relationship between IVR and solvent (ACN) assisted VET both qualitatively and quantitatively. Though the theoretical/experimental vibrational mode frequencies of tetrazoles are known, to comment on solvent assisted vibrational energy redistribution (IVR), instantaneous normal mode solvent spectrum that can be derived from force-force auto correlation functions is required.[48] Further, a few of the earlier reports[49-50] suggest that the solvent assisted IVR decays are longer in timescales and even could be extended to few picoseconds to nanoseconds. But the decay time scales obtained in the present experimental study are of the femtoseconds which confirms that there are no such significant solvent effects on IVR. Besides this, Hiromi et al.[51] mentioned that solute-solvent effects play a very little role in the process of IVR.

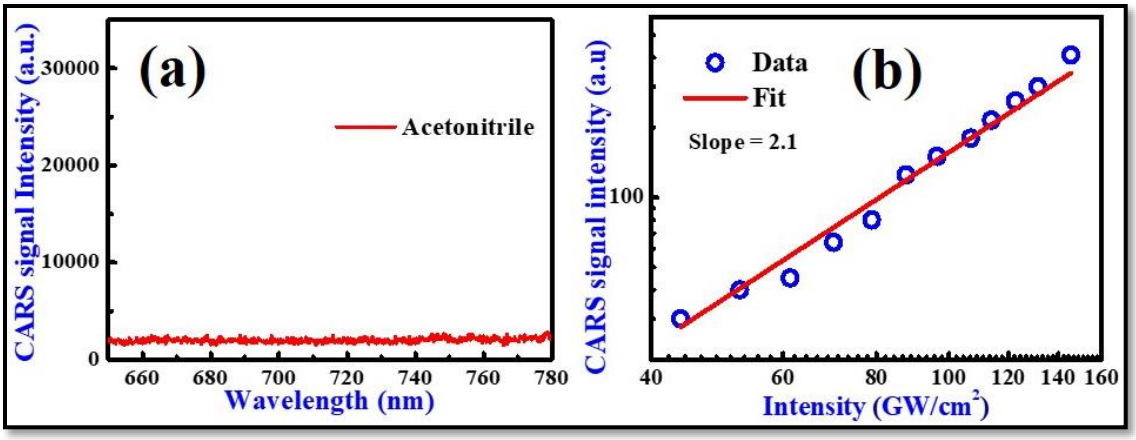

Figure 7.5 (a) Spectra of pure acetonitrile solvent at zero time delay (b) intensity dependent CARS signal.

Though we describe the decay quantum beats on the basis of intramolecular vibrational energy redistribution (IVR), the mentioned decay is complicated which comprises the contributions of many unidentified molecular dynamics those lead to the decoherence. In addition to the mentioned IVR, other possible decoherence processes include population decay, vibrational cooling (VC) may occurs within the molecule until it thermalizes the obtained excitation energy to the surrounding liquid phonon bath through the cascade vibrational relaxation processes.[52] Other possibility of the decoherence of the modes might be from the damping of vibrations of a particular molecule due to the inelastic collision with the surrounding molecules.[53]

Finally, We proclaim that, the results (quantum beats and temporal measurements of the decays) produced in the manuscript are certainly reproducible with the same accuracy. Moreover, as discussed by Nath et al.[54] recovery of Raman spectrum from time frequency domain in coherent Raman processes is less sensitive to experimental noises and fluctuations in pulse energies. Additionally, we could say the obtained beats from the FFT of the CARS trace beyond time zero are not experimental artefacts rather they are the Raman signatures of the solute. We could confirm this on the grounds of repeatability of the beats in different trails.

The beats were achieved by performing the FFT on the normalized CARS spectra. The corresponding FFT frequency is then converted to wavenumber by using following equation (1)

$$\nu\ (cm^{-1}) = \frac{FFT(frequency)*10^5}{3}. \qquad (1)$$

Coherent vibrational decay time (T_2) relates with the line width of the Raman mode under consideration as shown in the equation 2

$$\Delta\nu = \frac{1}{2\pi c\bar{T}_2} \qquad (2)$$

The Raman peak width corresponding to the 818 cm^{-1} was measured to be ~9.8 cm^{-1} whereas that from the measured average dephasing time (T_2) was ~35 cm^{-1}. This shows that, the decay must be longer than the estimated ~150 fs through the negative single exponential fit. But at the moment, we cannot completely and confidently explain the observed discrepancy. The fast decay of the coherent vibrational mode could possibly be explained in the following manner. In the present study, we the measured decay is the average dephasing time (T_2) of the corresponding modes that comprises two contributions namely the pure dephasing time (τ_{ph}) and life time of a vibrational excited state (T_1) of the as in the following equation (3)

$$\frac{1}{T2} = \frac{1}{2T1} + \frac{1}{\tau ph} \qquad (3)$$

(i) According to the report[56] it was evident that the how fast or slow the decay of a coherent vibration may be determined whether the mode of our interest is symmetric or asymmetric. According to Kozai et al.[56] coherent vibrational decay of an asymmetric mode is so fast compared to a symmetric vibrational mode. Accordingly, the asymmetry or symmetry of the mode 818 cm^{-1} corresponding to ring deformation, NO_2 scissoring, N=N-N wagging might result in the fast-coherent vibrational decay ~150 fs (ii) Another possibility for the measured fast decay of the vibrational mode corresponds to ~818 cm^{-1} may the quenching of the pure dephasing mechanisms.[57] Keifer et al.[34] also observed the fast average dephasing times (~350 fs) in the case of Imidazolium ionic liquids. As these tetrazole compounds are novel and this kind of work in these molecules is not yet attempted by any group, we can only explain the vibrational dynamics of tetrazole compounds limitedly. As we progress our work of time-resolved CARS studies on these molecules in future, we do hope that to retrieve the complete vibrational dynamics.

7.3.3 Steady-state absorption and emission spectra

Figure 7.6 shows the steady-state absorption and emission spectra of amino (6) and nitro (8) substituted tetrazole derivatives in DMF at ~50 µm concentration. The absorption spectra have two distinct bands located at 270 nm and 463 nm for sample 8 and 440 nm for sample 6. In contrast to sampling 8 the sample 6 showing its distinct vibrational signature at 525 nm. The peak at 270 nm is corresponds to the π - π* transition and the second peak at 463 nm and 443 nm are due to possible n - π* transitions.[58-61]

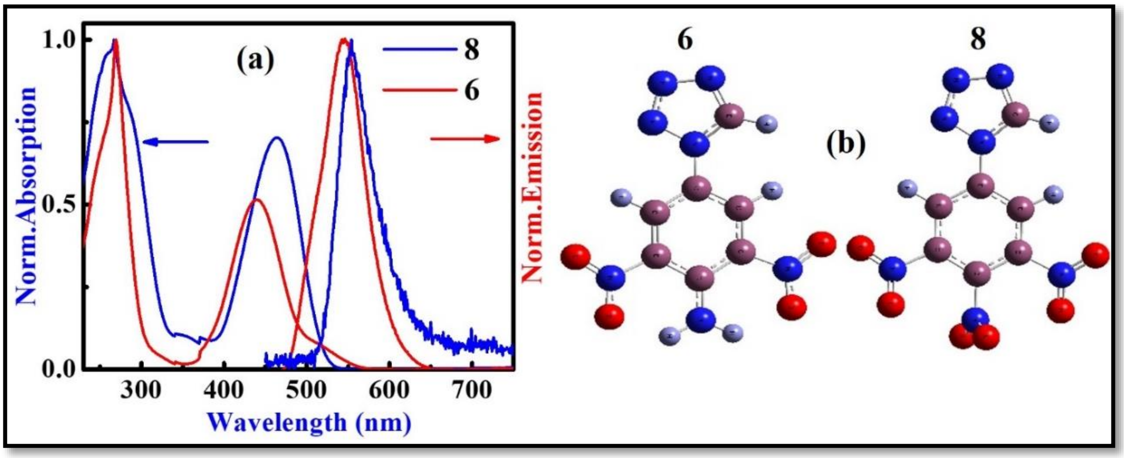

Figure 7.6 (a) Steady-state absorption and emission spectra and (b) molecular structure

Sample	Absorption (nm) [ε, M^{-1} cm^{-1}]		Emission (nm)	Radiative Lifetimes (µs)
	π-π*	n-π*		
6	269 [17000]	440 [10340] 525 [1516]	546	1.17
8	266 [18400]	463 [14040]	554	1.16

Table 7.3 Summary of the steady state absorption and emission peaks of two Amino (6) and Nitro (8) substituted tetrazoles measured in DMF (ε is the extinction coefficient).

Figure 7.6 right arrow shows the emission spectra of two molecules obtained by exciting with 400 nm wavelength and sample 6 emission at a maximum of 552 nm wherein the sample 8 the maximum emission is observed at 545 nm. It is evident from the data presented in figure 6, sample 8 seems to be less fluorescent compared to 6 due to the presence of nitro group. The photophysical parameters of the investigated molecules obtained from steady state measurements are summarized in table 7.3. As seen from figure 7.6 the presence of the nitro group increases the conjugation and reduces the band gap.

7.3.4 Transient absorption spectroscopy

The transient absorption (TA) experiments were performed at 400 nm photoexcitation with 0.2 µJ pump energy and probed with a white light continuum from 430-700 nm range in DMF as shown in figure 7.7. From figure 7.7(a), the TA spectra of compound 6 has negative signals at 450 nm and 545 nm wavelengths corresponding to the ground state bleach (GSB) or stimulated emission (SE). The negative band at 545 nm increased up to 5 ps and later it started decaying due to the depopulation of the excited states. The stimulated emission peak at 552 nm is overlaid within the ground state bleach signal at 545 nm. A positive absorption signal at 480 nm is observed due to the excited state absorption which is increased up to 1 ps time scale and later showed a decay, implying appearance of new excited state at this time scale. Later the positive band at 480 nm gradually dropped due to the depopulation of electronic excited states. A negative TA signal at 450 nm decayed within 1 ps probe delay, which possibly corresponds to the relaxation of higher electronic excited states (S_n) since the 400 nm photoexcitation allows the population to occupy higher electronic states. The TA spectra of compound 8 [figure 7.7(b)] has a strong bleach signal at 466 nm and a stimulated emission at 551 nm which decayed within 1 ps. It is evident from the TA spectra at 400 nm photoexcitation, compound 8 has recovered faster when compared to 6 and the presence of large nitrogen content in compound 8 allows the possible nonradiative decay pathways. The GSB signal at 468 nm increased up to 0.3 ps and later it decayed gradually. A positive band at 518 nm increased up to 3 ps time scale and later it starts decaying due to the depopulation of higher excited states and possible formation of new excited state at this time scale. To obtain a relevant information, a global analysis is performed based on a kinetic model[57] as shown in figure 7.8, and four-time constants are chosen to fit the TA spectra.

Figure 7.9 shows the results from the global analysis of compound 6 TA spectra. Figure 7.9(a) shows the species associated difference spectra (SADS), considering the 400 nm excitation the SADS1 is assigned to the internal conversion from S_n –S_1 state with strong negative bands at maximum of 450 nm and 575 nm, the population from S_n is transferred to hot S_1 state through internal conversion with life time of 350 fs. The SADS 2 has a positive signal at 480 nm and a negative signal at 550 nm which corresponding to the vibrational relaxation within S_1 state with lifetime of 50 ps. Whereas SADS3 corresponds to the excited singlet state S_1 with distinct peaks at 468 nm and 518 nm with lifetime of 116 ps which involves the intersystem crossing from S_1 to triplet state T_1. SADS4 corresponds to the T_1 state with life time of 1 μs this value is fixed with the value obtained from TRPL measurements. Figure 7.9(b) is the population decay profiles of corresponding species associated spectra and figure 7.9 (c-d) shows the goodness the fit initial and final probe delays and at different wavelengths.

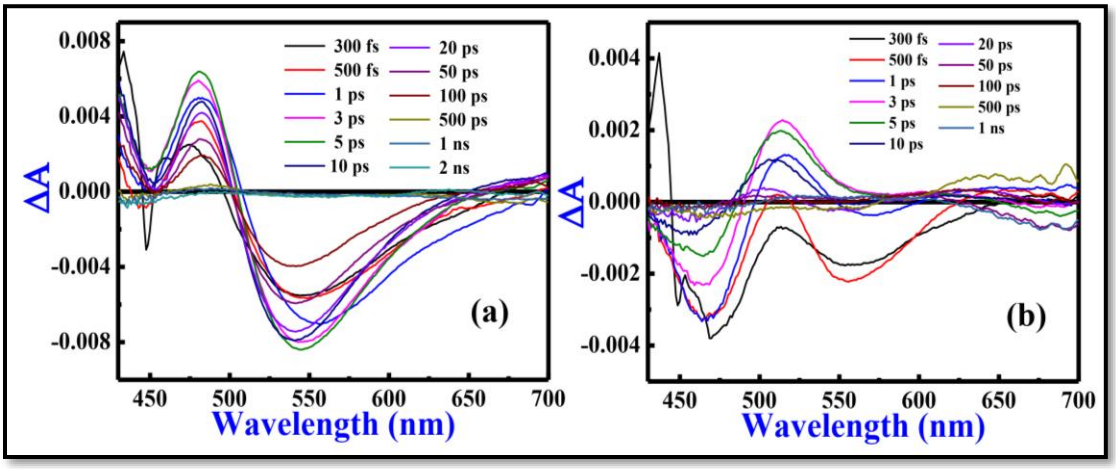

Figure 7.7 TA spectra of samples (a) 6 and (b) 8 at 400 nm photoexcitation.

Figure 7.10 shows the target analysis of compound 8 TA spectra. As seen from figure 7.10(a) the first SADS1 refers to the internal conversion to the higher excited electronic state Sn to the S1 state with strong negative signals at 454 nm and 546 having lifetime of 0.5 ps. The SADS2 spectra with life time of 1.8 ps is denote the vibrational relaxation within S_1, and SADS3 spectra corresponds to the S_1 state with lifetime of 7.4 ps, which contains possible intersystem crossing from S_1-T_0 with lifetime. The SADS4 spectra corresponds to the triplet state T_1 with life time of 1.1 μs. Figure 7.10(b) depicts the population decay profiles corresponding species associated spectra and figure 7.10(c) shows the goodness of fit at 0.3 ps and 1 ns probe delay times while figure 7.10(d) shows the kinetic profiles at different wavelengths.

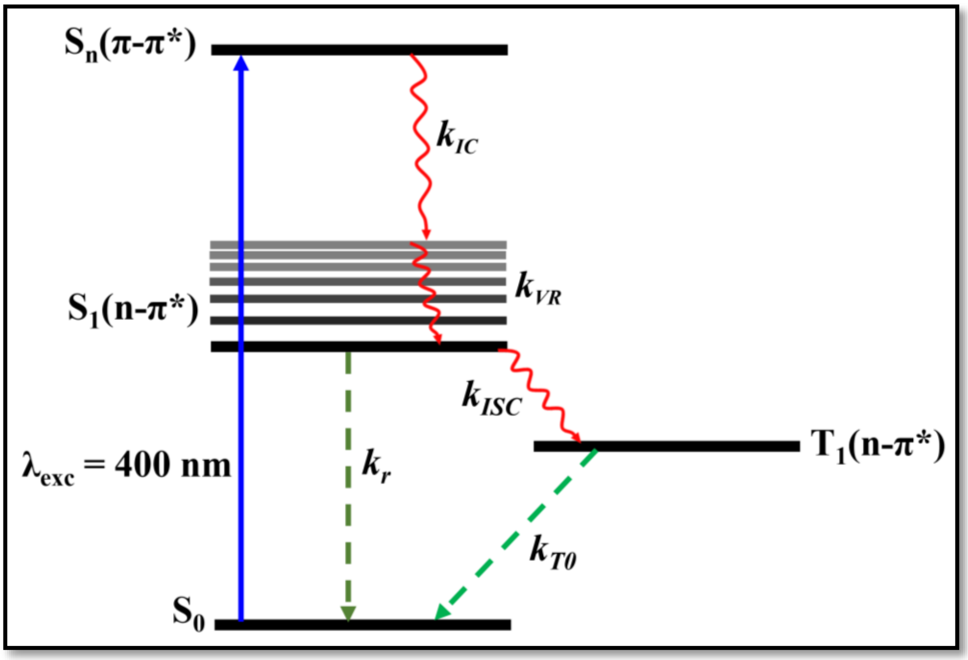

Figure 7.8 Schematic of the photophysical model used to fit the TA spectra.

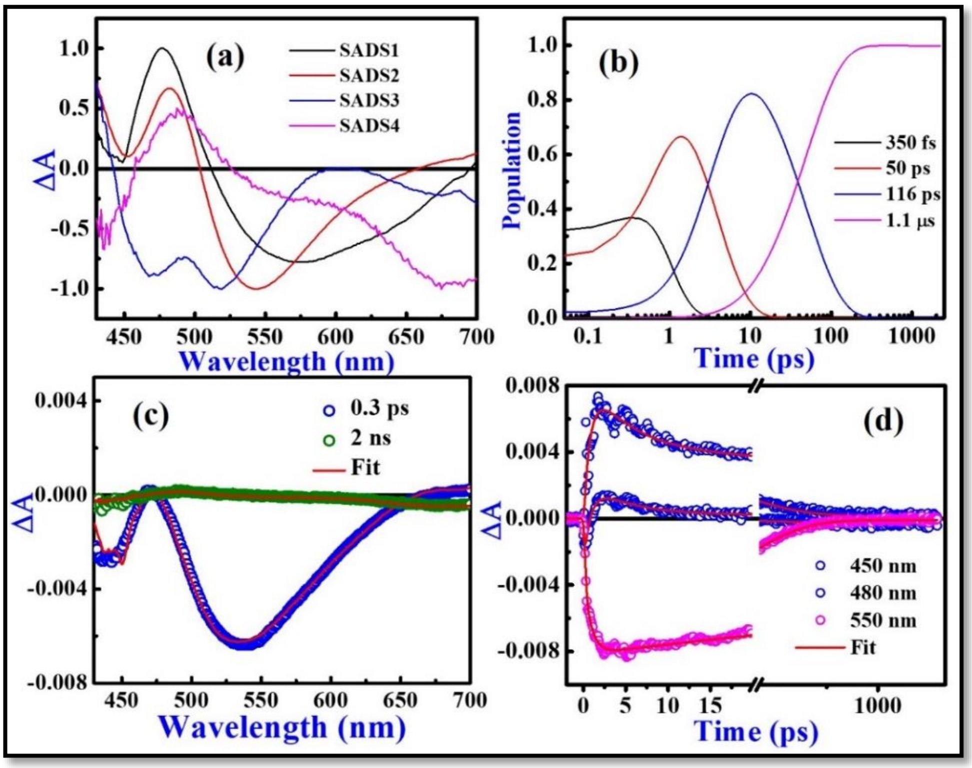

Figure 7.9 Global analysis of the TA spectra correspondent to compound 6 (a) species associated difference spectra (SADS) (b) Population decay profiles (c) global fit at 0.5 ps and 2 ns (d) kinetic profiles at different wavelengths after global fitting.

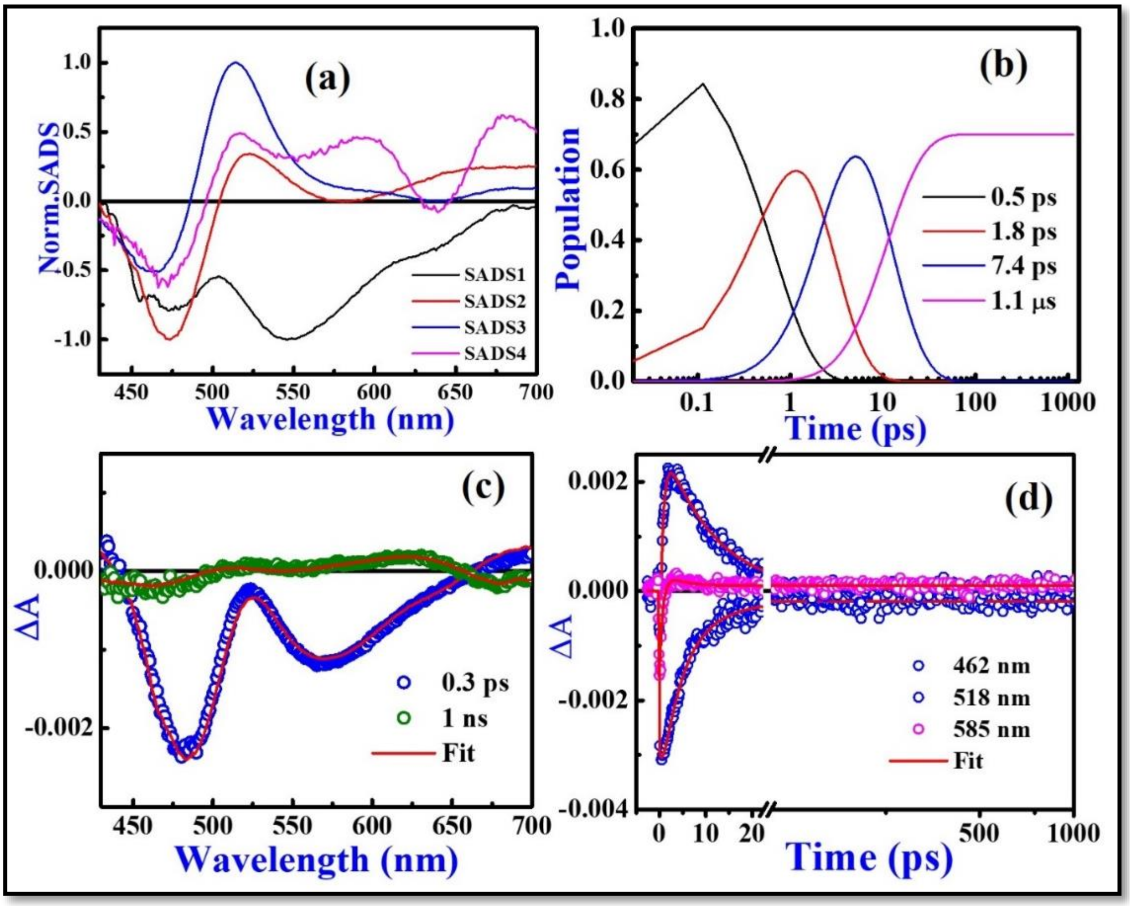

Figure 7.10 Global analysis of the TA spectra correspondent to compound 8 (a) global fit at 0.3 ps and 100 ps (b) kinetic profiles at different wavelengths after global fit (c) Evolution associated spectra (d) Population decay profiles (inset shows the short time scale).

In contrast to most nitroarenes the tetrazole molecules have weak fluorescence occurring from lowest singlet excited state as seen from the results obtained from the target analysis (figure 7.9-7.10).[61-62] The time scale of vibrational relaxation and intersystem crossing is faster in nitro substituted tetrazole which could be due to the steric effects or less conjugation between the nitro group and aromatic ring.[58, 63-66] It is observed that the nitro substituted tetrazole (8) shows the faster intersystem crossing (ISC) which depopulated the S_1 state within 1.8 ps. In contrast, the amino substituted tetrazole (6) have shown slower intersystem crossing with lifetime of 116 ps, which might be due to the push-pull effect arising from the amino group.[59, 64-66] Lopez-Arteaga et al.[68] studied photophysical properties of 2-nitrofluorene and 2-diethylamino-7-nitrofluorene they observed the amino 2-diethylamino-7-nitrofluorene exhibited slower ISC due to the stabilization of the first singlet excited state with respect to the triplet state due to the puss-pull effect induced by the diethylamino group. Vogt et.al.[69] have shown the intersystem crossing time of 200 fs in

2-methyl-1-nitronaphthalene, 2-nitronaphthalene, and 1-nitronaphthalene the population transfer S_1-T_1 is controlled by the energy gap between them. Further studies were needed to validate the obtained time constants such as fluorescence up-conversion and quantum mechanical calculations.

The lifetime of triplet state is recognized as an important feature in the energy conversion of EMs. Smit et al.[64] have proposed intramolecular steric hindrance effect on the triplet lifetime of HNS and 4, 4` and 2, 2`-DNS compounds in acetonitrile solution. He has observed that the triplet lifetime of HNS and 2, 2`-DNS is shorter than 4, 4`-DNS which is due to the steric effects this reduces the influence of the nitro groups on the triplet excited state conjugation, which might decrease a conjugation between the aromatic ring and ethylenic bridge or twisting can results in overlapping of potential energy surfaces of S_0 and T_1 in HNS. Chu et al.[58] have studied the excited state dynamics of 2,2`,4,4`,6,6`-hexanitrostilbene by using femtosecond TAS they have observed a fast ISC from S_1 to T_1 with lifetime of 6ps and long lived triplet state with 4 ns life time. Recently, Yi et.al.[59] investigated the ultrafast response of ortho-nitroaniline with the help of TAS and Chemometrics methods, and they have observed an intermediate state S^* in the ISC process. Also, the triplet state life time was found to be 2 ns, with ISC at 19 ps time scale from S^*-T_1. Nelson et al.[70] have investigated the photo-dissociation dynamics of nitromethane by using TAS and nonadiabatic excited-state molecular dynamics (NA-ESMD) simulations. They have found the formation of relatively fast NO_2 product with lifetime of 80 fs and slow product methyl nitrite with lifetime 480 fs at 266 nm photoexcitation. The UV excitation of HMX, RDX and imidazole energetic materials have shown the initial photo product of NO molecule.[14]

The intersystem crossing of the fluorescent state to triplet state plays a crucial role in the energy conversion process. The time scale of ISC is faster in nitro substituted tetrazole 7.4 ps than amino substituted tetrazole 116 ps, which might be due to the reducing coupling between triplet state due to stabilization of fluorescent state by the addition of electron donating amino group than electron withdrawing nitro group.[33] These studies of ultrafast dynamics helps to understand the decomposition of these energetic molecules at electronic excited states. However, in solid state these electronic excitations localize these excitations at different sites of the crystal (impurity defect or structure) leads to the formation of radicals by faster migration of electronic excitations in contrast to diffusion process where slow migration of heavy metal takes place.[8,44,71] The time-resolved photoluminescence (TRPL) was measured using FLS 1000 spectrometer (Edinburgh Instrument) using multichannel scaling technique. The samples were excited at 370 nm wavelength and the emission was observed at 544 nm and 521 nm for compound 8 and 6 in DMF solution as shown in figure 7.11. The experimental data was fitted using n-exponential decay function convolved with instrument response function (IRF).

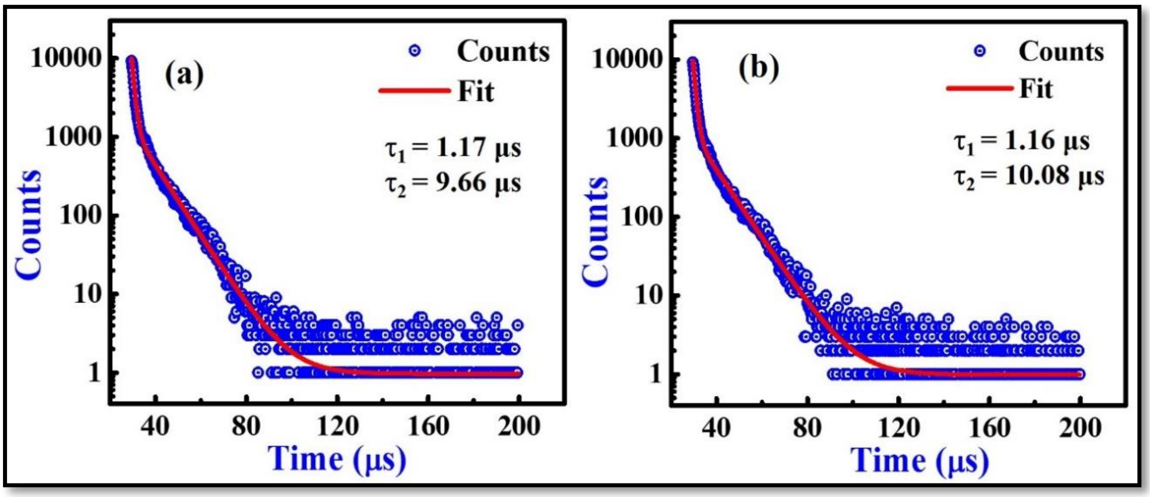

Figure 7.11 TRPL measurements of compound (a) 6 and (b) 8 in DMF at 370 nm photoexcitation.

7.4 Conclusions

Transient absorption spectroscopy on two nitro and amino substituted tetrazoles is performed at 400 nm photoexcitation. The target analysis of the TAS spectra reveals the possible relaxation mechanism. The nitro substituted tetrazole have shown faster vibrational relaxation at 1.8 ps and intersystem crossing time of 7.4 ps. The obtained time constants are nearly similar to the most of the energetic compounds. Also their ultrafast internal conversion and intersystem crossing suggest their application in energy deactivation or formation of radicals is quite faster as compared to other energetic materials. The tetrazole derivatives are showing fluorescence possibly from higher excited states at ultrafast time scale. The TRPL measurements confirms the long decay of triplet state with lifetime of ~1 µs which confirms the phosphorescence from its lowest triplet state to ground state. We believe, these studies help to understand the excited state molecular decomposition of energetic molecules.

From the fs TR-CARS experiments, the phase relaxation of vibrational modes (dephasing) as a function of probe delays observed to occur in a time scale ~120-200 fs and demonstrate that the intramolecular vibrational energy redistribution occurs in the same time scale. FFT of TR-CARS traces revealed the beat frequencies may be corresponding to the modes those involved in the inherent vibrational coupling of IVR. It was concluded that the modes at 1466 cm^{-1} (6) and 992 cm^{-1} (8) might be responsible for energy transfer in IVR. The results provided in this study might offer an intuition of the ultrafast response of these molecules and a basic insight of photon-induced chemistry of EMs.

References

1. Schmitt, M.; Knopp, G.; Materny, A.; Kiefer, W., The Application of Femtosecond Time-Resolved Coherent Anti-Stokes Raman Scattering for the Investigation of Ground and Excited State Molecular Dynamics of Molecules in the Gas Phase. *The Journal of Physical Chemistry A* **1998**, *102*, 4059-4065.
2. Schmitt, M.; Siebert, T.; Grabtchikov, A.; Orlovich, V.; Kiefer, W., Probing Molecular Dynamics by Femtosecond Time-Resolved Coherent Anti Stokes Raman Spectroscopy. *ASIAN JOURNAL OF PHYSICS* **2003**, *12*, 1.
3. Heid, M.; Schlücker, S.; Schmitt, U.; Chen, T.; Schweitzer-Stenner, R.; Engel, V.; Kiefer, W., Two-dimensional probing of ground-state vibrational dynamics in porphyrin molecules by fs-CARS. *Journal of Raman Spectroscopy*, **2001**, 32, 771-84.
4. Tolles, W. M.; Nibler, J. W.; McDonald, J. R.; Harvey, A. B., A Review of the Theory and Application of Coherent Anti-Stokes Raman Spectroscopy (CARS). *Applied Spectroscopy* **1977**, *31*, 253-271.
5. Heid, M.; Chen, T.; Schmitt, U.; Kiefer, W., Spectrally resolved fs-CARS as a probe of the vibrational dynamics of a large polyatomic molecule: magnesium octaethylporphyrin. *Chemical Physics Letters*. **2001**, 334, 119-126.
6. Sharma, J.; Beard, B. C.; Chaykovsky, M., Correlation of Impact Sensitivity with Electronic Levels and Structure of Molecules. *The Journal of Physical Chemistry* **1991**, *95*, 1209-1213.
7. Williams, F., Electronic States of Solid Explosives and Their Probable Role in Detonations. In *Advances in Chemical Physics*, John Wiley & Sons, Inc.: 2007; pp 289-302.
8. Kuklja, M. M.; Aduev, B. P.; Aluker, E. D.; Krasheninin, V. I.; Krechetov, A. G.; Mitrofanov, A. Y., Role of Electronic Excitations in Explosive Decomposition of Solids. *Journal of Applied Physics* **2001**, *89*, 4156-4166.
9. Bhattacharya, A.; Guo, Y.; Bernstein, E. R., Nonadiabatic Reaction of Energetic Molecules. *Accounts of Chemical Research* **2010**, *43*, 1476-1485.
10. Chu, G.; Lu, F.; Xin, J.; Xi, T.; Shui, M.; He, W.; Gu, Y.; Xiong, Y.; Cheng, K.; Xu, T., Excited-State Dynamics and Electron Transfer Process of 1,3,5-Triamino-2,4,6-Trinitrobenzene. *RSC Advances* **2016**, *6*, 55560-55567.

11. Adamo, C.; Jacquemin, D., The Calculations of Excited-State Properties with Time-Dependent Density Functional Theory. *Chem. Soc. Rev.* **2013**, *42*, 845-856.
12. Dreger, Z. A.; Gruzdkov, Y. A.; Gupta, Y. M.; Dick, J. J., Shock Wave Induced Decomposition Chemistry of Pentaerythritol Tetranitrate Single Crystals: Time-Resolved Emission Spectroscopy. *The Journal of Physical Chemistry B* **2002**, *106*, 247-256.
13. Zhurova, E. A.; Tsirelson, V. G.; Stash, A. I.; Yakovlev, M. V.; Pinkerton, A. A., Electronic Energy Distributions in Energetic Materials: Nto and the Biguanidinium Dinitramides. *The Journal of Physical Chemistry B* **2004**, *108*, 20173-20179.
14. Zhu, W.; Huang, H.; Huang, H.; Xiao, H., Initial Chemical Events in Shocked Octahydro-1,3,5,7-Tetranitro-1,3,5,7- Tetrazocine: A New Initiation Decomposition Mechanism. *The Journal of Chemical Physics* **2012**, *136*, 044516.
15. Ge, N.-N.; Wei, Y.-K.; Ji, G.-F.; Chen, X.-R.; Zhao, F.; Wei, D.-Q., Initial Decomposition of the Condensed-Phase Β-Hmx under Shock Waves: Molecular Dynamics Simulations. *The Journal of Physical Chemistry B* **2012**, *116*, 13696-13704.
16. Thurston, R.; Brister, M. M.; Tan, L. Z.; Champenois, E. G.; Bakhti, S.; Muddukrishna, P.; Weber, T.; Belkacem, A.; Slaughter, D. S.; Shivaram, N., Ultrafast Dynamics of Excited Electronic States in Nitrobenzene Measured by Ultrafast Transient Polarization Spectroscopy. *The Journal of Physical Chemistry A* **2020**.
17. Chen, M.-W.; You, S.; Suslick, K. S.; Dlott, D. D., Hot Spot Generation in Energetic Materials Created by Long-Wavelength Infrared Radiation. *Applied Physics Letters* **2014**, *104*, 061907.
18. Sun, Y.; Shui, M.; Xu, T.; Shu, Y.; Wang, X.; Zhao, Z.; Gu, Y., Laser-Induced Decomposition of 2,2',4,4',6,6'-Hexanitrostillbene at 263, 527 and 1053 Nm. *Asian Journal of Chemistry* **2013**, *25*, 4247-4250.
19. Dlott, D. D.; Fayer, M. D., Shocked Molecular Solids: Vibrational up Pumping, Defect Hot Spot Formation, and the Onset of Chemistry. *The Journal of Chemical Physics* **1990**, *92*, 3798-3812.
20. Chen, S.; Tolbert, W. A.; Dlott, D. D., Direct Measurement of Ultrafast Multiphonon up-Pumping in High Explosives. *The Journal of Physical Chemistry* **1994**, *98*, 7759-7766.

21. Nesbitt, D. J.; Field, R. W., Vibrational Energy Flow in Highly Excited Molecules: Role of Intramolecular Vibrational Redistribution. *The Journal of Physical Chemistry* **1996**, *100*, 12735-12756.
22. Rajchenbach, C.; Jonusauskas, G.; Rulliere, C., Sub-Picosecond Time-Resolved Spectroscopy of Energetic Materials : The Nitromethane and Nitro-Stilbenes. *Le Journal de Physique IV* **1995**, *05*, C4-365-C4-378.
23. Kenkre, V. M.; Tokmakoff, A.; Fayer, M. D., Theory of Vibrational Relaxation of Polyatomic Molecules in Liquids. *The Journal of Chemical Physics* **1994**, *101*, 10618-10629.
24. Menke, K., Organic Chemistry of Explosives, J. P. Agrawal, R. D. Hodgson. *Propellants, Explosives, Pyrotechnics* **2007**, *32*, 182-182.
25. Zeng, Z.; Guo, Y.; Twamley, B.; Shreeve, J. n. M., Energetic Polyazole Polynitrobenzenes and Their Coordination Complexes. *Chemical Communications* **2009**, 6014.
26. Gao, H.; Shreeve, J. n. M., Azole-Based Energetic Salts. *Chemical Reviews* **2011**, *111*, 7377-7436.
27. Kommu, N.; Ghule, V. D.; Kumar, A. S.; Sahoo, A. K., Triazole-Substituted Nitroarene Derivatives: Synthesis, Characterization, and Energetic Studies. *Chemistry - An Asian Journal* **2013**, *9*, 166-178.
28. Kumar, A. S.; Kommu, N.; Ghule, V. D.; Sahoo, A. K., Synthesis of Trifluoromethyl-Substituted N-Aryl-Poly-1,2,3-Triazole Derivatives. *Journal of Materials Chemistry A* **2014**, *2*, 7917.
29. Kommu, N.; Kumar, A. S.; Raveendra, J.; Ghule, V. D.; Sahoo, A. K., Synthesis, Characterization, and Energetic Studies of Polynitro Aryl-1,2,3-2 H-Triazoles. *Asian Journal of Organic Chemistry* **2015**, *5*, 138-146.
30. Kumar, A. S.; Ghule, V. D.; Subrahmanyam, S.; Sahoo, A. K., Synthesis of Thermally Stable Energetic 1,2,3-Triazole Derivatives. *Chemistry - A European Journal* **2012**, *19*, 509-518.
31. Kommu, N.; Balaraju, M.; Ghule, V. D.; Sahoo, A. K., Synthetic Manifestation of Nitro Substituted Tetrazole-N-(Hetero)Aryl Derivatives and Energetic Studies. *Journal of Materials Chemistry A* **2017**, *5*, 7366-7371.

32. Liu, X.; Zhang, W.; Song, Y.; Zheng, Z.; Lv, Z.; Yang, Y., Selective Excitation of Vibrational Modes and Probe for Asymmetric Intramolecular Energy Redistribution. *Physica Scripta* **2019**, *94*, 065402.
33. Wang, S.; Yang, Y.; Sun, Z.; Dlott, D. D., Fast Spectroscopy of Energy Release in Nanometric Explosives. *Chemical Physics Letters* **2003**, *368*, 189-194.
34. Namboodiri, M.; Kazemi, M. M.; Zeb Khan, T.; Materny, A.; Kiefer, J., Ultrafast Vibrational Dynamics and Energy Transfer in Imidazolium Ionic Liquids. *Journal of the American Chemical Society* **2014**, *136*, 6136-6141.
35. Zhao, Y.; Zhang, S.; Zhou, B.; Dong, Z.; Chen, D.; Zhang, Z.; Xia, Y., Spectrally Dispersed Femtosecond Cars Investigation of Vibrational Characteristics in Ethanol. *Journal of Raman Spectroscopy* **2014**, *45*, 826-829.
36. Niu, K.; Lee, S.-Y., Analysis of Time Resolved Femtosecond and Femtosecond/Picosecond Coherent Anti-Stokes Raman Spectroscopy: Application to Toluene and Rhodamine 6g. *The Journal of Chemical Physics* **2012**, *136*, 064504.
37. Wrzesinski, P. J.; Stauffer, H. U.; Kulatilaka, W. D.; Gord, J. R.; Roy, S., Time-Resolved Femtosecond Cars from 10 to 50 Bar: Collisional Sensitivity. *Journal of Raman Spectroscopy* **2013**, *44*, 1344-1348.
38. Kiefer, J.; Namboodiri, M.; Kazemi, M. M.; Materny, A., Time-Resolved Femtosecond Cars of the Ionic Liquid 1-Ethyl-3-Methylimidazolium Ethylsulfate. *Journal of Raman Spectroscopy* **2015**, *46*, 722-726.
39. Engel, S. R.; Miller, J. D.; Dedic, C. E.; Seeger, T.; Leipertz, A.; Meyer, T. R., Hybrid Femtosecond/Picosecond Coherent Anti-Stokes Raman Scattering for High-Speed Ch4/N2measurements in Binary Gas Mixtures. *Journal of Raman Spectroscopy* **2013**, *44*, 1336-1343.
40. Levitt, J. M.; Katz, O.; Silberberg, Y., Frequency-Encoded Multiplexed Cars Microscopy by Rapid Pulse Shaping. *Journal of Modern Optics* **2014**, *61*, 872-876.
41. Müller, N.; Brückner, L.; Motzkus, M., Invited Article: Coherent Raman and Mid-Ir Microscopy Using Shaped Pulses in a Single-Beam Setup. *APL Photonics* **2018**, *3*, 092406.
42. Kolesnichenko, P. V.; Tollerud, J. O.; Davis, J. A., Background-Free Time-Resolved Coherent Raman Spectroscopy (Csrs and Cars): Heterodyne Detection of Low-Energy Vibrations and Identification of Excited-State Contributions. *APL Photonics* **2019**, *4*, 056102.

43. Faeder, J.; Pinkas, I.; Knopp, G.; Prior, Y.; Tannor, D., Vibrational Polarization Beats in Femtosecond Coherent Anti-Stokes Raman Spectroscopy: A Signature of Dissociative Pump–Dump–Pump Wave Packet Dynamics. *The Journal of Chemical Physics* **2001**, *115*, 8440-8454.
44. Guo, Y.; Greenfield, M.; Bernstein, E., Decomposition of Nitramine Energetic Materials in Excited Electronic States: Rdx and Hmx. *The Journal of chemical physics* **2005**, *122*, 244310.
45. Patterson, J. E.; Dreger, Z. A.; Miao, M.; Gupta, Y. M., Shock Wave Induced Decomposition of Rdx: Time-Resolved Spectroscopy. *The Journal of Physical Chemistry A* **2008**, *112*, 7374-7382.
46. Yu, G.; Zeng, Y.; Guo, W.; Wu, H.; Zhu, G.; Zheng, Z.; Zheng, X.; Song, Y.; Yang, Y., Visualizing Intramolecular Vibrational Redistribution in Cyclotrimethylene Trinitramine (RDX) Crystals by Multiplex Coherent Anti-Stokes Raman Scattering. *The Journal of Physical Chemistry A* **2017**, *121*, 2565-2571.
47. Nath, S.; Urbanek, D. C.; Kern, S. J.; Berg, M. A., High-Resolution Raman Spectra with Femtosecond Pulses: An Example of Combined Time-and Frequency-Domain Spectroscopy. *Physical Review Letters* **2006**, *97*, 267401.
48. May, V.; Kühn, O., *Charge and Energy Transfer Dynamics in Molecular Systems*; John Wiley & Sons, 2008.
49. Assmann, J.; Benten, R. v.; Charvat, A.; Abel, B., Vibrational Energy Relaxation of Selectively Excited Aromatic Molecules in Solution: The Effect of a Methyl Rotor and Its Chemical Substitution. *Journal of Physical Chem. A* **2003**, *107*, 1904-1913.
50. Deàk, J. C.; Iwaki, L. K.; Rhea, S. T.; Dlott, D. D., Ultrafast Infrared–Raman Studies of Vibrational Energy Redistribution in Polyatomic Liquids. *Journal of Raman Spectroscopy* **2000**, *31*, 263-274.
51. Okamoto, H.; Yoshihara, K., Femtosecond Time-Resolved Coherent Raman Scattering from Β-Carotene in Solution. Ultrahigh Frequency (11 THz) Beating Phenomenon and Sub-Picosecond Vibrational Relaxation. *Chemical physics letters* **1991**, *177*, 568-572.
52. Shigeto, S.; Pang, Y.; Fang, Y.; Dlott, D.,Vibrational Relaxation of Normal and Deuterated Liquid Nitromethane. *Journal of Physical Chemistry* B, **2008**, 112, 232-241.

53. Wang W.; Sui, Y.; Zhang, N.; Wang, L.Q.; Wang, Y.H.; Wang, L.,; Wang, Q.; Kang, J.; Yang, Z.H.; Zhou, Y.Q.; Zhang, H.Z., Scanning the energy dissipation process of energetic materials based on excited state relaxation and vibration–vibration coupling. *Chinese Physics B*, **2018,** 27, 104205.
54. Nath, S.; Urbanek, D. C.; Kern, S. J.; Berg, M. A., High-Resolution Raman Spectra with Femtosecond Pulses: An Example of Combined Time- and Frequency-Domain Spectroscopy. *Physical Review Letters* **2006**, 97, 267401.
55. Sukhendu, N,; Urbanek, D.C,; Kern, S.J,; Berg, M.A., Simultaneous time and frequency detection in femtosecond coherent Raman spectroscopy. II. Application to acetonitrile. *Journal of Chemical Physics* **2007**, 127, 044307.
56. Kozai, T.; Kayano, Y.; Aoi, T.; Tsurumachia N.; Nakanishia, S., Coherent molecular vibrational dynamics of CH2 stretching modes in polyethylene studied by femtosecond-CARS. *Journal of Raman Spectroscopy*, **2015**, 46, 384–387.
57. Namboodiri, M.; Kazemi, M. M.; Khan, T. Z.; Materny, A.; Kiefer, J., Ultrafast Vibrational Dynamics and Energy Transfer in Imidazolium Ionic Liquids J. Raman Spectrosc. *Journal of American Chemical Society* **2014**, 136, 6136−6141.
58. Chu, G.; Shui, M.; Xiong, Y.; Yi, J.; Cheng, K.; Xu, T.; Xin, J.; Gu, Y., Investigation of Ultrafast Excited State Dynamics of 2,2′,4,4′,6,6′-Hexanitrostilbene Using Femtosecond Transient Absorption Spectroscopy. *RSC Adv.* **2014**, *4*, 60382-60385.
59. Yi, J.; Xiong, Y.; Cheng, K.; Li, M.; Chu, G.; Pu, X.; Xu, T., A Combination of Chemometrics and Quantum Mechanics Methods Applied to Analysis of Femtosecond Transient Absorption Spectrum of Ortho-Nitroaniline. *Scientific reports* **2016**, *6*, 19364-19364.
60. van Stokkum, I. H. M.; Larsen, D. S.; van Grondelle, R., Global and Target Analysis of Time-Resolved Spectra. *Biochimica et Biophysica Acta (BBA) - Bioenergetics* **2004**, *1657*, 82-104.
61. Khalil, O. S.; Bach, H. G.; McGlynn, S. P., Luminescence of Nitroaromatic Molecules. *Journal of Molecular Spectroscopy* **1970**, *35*, 455-460.
62. Lower, S. K.; El-Sayed, M. A., The Triplet State and Molecular Electronic Processes in Organic Molecules. *Chemical Reviews* **1966**, *66*, 199-241.
63. Sinha, H. K.; Yates, K., Ground- and Excited-State Dipole Moments of Some Nitroaromatics: Evidence for Extensive Charge Transfer in Twisted Nitrobenzene Systems. *The Journal of Chemical Physics* **1990**, *93*, 7085-7093.

64. Smit, K. J., Influence of Steric Effects on the Excited Triplet-State Lifetime of 2,2'-Dinitrostilbene and 2,2',4,4',6,6'-Hexanitrostilbene in Acetonitrile Solution. *The Journal of Physical Chemistry* **1992**, *96*, 6555-6558.
65. Orozco-Gonzalez, Y.; Coutinho, K.; Peon, J.; Canuto, S., Theoretical Study of the Absorption and Nonradiative Deactivation of 1-Nitronaphthalene in the Low-Lying Singlet and Triplet Excited States Including Methanol and Ethanol Solvent Effects. *The Journal of Chemical Physics* **2012**, *137*, 054307.
66. Plaza-Medina, E. F.; Rodríguez-Córdoba, W.; Peon, J., Role of Upper Triplet States on the Photophysics of Nitrated Polyaromatic Compounds: S1lifetimes of Singly Nitrated Pyrenes. *The Journal of Physical Chemistry A* **2011**, *115*, 9782-9789.
67. Ohta, K.; Naitoh, Y.; Tominaga, K.; Hirota, N.; Yoshihara, K., Femtosecond Transient Absorption Studies Oftrans- Andcis-1,3,5-Hexatriene in Solution. *The Journal of Physical Chemistry A* **1998**, *102*, 35-44.
68. López-Arteaga, R.; Stephansen, A. B.; Guarin, C. A.; Sølling, T. I.; Peon, J., The Influence of Push–Pull States on the Ultrafast Intersystem Crossing in Nitroaromatics. *The Journal of Physical Chemistry B* **2013**, *117*, 9947-9955.
69. Vogt, R. A.; Reichardt, C.; Crespo-Hernández, C. E., Excited-State Dynamics in Nitro-Naphthalene Derivatives: Intersystem Crossing to the Triplet Manifold in Hundreds of Femtoseconds. *Journal of Physical Chemistry A* **2013**, *117*, 6580-6588.
70. Nelson, T.; Bjorgaard, J.; Greenfield, M.; Bolme, C.; Brown, K.; McGrane, S.; Scharff, R. J.; Tretiak, S., Ultrafast Photodissociation Dynamics of Nitromethane. *The Journal of Physical Chemistry A* **2016**, *120*, 519-526.
71. Manaa, M. R.; Fried, L. E., Intersystem Crossings in Model Energetic Materials. *The Journal of Physical Chemistry A* **1999**, *103*, 9349-9354.

Chapter 8 Conclusions and Future Scope

8.1 Conclusions

To probe decomposition of energetic materials (EMs) at the molecular level and at sub-picosecond time scales is hugely challenging with impediments such as absorption in UV spectral range. The decomposition of EMs can directly be investigated by ultrafast spectroscopic techniques such as femtosecond (fs)/picosecond (ps) CARS and pump-probe techniques. Our main motive at ACRHEM is used to understand the behaviour of EMs upon ultrashort pulse illumination and probing their ultrafast processes at a molecular level; towards this, we have set up the CARS and TAS experiments at our department. We have initiated these studies in simple organic molecules (Porphyrins, Corroles, and phthalocyanines). We have performed extensive studies on their excited state dynamics and NLO properties using TAS (along with global and target analysis), Z-scan, and DFWM experiments. Further, we extend these studies to the EMs on tetrazole molecules.

We have performed broadband NLO studies of both organic and inorganic materials since their applications to lasers, photonic devices and biological applications. The materials possessing fast response and large $\chi^{(3)}$ are prerequisites for all these applications. Several substances of both organic and inorganic counterparts are engineered to meet the required optical properties for different applications. In the case of conjugated organic molecules and their delocalized π electrons plays a crucial role in tailoring NLO properties and excited-state dynamics. Therefore, it is essential to understand the nature of excited states upon photoexcitation in an ultrafast time domain. Where in the case of inorganic materials, we have specifically investigated the NLO properties and excited-state dynamics of perovskite nanocrystals (NCs) and metal nanoparticles (NPs). Recently, perovskite NCs have emerged as a promising material for optoelectronic device applications, possessing strong absorption and emission quantum yields with strong NLO properties (nonlinear absorption and refraction). They have found to exhibits large multi-photon absorption cross-section values, which are useful for biological, optical protection, photonic device applications. In this regard, we have done broadband NLO studies on $CsPbBr_3$ and Cs_4PbBr_6 NCs. The optical properties of perovskite NCs can be tuned by their dimensional reduction (thickness, size, morphology, surroundings/environment, and even preparation method). In the case of metal nanoparticles, the surface plasmon resonance (SPR) plays a vital role in their optical properties, which is use full for photodynamic therapy and optical device applications. The SPR can be tuned by the shape and size of the metal NPs from VIS-NIR range.

The primary outcomes from this thesis are outlined as follows,

- The development of state-of-the-art experimental techniques to characterize the light mater interaction upon ultrafast pulse illumination in our lab has been initiated. To investigate the NLO properties of organic/inorganic/perovskite materials, we have developed single-beam Z-scan and degenerate four-wave mixing (DFWM) techniques. The Z-scan provides both magnitude and sign of the nonlinear absorption and refractive index (n_2), which also contains the intuition into the change of population in their excited states. The DFWM data and analysis provides the true value of $\chi^{(3)}$ (third-order nonlinear susceptibility) as well as the response by performing the time-resolved DFWM experiment. So, both the techniques can be used to find the magnitude of $\chi^{(3)}$, where DFWM avoids the linear contribution and scattering effects that are usually found in Z-scan. Finally, these experimental setups were further implemented to develop the CARS experiment to investigate the ground states' vibrational dynamics of EMs. Apart from this, we have also used a commercial transient absorption spectrometer (HELIOS) to understand the molecular excited state dynamics. Thus, we have performed ground and excited-state dynamics of EMs to understand the decomposition mechanism, which is use full for end-user applications and further implementation of EMs.
- Ultrafast broadband NLO properties of $CsPbBr_3$ NCs this films were performed from 600 – 800 nm wavelength range using 1 kHz 50 fs laser pulses. We have found a large two-photon absorption cross-section values of ~10^5 GM and n_2 to be ~10^{-13} cm^2/W, originating from the quantum confinement effects. At higher input peak intensities, these NCs have shown a switching behaviour from RSA to SA. It was observed that $CsPbBr_3$ NCs and NRs depicted size and thickness dependent NLO properties with increasing saturation intensity at high peak intensities. On the other hand Cs_4PbBr_6 NCs (0D-PRM) have demonstrated large cross-section values compared to $CsPbBr_3$ NCs (The magnitudes of 2PA, 3PA, 4PA cross-sections were ~10^{-43}-10^{-44} cm^4s, ~10^{-75} cm^6s^2 and ~10^{-100} cm^8s^3, respectively). These higher NLO

coefficients and cross-sections are believed to be related to the strong confinement effects with a high dipole moment. DFWM measurements confirmed a fast response (~ 81-92 fs) of the order of input pulse duration, which ensures the pure electronic contribution to the obtained nonlinearity from these NCs and large $\chi^{(3)}$ (~10^{-9} esu). Therefore, the fast response, large $\chi^{(3)}$ and multi-photon absorption capabilities of these NCs are suitable for next-generation bio-imaging and photonic device applications.

- In the case of metal nanoparticles (NPs), we have successfully synthesized Au and $Au_{50}Ag_{50}$ alloy NPs using femtosecond laser ablation and studied their electron dynamics and NLO properties in aqueous medium using TAS and Z-scan methods. The $Au_{50}Ag_{50}$ alloy NPs has shown a fast response and possessed strong NLO coefficients. The obtained $\chi^{(3)}$ values were smaller compared to perovskite NCs which shows the superiority of perovskite NCs over metal NPs, along with their poor stability. The tunability of the plasmonic band and the fast response of these NPs are prerequisites in optical switching devices and biological applications.
- In the case of porphyrins (organic molecules), phenothiazine-porphyrin-phenothiazine (D-π-D) base porphyrins (HPHT, CPPHT, ZPPHT) molecules were synthesised, and their ultrafast photophysical and third-order NLO properties were investigated in solution form. It was observed that these porphyrins have depicted sizeable two-photon absorption cross-section values (~10^3 GM). We have also found that the TPA was the dominant mechanism contributing to the $\chi^{(3)}$. From the transient absorption studies, and with the help of global and target analysis, we have estimated the different rate constants corresponding to various photophysical processes. The copper and zinc-based porphyrin molecules have demonstrated faster internal conversion and vibrational relaxation compared to free-base porphyrin. This could be attributed to either a higher triplet quantum yield through intersystem crossing or reduction in the radiative lifetime in the case of ZPPHT due to the incorporation of Zinc in HPPHT. The TR-DFWM measurements confirmed the real electronic contribution to the obtained $\chi^{(3)}$.
- In the case of corroles, through the transient absorption experiments, and along with global and target analysis, we have found that the phosphorous corrole demonstrated faster internal conversion and vibrational also radiative and triplet relaxation compared to free-base corrole molecule. From the Z-scan measurements,

the Phosphorus corrole exhibited a strong two-photon absorption coefficient (4.6×10^{-13}cm/W) compared to free base corrole. This confirmed the effect of phosphorous ion due to its strong electron-withdrawing nature from the pentafluorophenyl group and possibly a strong intramolecular charge transfer between phosphorus and pentafluorophenyl group which creates the significant dipole moments. Also, the DFWM measurements confirm the slightly higher $\chi(3)$ value for phosphorous corrole with instantaneous response.

- Finally, we have extensively investigated the new tetrazole-N-(hetero)aryl derivatives for understanding their potential in energetic applications. We have applied fs TR-CARS and transient absorption techniques to comprehend the ground state vibrational dynamics and excited-state dynamics occurring in the sub-ps timescales. The TR-CARS experiment deliberates the possible IVR mechanism and phase relaxation (dephasing) of vibrational modes. From the CARS experimental data, we observed that the nitro substituted tetrazole demonstrated a faster dephasing time compared to an amino-substituted tetrazole. The transient absorption at 400 nm photoexcitation revealed that the nitro substituted tetrazole has a faster vibrational relaxation (S_1-S_1^*) and a faster intersystem crossing (S_1-T_0). This data confirmed the nitrogen-rich nitro substituted tetrazole demonstrated a faster relaxation due to its high nitrogen content with possible formation of nonradiative relaxation pathways. The time-resolved photoluminescence experiment proves the phosphorescence from T_0-S_0 nearly similar time scales (1 μs).

8.2 Future Plans

Ultrafast laser pulses (femtosecond - attosecond) are extensively used in time-resolved optical spectroscopy to unravel several quantum mechanical processes in materials. Multi-dimensional (temporal and spectral) spectroscopic methods are available, which provide information on molecular structure, chemical dynamics, intramolecular energy transfer processes, and many-body interactions. In the case of 2D spectroscopy, three distinct laser pulses will be used to excite the system, and the amplitude and phase of the third-order nonlinear signal could be recorded by a heterodyning method wherein, a fourth pulse - local oscillator interferes with the emitted field. By collecting the signal using a spectrometer [which gives the Fourier transform (FT)] along with spectral interferometry, one can obtain $\chi^{(3)}(t_1, t_2, \omega_3)$. With the help of additional FT concerning t_1, one gets the 2D map as a function of ω_1 (pump), ω_3 (probe), $\chi^{(3)}$. Thus, such 2D spectroscopy resembles the transient absorption spectra recorded at different values of ω_1. Therefore, 2D spectroscopy resolves both probe s well as pump frequency and permits one to find correlations between excitation and detection frequencies which provides information about spectral diffusion and energy relaxation. It overcomes the barrier of frequency and time resolution in conventional TAS.

In contrast to TAS, a broadband pump pulse gives both frequency and time resolution simultaneously with the help of FT. Also, the multiplex CARS with broadband stokes pulses helps to understand the IVR processes in EMs. Therefore, one can probe the decomposition processes easily. Along with this, the complicated CARS experiment can be simplified using pulse shaping techniques which can be used for standoff detection of hazardous materials/explosives. Hence, with the help of NIR TAS and multiplex CARS studies one can understand the complete vibrational dynamics and structural changes in energetic materials.

* * *

Intentional blank page

APPENDIX

Publications (From the thesis)

1. **Katturi, Naga Krishnakanth**, Shivaprasad Achari Balahoju, A. R. Ramya, Chinmoy Biswas, Sai Santhosh Kumar Raavi, Lingamallu Giribabu, and Venugopal Rao Soma. "Ultrafast photophysical and nonlinear optical properties of novel free base and axially substituted phosphorus (V) corroles." *Journal of Molecular Liquids* (2020): 113308.
2. **Katturi, Naga Krishnakanth**, Govind Reddy, Chinmoy Biswas, Sai Santosh Kumar Raavi, Lingamallu Giribabu, and Venugopal Rao Soma. "Ultrafast nonlinear optical properties and excited-state dynamics of Soret-band excited D-π-D porphyrins." *Optical Materials* 107 (2020): 110041.
3. **Katturi Naga Krishnakanth,** Byram Chandu, M. S. S. Bharathi, Sai Santhosh Kumar Raavi, and S. Venugopal Rao. "Ultrafast excited state dynamics and femtosecond nonlinear optical properties of laser fabricated Au and Ag50Au50 nanoparticles." *Optical Materials* 95 (2019): 109239.
4. **Katturi Naga Krishnakanth,** Sudipta Seth, Anunay Samanta, and S. Venugopal Rao. "Broadband ultrafast nonlinear optical studies revealing exciting multi-photon absorption coefficients in phase pure zero-dimensional Cs 4 PbBr 6 perovskite films." *Nanoscale* 11, no. 3 (2019): 945-954.
5. **Katturi Naga Krishnakanth,** Sudipta Seth, Anunay Samanta, and Soma Venugopal Rao. "Broadband femtosecond nonlinear optical properties of CsPbBr 3 perovskite nanocrystals." *Optics Letters* 43, no. 3 (2018): 603-606.
6. **Naga Krishnakanth Katturi**, Sarang Dev G, Nagarjuna Kommu, Gopala Krishna Podagatlapalli, Venugopal Rao Soma,. Ultrafast Coherent Anti-Stokes Raman Spectroscopic Studies of Nitro/Nitrogen Rich Aryl-Tetrazole Derivatives. Chemical Physics letters (*under review*).

Other Publications

7. Jagannath, G., Eraiah, B., Jayanthi, K., Keshri, S.R., Som, S., Vinitha, G., Pramod, A.G., **Krishnakanth, K.N.**, Devarajulu, G., Balaji, S. and Rao, S.V., 2020. Influence of gold nanoparticles on the nonlinear optical and photoluminescence properties of Eu

2 O 3 doped alkali borate glasses. *Physical Chemistry Chemical Physics*, *22*(4), pp.2019-2032.

8. Biswas, C., **Krishnakanth, K.N**., Lade, J.J., Chaskar, A.C., Tripathi, A., Chetti, P., Soma, V.R. and Raavi, S.S.K., 2019. Linear and femtosecond nonlinear optical properties of soluble pyrrolo [1, 2-a] quinoxalines. *Chemical Physics Letters*, *730*, pp.638-642.
9. Ketavath, R., **Katturi, N.K.,** Ghugal, S.G., Kolli, H.K., Swetha, T., Soma, V.R. and Murali, B., 2019. Deciphering the Ultrafast Nonlinear Optical Properties and Dynamics of Pristine and Ni-Doped CsPbBr3 Colloidal Two-Dimensional Nanocrystals. *The Journal of Physical Chemistry Letters*, *10*(18), pp.5577-5584.
10. Jagannath, G., Eraiah, B., Gaddam, A., Fernandes, H., Brazete, D., Jayanthi, K., **Krishnakanth, K.N.,** Venugopal Rao, S., Ferreira, J.M., Annapurna, K. and Allu, A.R., 2019. Structural and femtosecond third-order nonlinear optical properties of sodium borate oxide glasses: effect of antimony. *The Journal of Physical Chemistry C*, *123*(9), pp.5591-5602.
11. Gangareddy, J., Bheemaiah, E., Gandhiraj, V., James, J.T., Jose, J.K., **Naga, K.K**. and Soma, V.R., 2018. Nonlinear optical studies of sodium borate glasses embedded with gold nanoparticles. *Applied Physics B*, *124*(10), p.205.
12. Kolavekar, S.B., Ayachit, N.H., Jagannath, G., **NagaKrishnakanth, K**. and Rao, S.V., 2018. Optical, structural and Near-IR NLO properties of gold nanoparticles doped sodium zinc borate glasses. *Optical Materials*, *83*, pp.34-42.
13. Patil, P.S., Maidur, S.R., Shkir, M., AlFaify, S., Ganesh, V**., Krishnakanth, K.N**. and Rao, S.V., 2018. Crystal growth and characterization of second-and third-order nonlinear optical chalcone derivative:(2E)-3-(5-bromo-2-thienyl)-1-(4-nitrophenyl) prop-2-en-1-one. *Journal of Applied Crystallography*, *51*(4), pp.1035-1042.
14. Jagannath, G., Eraiah, B., **NagaKrishnakanth, K**. and Rao, S.V., 2018. Linear and nonlinear optical properties of gold nanoparticles doped borate glasses. *Journal of Non-Crystalline Solids*, *482*, pp.160-169.
15. Saripalli, R.K., **Katturi, N.K**., Soma, V.R., Bhat, H.L. and Elizabeth, S., 2017. Non-critically phase-matched second harmonic generation and third order nonlinearity in organic crystal glucuronic acid γ-lactone. *Journal of Applied Physics*, *122*(22), p.223110.

16. Sarma, M., Chatterjee, T., Bodapati, R., **Krishnakanth, K.N**., Hamad, S., Venugopal Rao, S. and Das, S.K., 2016. Cyclometalated iridium (III) complexes containing 4, 4′-π-conjugated 2, 2′-bipyridine derivatives as the ancillary ligands: Synthesis, photophysics, and computational studies. *Inorganic Chemistry*, *55*(7), pp.3530-3540.

International/national Conference Papers

17. **Katturi, N.K**., Jonnadula, V.S.K., Biswas, C., Raavi, S.S.K., Giribabu, L. and Soma, V.R., 2020, April. Ultrafast photophysical studies and femtosecond third-order nonlinear optical properties of a Soret-band excited zinc phthalocyanine. In *Organic Electronics and Photonics: Fundamentals and Devices II* (Vol. 11365, p. 113650W). International Society for Optics and Photonics.
18. **Krishnakanth, K.N.,** Bharathi, M.S.S., Hamad, S. and Rao, S.V., 2018, April. Femtosecond nonlinear optical properties of laser ablated gold nanoparticles in water. In *AIP Conference Proceedings* (Vol. 1942, No. 1, p. 050122). AIP Publishing LLC.
19. Maidur, S.R., Patil, P.S., **Krishnakanth, K.N**. and Rao, S.V., 2020, April. Ultrafast third-order nonlinear optical properties of a novel 4-methoxy-4’-nitro chalcone by z-scan and degenerate four-wave mixing techniques. In *Nonlinear Optics and its Applications 2020* (Vol. 11358, p. 113581C). International Society for Optics and Photonics.
20. Jagannath, G., Eraiah, B., **Krishnakanth, K.N**. and Rao, S.V., 2019, August. Influence of Eu3+ ions on nonlinear optical properties of alklai borate glasses at near-infrared wavelengths. In *AIP Conference Proceedings* (Vol. 2142, No. 1, p. 070024).
21. Ramesh, P., Jagannath, G., Pramod, A.G., **Krishnakanth, K.N**., Rao, S.V. and Kokila, M.K., 2019, August. Femtosecond nonlinear optical properties of heavy metal borate glasses studied using Z–scan technique. In *AIP Conference Proceedings* (Vol. 2142, No. 1, p. 070025).
22. **Krishnakanth, K.N.,** Rajesh, D. and Sunandana, C.S., 2016, May. Selective growth of ZnO thin film nanostructures: Structure, morphology and tunable optical properties. In *AIP Conference Proceedings* (Vol. 1731, No. 1, p. 080041).

Ultrafast Molecular Dynamics and Third-order Nonlinear Optical Studies of Novel Organic, Inorganic and Energetic Materials

by Katturi Naga Krishnakanth

Submission date: 24-Jul-2020 12:59PM (UTC+0530)
Submission ID: 1361519829
File name: Final_thesis_Kk.pdf (12.97M)
Word count: 43879
Character count: 231584

S. Venugopal Rao
24/7/2020

Dr. S. VENUGOPAL RAO
Professor
Advance Centre of Research in
High Energy Materials (ACRHEM)
UNIVERSITY OF HYDERABAD
Hyderabad-500 046. T.S. INDIA.

Ultrafast Molecular Dynamics and Third-order Nonlinear Optical Studies of Novel Organic, Inorganic and Energetic Materials

ORIGINALITY REPORT

39%	14%	38%	7%
SIMILARITY INDEX	INTERNET SOURCES	PUBLICATIONS	STUDENT PAPERS

PRIMARY SOURCES

1	✓ Naga Krishnakanth Katturi, Govind Reddy, Chinmoy Biswas, Sai Santosh Kumar Raavi, Lingamallu Giribabu, Venugopal Rao Soma. "Ultrafast nonlinear optical properties and excited-state dynamics of Soret-band excited D-π-D porphyrins", Optical Materials, 2020 Publication	8%
2	✓ Naga Krishnakanth Katturi, Shivaprasad Achary Balahoju, A.R. Ramya, Chinmoy Biswas et al. "Ultrafast photophysical and nonlinear optical properties of novel free base and axially substituted phosphorus (V) corroles", Journal of Molecular Liquids, 2020 Publication	8%
3	✓ Nagakrishakanth Katturi, Sudipta Seth, Anunay Samanta, Venugopal Rao Soma. "Broadband Ultrafast Nonlinear Optical Studies Revealing Exciting Multi-photon Absorption Coefficients in Phase Pure Zero-dimensional Cs4PbBr6 Perovskite Films", Nanoscale, 2018	5%

S. Venugopal Rao
24/3/2020

Dr. S. VENUGOPAL RAO
Professor
Advance Centre of Research in
High Energy Materials (ACRHEM)
UNIVERSITY OF HYDERABAD
Hyderabad-500 046. T.S. INDIA.

S. Venugopal Rao

Dr. S. VENUGOPAL RAO
Professor
Advance Centre of Research in
High Energy Materials (ACRHEM)
UNIVERSITY OF HYDERABAD
Hyderabad-500 046. T.S. INDIA.

S. Venugopal Rao

All selected publications belong to the students own papers

Effective similarity is 6% as per University norms (<10%).

S. Venugopal Rao
24/3/2020

Dr. S. VENUGOPAL RAO
Professor
Advance Centre of Research in
High Energy Materials (ACRHEM)
UNIVERSITY OF HYDERABAD
Hyderabad-500 046. T.S. INDIA.

Publication

---

4 ✓ K.N. Krishnakanth, Byram Chandu, M.S.S. Bharathi, Sai Santhosh Kumar Raavi, S. Venugopal Rao. "Ultrafast excited state dynamics and femtosecond nonlinear optical properties of laser fabricated Au and Ag50Au50 nanoparticles", Optical Materials, 2019

Publication

5%

S.Venugopal Rao

Dr. S. VENUGOPAL RAO
Professor
Advance Centre of Research in
High Energy Materials (ACRHEM)
UNIVERSITY OF HYDERABAD
Hyderabad-500 046. T.S. INDIA.

---

5 ✓ www.acrhem.org

Internet Source

3%

S.Venugopal Rao

Dr. S. VENUGOPAL RAO
Professor
Advance Centre of Research in
High Energy Materials (ACRHEM)
UNIVERSITY OF HYDERABAD
Hyderabad-500 046. T.S. INDIA.

---

6 ✓ acrhem.org

Internet Source

3%

S.Venugopal Rao

---

7 ✓ Naga Krishnakanth Katturi, Shivaprasad Achari Balahoju, A.R. Ramya, Chinmoy Biswas et al. "Ultrafast photophysical and nonlinear optical properties of novel free base and axially substituted phosphorus (V) corroles", Journal of Molecular Liquids, 2020

Publication

1%

S.Venugopal Rao

Dr. S. VENUGOPAL RAO
Professor
Advance Centre of Research in
High Energy Materials (ACRHEM)
UNIVERSITY OF HYDERABAD
Hyderabad-500 046. T.S. INDIA.

---

8 Submitted to University of Hyderabad, Hyderabad

Student Paper

1%

---

9 Govind Reddy, Pratyay Basak, Lathe A. Jones, Enrico Della Gaspera, Nanaji Islavath, Lingamallu Giribabu. "Crystalline D-π-D porphyrin molecules as a hole-transporting

<1%

All selected publications belong to the student's own papers

Effective similarity is 6% as per university norms.
(< 10%.)

S.Venugopal Rao
24/7/2020

Dr. S. VENUGOPAL RAO
Professor
Advance Centre of Research in
High Energy Materials (ACRHEM)
UNIVERSITY OF HYDERABAD
Hyderabad-500 046. T.S. INDIA.

59	Submitted to King Abdullah University of Science and Technology (KAUST) Student Paper	<1%
60	Submitted to VIT University Student Paper	<1%
61	W. G. Fisher, E. A. Wachter, Michael Armas, Colin Seaton. "Titanium: Sapphire Laser as an Excitation Source in Two-Photon Spectroscopy", Applied Spectroscopy, 2016 Publication	<1%
62	Govind P. Agrawal. "Fiber-Optic Communication Systems", Wiley, 2010 Publication	<1%
63	Somdatta Bhattacharya, Chinmoy Biswas, Sai Santosh Kumar Raavi, Jonnadula Venkata Suman Krishna et al. "Synthesis, Optical, Electrochemical, DFT Studies, NLO Properties, and Ultrafast Excited State Dynamics of Carbazole-Induced Phthalocyanine Derivatives", The Journal of Physical Chemistry C, 2019 Publication	<1%

Exclude quotes	On	Exclude matches	< 14 words
Exclude bibliography	On		

S.Venugopal Rao
24/7/2020

Dr. S. VENUGOPAL RAO
Professor
Advance Centre of Research in
High Energy Materials (ACRHEM)
UNIVERSITY OF HYDERABAD
Hyderabad-500 046. T.S. INDIA.

material for printable perovskite solar cells", Solar Energy, 2020
Publication

---

10 pubs.rsc.org <1%
Internet Source

---

11 Danilo Dini, Mário J. F. Calvete, Michael Hanack. "Nonlinear Optical Materials for the Smart Filtering of Optical Radiation", Chemical Reviews, 2016 <1%
Publication

---

12 Guoyang Yu, Yangyang Zeng, Wencan Guo, Honglin Wu, Gangbei Zhu, Zhaoyang Zheng, Xianxu Zheng, Yunfei Song, Yanqiang Yang. "Visualizing Intramolecular Vibrational Redistribution in Cyclotrimethylene Trinitramine (RDX) Crystals by Multiplex Coherent Anti-Stokes Raman Scattering", The Journal of Physical Chemistry A, 2017 <1%
Publication

---

13 Jing Yi, Ying Xiong, Kemei Cheng, Menglong Li, Genbai Chu, Xuemei Pu, Tao Xu. "A Combination of Chemometrics and Quantum Mechanics Methods Applied to Analysis of Femtosecond Transient Absorption Spectrum of Ortho-Nitroaniline", Scientific Reports, 2016 <1%
Publication

---

14 "Ultrafast Phenomena XIV", Springer Nature,

S Venugopal Rao 24/7/2020

Dr. S. VENUGOPAL RAO
Professor
Advance Centre of Research in
High Energy Materials (ACRHEM)
UNIVERSITY OF HYDERABAD
Hyderabad-500 046. T.S. INDIA.

Venugopal Rao Soma <soma_venu@uohyd.ac.in>

(no subject)

Antiplagiarism IGML <antiplagiarism@uohyd.ac.in> Fri, Jul 24, 2020 at 1:14 PM
To: Venugopal Rao Soma <soma_venu@uohyd.ac.in>
Cc: Krishnakanth K N <k.n.krishnakanth@uohyd.ac.in>

Good Afternoon!!
I am hereby sending the final report, submitted to Repository.

Ultrafast Molecular Dynamics and Third-order No...

--
With best regards

Librarian, IT Services
Indira Gandhi Memorial Library,
University of Hyderabad
E-mail: antiplagiarism@uohyd.ac.in
Phone: 91-40-23132616

[Quoted text hidden]